Red Galaxies at High Redshift

Red Galaxies at High Redshift

Proefschrift

ter verkrijging van
de graad van Doctor aan de Universiteit Leiden,
op gezag van de Rector Magnificus prof. mr. P.F. van der Heijden,
volgens besluit van het College voor Promoties
te verdedigen op donderdag 27 september 2007
klokke 16.15 uur

door

Stijn Elisabeth Raphaël Wuyts

geboren te Mortsel
in 1980

Promotiecommissie

Promotores:	Prof. dr. M. Franx Prof. dr. P. G. van Dokkum (Yale University)
Referent:	Dr. S. C. Trager (Rijksuniversiteit Groningen)
Overige leden:	Prof. dr. P. T. de Zeeuw Prof. dr. K. H. Kuijken Dr. P. van der Werf Dr. J. Schaye

Aan mijn ouders

Cover: Acryl on canvas by Imelda Wuyts

Table of contents

Chapter 1

Introduction

1.1 Large-scale structure formation

STANDARD Cold Dark Matter (CDM) theory explains the formation of large-scale structure from a nearly homogeneous soup to the cosmic web observed today by gravitational instabilities that grow over time (Press & Schechter 1974). Cold Dark Matter dominates the mass content of the universe and clumps into so-called halos. Primordial gas will sink to the bottom of the potential wells outlined by the dark matter halos, where it can cool and form small units of stars. As time evolves, CDM halos, and with it their baryonic content, will merge to build up larger structures (White & Rees 1978). Eventually, this results in web-like structure where filaments of young galaxies and ionized gas are surrounded by large, nearly empty voids. Large clusters of galaxies reside where the filaments meet. The bottom-up fashion of structure formation stems from the fact that the initial density fluctuations had most power at small scales.

Observations of the large-scale structure by the Sloan Digital Sky Survey (SDSS, York et al. 2000; Tegmark et al. 2004) and the 2 degree Field Galaxy Redshift Survey (2dFGRS, Colless et al. 2001; Sánchez et al. 2006) show a remarkable agreement with theoretical predictions and state-of-the-art simulations based thereupon (Springel et al. 2005). The evolution of the baryonic content, however, depends on complex dissipational processes that are far from understood.

1.2 Galaxy formation

What is the number of galaxy collisions, if any, needed to build up an M_* galaxy in the local universe? When in the history of the universe did most of the hierarchical build-up take place? What fraction of stars was formed in merger-triggered starbursts as opposed to quiescent episodes of star formation? What role do supermassive black holes at the centers of galaxies play in their evolution? How can the wide range in galaxy colors, from blue to red, be explained? These are all questions that astronomers are just about to address.

Observed scaling relations between galaxy properties provide stringent constraints in this quest for evolutionary scenarios. Apart from explaining the local color-magnitude relation (e.g., Sandage 1972; Bower, Lucey,& Ellis 1992), the Fundamental Plane (Djorgovski & Davis 1987; Dressler et al. 1987) and the correlation between the mass of supermassive black holes and their hosts (Magorrian et al. 1998), any model for galaxy formation should also account for the evolution of these scaling relations with redshift (e.g., Holden et al. 2004; van Dokkum & van der Marel 2007; Peng et al. 2006). Other

observations that need to be reproduced are the wide range of galaxy colors at low and high redshift, and their correlation with mass, morphology and environment.

The local universe

In the local universe, the bimodal color distribution of galaxies is well established (e.g., Stateva et al. 2001; Blanton et al. 2003; Baldry et al. 2004; Balogh et al. 2004). Blue galaxies are more abundant in numbers than red galaxies, but since the latter tend to be more massive, it is the population of red galaxies that contributes most (50% - 75%) to the total stellar mass in the nearby universe (e.g., Bell et al. 2003). Nearby blue galaxies generally have a disk-like morphology with spiral arms, whereas red galaxies show elliptical shapes. The morphological classification of galaxies into spirals and ellipticals goes back to Hubble (1926). The fraction of red, elliptical galaxies increases significantly as we probe denser environments (Oemler 1974; Davis & Geller 1976; Dressler 1980).

The distant universe

Determining if and how the described trends and scaling relations are present at high redshift, is a challenging task. First of all, it is crucial to obtain unbiased samples of distant galaxies.

Until the 1990s, radio galaxies and quasars were the only objects known at $z > 2$ (e.g., Schmidt 1974). Their extremely high luminosities are believed to be powered by an accreting central supermassive black hole. The searches for 'normal' distant galaxies, with a stellar origin of the light, have only been successful since the 1990s. Brute force spectroscopic surveys of all objects brighter than an optical magnitude limit in a field are not an efficient means of constructing representative high redshift galaxy samples. First, because only a small fraction of such a magnitude-limited sample will lie at high redshift. For example, less than 5% of the I-band limited $m_I < 24$ sample by Le Fèvre et al. (2005) has a redshift $z > 2.5$. Second, because distant galaxies with considerable mass but largely devoid of rest-frame UV emission would be missed by such surveys.

Over the past decade, several color selection criteria have been designed, often aided by technological developments, to identify galaxies in the redshift range $1.5 < z < 3.5$. Steidel and collaborators (e.g., Steidel et al. 1996) were the first to efficiently select distant galaxies with relatively unobscured star formation using the state-of-the-art optical observatories (probing the rest-frame UV light). With the advent of first near-infrared and then mid-infrared instruments on ground- and space-based telescopes, new selection methods became possible to select $z \sim 2$ galaxies (e.g., Franx et al. 2003; Daddi et al. 2004; Yan et al. 2004), resulting in samples that were often complementary to the optically selected objects.

Each of these color-selected samples is subject to its own biases. Small amounts of unobscured star formation may shift galaxies into or out of the selection window. Furthermore, due to the range in redshifts and galaxy types, the observed-frame colors used for their selection alone are not uniquely related to the physical properties of the galaxies. In view of a grand theory of galaxy evolution, it is important to un-

derstand the physical conditions such as mass, age and dust extinction for the various color-selected samples. Ideally, we want to go beyond selecting galaxies by color, and characterize the stellar population properties for a sample of galaxies that is complete above a certain mass limit, since mass is a more fundamental parameter than (observed-frame) color.

The nature of distant galaxies

The measurement of dynamical masses, used for the study of cluster early-types up to $z = 0.83$ in Chapter 2 of this thesis, becomes increasingly more difficult above $z \gtrsim 1$ (e.g., van Dokkum & Stanford 2003; Holden et al. 2005). We therefore rely on stellar mass estimates derived by modeling the broad-band spectral energy distributions (SEDs) over a wide wavelength range with stellar population synthesis codes (e.g., Bruzual & Charlot 2003; Maraston 2005).

Likewise, determining spectroscopic redshifts, although requiring less signal-to-noise than the measurement of velocity dispersions, becomes increasingly demanding in terms of telescope time as we move to higher redshifts and fainter sources. Instead, the study of mass-limited samples at high redshift relies mostly on photometric redshift estimates.

A reliable interpretation of the multi-wavelength views of distant galaxies in terms of physical properties such as mass, age, and dust content, is the key to a robust test of galaxy formation models.

1.3 This thesis

In this thesis, we measure the masses, ages, and dust extinctions of high redshift galaxies, with an emphasis on red galaxies. We aim to establish the accuracy with which these properties can be determined and identify biases that may occur. Finally, we use our observations to build a mass-limited sample of $1.5 < z < 3$ galaxies and test a model that explains the formation of red galaxies by collisions of gas-rich disk galaxies, during which a quasar phase is triggered (Hopkins et al. 2006).

Chapter 2

In Chapter 2, we examine the fundamental plane (FP) of early-type galaxies in two high-redshift clusters: MS 2053–04 at $z = 0.58$ and MS 1054–03 at $z = 0.83$. In particular, we focus on the zeropoint and scatter of this scaling relation between galaxy size, velocity dispersion and surface brightness, and its evolution with redshift between $z = 0$ and $z = 0.83$. We study the residuals from the FP as a function of color, mass, $H\beta$ linestrength and position within the cluster. We find that the residuals from the FP of MS 2053–04 are correlated with the residuals from the $H\beta - \sigma$ relation, suggesting that stellar populations are playing a role in shaping the FP. Considering only massive ($M > 10^{11}\ M_{\odot}$) early-type galaxies to avoid selection biases in our magnitude limited sample, we conclude that their B-band mass-to-light ratio evolves as $\log M/L_B \sim -0.47z$ and we find a formation redshift $z_{form} \sim 2.95$.

Chapter 3

Chapter 3 consists of two parts. First, we describe the construction of a B-to-24 μm multi-wavelength catalog for the GOODS Chandra Deep Field South (CDFS). The catalog contains optical, near-infrared and mid-infrared photometry for sources over an area of 138 arcmin^2 down to $K_{s,AB}^{tot} \lesssim 24.3$ (5σ). The photometry is based on observations with the Advanced Camera for Surveys (ACS) on the Hubble Space Telescope (HST), the ISAAC camera on the Very Large Telescope (VLT) and the IRAC and MIPS instruments on board the Spitzer Space Telescope. We cross-correlate our catalog with the 1 Ms X-ray observations (Giacconni et al. 2002) and with a large database of spectroscopic redshifts in the field. The latter allows us to quantify the reliability of photometric redshift estimates.

Next, we exploit the multi-wavelength data to estimate total IR luminosities for K_s-selected galaxies at $1.5 < z < 2.5$. We investigate which galaxies have the brightest total IR luminosities and which galaxies contribute most to the integrated total IR emission. We conclude that galaxies with red colors in the rest-frame UV, rest-frame optical, and rest-frame optical-to-NIR are dominating in the IR. However, at the reddest rest-frame optical colors, there also exists a population of galaxies that is undetected at 24 μm and therefore has low estimates for the total IR luminosity.

Chapter 4

Chapter 4 describes the optical spectroscopic follow-up of a sample of Distant Red Galaxies (DRG, Franx et al. 2003) with $K_{s,Vega}^{tot} < 22.5$, selected by the simple color criterion $J - K > 2.3$. All the successful redshift determinations (22% of the targeted sample) were based on emission lines. With 15 spectroscopic redshifts identified with only 2 at $z < 2$, we confirm the efficiency of this simple criterion to select red galaxies at high redshift. The two lower redshift sources are best fitted by a dusty stellar population. Two other DRGs show CIV in emission, indicative of the presence of an active galactic nucleus (AGN). We find that the photometric redshift code by Rudnick et al. (2003) is able to determine redshifts for DRGs (or at least the subclass with emission lines) to an accuracy of $\Delta z/(1+z) \sim 0.06$.

Chapter 5

In Chapter 5, we address the question what new insights the IRAC camera onboard Spitzer can reveal on the nature of galaxies at $2 < z < 3.5$. We approach this question by modeling the spectral energy distributions of distant galaxies in the Hubble Deep Field South (HDFS) up to very faint magnitudes ($K_{s,AB}^{tot} = 25$), including and excluding the IRAC photometric datapoints. We find that for blue galaxies in a field where deep NIR data is already available, the addition of IRAC offers little improvement. For red galaxies, on the other hand, the uncertainties in the estimated stellar mass decrease by a factor ~ 3 by adding IRAC. We caution however that significant systematic uncertainties in stellar mass estimates remain due to the differences between stellar population synthesis codes. Furthermore, IRAC helps to break the degeneracy between star-forming and quiescent red galaxies. Finally, we find that, as in the local universe, the most massive galaxies at high redshift are redder than lower mass galaxies, even

when allowing for complex star formation histories.

Chapter 6

A problem with addressing the quality of estimated stellar population properties of observed galaxies is that the 'true answer' is often not available. Therefore, we test the standard SED modeling using simulated galaxies for which we know exactly the ages and masses of its stellar components and the distribution of gas and dust in between. In order to do this, we derived synthetic broad-band photometry from snapshots of hydrodynamical merger simulations by Robertson et al. (2006) as they would be observed when placed at redshifts $1.5 < z < 3$. The choice for merger simulations allows us to test the performance of standard SED modeling for different types of galaxies: from disks to mergers and eventually ellipticals. We discuss the impact of the star formation history, dust distribution, metallicity and AGN activity on the recovered mass, age, dust reddening and extinction. Systematic underestimates in all these parameters occur during the star-forming episodes. The properties of red quiescent merger remnants, on the other hand, are recovered very well.

Chapter 7

Multi-wavelength studies of deep fields have revealed a large variety of galaxy types in the early universe: from relatively unobscured star-forming galaxies to dusty starbursts to quiescent massive red galaxies. Especially the existence of the latter population, whose strongly suppressed star formation has been confirmed by spectroscopic identifications of their Balmer/4000Å breaks, poses a strong constraint on galaxy formation models.

In the final Chapter of this thesis, we combine the observations of three deep fields (HDFS, MS 1054–03, and CDFS) to test a model by Hopkins et al. (2006) that aims to explain the formation of red galaxies. Briefly, the model assumes that every observed quasar is triggered by the collision between two gas-rich disk galaxies. Starting from that assumption, it is then possible to translate the observed quasar luminosity function at a range of redshifts (e.g., Ueda et al. 2003; Hasinger, Miyaji,& Schmidt 2005; Richards et al. 2005) to the demographics of galaxies expected in a particular redshift interval. Using the same simulations as described in Chapter 6, we compute the colors, number and mass densities of massive galaxies at $1.5 < z < 3$ predicted by this model and compare it to observed samples subject to identical selection criteria.

We find that post-quasar galaxies have similar colors as red quiescent galaxies. The observed number and mass densities of quiescent galaxies are consistent with the model predictions. The model is also able to account for the abundance of star-forming galaxies, albeit with large uncertainties. However, the color distribution of star-forming galaxies is not well reproduced, in particular the observed dusty starbursts have no counterparts in the model predictions. Several possible reasons for this discrepancy are discussed.

References

Baldry, I. K., Glazebrook, K., Brinkmann, J., Ivezić, Ž, Lupton, R. H., Nichol, R. C.,& Szalay, A. S. 2004, ApJ, 600, 681
Balogh, M. L., Baldry, I. K., Nichol, R., Miller, C., Bower, R.,& Glazebrook, K. 2004, ApJ, 615, L101
Blanton, M. R., et al. 2003, ApJ, 594, 186
Bower, R. G., Lucey, J. R.,& Ellis, R. S. 1992, MNRAS, 283, 1361
Bruzual, G.,& Charlot, S. 2003, MNRAS, 344, 1000
Colless, M., et al. 2001, MNRAS, 328, 1039
Daddi, E., Cimatti, A., Renzini, A., Fontana, A., Mignoli, M., Pozzetti, L., Tozzi, P.,& Zamorani, G. 2004, ApJ, 617, 746
Davis, M. & Geller, M. J. 1976, ApJ, 208, 13
Djorgovski, S.,& Davis, M. 1987, ApJ, 313, 59
Dressler, A. 1980, ApJ, 236, 351
Dressler, A., Lynden-Bell, D., Burstein, D., Davies, R. L., Faber, S. M., Terlevich, R. J.,& Wegner, G. 1987, ApJ, 313, 42
Franx, M., et al. 2003, ApJ, 587, L79
Hasinger, G., Miyaji, T.,& Schmidt, M. 2005, A&A, 441, 417
Holden, B. P., Stanford, S. A., Eisenhardt, P.,& Dickinson, M. 2004, AJ, 127, 2484
Holden, B. P., et al. 2005, ApJ, 620, 83
Hopkins, P. F., Hernquist, L., Cox, T. J., Robertson, B.,& Springel, V. 2006, ApJS, 163, 50
Magorrian, J., et al. 1998, AJ, 115, 2285
Maraston, C. 2005, MNRAS, 362, 799
Oemler, A. J. 1974, ApJ, 194, 1
Peng, C. Y., Impey, C. D., Rix, H.-W., Kochanek, C. S., Keeton, C. R., Falco, E. E., Lehár, J.,& McLeod, B. A. 2006, ApJ, 649, 616
Richards, G. T., et al. 2005, MNRAS, 360, 839
Robertson, B., Cox, T. J., Hernquist, L., Franx, M., Hopkins, P. F., Martini, P.,& Springel, V. 2006, ApJ, 641, 21
Sánchez, A. G., et al. 2006, MNRAS, 366, 189
Sandage, A. 1972, ApJ, 176, 21
Schmidt, M. 1974, ApJ, 193, 505
Springel, V., et al. 2005, Nature, 435, 629
Strateva, I., et al. 2001, AJ, 122, 1861
Tegmark, M. et al. 2004, ApJ, 606, 702
Ueda, Y., Akiyama, M., Ohta, K.,& Miyaji, T. 2003, ApJ, 598, 886
van Dokkum, P. G.,& Stanford, S. A. 2003, ApJ, 585, 78
van Dokkum, P. G.,& van der Marel, R. P. 2007, ApJ, 655, 30
Yan, H., et al. 2004, ApJ, 616, 63
York, D. G., et al. 2000, AJ, 120, 1579

Chapter 2

The detailed fundamental plane of two high-redshift clusters: MS 2053–04 at $z = 0.58$ and MS 1054–03 at $z = 0.83$

Abstract. We study the fundamental plane relation in high-redshift clusters using a sample of 26 galaxies in MS 2053–04 ($z = 0.583$) and 22 galaxies in MS 1054–03 ($z = 0.83$). The zero point and scatter are compared to results for lower redshift clusters in order to trace evolutionary effects. Furthermore, our large sample enables us to investigate correlations between residuals from the fundamental plane and other characteristics of the galaxies, such as color, $H\beta$ linestrength, spatial distribution, and mass. The observed scatter of the early-type galaxies with $\sigma > 100\ km\ s^{-1}$ around the fundamental plane is 0.134 and 0.106 in $\log r_e$ for MS 2053–04 and MS 1054–03 respectively. The residuals from the fundamental plane of MS 2053–04 are correlated with residuals from the $H\beta - \sigma$ relation, suggesting that stellar populations are playing a role in shaping the fundamental plane. The measured evolution in $\log M/L$ is influenced by selection effects, as galaxies with lower M/L in the Johnson B-band enter a magnitude-limited sample more easily. When we select high mass early-type galaxies to avoid this bias, we find $\log M/L_B \sim -0.47z$ and a formation redshift $z_{form} \sim 2.95$, similar to earlier results.

S. Wuyts, P. G. van Dokkum, D. D. Kelson, M. Franx & G. D. Illingworth
The Astrophysical Journal, **605**, 677 (2004)

2.1 Introduction

In the local universe early-type galaxies follow a tight scaling relation, known as the Fundamental Plane (FP). The relation between effective radius, central velocity dispersion and surface brightness $r_e \sim \sigma^{\alpha} I_e^{\beta}$, which is a plane in $(\log r_e, \log \sigma, \log I_e)$ space, was discovered by Djorgovski & Davis (1987) and Dressler et al. (1987). In combination with the virial theorem

$$M/L \sim \sigma^2 r^{-1} I_e^{-1} \tag{2.1}$$

the small scatter around the FP implies that, under the assumption of homology, the M/L ratios of early-type galaxies are well behaved and scale as

$$M/L \sim \sigma^{\alpha/\beta+2} r_e^{-(1+\beta)/\beta}. \tag{2.2}$$

As the M/L ratio increases with ageing of a stellar population, the FP is a useful tool in research on galaxy formation and evolution. Based on a sample of 226 E and S0 galaxies in 10 clusters of galaxies, Jørgensen, Franx,& Kjærgaard (1996, hereafter JFK96) concluded the local plane in the Johnson B band has the form:

$$\log r_e = 1.20 \log \sigma - 0.83 \log I_e + \gamma \tag{2.3}$$

which implies that

$$M/L \sim M^{0.28} r_e^{-0.07}. \tag{2.4}$$

Later studies on intermediate and high-redshift clusters of galaxies used the zero-point shift of the plane to estimate average formation redshifts of the stars in early-type galaxies (e.g., Bender et al. 1998; van Dokkum et al. 1998, hereafter vD98; Jørgensen et al. 1999; Kelson et al. 2000c, hereafter K2000; Pahre et al. 2001; van Dokkum & Stanford 2003). The scatter around the plane provides constraints on the spread in galaxy ages.

The slope of the FP (and other scaling relations) constrains systematic age trends with mass and other parameters. Any evolution of the slope of the FP with redshift implies that the ages of the stellar populations are correlated with galaxy mass. For the cluster CL1358+62 at z = 0.33 K2000 finds that the slope of the FP has not evolved significantly over the past ~ 4 Gyr. The sample of 5 bright MS 2053–04 galaxies used by Kelson et al. (1997, hereafter K97) to study the FP at z = 0.583 seemed to agree with the values of coefficients α and β as given by JFK96. However, the sample was too small to perform a proper fit. The same conclusions were drawn for MS 1054–03 at z = 0.83 based on 6 early-type galaxies (vD98). In this chapter, we investigate the FP of MS 2053–04 and MS 1054–03 early-type galaxies using larger samples spread over a larger range of distances from the brightest cluster galaxies (BCG). In Sect. 2.2 we discuss the spectroscopy, sample selection and velocity dispersions. Imaging and measurement of the structural parameters is described in Sect. 2.3. Zero point of the FP with JFK96 coefficients and scatter around the plane are discussed in Sect. 2.4. In Sect. 2.5 we study correlations between the residuals from the FP and various other properties of the galaxies. Finally the conclusions are summarized in Sect. 2.7. VEGA magnitudes are used throughout this chapter. We use $H_0 = 70\ km\ s^{-1}\ Mpc^{-1}$, $\Omega_\Lambda = 0.7$, and $\Omega_M = 0.3$, but note that our results are independent of the value of the Hubble constant.

2.2 Spectroscopy

2.2.1 Sample selection and observations

All spectra used in the FP analysis were obtained with the LRIS spectrograph (Oke et al. 1995) on the 10 m W.M. Keck Telescope. The data were obtained in a series of observing runs from 1996 to 2002. The majority of galaxies in our final sample were selected on the basis of their spectroscopic redshift and their I- or F814W-band magnitude. The samples were limited at $I \approx 22$ for all runs; galaxies with $I \lesssim 21$ were given highest priority in the mask designs. The redshift information came from a large I-selected spectroscopic survey of both clusters described in detail in Tran et al. (1999), van Dokkum et al. (2000), and Tran (2002). For the initial MS 1054–03 observing runs only limited redshift information was available, and we applied color criteria to select likely cluster members. Galaxies having $\Delta(R-I) - 0.25\Delta(B-R) < -0.4$, with $\Delta(R-I)$ and $\Delta(B-R)$ colors relative to the central galaxy, were excluded. The color ranges were chosen such that blue cluster members were unlikely to be excluded. The final FP sample of MS 1054–03 contains 19 galaxies that were selected with these mild color constraints. No morphological information was used in the selection process.

For most observations we used the 600 lines mm^{-1} grating blazed at 7500 Å; some of our earlier data were taken with the 831 lines mm^{-1} grating blazed at 8200 Å (see vD98). The wavelength coverage was typically ~ 3500 to $\sim 5400 \AA$ in the rest frame. Exposure times ranged from 7500 s to 33400 s and from 10500 s to 22800 s for the MS 2053–04 and MS 1054–03 galaxies respectively. The instrumental resolution was typically $\sigma_{inst} \sim 40 - 80\ km\ s^{-1}$ and signal-to-noise ratios ranged from 20 to $100 \AA^{-1}$ in the observed-frame (in the continuum).

A total of 43 galaxies (26 early-type) were observed in MS 2053–04. The MS 1054–03 sample contained 30 galaxies (14 early-type). The morphological classification is described in Sect. 2.3.3. Early-type galaxies include E, E/S0 and S0 morphologies.

2.2.2 Basic reduction

The spectra were reduced using our own software and standard IRAF software routines (see, e.g., Kelson et al. 2000b). The wavelength calibration was performed using the night sky emission lines. The typical rms scatter about the fitted dispersion solutions is about 1/15 of a pixel. Since the dispersion is about 1.28 Å pixel^{-1} for the data taken with the 600 mm^{-1} grating (and 0.92 Å pixel^{-1} for the 831 mm^{-1} data), the rms scatter is equivalent to velocity errors smaller than 5 km s^{-1}.

The flat-fielding accuracy is generally better than a percent, on small scales. The data have not been accurately flux-calibrated so on large scales, the notion of flat-fielding accuracy is not meaningful. There tend to be moderate-scale (k=100 Å^{-1}) residuals in the flat-fielding that are the result of a mismatch between the fringing in the flat-fields and the fringing in the data. Such inaccuracies in de-fringing the data have no effect on the velocity dispersions because the spectra are effectively filtered on those scales (and larger) in the process of matching the continua of the template and galaxy spectra.

The subtraction of the sky was performed using standard, published, and well-tested methods: for each galaxy the two-dimensional spectra were first rectified, and

then 1st- or 2nd-order polynomials were fit to the pixels on both sides of the galaxy, typically excluding the few arcsec where the galaxy is bright. An iterative, clipping routine was used to reject any remaining bad pixels from the fit, similar to what IRAF allows the user to do. These methods have been discussed elsewhere at great length and we choose not to bore the reader with very familiar territory. While more complicated and precise means of sky subtraction are now available (see Kelson 2003), these data were analyzed before such methods became available, and the accuracy of the sky subtraction performed in the "traditional" way is satisfactory for our purposes.

The slit widths varied slightly with each run, ranging from $0\farcs90$ to $1\farcs05$. The extraction apertures for MS 2053–04 and MS 1054–03 were 7 CCD rows (or $1\farcs5$).

2.2.3 Velocity dispersions

Velocity dispersions were measured with a direct fitting method (Kelson et al. 2000b). Details of the fitting procedure are given in Kelson et al. (2006). Direct fitting methods provide several advantages over Fourier-based techniques. Most importantly, pixels are no longer weighted uniformly in the computation of the fitting metric (in this case χ^2). As in Kelson et al. 2000b, we weight each pixel by the inverse of the expected noise (photon and electronic read noise). Furthermore, the spectra that exhibit strong Balmer absorption had those features given zero weight in the fitting, in order to minimize the contribution of those features to template mismatch error, and also to ensure that our estimates of σ reflected the old, underlying stellar populations. We typically fit the spectra over a $\sim 1000\,\AA$ wavelength range (in the rest frame). We used a range of template stars, from G5 through K3 and adopted the template star that gave the lowest mean χ^2. In both clusters, HD102494, a G9IV star, was the "best" template.

Both observations and simulations by Jørgensen et al. (1995b) showed that, at low S/N, measured velocity dispersions were systematically too large. At the same S/N, this systematic effect was largest for the galaxies with velocity dispersions below $100\,km\,s^{-1}$. Therefore, we omit all galaxies with $\sigma < 100\,km\,s^{-1}$ from our samples. Furthermore, we limit our samples to sources with an error in σ smaller than 15 %. Errors in the dispersion and velocity are initially determined from the local topology of the $\chi^2(\sigma, V)$ surface.

Seven MS 2053–04 galaxies with $\sigma > 100\,km\,s^{-1}$ were observed both during the 1997 and 2001 observing run. A direct comparison between the derived velocity dispersions (prior to the aperture correction) is presented in Figure 2.1. Generally, the agreement is good, with one outlier. All spectra have similar S/N. The rms value of $\frac{\sigma_{97}-\sigma_{01}}{\sqrt{d\sigma_{97}^2+d\sigma_{01}^2}}$ is 1.23, slightly higher than the expected value of 1. The mean deviation between the two runs is $-2 \pm 5\%$, consistent with zero. We conclude there is no evidence for systematic effects and conservatively multiply all errors by the factor 1.23.

The final sample consists of 26 galaxies (19 early-type) in MS 2053–04 and 22 galaxies (12 early-type) in MS 1054–03. We applied an aperture correction to a nominal aperture of $D = 3\farcs4$ at the distance of Coma (see JFK96). The final velocity dispersions have therefore been multiplied by a factor of 1.057 for MS 2053–04 and 1.062 for MS 1054–03. This correction allows for a fair comparison between clusters at a range of redshifts. The data are tabulated in Table 2.1.

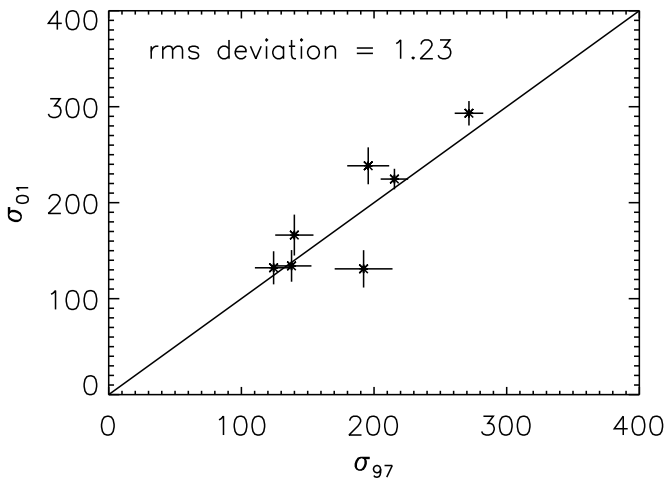

Figure 2.1 — A direct comparison of velocity dispersions for 7 galaxies in MS 2053–04. Measured σ values, prior to aperture correction, for the 2001 run are plotted against σ values from the 1997 spectra. Formal errors derived from $\chi^2(\sigma, V)$ are drawn. Based on this overlap sample, actual error bars are estimated to be 23% larger.

2.3 Imaging

For both MS 2053–04 and MS 1054–03 large HST WFPC2 mosaics were obtained, each consisting of 6 pointings. Both clusters were observed in the F606W and F814W filters. The layout of the MS 2053–04 mosaic is described in Hoekstra et al. (2002). Exposure times were 3300 s in F606W and 3200 s in F814W per pointing. The MS 1054–03 mosaic is described in van Dokkum et al. (2000); exposure times were 6500 s for each pointing and in each filter. Interlacing of the images improved the sampling by a factor $\sqrt{2}$ for MS 1054–03.

2.3.1 Structural parameters

In this section, we describe the measurement of effective radii r_e and surface brightnesses at those radii I_e. For the Johnson B passband, I_e in $L_\odot\ pc^{-2}$ is related to μ_e in *mag arcsec*$^{-2}$ as

$$\log I_e = -0.4(\mu_e - 27.0). \tag{2.5}$$

We created postage stamps sized $12\farcs8 \times 12\farcs8$ for the 26 MS 2053–04 and 22 MS 1054–03 galaxies and fit 2D $r^{1/n} (n = 1, 2, 3, 4)$ law profiles, convolved with Point Spread Functions (PSF), to the galaxy images. As PSFs depend on the positions of objects on the CCDs, we used Tiny Tim v6.0 to create an appropriate PSF for each galaxy. Other parameters determining the shape of the PSF are template spectrum (M type star), PSF size (3″), sampling and filter (F814W). The code allows simultaneous fitting of the object of interest and any neighbouring objects. The fits were restricted to radii of 3″ to 5″ around the objects, depending on their size. Image defects were masked in the fit, as well as neighbouring galaxies not well fitted by $r^{1/4}$ laws. All other pixels got uniform weight.

We performed the $r^{1/n}$ fits for Sersic numbers n = 1 (exponential), 2, 3 and 4 (de Vaucouleurs law). In this chapter, we always use r_e and I_e based on $r^{1/4}$ fits to all galaxies on the postage stamps, even if other Sersic numbers result in a better χ^2 of the fit. Fitting a $r^{1/4}$ profile resulted in a $\chi^2 < 1.5$ for 69% of all galaxies; 86% have $\chi^2 < 2$.

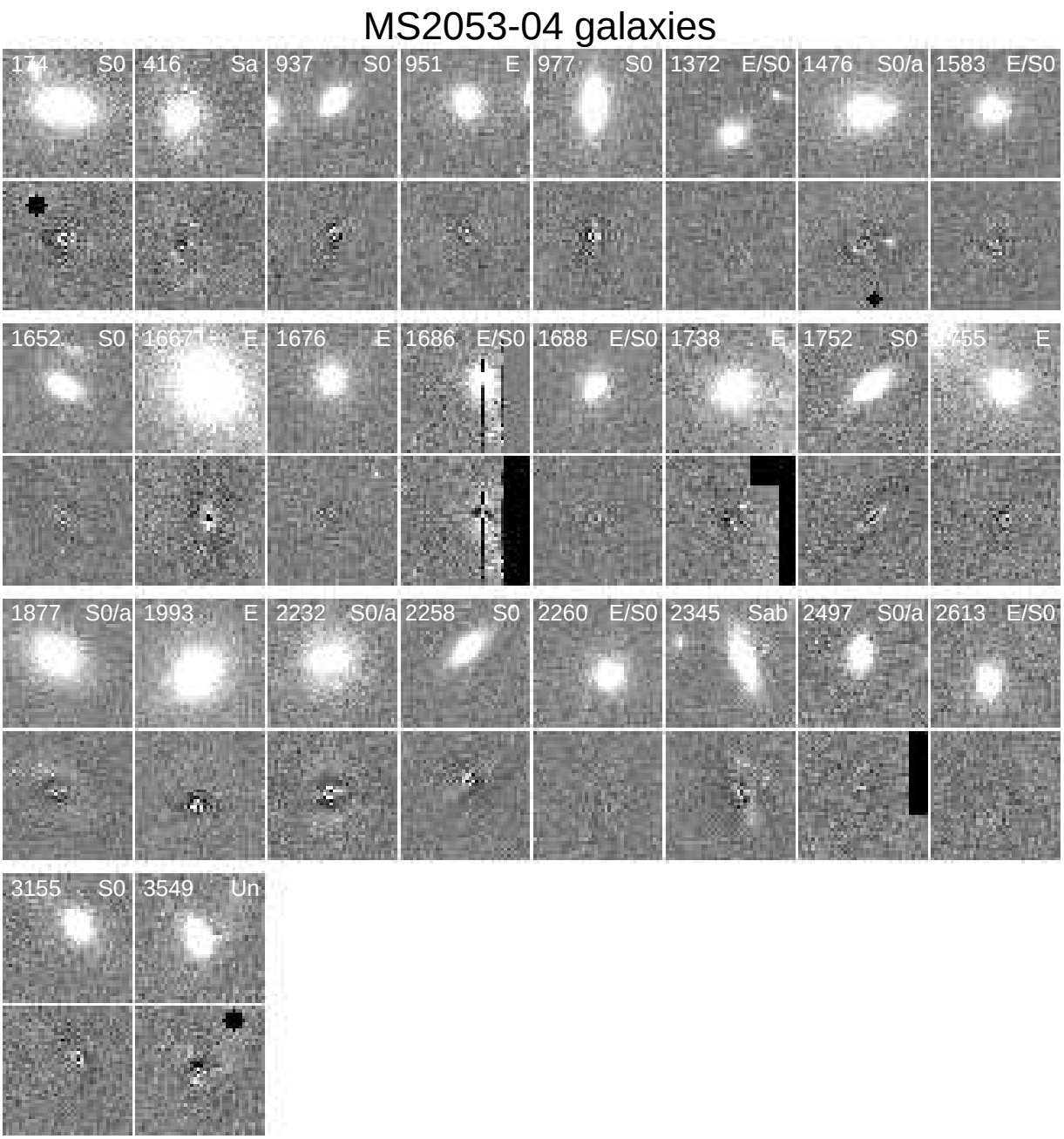

Figure 2.2 — $4'' \times 4''$ images (*upper*) and residuals (*lower*) after $r^{1/4}$ profile fitting for the galaxies in MS 2053–04. Masked regions are indicated in black. The postage stamps prove that our results for the early-type galaxies are not suffering from misclassifications or bad profile fitting.

The galaxies in our final samples together with the residuals after profile fitting are presented in Figure 2.2 (MS 2053–04) and Figure 2.3(MS 1054–03).

2.3.2 Error in the structural parameters

For MS 1054–03 each of the 6 pointings was observed twice, with a shift of 0.5 pixels, providing a direct way to measure the error in the structural parameters. From fits

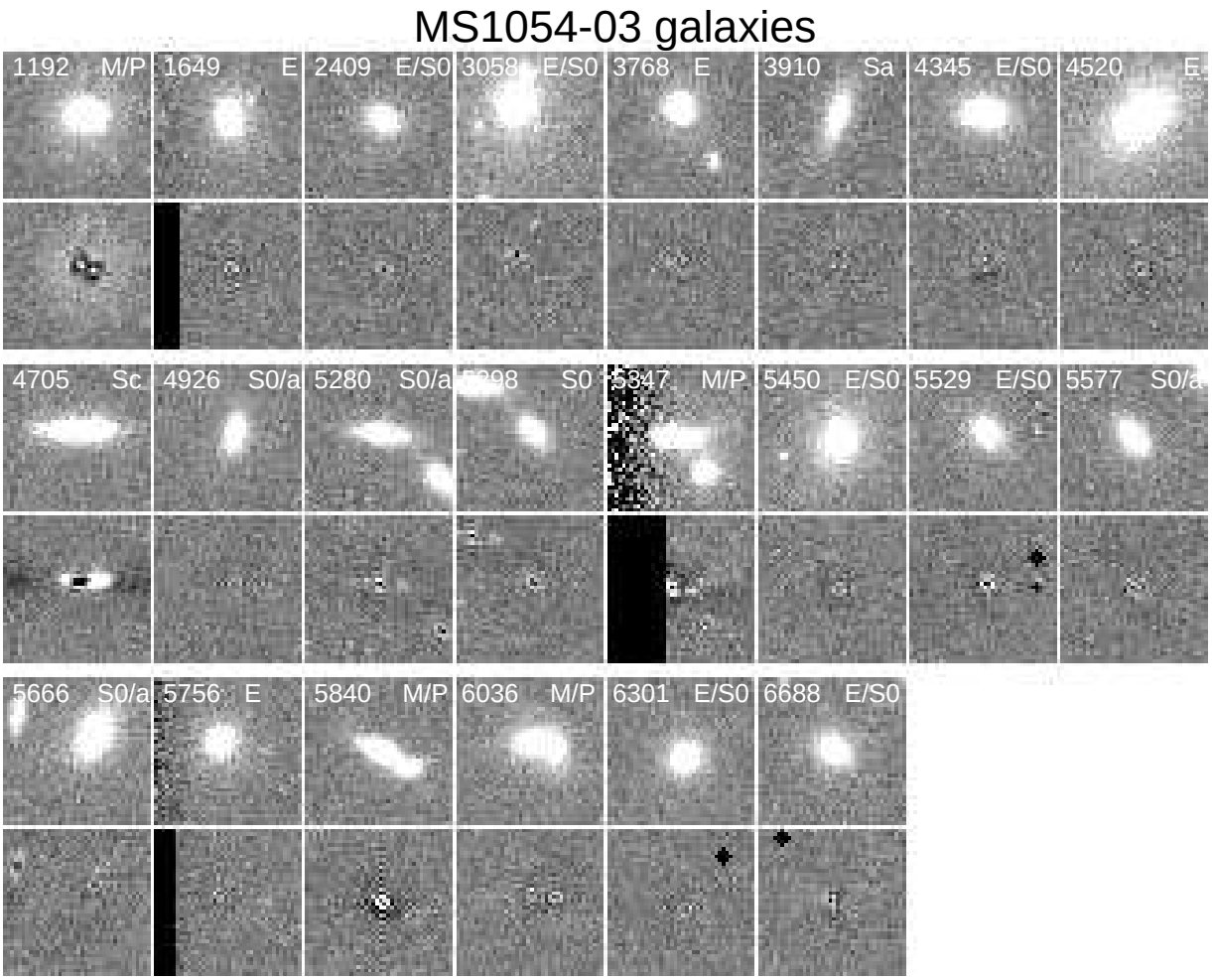

Figure 2.3 — $4'' \times 4''$ images (*upper*) and residuals (*lower*) after $r^{1/4}$ profile fitting for the galaxies in MS 1054–03. Masked regions are indicated in black. The postage stamps prove that our results for the early-type galaxies are not suffering from misclassifications or bad profile fitting.

to the two independent observations we infer that errors are small ($< 4\%$ in r_e) for galaxies larger than $0\farcs83$. The error in r_e rises to at most 18.5% for smaller sources. Though this might seem problematic, we note that this large error does not enter the FP analysis as the combination $r_e I_e^{-\beta}$ enters the FP. Using $\beta = -0.83$ from JFK96, the error in the FP parameter $r_e I_e^{0.83}$ is limited to $\sim 2.1\%$ rms, ignoring one outlier with 30% offset. The fit of a de Vaucouleurs profile to the outlier ID5347 with merger/peculiar morphology is clearly unstable. The uncertainty in the FP parameter is comparable to the $\sim 2.5\%$ rms error estimate from Kelson et al. (2000a). The small error in the FP parameter is an artifact of the slope of the de Vaucouleurs growth curve. Hereafter, we use the average of the independent r_e measurements (which reduces the error by $1/\sqrt{2}$) and the I_e corresponding to this average value, using the empirical result that $r_e I_e^{0.66}$ is the most stable combination of the structural parameters. In general we can conclude from the error analysis that random errors are small. Therefore the scatter found around the FP will not be due to errors in the photometry.

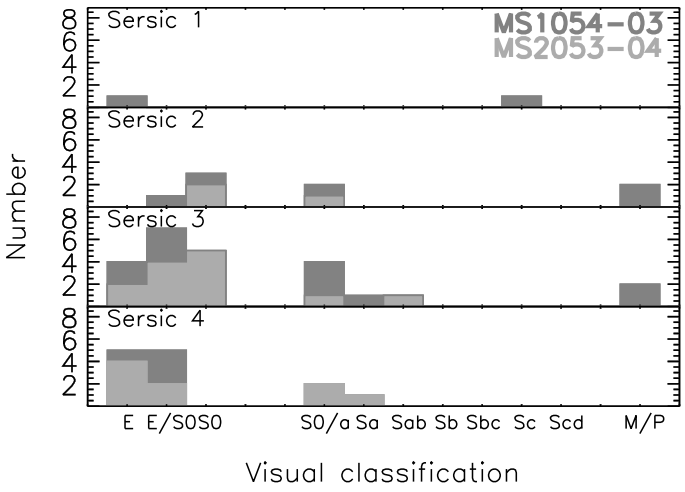

Figure 2.4 — Visual classification histogram for different best fitting Sersic numbers. Early-type morphologies generally correspond to Sersic numbers 3 and 4. A different greyscale is used for MS 2053–04 and MS 1054–03.

2.3.3 Visual and quantitative classifications

Galaxies were visually classified by P.G. van Dokkum, M. Franx,& D. Fabricant using the procedure as described in Fabricant, Franx,& van Dokkum (2000). In this chapter, we consider cluster members with early-type morphology (E, E/S0, S0). Late-type morphologies are also plotted, but are not included in fitting procedures unless mentionned otherwise. A quantitative alternative to the classification by eye is based on the Sersic number that results in the smallest χ^2 of the profile fit.

Figure 2.4 shows histograms of the visual classifications for the galaxies with best fitting Sersic number 1, 2, 3 and 4. As could be expected, early-type morphologies generally correspond to Sersic numbers 3 and 4. We note that the difference in χ^2 between n = 3 and 4 is often too small to consider them as a seperate class of objects. We conclude that the visual and quantitative classifications divide the sample in roughly the same bulge and disk dominated classes.

2.3.4 Transformation to rest-frame magnitude

In order to compare the FP of MS 2053–04 and MS 1054–03 with the FP of Coma at $z = 0.023$ we have to transform the effective radius to units of kpc. Furthermore, for a meaningful comparison it is necessary to study all data in a common photometric band in the rest frame of the galaxies. The observed F606W and F814W filters straddle the redshifted B_z band for $0.5 \leq z \leq 0.8$. Therefore, we transform the observed surface brightnesses to rest-frame B. The procedure is described in van Dokkum & Franx (1996). It involves an interpolation between F606W and F814W, and is different from applying a "K-correction". For $z = 0.583$ we find

$$\mu_{B_z} = \mu_{F814W} + 0.42(F606W - F814W) + 0.84, \tag{2.6}$$

and for $z = 0.83$

$$\mu_{B_z} = \mu_{F814W} + 0.01(F606W - F814W) + 1.13. \tag{2.7}$$

Table 2.1. FP sample

MS 2053–04								MS 1054–03							
ID	$\Delta R.A.$[a] [″]	ΔDec[a] [″]	$\log r_e$ [kpc]	μ_{B_z}[b] [$mag\ ''^{-2}$]	σ [km/s]	$F814W^T$ [mag]	Type	ID	$\Delta R.A.$[c] [″]	ΔDec[c] [″]	$\log r_e$ [kpc]	μ_{B_z}[b] [$mag\ ''^{-2}$]	σ [km/s]	$F814W^T$ [mag]	Type
174	9.34	-206.60	0.588	21.19	225 ± 13	19.68	S0	1192	136.10	-58.31	0.518	20.51	138 ± 15	20.24	M/P
416	29.26	-150.90	0.833	22.92	144 ± 14	20.48	Sa	1649	122.30	-16.89	0.565	20.80	243 ± 28	20.69	E
937	-30.58	-119.80	-0.223	18.20	127 ± 11	20.70	S0	2409	84.18	-24.01	0.574	21.26	287 ± 33	21.36	E/S0
951	-31.74	-118.00	0.288	20.88	151 ± 13	20.81	E	3058	52.73	-9.72	1.227	22.97	303 ± 33	19.83	E/S0
977	-72.15	-132.10	0.261	19.92	249 ± 11	20.03	S0	3768	38.86	-0.38	0.507	20.78	222 ± 24	21.04	E
1372	-39.50	-72.32	0.153	20.88	164 ± 14	21.55	E/S0	3910	32.00	-11.84	0.457	20.67	295 ± 42	21.23	Sa
1476	-38.26	-54.80	0.505	21.33	143 ± 16	20.04	S0/a	4345	21.51	-13.22	0.643	20.98	336 ± 34	20.55	E/S0
1583	-24.76	-41.87	0.289	21.04	143 ± 10	21.04	E/S0	4520	0	0	1.141	22.29	322 ± 30	19.48	E
1652	-9.65	-27.37	0.475	21.94	181 ± 13	21.12	S0	4705	6.10	8.34	1.006	22.22	253 ± 36	20.61	Sc
1667	0	0	1.103	22.65	292 ± 10	18.56	E	4926	-4.07	-3.68	0.387	20.43	310 ± 38	21.32	S0/a
1676	47.76	0.89	0.415	21.56	125 ± 14	20.76	E	5280	-20.46	20.82	0.548	21.06	259 ± 31	21.17	S0/a
1686	14.28	-12.29	0.408	21.58	129 ± 15	20.95	E/S0	5298	-21.74	19.24	0.550	21.38	284 ± 39	21.52	S0
1688	-9.00	-22.49	0.392	21.78	138 ± 13	21.31	E/S0	5347	-34.24	56.37	0.795	21.54	254 ± 24	20.58	M/P
1738	-23.00	-17.84	0.667	22.04	124 ± 13	20.01	E	5450	-46.30	-3.51	0.866	21.72	234 ± 26	19.98	E/S0
1752	-1.54	-9.86	0.353	21.08	151 ± 17	20.88	S0	5529	-37.79	31.29	0.549	20.99	182 ± 23	21.01	E/S0
1755	-1.14	-3.41	0.482	21.48	234 ± 23	20.23	E	5577	-43.54	48.16	0.501	20.75	305 ± 40	21.05	S0/a
1877	19.96	15.62	0.683	22.07	169 ± 14	20.17	S0/a	5666	-58.07	-83.77	0.731	21.20	286 ± 23	20.50	S0/a
1993	49.67	43.54	0.540	20.86	212 ± 8	19.40	E	5756	-59.26	97.86	0.551	20.91	232 ± 27	20.93	E
2232	-82.50	13.16	0.664	22.01	141 ± 12	20.16	S0/a	5840	-52.17	23.03	0.090	18.38	212 ± 26	20.66	M/P
2258	-2.50	45.70	0.264	20.77	134 ± 18	20.93	S0	6036	-63.37	-29.09	0.559	21.17	254 ± 22	21.18	M/P
2260	46.61	67.51	0.490	21.80	140 ± 14	20.81	E/S0	6301	-70.57	25.38	0.565	21.03	249 ± 24	20.99	E/S0
2345	16.82	67.38	0.601	21.99	152 ± 19	20.58	Sab	6688	-91.54	-41.79	0.458	20.50	274 ± 37	20.82	E/S0
2497	15.46	78.88	0.451	21.71	244 ± 14	21.13	S0/a								
2613	-23.80	71.80	0.584	22.39	171 ± 25	21.07	E/S0								
3155	-90.37	98.46	0.376	21.09	203 ± 18	20.64	S0								
3549	-29.45	165.70	0.307	20.70	155 ± 19	20.45	Un								

[a]Coordinates with respect to the BCG of MS 2053–04: ID1667 at (20:56:21.4; -04:37:50.8) (J2000).

[b]Surface brightnesses μ_{B_z} are corrected for galactic extinction and cosmological dimming.

[c]Coordinates with respect to the BCG of MS 1054–03: ID4520 at (10:56:59.9; -03:37:37.3) (J2000).

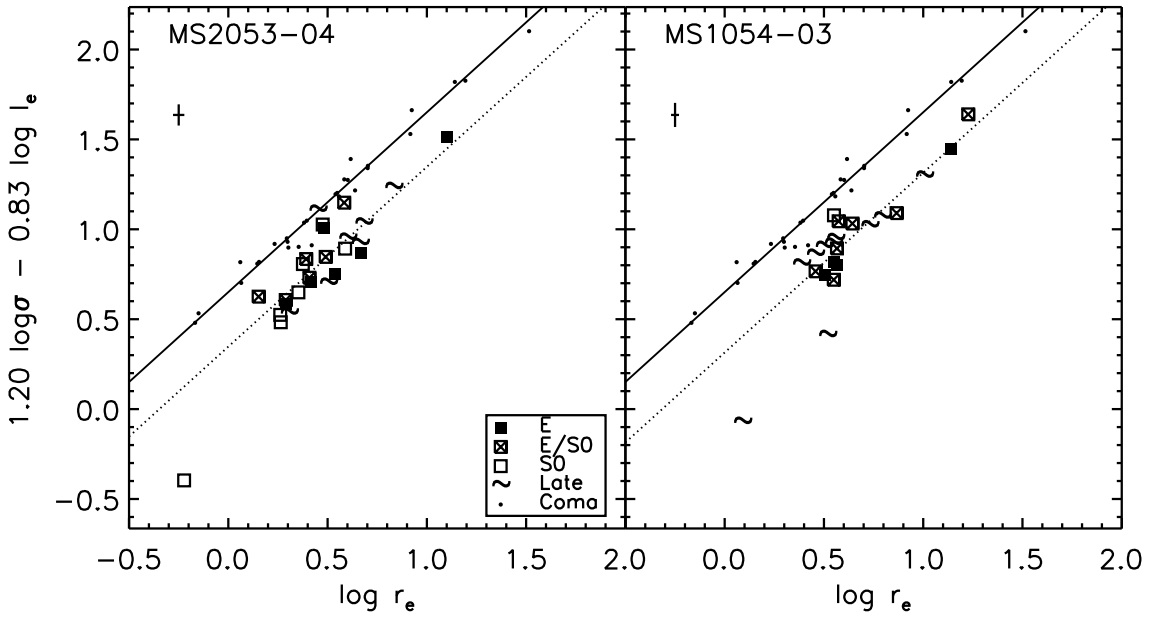

Figure 2.5 — The fundamental plane of clusters MS 2053–04 (z=0.583) and MS 1054–03 (z=0.83). The Coma FP is drawn for reference. Typical error bars are plotted in the upper left corner. Cluster galaxies in the higher redshift clusters follow the FP scaling relation, but with an offset with respect to Coma. Galaxies with early-type morphologies show a larger scatter than in the local universe.

The $F606W - F814W$ colors in (2.6) and (2.7) are obtained using SExtractor (Bertin & Arnouts 1996) with fixed apertures of $0\farcs7$ diameter. Extinction corrections for both fixed aperture colors and surface brightnesses were derived from Schlegel et al. (1998). Another correction compensates for cosmological dimming $\propto (1+z)^4$. The final samples are summarized in Table 2.1. Included are the coordinates with respect to the BCG, aperture corrected σ, r_e, μ_{B_z} corrected for galactic extinction and cosmological dimming, total $F814W^T$ magnitudes and morphological classifications.

2.4 The fundamental plane

In this section we discuss the FP relation in MS 2053–04 and MS 1054–03. For determination of the zero point and scatter we adopt the slope $(\alpha, \beta) = (1.20, -0.83)$ that JFK96 found for the local B-band FP. In Figure 2.5 we show the edge-on view of the FP for both clusters. Different symbols indicate different morphological types. For comparison the Coma FP is drawn as well. The galaxies in MS 2053–04 and MS 1054–03 follow a similar FP, but with an offset with respect to Coma.

2.4.1 Zero point and scatter

2.4.1.1 MS 2053–04

Using the biweight mean (Beers et al. 1990) we fit a zero point of the FP to the early-type galaxies in MS 2053–04. Under the assumption of homology, the zero-point shift of the FP traces the mean evolution of the galaxy M/L ratio. The observed zero-point off-

Table 2.2. MS 2053–04 and MS 1054–03 zero point and scatter around FP. Earlier results from K97 and vD98 are also in this Table.

Sample	# objects	$\Delta\log(M/L_B)$ (biweight mean)	$\Delta\log(M/L_B)$ (median)	Scatter in $\log r_e$ (biweight)
MS 2053–04 early-type	19	-0.365 ± 0.037	-0.404 ± 0.037	0.134 ± 0.034
MS 2053–04 Sersic34	23	-0.382 ± 0.028	-0.404 ± 0.028	0.111 ± 0.024
MS 2053–04 K97	5	-0.280 ± 0.036	-0.257 ± 0.036	0.058 ± 0.018
MS 1054–03 early-type	12	-0.405 ± 0.037	-0.418 ± 0.037	0.106 ± 0.023
MS 1054–03 Sersic34	15	-0.368 ± 0.027	-0.392 ± 0.027	0.086 ± 0.026
MS 1054–03 vD98	6	-0.393 ± 0.040	-0.405 ± 0.040	0.049 ± 0.018

set is $\Delta\log(M/L_B) = -0.365 \pm 0.037$, larger than $\Delta\log(M/L_B) = -0.280 \pm 0.036$ found by K97 based on older data for a sample of 5 bright galaxies. We will return to this issue in Sect. 2.5.

We find a biweight scatter for the early-type population in MS 2053–04 as large as 0.134 ± 0.034 in $\log r_e$, with the error derived from bootstrapping. This is significantly larger than the observed scatter of 0.071 around the B-band FP of local clusters (JFK96). After subtraction of the measurement uncertainties in quadrature, we find the intrinsic scatter for the early-type galaxies to be 0.124 ± 0.037. We conclude that measurement uncertainties cannot account for all of the enhanced scatter. Not only is the scatter larger than in the local universe, it also exceeds the previous result of 0.058 ± 0.018 obtained by K97. Our new measurements for 4 early-type galaxies that were also in the K97 sample give a scatter of 0.116 ± 0.035 (as opposed to 0.050 ± 0.018 for the original K97 data on these 4 galaxies). A larger sample and new data on previously studied objects leads to the conclusion that the early-type galaxies in MS 2053–04 show a considerably larger spread around the FP than early-type galaxies in the local universe.

We next analyzed the scatter of the bulge-dominated systems selected by Sersic index (3 and 4), which is a more objective method of classifying. The scatter drops by about 20% with respect to the classification by eye, to 0.111 ± 0.024. Using both visual and quantitative classifications, we find that bulge-dominated systems in MS 2053–04 are less tightly confined to a plane than in the local universe by a factor 1.5 to 2.

Zero-point shifts and scatters from biweight statistics are summarized in Table 2.2. Median zero-point shifts are given for comparison.

2.4.1.2 MS 1054–03

For the early-type galaxies in MS 1054–03 the zero-point offset agrees well with the previous result from vD98 ($\Delta\log(M/L_B) = -0.405 \pm 0.037$ for the new sample and $\Delta\log(M/L_B) = -0.393 \pm 0.040$ from vD98). The observed scatter is 0.106 ± 0.024, and the intrinsic scatter is 0.086 ± 0.028, consistent with the scatter in local clusters (JFK96). Using new measurements of 5 MS 1054–03 early-type galaxies studied by vD98, we obtain a biweight scatter of 0.062 ± 0.018, consistent with 0.047 ± 0.024 for the original vD98 data on these objects. As for MS 2053–04, the scatter decreases by roughly 20% if we select bulge-dominated systems by Sersic index (3 and 4) instead of by eye.

2.5 Correlations with other parameters

One of the striking effects we found in Sect. 2.4.1 is the large FP scatter for MS 2053–04. Here we investigate the cause of this enhanced scatter. In the case of a stellar population effect such as variations in age, metallicities or dust content, we expect the residual from the FP to correlate with color and linestrength indices. We also discuss the residual from the FP as a function of environment and investigate the dependence on galaxy mass. Hereafter, we again adopt the JFK96 slope and we express residuals from the FP as deviations in $\log(M/L_B)$. A positive residual means the galaxy has a higher M/L than the FP prediction based on its r_e and σ. The approach of measuring offsets along the surface brightness axis is physically intuitive since -if we ignore mergers- a galaxy only moves along this axis during its lifetime. For consistency with our FP analysis, we adopt locally determined slopes for all other considered scaling relations as well. In Figure 2.6 the residual from the FP is plotted against various properties for both clusters. Different symbols refer to different morphological classes. For each panel, the probability that a random sample has the same Spearman rank order correlation coefficient as the early-type galaxies in our sample, is printed in the corner.

2.5.1 The color-magnitude relation

The most straightforward interpretation for the large scatter is a stellar population effect. For age, metallicity, and dust trends, we expect lower M/L ratios than the FP prediction to correlate with bluer colors than the CMR prediction. We refer the reader to Tran et al. (2003) for the color-magnitude relation of MS 2053–04 and to van Dokkum et al. (2000) for the MS 1054–03 CMR. Similar to our FP analysis, we assume that the slope of the relation does not evolve and adopt the slope measured in the Coma cluster by Bower, Lucey,& Ellis (1992b). After conversion of the (F606W,F814W) photometry to Johnson U and V (using the same procedure as K2000), we fit a CMR zero point to the early-type galaxies in our samples. A positive residual ΔCMR in Figure 2.6a and Figure 2.6b corresponds to a redder color of the galaxy than the CMR prediction based on its total V magnitude. The Spearman rank order correlation coefficient points in the expected direction for a stellar population effect. However, the level of significance is insufficient to confirm that galaxies with lower M/L than the FP prediction are bluer and the higher (more evolved) ones are redder than the CMR prediction.

2.5.2 $H\beta$ linestrength

Apart from M/L ratio (residual from FP) and color (residual from CMR), strengths of absorption lines are a valuable tool for tracing stellar population effects. In this section we discuss the $H\beta$ index (expressed in $\AA$, see Trager et al. 1998). $H\beta$ is an age-sensitive parameter with only a minor contribution due to metallicity. For spectral reduction and derivation of linestrengths we refer the reader to Kelson et al. (2006).

The $H\beta - \sigma$ relation for early-type galaxies in the Coma cluster was derived from the $H\beta_G - \sigma$ relation presented by Jørgensen (1999). The $H\beta_G$ index is related to the Lick/IDS $H\beta$ index as $H\beta_G = 0.866 H\beta + 0.485$ (Jørgensen 1997). Assuming a non-evolving slope of the $H\beta - \sigma$ scaling relation, we fit a zero point to the relation in MS 2053–04 and MS 1054–03.

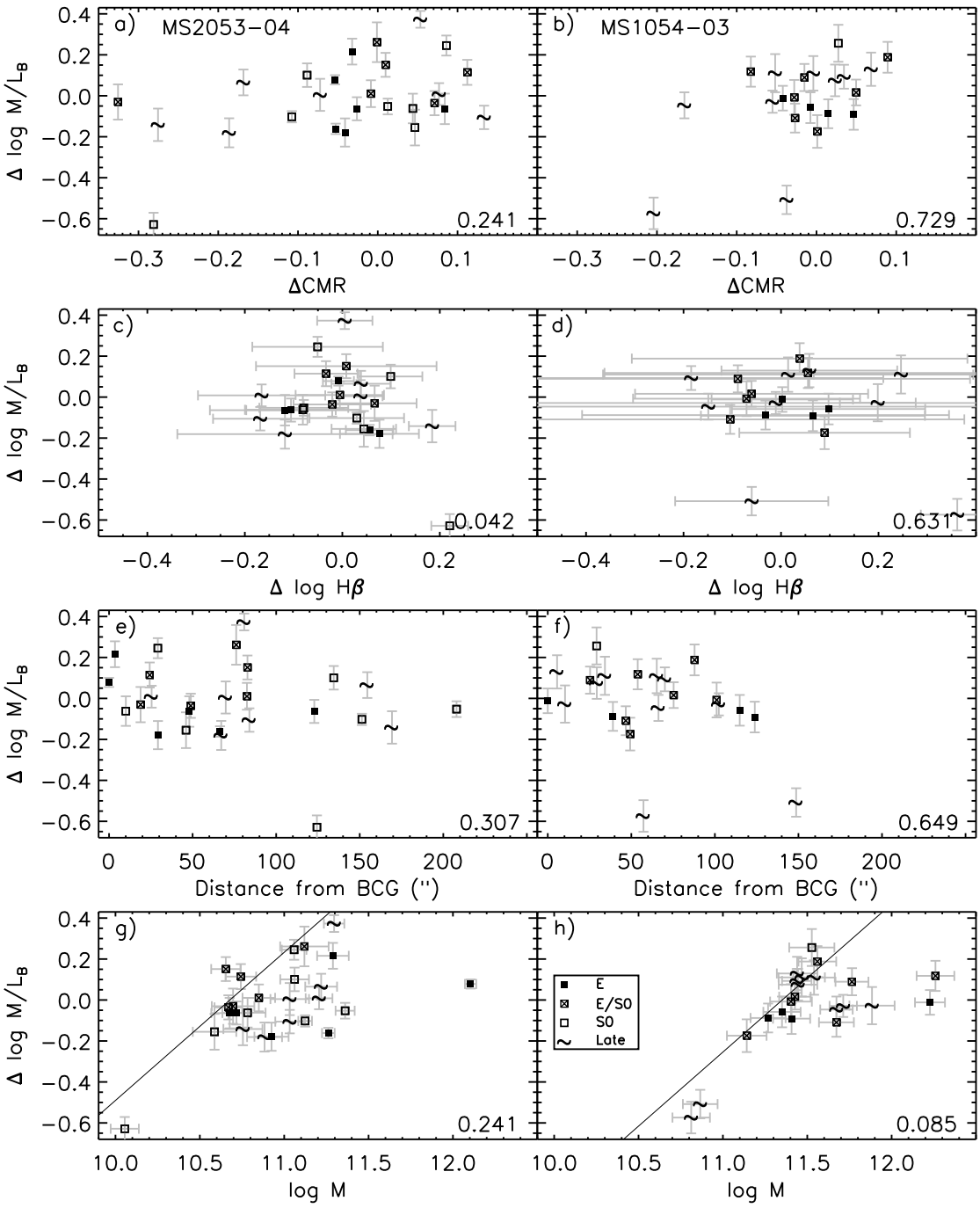

Figure 2.6 — Residual from the fundamental plane $\Delta\log(M/L_B)$ plotted against residual from the color-magnitude relation ΔCMR, residual from the $H\beta - \sigma$ relation, distance from BCG and galaxy mass. Different symbols refer to different morphological types. Error bars for colors and angular distances are assumed to be smaller than the symbol sizes. For the early-type galaxies, the p-values for statistical significance from the Spearman rank order correlation test are printed in the lower right corners. In panels g) and h) the magnitude limit $I \approx 21.15$ at which serious incompleteness due to uncertainties in the σ measurements sets in, is indicated with the solid line.

The residuals from this relation (positive means stronger $H\beta$) are plotted against the FP residual in Figure 2.6c and Figure 2.6d. Only for MS 2053–04 are the error bars small enough to draw robust conclusions. A correlation is present, with confidence level 95.8%. $H\beta$ absorption lines are stronger for younger stellar populations, and the correlation with $\Delta\log(M/L_B)$ could confirm that the scatter in the FP is not random noise, but determined by age variations among the galaxies.

2.5.3 Location in the cluster

Here we consider if the enhanced scatter reported in Sect. 2.4.1 is related to environment. Clusters of galaxies are not isolated systems, as infall of galaxies from the field occurs. FP studies of field early-type galaxies indicate that their stellar populations may be somewhat younger than those of their counterparts in clusters (van Dokkum et al. 2001; Treu et al. 2002; van de Ven, van Dokkum,& Franx 2003; Rusin et al. 2003; van Dokkum & Ellis 2003; Gebhardt et al. 2003). In the cluster CL1358+62 van Dokkum et al. (1998) reported evidence for disky galaxies to be systematically bluer and to show a larger scatter in the CMR at larger radii (with the sample ranging to $\sim 1Mpc$). As earlier studies of both clusters (K97; vD98) were based on one pointing, the larger scatter we find could be explained if residuals from the FP increase with distance from the BCG. Therefore, we might expect to see a gradient in age and larger scatter around the FP going to a larger range in cluster radii. For both clusters our samples extend to roughly $1Mpc$ from the BCG. Figure 2.6e and Figure 2.6f do not show a significant correlation.

2.5.4 Galaxy mass and selection effects

Finally we try to explain the range of FP residuals as a function of galaxy mass. The mass M in solar units of a galaxy is calculated as follows (see JFK96):

$$\log M = 2\log\sigma + \log r_e + 6.07 \tag{2.8}$$

Figure 2.6g and Figure 2.6h show residual from the FP against $\log M$. Only if we were to include the 6 galaxies with $\sigma < 100\ km\ s^{-1}$, the trend of lower mass galaxies to have lower M/L ratios than predicted by the FP with JFK96 coefficients is significant at the 95% level.

For a good understanding of Figure 2.6g and Figure 2.6h, we need to take into account that our FP samples are magnitude-limited, and not mass-limited. The FP can be rewritten as

$$M/L \sim M^{0.28} r_e^{-0.07}. \tag{2.9}$$

In the following, we ignore the dependence on r_e. Hence the residual is given by

$$\Delta M/L = \frac{M_{obs}/L_{obs}}{(M/L)_{FP}} = \frac{M_{obs}^{0.72}}{L_{obs}}. \tag{2.10}$$

For a fixed luminosity we expect all galaxies to fall on a line in a plot of $\Delta\log M/L$ versus $\log M$. In Figure 2.6g and Figure 2.6h this line is drawn for I=21.15. At this

magnitude serious incompleteness due to uncertainties in the σ measurements sets in. The lowest mass galaxies in Figure 2.6a and Figure 2.6b lie close to the line representing the magnitude limit. Low mass galaxies that lie on or above the FP would be too faint to allow for accurate dispersion measurements and would not enter the FP samples. Hence the few remaining low mass galaxies in our samples are brighter than their FP prediction based on r_e and σ.

Selection effects are clearly less relevant at the high mass end, and hence we determine the offset and scatter of the MS 2053–04 FP seperately for the subsample of early-type galaxies with $M > 10^{11} M_{\odot}$ (following van Dokkum & Stanford 2003). For this subsample of 8 early-type galaxies we derive a zero-point shift with respect to Coma of $\Delta \log(M/L_B) = -0.288 \pm 0.056$ and a scatter of 0.132 ± 0.039 in $\log r_e$. As expected, this is slightly different from the zero-point shift of $\Delta \log(M/L_B) = -0.365 \pm 0.037$ for the full early-type sample. The zero-point offset is now in good agreement with K97, but the scatter is still larger.

If we apply a mass cut for the MS 1054–03 early-type galaxies of $M > 10^{11.5} M_{\odot}$, we find a shift in zero point of $\Delta \log(M/L_B) = -0.311 \pm 0.051$ compared to $\Delta \log(M/L_B) = -0.405 \pm 0.037$ for the full early-type sample. The scatter of the high mass subsample (0.104 ± 0.030 in $\log r_e$) is similar to that of the full early-type sample (0.106 ± 0.023 in $\log r_e$).

2.5.5 Summary of correlations

We did not find evidence that FP residuals are related to environment. Instead, stellar population effects are playing a role in shaping the FP and selection effects in our magnitude-limited samples need to be taken into account.

First, early-type galaxies with stronger $H\beta$ absorption also tend to have lower M/L ratios than predicted by their r_e and σ. This correlation supports the interpretation of FP scatter as a measure of age variation among early-type galaxies. The larger FP scatter in MS 2053–04 therefore reflects a larger spread in relative ages than in the local universe. Comparison of FP residuals with residuals from the CMR cannot confirm or rule out the presence of such a stellar population effect.

Second, the fact that we do not see galaxies with low masses that lie on or above the FP, may be entirely explained by selection effects. Only low mass galaxies that are brightened by some recent star formation enter the FP sample. Their older counterparts are fainter than the magnitude limit for the dispersion measurements.

2.6 Evolution of M/L ratio

Correlations with residual from the $H\beta - \sigma$ relation show that differences in FP zero point can be explained by age differences of the stellar population. In this section we study the evolution of the M/L ratio as a function of redshift and use this to estimate the mean formation redshift of cluster early-type galaxies. In Figure 2.7a we show the evolution of the M/L ratio with respect to Coma. Crosses refer to measured zero-point shifts from the literature: Coma at $z = 0.023$ (JFK96), CL1358+62 at $z = 0.33$ (K2000), CL0024+16 at $z = 0.39$ (van Dokkum,& Franx 1996), MS 2053–04 at $z = 0.583$

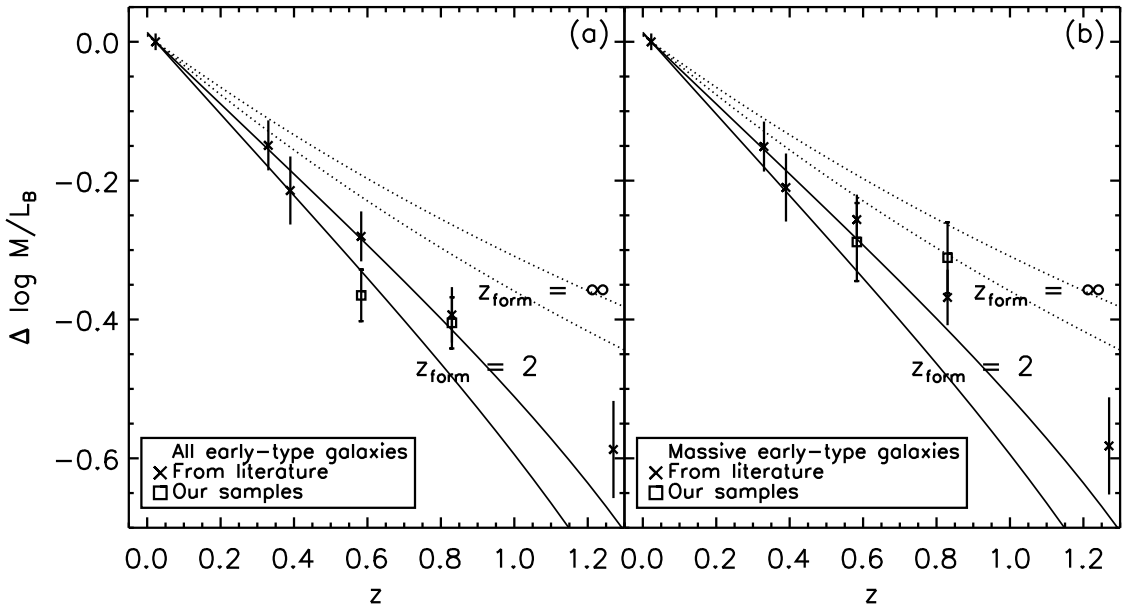

Figure 2.7 — Evolution of the M/L ratio with redshift. The cross symbols are results from the literature, namely Coma at $z = 0.023$ (JFK96), CL1358+62 at $z = 0.33$ (K2000), CL0024+16 at $z = 0.39$ (van Dokkum & Franx 1996), MS 2053–04 at $z = 0.583$ (K97), MS 1054–03 at $z = 0.83$ (vD98) and J0848+4453 at $z = 1.27$ (van Dokkum & Stanford 2003). Boxes denote the shift in M/L ratio based on our larger samples for MS 2053–04 and MS 1054–03. Single burst models for $z_{form} = 2$ and ∞, assuming a Salpeter IMF ($x = 2.35$) and a range of metallicities, are drawn with solid and dotted curves resp. Panel (a) is based on all early-type galaxies, panel (b) shows results for the subsample of massive early-type galaxies ($M > 10^{11} M_\odot$ for clusters up to $z = 0.583$ and $M > 10^{11.5} M_\odot$ for the two higher redshift clusters).

(K97), MS 1054–03 at $z = 0.83$ (vD98) and J0848+4453 at $z = 1.27$ (van Dokkum,& Stanford 2003). The new results for MS 2053–04 and MS 1054–03, based on our larger samples, are plotted with boxes. Single burst evolutionary models for a formation redshift $z_{form} = 2$ and $z_{form} = \infty$ are drawn with a solid and dotted curve respectively. They represent a galaxy that is fixed in mass and whose luminosity evolves as:

$$L(t) \sim 1/(t - t_{form})^{\kappa} \tag{2.11}$$

Here t_{form} represents the age of the universe at the moment the stars were formed. κ depends on the slope of the IMF, passband and metallicity. For a Salpeter (1955) IMF and $-0.5 < [Fe/H] < 0.5$, the models of Bruzual & Charlot (2003), Vazdekis et al. (1996) and Worthey (1998) give $0.86 < \kappa_B < 1.00$. Using the new offsets for the two higher z clusters, the single burst model for a Salpeter IMF and solar metallicity favoured by the least square method has $z_{form} \sim 2.26^{+0.28}_{-0.20}$. The 1σ confidence level was derived from the difference in χ^2 between the model and the overall minimum, $\Delta\chi^2 = \chi^2 - \chi^2_{min}$, to which Gaussian confidence levels were assigned (e.g., Press et al. 1992). As we showed in Sect. 2.5.4, the point of MS 2053–04 deviates from the earlier result (K97) since at low mass only galaxies with low M/L enter the magnitude-limited sample.

To avoid this bias, we apply a mass cut of $M > 10^{11} M_{\odot}$ to all clusters up to $z = 0.583$. A mass cut of $M > 10^{11.5} M_{\odot}$ was applied to MS 1054–03 and J0848+4453 since at these higher redshifts the selection effect sets in at a higher galaxy mass. For J0848+4453 two galaxies are left after omitting the one low mass outlier. As the biweight location estimator is robust against outliers, the zero-point shift only changes slightly for this cluster. We obtain the evolution of the M/L ratio as presented in Figure 2.7b. Now the zero point of the MS 2053–04 FP follows the trend seen for the other clusters in Figure 2.7. If we constrain the analysis of the evolution in M/L ratio to massive early-type galaxies, a simple linear fit gives $\log M/L_B \sim -0.47z$, agreeing well with earlier determinations based on smaller samples or lower redshift (see, e.g., vD98). The formation redshift favoured by a least squares method is $z_{form} \sim 2.95^{+0.81}_{-0.46}$, slightly higher than the mean formation redshift for all early-type galaxies. A similar formation epoch for early-type galaxies in clusters was found by Kelson et al. (2001) based on the evolution of Balmer absorption-line strengths with redshift. It is remarkable how earlier studies of clusters based on smaller samples (see, e.g., K97; vD98) gave similar results.

2.7 Summary

We used visual and quantitative classifications to select bulge-dominated systems in our MS 2053–04 and MS 1054–03 samples. For MS 2053–04 we find a zero-point offset with respect to Coma of $\Delta \log(M/L_B) = -0.365 \pm 0.037$, larger than determined earlier on the basis of a smaller sample (K97). The scatter around the MS 2053–04 FP is 0.134 ± 0.034 in $\log r_e$, enhanced with respect to both K97 and the scatter in local clusters. The FP zero point of MS 1054–03 ($\Delta \log(M/L_B) = -0.405 \pm 0.037$) agrees well with the earlier result of $\Delta \log(M/L_B) = -0.393 \pm 0.040$ by vD98. The scatter of 0.106 ± 0.024 in MS 1054–03 is larger than reported by vD98 for a smaller sample of MS 1054–03 early-type galaxies. However, taking into account measurement uncertainties, the scatter is consistent with that in local clusters (JFK96). Late-type galaxies also follow the FP scaling relation and show a similar scatter around the FP as the early-type galaxies. Adding the late-type galaxies to the early-type sample results in a scatter of 0.136 ± 0.029 for MS 2053–04 and 0.117 ± 0.031 for MS 1054–03. The larger samples presented in this chapter allow us to study correlations with other properties of the early-type galaxies. We do not find evidence that the formation history depends on environment in the cluster. No significant correlation of FP residuals with CMR residuals was found. The presence of a correlation between FP residuals and residuals from the $H\beta - \sigma$ relation indicates that stellar population effects are playing a role. Assuming non-evolving slopes for all scaling relations, we find that galaxies with lower M/L than the FP prediction tend to show stronger $H\beta$ than predicted based on the $H\beta - \sigma$ relation. Finally, we show that the lack of low mass galaxies on or above the FP may be entirely due to selection effects. To avoid a bias induced by the magnitude limit of our sample, we focus on the high mass end, where selection effects are less relevant. Applying a mass cut at $M > 10^{11} M_{\odot}$ to all 4 considered clusters below $z \sim 0.6$ and at $M > 10^{11.5} M_{\odot}$ to the 2 higher redshift clusters at $z = 0.83$ and $z = 1.27$, increases the best fitting formation redshift from $z_{form} = 2.26^{+0.28}_{-0.20}$ to $z_{form} = 2.95^{+0.81}_{-0.46}$. The mass cut at $M = 10^{11} M_{\odot}$ is well below the typical mass of early-type galaxies: galaxies with

$M = 10^{11} M_{\odot}$ have dispersions of ~ 168 *km* s^{-1} which is significantly lower than the σ_* dispersion of early-type galaxies which is 228 ± 14 *km* s^{-1} (Kochanek 1994).
The implication of this work is that selection effects need to be taken into account, especially if the scatter is high. The scatter in MS 2053–04 is slightly higher than at low redshift; the scatter in the field at high redshift seems to be even higher (e.g., Gebhardt et al. 2003; van Dokkum & Ellis 2003). Hence those studies are likely to suffer from much more significant selection effects.

Acknowledgments

We thank Arjen van der Wel for useful discussions on the fundamental plane. Based on data obtained at the W. M. Keck Observatory, which is operated as a scientific partnership among the California Institute of Technology, the University of California and the National Aeronautics and Space Administration. The Observatory was made possible by the generous financial support of the W. M. Keck Foundation. The authors wish to recognize and acknowledge the very significant cultural role and reverence that the summit of Mauna Kea has always had within the indigenous Hawaiian community. We are most fortunate to have the opportunity to conduct observations from this mountain.

References

Beers, T. C., Flynn, K.,& Gebhardt, K. 1990, AJ, 100, 32
Bender, R., Saglia, R. P., Ziegler, B., Belloni, P., Greggio, L., Hopp, U.,& Bruzual, G. 1998, ApJ, 493, 529
Bertin, E.,& Arnouts, S. 1996, A&AS, 117, 393
Bower, R. G., Lucey, J. R.,& Ellis, R. S. 1992b, MNRAS, 254, 589
Bruzual, G.,& Charlot, S. 2003, MNRAS, 344, 1000
Djorgovski, S.,& Davis, M. 1987, ApJ, 313, 59
Dressler, A., Lynden-Bell, D., Burstein, D., Davies, R. L., Faber, S.M., Terlevich, R. J.,& Wegner, G. 1987, ApJ, 313, 42
Fabricant, D., Franx, M.,& van Dokkum, P. G. 2000, ApJ, 539, 577
Gebhardt, K., et al. 2003, ApJ, in press
Hoekstra, H., Franx, M., Kuijken, K., van Dokkum, P. G. 2002, MNRAS, 333, 911
Jørgensen, I., Franx, M.,& Kjærgaard, P. 1995b, MNRAS, 276, 1341
Jørgensen, I., Franx, M.,& Kjærgaard, P. 1996, MNRAS, 280, 167 (JFK96)
Jørgensen, I. 1997, MNRAS, 288, 161
Jørgensen, I. 1999, MNRAS, 306, 607
Jørgensen, I., Franx, M., Hjorth, J.,& van Dokkum, P. G. 1999, MNRAS, 308, 833
Kelson, D. D., van Dokkum, P. G., Franx, M., Illingworth, G. D.,& Fabricant, D. 1997, ApJ, 478, L13 (K97)
Kelson, D. D., Illingworth, G. D., Franx, M.,& van Dokkum, P. G. 2000a, ApJ, 531, 137
Kelson, D. D., Illingworth, G. D., Franx, M.,& van Dokkum, P. G. 2000b, ApJ, 531, 159
Kelson, D. D., Illingworth, G. D., Franx, M.,& van Dokkum, P. G. 2000c, ApJ, 531, 184 (K2000)
Kelson, D. D., Illingworth, G. D., Franx, M.,& van Dokkum, P. G. 2001, ApJ, 552, L17
Kelson, D. D. 2003, PASP, 115, 688
Kelson, D. D., Illingworth, G. D., Franx, M.,& van Dokkum, P. G. 2006, ApJ, 653, 159
Kochanek, C. S. 1994, ApJ, 436, 56
Oke, J. B., et al. 1995, PASP, 107, 375
Press, W. H., Teukolsky, S. A., Vetterling, W. T.,& Flannery, B. P. 1992, Numerical Recipes. Cambridge Univ. Press, Cambridge
Rusin, D., et al. 2003, ApJ, 587, 143

Salpeter, E. 1955, ApJ, 121 161
Schlegel, D. J., Finkbeiner, D. P.,& Davis, M. 1998, ApJ, 500, 522
Trager, S. C., Worthey, G., Faber, S. M., Burstein, D.,& Gonzalez, J. J. 1998, ApJS, 116, 1
Tran, K. V., Kelson, D. D., van Dokkum, P. G., Franx, M., Illingworth, G. D.,& Magee, D. 1999, ApJ, 522, 39
Tran, K. V. 2002, PhD thesis, Univ. California at Santa Cruz
Tran, K. V., et al. 2003, submitted to ApJ
Treu, T., Stiavelli, M., Casertano, S., Møller, P.,& Bertin, G. 2002, ApJ, 564, L13
van de Ven, G., van Dokkum, P.G.,& Franx, M. 2003, MNRAS, 344, 924
van Dokkum, P. G.,& Franx, M. 1996, MNRAS, 281, 985
van Dokkum, P. G., Franx, M., Kelson, D. D., Illingworth, G. D., Fisher, D.,& Fabricant, D. 1998, ApJ, 500, 714
van Dokkum, P. G., Franx, M., Kelson, D. D.,& Illingworth, G. D. 1998, ApJ, 504, L17 (vD98)
van Dokkum, P. G., Franx, M., Fabricant, D., Illingworth, G. D.,& Kelson, D. D. 2000, ApJ, 541, 95
van Dokkum, P. G., Franx, M., Kelson, D. D.,& Illingworth, G. D. 2001, ApJ, 553, 39
van Dokkum, P. G.,& Stanford, S. A. 2003, ApJ, 585, 78
van Dokkum, P. G.,& Ellis, R.S. 2003, ApJ, 592, 53
Vazdekis, A., et al. 1996, ApJS, 106, 307
Worthey, G. 1998, PASP, 110, 888W

Chapter 3

B-to-24 μm photometry of the GOODS-CDFS: multi-wavelength catalog and total IR properties of distant K_S-selected galaxies

Abstract. We present a K_s-selected catalog for the Chandra Deep Field South (CDFS) containing photometry in B_{435}, V_{606}, i_{775}, z_{850}, J, H, K_s, [3.6 μm], [4.5 μm], [5.8 μm], [8.0 μm], and the MIPS [24 μm] band. The imaging has a typical $K_{s,AB}^{tot}$ limit of 24.3 mag (5σ) and coverage over 113 arcmin^2 in all bands and 138 arcmin^2 in all bands but H. We cross-correlate our catalog with the 1 Ms X-ray catalog by Giacconi et al. (2002) and with all available spectroscopic redshifts to date. We find systematic differences due to aperture corrections in a comparison with the '$z + K_s$'-selected GOODS-MUSIC catalog that covers $\sim$90% of the field. We exploit the B-to-24 μm photometry to determine which K_s-selected galaxies at $1.5 < z < 2.5$ have the brightest total IR luminosities and which galaxies contribute most to the integrated total IR emission. The answer to both questions is that red galaxies are dominating in the IR. This is true no matter whether color is defined in the rest-frame UV, optical, or optical-to-NIR. We do find however that among the reddest galaxies in the rest-frame optical, there is a population of sources with only little mid-IR emission.

S. Wuyts, N. M. Förster Schreiber, M. Franx, I. Labbé, G. Rudnick & P. G. van Dokkum

3.1 Introduction

SINCE the original Hubble Deep Field (Williams et al. 1996), deep multi-wavelength observations of blank fields have revolutionized our understanding of the high-redshift universe. Especially the epoch around $z \sim 2$ is of great interest since it is then that the cosmic star formation rate density was peaking (Hopkins & Beacom 2006). At $z \sim 2$, the observed optical probes the redshifted rest-frame UV emission of young O and B stars, making it a good tracer for relatively unobscured star formation. Near-Infrared (NIR) observations of distant galaxies, such as undertaken by the FIRES survey in the Hubble Deep Field South (HDFS, Labbé et al. 2003, hereafter L03) and the MS 1054–03 field (Förster Schreiber et al. 2006, hereafter FS06), show relatively small variations in the mass-to-light ratio. Selecting galaxies in the K_s-band (e.g., L03; FS06) thus provides a good probe of the massive galaxy content at high redshift.

In the presence of dust, large amounts of rest-frame UV emission can be absorbed and re-emitted in the Far-Infrared (FIR). Dust corrections of the UV luminosities of such systems involve large uncertainties. Direct observations of the dust emission are therefore crucial to get a better census of the bolometric energy output. Unfortunately, current submillimeter observations (e.g., Smail et al. 1997) are only sensitive enough to detect the most luminous dust-enshrouded starbursts. In order to study the bolometric properties of typical galaxies at $z \sim 2$, infrared luminosities have been derived from the observed 24 μm flux by means of IR spectral energy distribution (SED) templates (e.g., Papovich et al. 2005; Reddy et al. 2006). Despite the extra model uncertainty involved, this approach adds complementary information to the shorter wavelength studies of high-redshift galaxies.

In this chapter, we present a K_s-band selected multi-wavelength catalog for the GOODS-CDFS, comprising ACS *BViz*, ISAAC JHK_s, IRAC 3.6-8.0 μm and MIPS 24 μm imaging. We adopt a similar format as for the FIRES catalogs of the HDFS and MS 1054–03. This allows the user to exploit the combined photometry of the CDFS, MS 1054–03, and the HDFS in a straightforward manner. The fields are complementary in depth (5σ for point sources $K_{s,AB}^{tot} = 24.3$, $K_{s,AB}^{tot} = 25.0$, and $K_{s,AB}^{tot} = 25.6$ respectively) and area (138 arcmin^2, 24 arcmin^2, and 5 arcmin^2 respectively).

An analysis of the space density and colors of massive galaxies at $2 < z < 3$ (van Dokkum et al. 2006), of the rest-frame optical luminosity density and stellar mass density up to $z \sim 3$ (Rudnick et al. 2006), and of the rest-frame luminosity functions of galaxies at $2 < z < 3.5$ (Marchesini et al. 2006) were partly based on the presented catalog for the GOODS-CDFS presented here.

After describing the catalog construction, we particularly address the questions which K_s-selected galaxies at $1.5 < z < 2.5$ are brightest at 24 μm, which galaxies have the largest total infrared luminosity L_{IR} ($\equiv L(8 - 1000\ \mu\text{m})$) and contribute most to the total integrated IR luminosity emitted by K_s-selected galaxies. We address this question by studying the IR emission as function of color defined in three wavelength regimes: the rest-frame UV, optical, and optical-to-NIR.

An overview of the observations is presented in §4.3. §3.3 describes the construction of the final mosaics. Source detection and photometry is discussed in §3.4. Next, we present our photometric redshifts (z_{phot}) and cross-correlation with the available

spectroscopic surveys in §3.5. §3.6 summarizes the catalog content. A photometric comparison for the wavelength bands in common with the GOODS-MUSIC catalog by Grazian et al. (2006a) and a z_{phot} comparison with the same authors is discussed in §3.7. Results on 24 μm properties and total infrared luminosities of K_s-selected galaxies at $1.5 < z < 2.5$ are discussed in §3.8. §7.11 summarizes the chapter.

AB magnitudes are used throughout this chapter.

3.2 Observations

3.2.1 The GOODS Chandra Deep Field South

Centered on (α, δ) = (03:32:30, -27:48:30), the CDFS (Giaconni et al. 2000) has been targeted by most of today's major telescope facilities, both in imaging mode over the whole spectral range and in spectroscopic mode. In this section, we describe the public GOODS-South dataset that we used to build a K_s-band selected catalog containing homogeneous colors from the optical to 24 μm.

3.2.2 The ACS BViz data

During 5 epochs of observations, the ACS camera on HST acquired imaging of the GOODS-South field in 4 filter bands: F435W, F606W, F775W, and F850LP (hereafter referred to as B,V,i, and z). Exposure times amounted to 7.2, 6, 6, and 12 ks respectively. The mosaics (version v1.0; Giavalisco et al. 2004), were drizzled onto a pixelscale of $0\farcs03$ pixel^{-1}. From the 150 arcmin^2 area that is well covered by the K_s-band detection image, 138 arcmin^2 is well exposed with ACS. We restrict our analysis of the IR properties of the distant galaxy population in §3.8 to this overlap region.

3.2.3 The ISAAC JHK$_s$ data

We use the ESO/GOODS data release v1.5[1] to complement the optical observations with NIR imaging by the Very Large Telescope (VLT). For a full description of the dataset, we refer the reader to Vandame et al. (in preparation). Briefly, the v1.5 data release consists of 24 fully reduced VLT/ISAAC fields in the J and K_s bands and 19 fields in the H-band, each with a $2\farcs5$x$2\farcs5$ FOV and $0\farcs15$ pixel^{-1} scale. The ISAAC data were reduced using the ESO/MVM image processing pipeline (v1.9, see Vandame 2002 for the description of an earlier version). Exposure times varied from field to field, with typical exposures of 11.5 ks, 15 ks, and 18 ks in J, H, and K_s-band respectively, and respective ranges between ISAAC fields of 7-18 ks, 7-22 ks, and 13-27 ks. The variations in depth resulting from the unequal exposure times are discussed in §3.3.5. A total area of 113 arcmin^2 is well exposed in all optical and NIR filter bands. Without a restriction on the H-band, the covered area increases to 138 arcmin^2.

3.2.4 The IRAC 3.6-8.0 μm data

As a Spitzer Space Telescope Legacy Program, superdeep images of the GOODS-South field were taken with the Infrared Array Camera (IRAC, Fazio et al. 2004) on-board

[1] http://www.eso.org/science/goods/releases/20050930/

Spitzer. Over 2 epochs the whole field was covered in the 3.6 μm, 4.5 μm, 5.8 μm, and 8.0 μm bands. For each epoch, exposure times per channel per sky pointing amounted to 23 hours. With the telescope orientation being rotated by 180 degrees between the two epochs, the second epoch IRAC channel 1 and 3 observations targeted the area covered by IRAC channel 2 and 4 during the first epoch, and vice versa. An overlap region of roughly 40 arcmin^2, including the Hubble Ultra Deep Field (Beckwith et al. 2003), got twice the exposure time. We use the data releases DR2 and DR3 for the second and first epoch respectively. Images were released on a $0\farcs60$ pixel^{-1} scale. A full description of the observations and reduction will be presented by Dickinson et al. (in preparation).

3.2.5 The MIPS 24 μm data

The GOODS-South field was observed at 24 μm with the Multiband Imaging Photometry for Spitzer (MIPS, Rieke et al. 2004) on-board Spitzer, closely overlapping the IRAC fields with a position angle that is rotated with respect to the IRAC observations by approximately 3 degrees. The MIPS campaign led to a nearly uniform exposure time of 10 hours. We use the version v0.30 reduced images, released on a $1\farcs20$ pixel^{-1} scale, based on the Spitzer Science Center (SSC) Basic Calibrated Data (BCD) pipeline (version S11.0.2).

3.3 Final images

In this section, we describe the image quality of the publicly released data products, the subsequent steps undertaken to obtain the final mosaics from which the photometric catalog is extracted, and the limiting depths reached at all wavelengths.

3.3.1 Pixel scales and large scale backgrounds

First, we converted the ACS images to the $0\farcs15$ pixel^{-1} scale of the K_s-band detection image, using the IRAF blkavg task with flux conservation. All optical and NIR photometry was performed on this pixel scale using the SExtractor software version 2.2.2 (Bertin & Arnouts 1996) (see §3.4).

A source fitting algorithm developed by Labbé et al. (in preparation), especially suited for heavily confused images for which a higher resolution prior (in this case the K_s-band image) is available, was used to extract photometry from the IRAC and MIPS images. The algorithm requires a higher resolution image than provided by the IRAC and MIPS images. However, the native K_s-band pixel scale makes it more computationally expensive without benefit in accuracy. A version of the K_s-band mosaic was therefore produced on a $0\farcs3$ pixel^{-1} scale. We registered the publicly released IRAC and MIPS images onto this K_s-band image using the WCS information in the image header in combination with a minor additional shift, again forcing flux conservation. We note that the source fitting algorithm takes care of residual shifts. Since the programme does not take into account large scale background variations, these were removed a priori by subtracting SExtractor background images produced with large background mesh settings.

3.3.2 Image quality and PSF matching

3.3.2.1 Optical-to-NIR wavelengths

In order to obtain consistent color measurements, we match all optical and NIR images to a common resolution, namely that of the field with the broadest point spread function (PSF). In this section, we describe the selection of stars used to build the PSFs, the construction of the PSFs for the ACS *B*-, *V*-, *i*-, and *z*-mosaics and for each of the ISAAC fields in the *J*-, *H*-, and K_s-band, the construction of the convolving kernels, and the quality of the PSF matching.

First, we compiled a list of bright, isolated, unsaturated stars. Initially, well covered objects with $(J - K_s)_{AB} < 0.04$ and $K^{tot}_{s,AB} < 22.86$ mag were selected from a preliminary catalog of the CDFS. For ISAAC fields where the number of $J - K_s$ selected stars was low, we complemented the sample with stars from the EIS stellar catalog (Groenewegen et al. 2002). During a first iteration, the list was cleaned from galaxy-like objects, stars with neighbors within 3″ radius, stars too close to the edge of an image and objects that were not identified in the ACS r1.1z catalog (Giavalisco et al. 2004) or with a FWHM in the *z*-band larger than 0.″13. Measurements of the FWHM were performed by fitting Moffat profiles to the stars using the imexam task in IRAF. We excluded stars based on a 2σ clipping of the measured FWHMs. Finally, we inspect by eye the radial profiles and curves of growth, produced with the IRAF tasks radprof and phot respectively. For each ISAAC field the PSF was determined, and the same stars were used to build the *J*-, *H*-, and K_s-band PSF. The number of stars ranged from 3 to 5 stars per ISAAC field, with the exception for field f30, for which only 1 good star was available. The numbers of stars used to build the ACS PSFs were 31, 45, 49 and 53 for the *B*, *V*, *i*, and *z* mosaics respectively.

Next, we computed PSF images per ISAAC field by averaging the registered and flux-normalized images of the selected stars. The flux was normalized within 1.″5 diameter apertures rather than the total aperture to optimize the signal-to-noise and avoid contributions from residual neighboring sources. Any neighbors in the ISAAC images of good stars, sufficiently far not to bias the FWHMs and PSFs, were masked while averaging. This method was preferred over taking the median, since only a handful of good stars per ISAAC field were available to build a PSF. PSFs for the ACS mosaics were constructed from a large enough number of stars to average out any influence of faint neighboring sources without masking.

The ACS PSFs in the *B*-, *V*-, *i*-, and *z*-band, as measured using Mofat profiles on the 5x5 blocked ACS mosaics, had a FWHM of 0.″22, 0.″22, 0.″21, and 0.″22 respectively. The seeing FWHM of the NIR ISAAC observations varied from 0.″35 to 0.″65, with median values of 0.″47, 0.″48, and 0.″47 in *J*, *H*, and K_s respectively. Figure 3.1 illustrates the distribution of FWHMs of the natural PSFs for the individual ISAAC fields. In all of the considered bands and fields, the FWHM of the individual stars were within ≈10% of that measured on the final PSF. We adopted the 0.″65 *H*-band PSF of ISAAC field f15 as target to which all higher resolution images were matched.

We computed the kernel for convolution for each ISAAC field and band separately, using the Lucy-Richardson deconvolution algorithm. The ratio of the growth curve of the convolved PSF over that of the target PSF is a good measure for the PSF matching

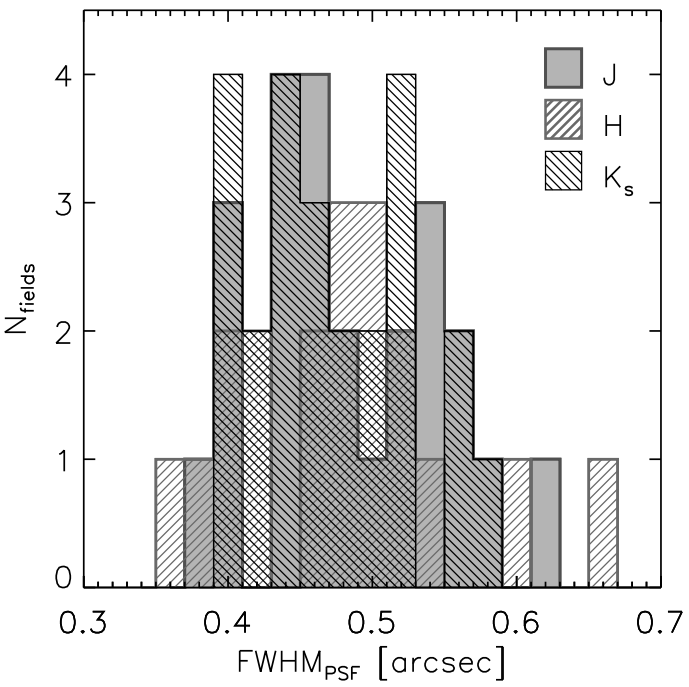

Figure 3.1 — Distributions of seeing FWHM for the ISAAC J, H, and K_s observations. Moffat profiles were fitted to the PSFs that were built from bright, isolated, unsaturated stars for each field and band separately.

accuracy. In order to minimize the discrepancies between both growth curves, we performed the deconvolution using a series of sizes for the postage stamp images of the PSFs, from 1.″7 to 5.″9 on a side. The kernel corresponding to the box size that gave the curve of growth ratio closest to unity was adopted for the final convolution. Overall, the ratio of growth curves deviated by at most 5.1% from unity for apertures between 1″ (≈1.5FWHM of the PSF of the smoothed field maps) and 6″ (the reference aperture for photometric calibration), with an average of $0.54\% \pm 0.90\%$. Flux is well conserved during the convolution process, with an average deviation of 0.37% and maximum discrepancy of 4.2% for one of the fields.

The construction of convolving kernels for the ACS mosaics required an extra step. The kernels obtained from deconvolution with the IRAF Lucy task had significant noise in the outer parts, leading to noise spikes around bright point-like sources in the convolved ACS mosaics. To remove these artifacts, we modeled the ACS-to-ISAAC kernels by fitting isophotes using the IRAF tasks ellipse and bmodel, and used the modeled kernels for the convolution. This is possible because the kernels are otherwise well behaved and very azimutally symmetric.

Because of the different basic shapes of the ACS and ISAAC PSFs, an excellent matching over the relevant radii is more difficult than in general among ISAAC fields. Nevertheless, the offsets of the growth curve ratios between 1″ and 6″ are limited to below 4.7%, with an average of $1.58\% \pm 1.32\%$. The average over all stars of the ratio of the flux measured in the convolved and that measured in the natural image showed a flux conserving accuracy of 0.7% or better for all ACS bands.

3.3.2.2 MIR wavelengths: IRAC and MIPS 24 μm

The instrumental PSF at Mid-Infrared wavelengths is significantly broader than that of our K_s-band detection image. The FWHM measured on the average image of bright,

Table 3.1 — *H*-band zero points in the AB system derived from the NIR stellar locus

Field	*H*-band zero point
03	25.99
04	26.02
05	26.07
08	25.89
09	25.92
10	25.94
11	25.93
13	26.02
14	25.82
15	26.07
16	25.97
19	25.86
20	25.89
21	25.97
22	26.03
23	26.07
24	25.95
25n	25.94
26n	26.09

isolated stars in the IRAC images amounts to 1.″6, 1.″7, 1.″9, and 2.″0 for the 3.6 μm, 4.5 μm, 5.8 μm, and 8.0 μm bands respectively. The MIPS 24 μm beam even has a FWHM as large as 6″. Since confusion and blending effects are unavoidable in deep observations at this resolution, we decide not to degrade the optical and NIR images to the MIR resolution. Instead, we construct PSFs and convolving kernels similarly as described in §3.3.2.1, but apply them using a source fitting algorithm that makes fully use of the higher resolution information in the K_s-band detection image (see §3.4.2.2).

3.3.3 Zero points

The zero-point calibrations for all bands but the *H*-band were taken from the respective GOODS data release. In the case of the NIR ISAAC observations, the publicly released zero points were based on SOFI images of the EIS-DEEP and DPS infrared surveys conducted over the same region (Vandame et al. 2001), which themselves were photometrically calibrated using standard stars from Persson et al. (1998). That procedure yielded zero points with rms scatters ranging between 0.01 and 0.06 mag in the *J*-band, 0.01 and 0.08 mag in the K_s-band and up to 0.17 mag in the *H*-band.

To improve on the *H*-band calibration, we make use of stellar photometry in the FIRES HDFS (L03) and MS 1054–03 (FS06) fields, for which *H*-band zero points were determined to a ~ 0.03 mag accuracy. For each of the 19 ISAAC fields with *H*-band coverage, we measured the mean offset of the stars used for PSF matching along the $J-H$ axis of a $J-K_s$ versus $J-H$ color-color diagram with respect to the stellar locus in the FIRES fields. Assuming the *J*- and K_s-bands are well calibrated, this immediately provides us with the H-band zero point corrections to be applied. We list the derived *H*-band zero points in Table 3.1. Zero-point corrections ranged from -0.18 mag to 0.09 mag, with a median correction over all fields of -0.03 mag. After applying the zero-point correction, the median absolute deviation in $J-H$ color of individual

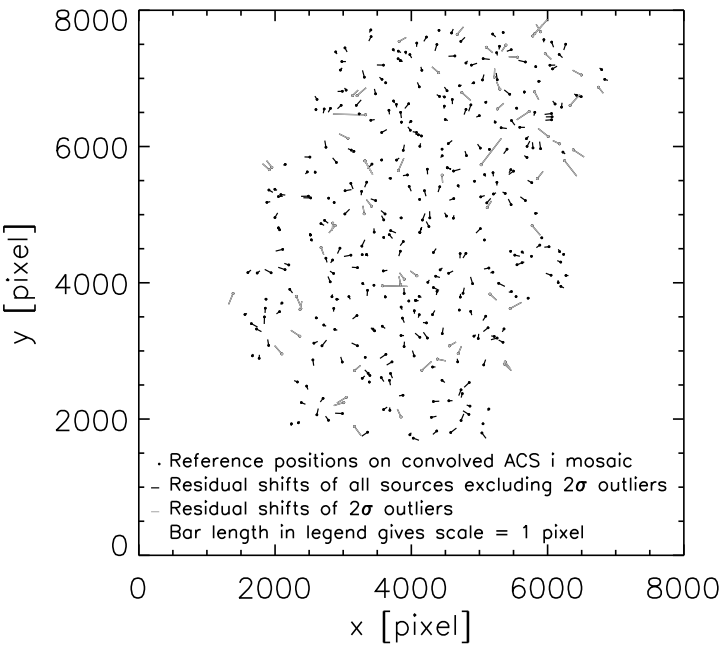

Figure 3.2 — Map of residual shifts of compact sources in the K_s-band mosaic with respect to the reference ACS *i*-band mosaic. 2σ-clipped reference sources used for the alignment are indicated in black. Grey vectors represent the residual shift of the 2σ outliers.

stars around the stellar locus is 0.03 mag, similar as measured for the FIRES HDFS and MS 1054–03 fields.

3.3.4 Mosaicing and astrometry

Here, we describe the combination of the smoothed ISAAC NIR fields and the astrometric precision of the final mosaics. The 5x5 blocked and smoothed ACS *i*-band mosaic was adopted as astrometric reference image. The astrometric solution for the ACS data itself was based on a cross-identification of sources with deep ground-based WFI data that on its turn was astrometrically matched to stellar positions in the Guide Star Catalog 2 (GSC2, STScI 2001). The final solution had a clipped rms deviation of $\lesssim 0\farcs01$ in ACS-to-ACS and $0\farcs12$ in ACS-to-ground difference.

The smoothed ISAAC fields were registered onto the smoothed ACS *i*-band mosaic by applying simple x- and y- shifts without further distortion corrections. In each ISAAC field, we measured the shift with respect to the ACS *i*-band mosaic for stars and compact sources using the imexam task in IRAF. A 2σ clipped sample of reference sources typically consisted of 15-20 objects per ISAAC field. The difference between the shifts implied by individual reference sources and the final astrometric solution had a standard deviation of less than $0\farcs6$ in all NIR bands. A map of residual shifts for the K_s-band mosaic with respect to the convolved ACS *i*-band mosaic is presented in Figure 3.2.

First we applied the fractional pixel shift for each ISAAC field in each band using the IRAF imshift task with a cubic spline interpolation. Next, we summed the integer pixel shifted fields applying an identical weighing scheme as described by FS06 to optimize the S/N for point sources, namely:

$$w_{pix} = \frac{w_{norm}}{(rms_{1.5FWHM})^2} \tag{3.1}$$

where the weight factor for a given pixel w_{pix} equals its value in the normalized weight map w_{norm}, scaled with the square of the rms noise measured within an aperture of 1.5FWHM diameter.

We chose not to combine the 2 epochs of IRAC observations into one mosaic because the 180 degrees difference in position angle would lead to a different PSF shape in the overlap region than in either of both single epoch areas, demanding the use of a different convolving kernel over different parts of the field. Instead, we treat each of the IRAC epochs independently, providing an empirical quality check of the photometry in the overlap region. The registration of each of the IRAC images (epoch 1 and 2) onto the 2x2 blocked K_s-band image has a positional accuracy of better than $0\farcs4$, as measured from offsets between bright star positions on IRAC and K_s-band images. The positional accuracy for the MIPS images is of the order of $0\farcs3$ rms. We note that minor positional offsets between the K_s and IRAC/MIPS image are solved for by the source fitting algorithm applied to IRAC and MIPS photometry (see §3.4.2.2).

3.3.5 Signal to noise and limiting depths

We analyzed the noise properties of the optical-to-24 μm imaging following the same approach as for the FIRES HDFS (L03) and MS 1054–03 (FS06) data. Briefly, the technique uses aperture photometry on empty parts of the image to quantify the rms of background pixels within the considered aperture size. For each convolved ISAAC field in each band, between 200 and 400 non-overlapping apertures were randomly placed at a safe distance from the nearest segmentation pixels in a SExtractor segmentation map. For a given aperture size, the distribution of empty aperture fluxes is well-fitted by a Gaussian, as illustrated in Figure 3.3(a). We applied a 5σ clipping in determining the background rms. Panel (b) of Figure 3.3 shows that a simple linear scaling of the measured background rms $\sigma(N) = N\bar{\sigma}$, where N is the linear size of the aperture and $\bar{\sigma}$ is the pixel-to-pixel rms, would lead to underestimated flux uncertainties. The reason is that correlations between neighboring pixels were introduced during the reduction and PSF matching. We model the background rms as a function of aperture size with a polynomial of the form

$$\sigma_i(N) = \frac{N\bar{\sigma}(a_i + b_i N)}{\sqrt{w_i}} \tag{3.2}$$

where i refers to the considered band and field, and the weight term w_i is derived from the weight map of the respective field. Figure 3.3(b) illustrates the variations in depth for the different ISAAC fields, originating from variable integration times and observing conditions, and reflected in the range of flux uncertainties for objects with similar color aperture in the final catalog. For example, the upper two curves in the ISAAC K_s panel correspond to fields f03 and f04 that had the lowest integration time.

For the ACS mosaics, we used the same empty apertures as for the NIR, provided they were within the ACS FOV. Every object below the K_s-band detection threshold, even though detectable in the ACS imaging, contributes to the background noise and photometric uncertainties of K_s-band detected sources. If we were to restrict our empty aperture analysis to apertures that contain neither K_s-band nor ACS segmentation pixels, the background rms estimates for the ACS mosaics would decrease by 3 to 9%. In

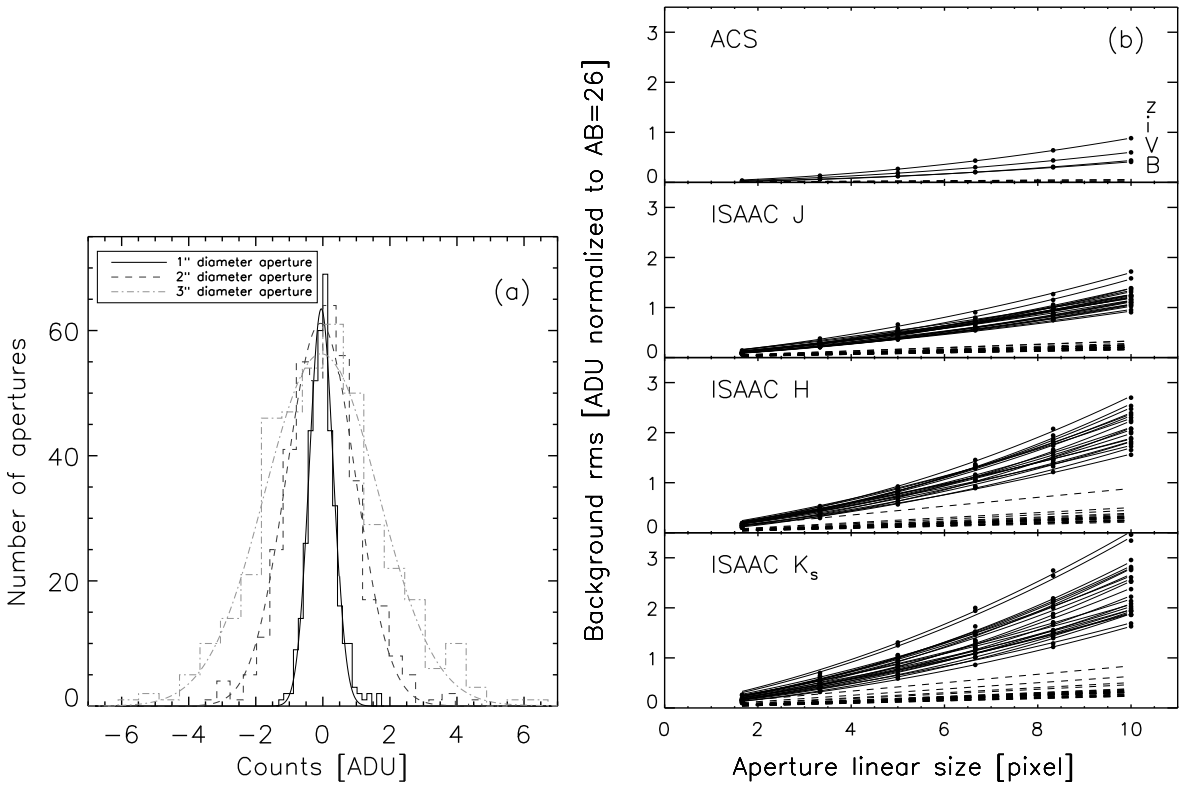

Figure 3.3 — The background rms derived from the distribution of fluxes within empty apertures. (a) Distribution of empty aperture fluxes within a 1″, 2″, and 3″ aperture diameter on the K_s-band image of ISAAC field f15. The distribution is well described by a Gaussian with an increasing width for increasing aperture size. (b) Background rms as derived from flux measurements within empty apertures versus aperture size for the ACS bands and the J, H, and K_s ISAAC fields. Solid lines represent the functional form from Eq. 3.2 fit to the observed rms noise values. Dashed lines indicate a linear extrapolation of the pixel-to-pixel rms. Correlations between pixels introduce a stronger than linear scaling with aperture size.

Figure 3.3(b), we scaled the background rms measured on the ACS and ISAAC images to the flux corresponding to AB = 26.

To characterize the noise for each object, we applied the noise as measured with an aperture of the same size as that used for the photometry.

3.4 Source detection and photometry

3.4.1 K_s-band detection

We aimed to construct a catalog that is especially suited to extract stellar mass-limited samples from (e.g., van Dokkum et al. 2006). Although the rest-frame NIR, probed by IRAC, is a better tracer for stellar mass than the rest-frame optical, the downside is its coarser resolution, leading to severe confusion. Therefore, we decided to detect sources in the observed K_s-band.

We used the SExtractor v2.2.2 source extraction software by Bertin & Arnouts (1996) to detect sources with at least 1 pixel above a surface brightness threshold of $\mu(K_{s,AB}) = 24.6$ mag arcsec^{-2}, corresponding to $\approx 5\sigma$ of the rms background for a typical K_s-band

field. Setting the threshold to the same number of ADUs across the image instead of adopting a S/N criterion was favored, since in the latter case the varying noise properties in the K_s-band mosaic would lead to different limiting magnitudes and limiting surface brightnesses from one field to the other. We smoothed the detection map with a gaussian filter of $FWHM = 0\farcs65$, the size of the PSF in the detection image. This procedure optimizes the detection of point sources.

The resulting catalog contains 6308 sources, 5687 of which have a weight in K_s above 30% of the median weight, which is above $\sim 10\%$ of the maximum weight that is reached in one of the overlap regions between ISAAC fields. Running SExtractor with identical parameters on the inverse detection map, we obtain a total of 43 spurious sources in the area with more than 30% of the median weight. Only one of these has $S/N_{K_s} > 5$. The estimated fraction of false detections increases from $< 1\%$ to $< 3\%$ ($< 8\%$) as we lower the weight criterion from 30% to 20% (10%) of the median weight in the K_s-band mosaic. The estimated fraction of false detections with $S/N_{K_s} > 5$ stays below 0.6% in the area with more than 10% of the median weight.

SExtractor flagged 12% of the detected sources as blended and/or biased. These sources were treated separately in doing the photometry.

3.4.2 Photometry

3.4.2.1 Optical and NIR photometry

We performed the photometry on the convolved B-to-K_s mosaics using SExtractor in dual image mode, with the K_s-band mosaic as detection map. We derive the color and total aperture from the detection image. The same apertures were used in each band. We follow L03 and FS06 in defining the color aperture based on the K_s-band isophotal aperture, more precisely on the equivalent circularized isophotal diameter $d_{iso} = 2(A_{iso}/\pi)^{1/2}$, where A_{iso} is the area of the isophotal aperture. For isolated sources, we apply

$$APER(COLOR) = \begin{cases} APER(ISO), & 1\farcs0 < d_{iso} < 2\farcs0 \\ APER(1\farcs0), & d_{iso} \leq 1\farcs0 \\ APER(2\farcs0), & d_{iso} \geq 2\farcs0 \end{cases} \tag{3.3}$$

where APER(ISO) refers to the isophotal aperture defined by the surface brightness detection threshold. Blended sources (indicated with SExtractor flag "blended" or "biased") were treated separately,

$$APER(COLOR) = \begin{cases} APER(d_{iso}/s), & 1\farcs0 < d_{iso}/s < 2\farcs0 \\ APER(1\farcs0), & d_{iso}/s \leq 1\farcs0 \\ APER(2\farcs0), & d_{iso}/s \geq 2\farcs0 \end{cases} \tag{3.4}$$

where the reduction factor s for the aperture sizes is introduced to minimize contamination by close neighbors. We adopt the optimal value of $s = 1.4$ that was determined from experimentation by L03 and FS06.

The motivation for the tailored isophotal apertures defined in Eq. 3.3 and Eq. 3.4 is that it maximizes the S/N of the flux measurement. The minimum diameter of 1.″0 corresponds to 1.5 $\times$ FWHM of the PSF-matched mosaics. The maximum diameter of 2.″0 was adopted to avoid flux from neighboring sources and avoid the large uncertainties corresponding to large isophotal apertures.

SExtractor's "MAG_AUTO" was used to derive the total flux of the K_s-band detected objects, unless the source was blended, in which case the total aperture was set to the color aperture:

$$APER(TOTAL) = \begin{cases} APER(AUTO), & \textit{isolated sources} \\ APER(COLOR), & \textit{blended sources} \end{cases} \tag{3.5}$$

Finally, an aperture correction was applied to compute the total integrated flux. The correction factor equaled the ratio of the total flux of a star inside a 3″ radius to its flux inside a radius r_{tot}, where $r_{tot} = (A_{tot}/\pi)^{1/2}$ is the radius of a circle with the same area as the total aperture.

Flux uncertainties in both color and total aperture were derived from Eq. 3.2. The quoted uncertainties thus take into account both the aperture size used for the flux measurement and the limiting depth in the respective region of the mosaic.

3.4.2.2 IRAC and MIPS 24 μm photometry

The photometry of K_s-band detected objects in the Spitzer IRAC and MIPS 24 μm imaging of the CDFS was performed by IL. For an in-depth discussion of the source fitting algorithm used, and simulations of its performance, we refer the reader to Labbé et al. (in preparation). A short description with illustration was also presented by Wuyts et al. (2007). Briefly, the information on position and extent of sources based on the higher resolution K_s-band segmentation map was used to model the lower resolution 3.6 μm to 24 μm images. Each source was extracted separately from the K_s-band image and, under the assumption of negligible morphological K-corrections, convolved to the IRAC or the MIPS resolution as needed. A fit to the IRAC/MIPS image was then made for all sources simultaneously, where the fluxes of the objects were left as free parameters. Next, we subtracted the modeled light of neighboring objects and measured the flux on the cleaned IRAC/MIPS maps within a fixed aperture, 3″ for the IRAC bands and 6″ for the MIPS 24 μm band. Using growth curves of the IRAC and K_s-band PSFs, we then scaled the photometry to the same color apertures that were used for the optical and NIR photometry, allowing a straightforward computation of colors over a B-to-8 μm wavelength baseline. An aperture correction based on the growth curve of the 24 μm PSF was applied to scale the 24 μm flux measurents to the integrated 24 μm flux.

Uncertainties in the measured fluxes in the 3.6 μm to 24 μm wavelength bands have a contribution from the background rms (see §3.3.5) and from the residual contamination of the subtracted neighbors. Here, we follow an empirical approach to validate the size of the uncertainties in the IRAC photometry. We exploit the overlap region between the 2 independent observation epochs of the CDFS with the IRAC instrument. The position angle was rotated over 180 degrees, causing the PSF to have a different

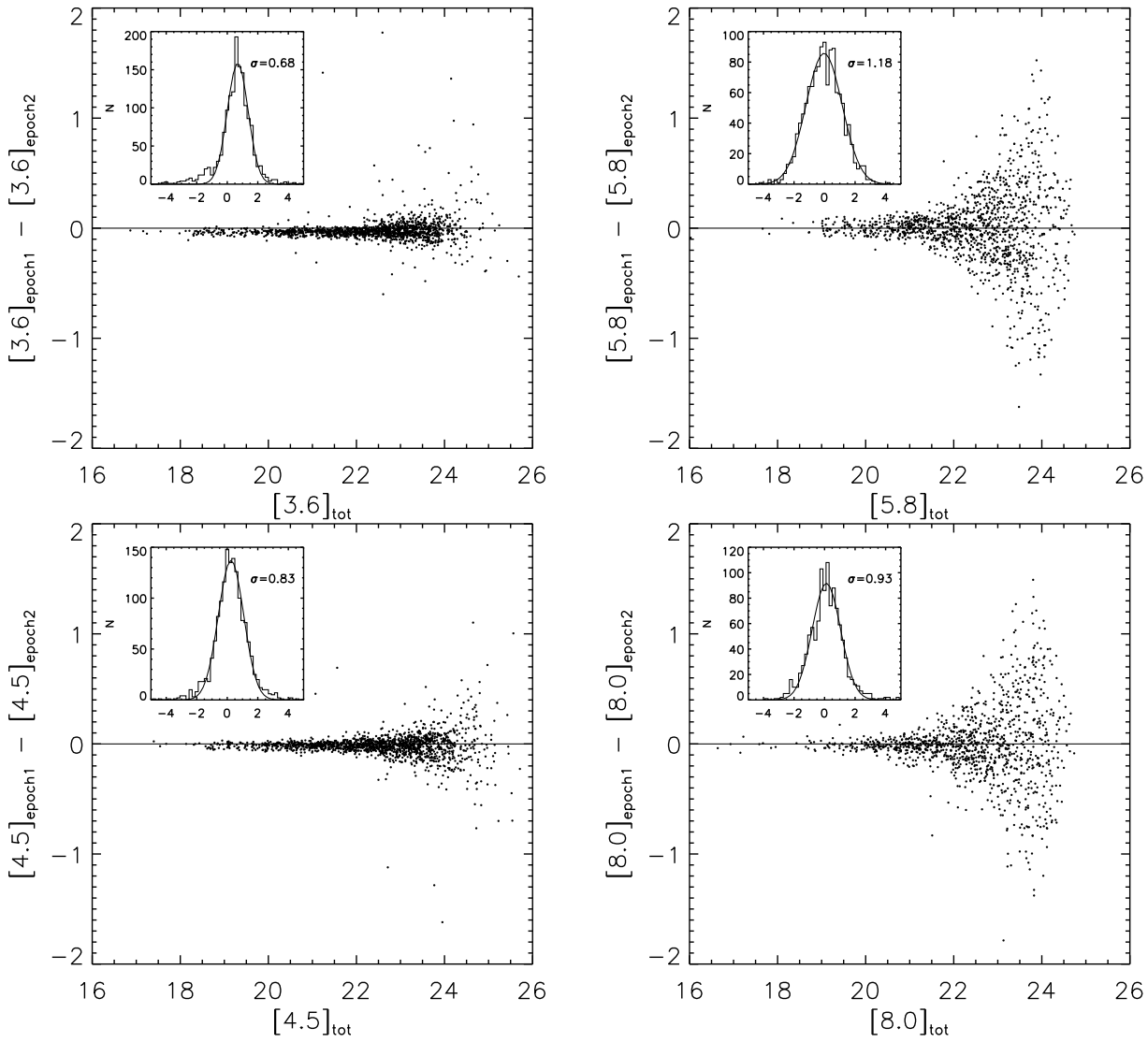

Figure 3.4 — Comparison between IRAC observations from epoch 1 and epoch 2 for K_s-band detected sources in the overlap region between the 2 epochs. The large panels show a good correspondence between the 2 independent photometric measurements, with a slight zero-point drift of 0.03 mag in the 3.6 μm band. The inset panels shows the distribution of $(f_{epoch1} - f_{epoch2})/\sqrt{err^2_{epoch1} + err^2_{epoch2}}$, where a minimum relative error of 3% was assumed to account for relative zero-point uncertainties over the field. The standard deviation of the distribution is of order unity, meaning that estimated flux errors account well for the empirically determined uncertainties.

orientation with respect to the positions of neighboring sources. In Figure 3.4, we show the difference between the IRAC magnitude measured during epoch 1 and epoch 2. The rms ranges from 5% in the 4.5 μm band to 10% in the 8.0 μm band for sources with an AB magnitude brighter than 22. The largest systematic offset was measured for the 3.6 μm band, where a zero-point drift of 0.03 mag was measured between the 2 epochs. In the inset panels the distribution of $(f_{epoch1} - f_{epoch2})/\sqrt{err^2_{epoch1} + err^2_{epoch2}}$ is plotted. The distribution is well described by a gaussian. For well estimated errors the expected

Table 3.2. Spectroscopic redshifts for K_s-band detected objects

Survey	High quality flags	Number[a]
FORS2 (v2.0)	A	324
K20 (Mignoli et al. 2005)	1	263
VVDS (v1.0, Le Fèvre et al. 2004)	4,3	247
CXO (Szokoly et al. 2004)	3,2,1	92
Norman et al. (2002)	all	1
Croom et al. (2001)	all	20
van der Wel et al. (2004)	all	21
Cristiani et al. (2000)	all	3
Strolger et al. (2004)	all	7
Daddi et al. (2004)	all	7
IMAGES (Ravikumar et al. 2006)	1	107
LCIRS (Doherty et al. 2005)	3	3
Wuyts et al. (Chapter 4)	all	7
Kriek et al. (2007)	all	2

[a]The numbers are non-redundant. For objects targeted during multiple surveys, the redshift with the highest quality flag was adopted.

standard deviation of the distribution is 1. We adopted a minimum relative uncertainty in the flux of 3% to account for zero-point variations over the field. This is particularly relevant for the 3.6 μm and 4.5 μm band, where the sources are detected with a high signal-to-noise. The standard deviation of $(f_{epoch1} - f_{epoch2})/\sqrt{err^2_{epoch1} + err^2_{epoch2}}$ in these bands is smaller than 1. Adopting a more conservative minimum relative uncertainty would only decrease this value, suggesting that zero-point variations within the field are limited to the few percent level. In the less sensitive 5.8 μm and 8.0 μm bands, where the minimum relative uncertainty is not reached, we find a distribution of $(f_{epoch1} - f_{epoch2})/\sqrt{err^2_{epoch1} + err^2_{epoch2}}$ with a standard deviation of nearly unity, confirming empirically the validity of our estimated uncertainties.

3.5 Redshifts

3.5.1 Spectroscopic redshifts

The CDFS-GOODS area has been targeted intensively by various spectroscopic surveys, listed in Table 3.2. The combined sample of spectroscopic redshifts forms a heterogeneous family of objects, with selection criteria varying from pure I-band (VVDS, Le Fèvre et al. 2004), K_s-band (Mignoli et al. 2005) or X-ray (Szokoly et al. 2004) flux limits to various color criteria (e.g., Doherty et al. 2005; Chapter 4). It is therefore impossible to build a combined spectroscopic sample that is complete in any sense. Rather, we aim to provide a list of trustworthy spectroscopic redshifts that are reli-

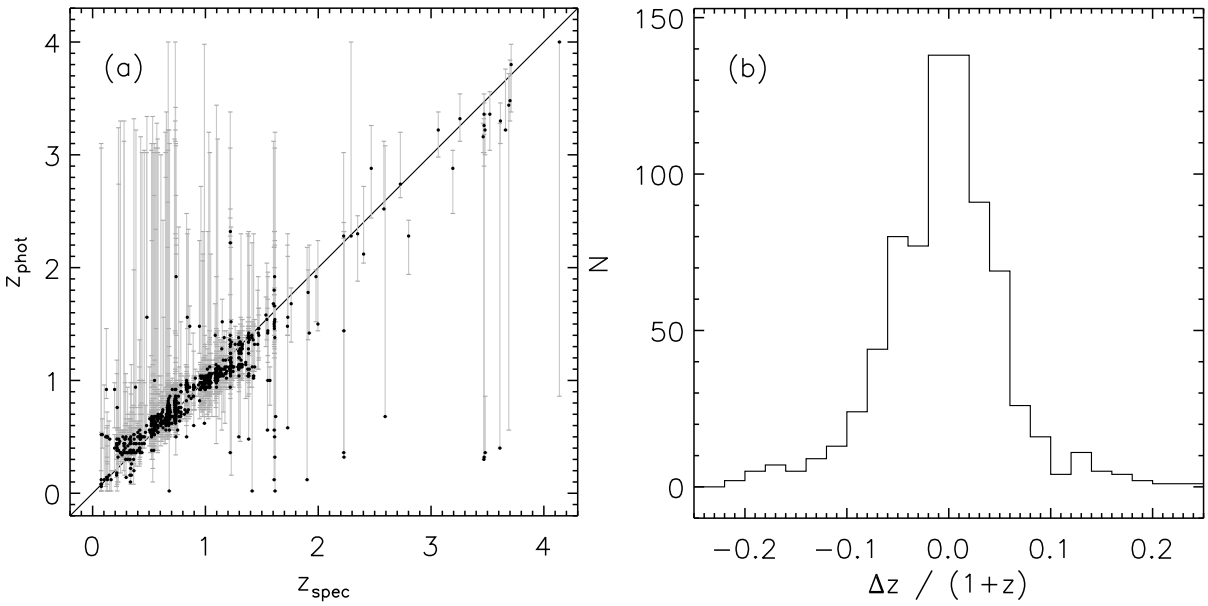

Figure 3.5 — Comparison between photometric and spectroscopic redshifts for 814 K_s-band detected sources with reliable z_{spec} identification and coverage in all wavelength bands. (a) A direct comparison with 68% confidence intervals determined from Monte Carlo simulations. (b) The distribution of $\Delta z/(1+z)$. 5% of the sources fall outside the plotted range.

ably cross-identified with a K_s-band detection in our catalog. To do so, we apply a conservative quality cut based on the quality flags that come with each of the spectroscopic catalogs, and assign the redshift to the nearest K_s-band selected object within a radius of $1\farcs2$. The quality flags and number of sources included in our reliable list of cross-correlated spectroscopic redshifts are summarized in Table 3.2. We mark these sources with a "zsp_qual" flag of 1 in our catalog. For completeness, other spectroscopic redshifts for K_s-band detected objects are also listed in our catalog, marked with a "zsp_qual" flag lower than 1, together with the original quality flag from the respective survey. We proceed to use only the 1104 spectroscopic redshifts with zsp_qual = 1.

3.5.2 Photometric redshifts

Together with the observed photometry, we release a list of photometric redshifts computed with the algorithm described by Rudnick et al. (2001; 2003). The algorithm fits a linear combination of template spectra to the optical-to-NIR spectral energy distribution. The template set consisted of 10 Single Stellar Population (SSP) templates with a Salpeter (1955) initial mass function and solar metallicity from the Bruzual & Charlot (2003) stellar population synthesis code, with ages logarithmically spaced between 50 Myr and 10 Gyr. We allowed each of the templates to be attenuated according to the Calzetti et al. (2000) law by $E(B-V) = 0.0$, 0.1, 0.3, or 0.6.

The accuracy of the photometric redshifts z_{phot} is quantified by a comparison to the spectroscopic redshifts with zsp_qual = 1. Figure 3.5(a) shows the correspondence between z_{phot} and z_{spec} for all 814 sources with $K_{s,AB}^{tot} < 24.3$ that are covered by all bands and for which a reliable spectroscopic redshift is available. The uncertainties

on z_{phot} are derived from Monte Carlo simulations and indicate the 68% confidence intervals. Figure 3.5(b) presents the distribution of $\Delta z/(1+z)$, which is commonly used to determine the accuracy of photometric redshifts. We find a median $\Delta z/(1+z)$ of 0.001 and a normalized median absolute deviation (equal to the rms for a Gaussian distribution) of $\sigma_{NMAD} = 0.053$. 5% of the objects with spectroscopic redshift have $|\Delta z|/(1+z) > 5\sigma_{NMAD}$ and fall outside the plotted range of Figure 3.5(b). Considering the 95 spectroscopically confirmed sources with a cross-identification within 2.″0 in the 1Ms X-ray catalog by Giacconi et al. (2002), we find a scatter of $\sigma_{NMAD} = 0.064$. It is reassuring that despite the lack of AGN spectrum in our template set, the overall performance of our photometric redshift code for AGN candidates remains good. We do note however that, independent of redshift, the fraction of catastrophic outliers ($|\Delta z|/(1+z) > 5\sigma_{NMAD}$) is 2.5 times larger for the AGN candidates than for the total sample of spectroscopically confirmed sources.

3.6 Catalog parameters

Here we describe the entries of our K_s-band selected catalog of the GOODS-CDFS. The format is similar to the FIRES catalogs of the HDFS (L03) and MS 1054–03 (FS06), making a straightforward combination of all three fields possible for the user.

- ID– Unique identification number
- x, y– Pixel position of the object, based on the K_s-band detection map. The pixelscale is 0.″15 pixel^{-1}.
- RA, DEC– Right ascension and declination coordinates for equinox J2000.0.
- [$band$]_colf– Flux in microjanskies measured within the color aperture (§ 3.4.2.1). The bandpasses are B,V,i,z,J,H,K_s, [3.6 μm], [4.5 μm], [5.8 μm], and [8.0 μm].
- [$band$]_colfe– Uncertainty in the [$band$]_colf flux measurement, derived from the noise analysis (§ 3.3.5). The units are microjanskies.
- K_s_totf– Total K_s-band flux in microjanskies, measured within the total aperture and scaled by the aperture correction (§ 3.4.2.1). Total fluxes in other bandpasses can be calculated by [$band$]$\_totf$ = [$band$]$\_colf \times (K_s\_totf/K_s\_colf)$.
- K_s_totfe– Uncertainty associated with K_s_totf, also in microjanskies.
- [24 μm]_totf– Total MIPS 24 μm-band flux in microjanskies, measured within a 6″ diameter circular aperture and then aperture corrected (§ 3.4.2.2).
- [$band$]w– Effective weight in the bandpass [$band$], normalized to the median effective weight of all sources in that band.
- ap_col– Aperture diameter in arcsec within which [$band$]_colf was measured. In cases where the color aperture was the isophotal aperture defined by the surface brightness threshold of $\mu(K_{s,AB}) = 24.6$ mag arcsec^{-2}, ap_col is the diameter in arcsec of a circular aperture with equal area.
- ap_tot– Aperture diameter in arcsec used for measuring the total K_s-band flux. When the isophotal or SExtractor's "MAG_AUTO" aperture was used, this entry contains the equivalent circularized diameter corresponding to that aperture.
- f_deblend1– Flag equal to 1 when the source was deblended somewhere in the process (SExtractor's "blend").
- f_deblend2– Flag equal to 1 when the photometry is affected by a neighboring

source (SExtractor's "bias").
- Kr50– Half light radius in arcsec, measured on the K_s-band image (SExtractor's flux_radius scaled to arcsec).
- Keps– Ellipticity of the isophotal area, measured on the K_s-band image.
- Kposang– Position angle of the isophotal area, measured on the K_s-band image.
- zph_best– Best estimate of the photometric redshift (§ 4.6).
- zph_low, zph_high– Lower and upper edge of the 68% confidence interval around zph_best.
- zsp– Spectroscopic redshift (set to -99 when no spectroscopic information is available).
- zsp_qual– Quality flag from 0 to 1 assigned to the spectroscopic redshift. Only zsp_qual=1 entries are considered reliable.
- zsp_source– Spectroscopic survey from which zsp was taken (Tab. 3.2).
- zsp_qual_orig– Original quality flag for zsp from the respective spectroscopic survey.
- XID– Identification number from the 1Ms X-ray catalog by Giacconi et al. (2002), set to -99 when no cross-identification within 2″ was found. Note that we accounted for the $\sim 1\farcs3$ systematic offset in the Giacconi et al. (2002) X-ray centroids, as pointed out before by Roche et al. (2003).

3.7 Comparison to the GOODS-MUSIC catalog

3.7.1 Differences in data and strategy

Recently, Grazian et al. (2006a) presented a multicolor catalog for the GOODS-CDFS field, referred to as the GOODS-MUSIC catalog. The clustering evolution of distant red galaxies was quantified based on this sample (Grazian et al. 2006b), as was the contribution of various color-selected samples of distant galaxies to the stellar mass density (Grazian et al. 2007). Despite the overlap in public data used to compile the GOODS-MUSIC and our catalog, there are a number of marked differences.

First, our catalog is purely K_s-band selected. Since the K_s-band magnitude is a good proxy for stellar mass, this makes it ideally suited to extract mass-limited samples from. The GOODS-MUSIC sample on the other hand is to first order z-band selected (at the ACS resolution), with an addition of the remaining K_s-band sources that are detected in a map with masked z-band detections. Although valuable in its own respect, this makes it less trivial to understand the completeness of the sample.

Second, we based our catalog on the ESO/GOODS data release v1.5, consisting of 3 extra ISAAC pointings in J and K_s, and 7 more in H with respect to the v1.0 release used by Grazian et al. (2006a).

Finally, we include MIPS 24 μm measurements, enabling us to constrain the total IR luminosity of the K_s-band selected galaxies. Before doing so, we compare the photometry in common between both catalogs, and the photometric redshifts derived from it.

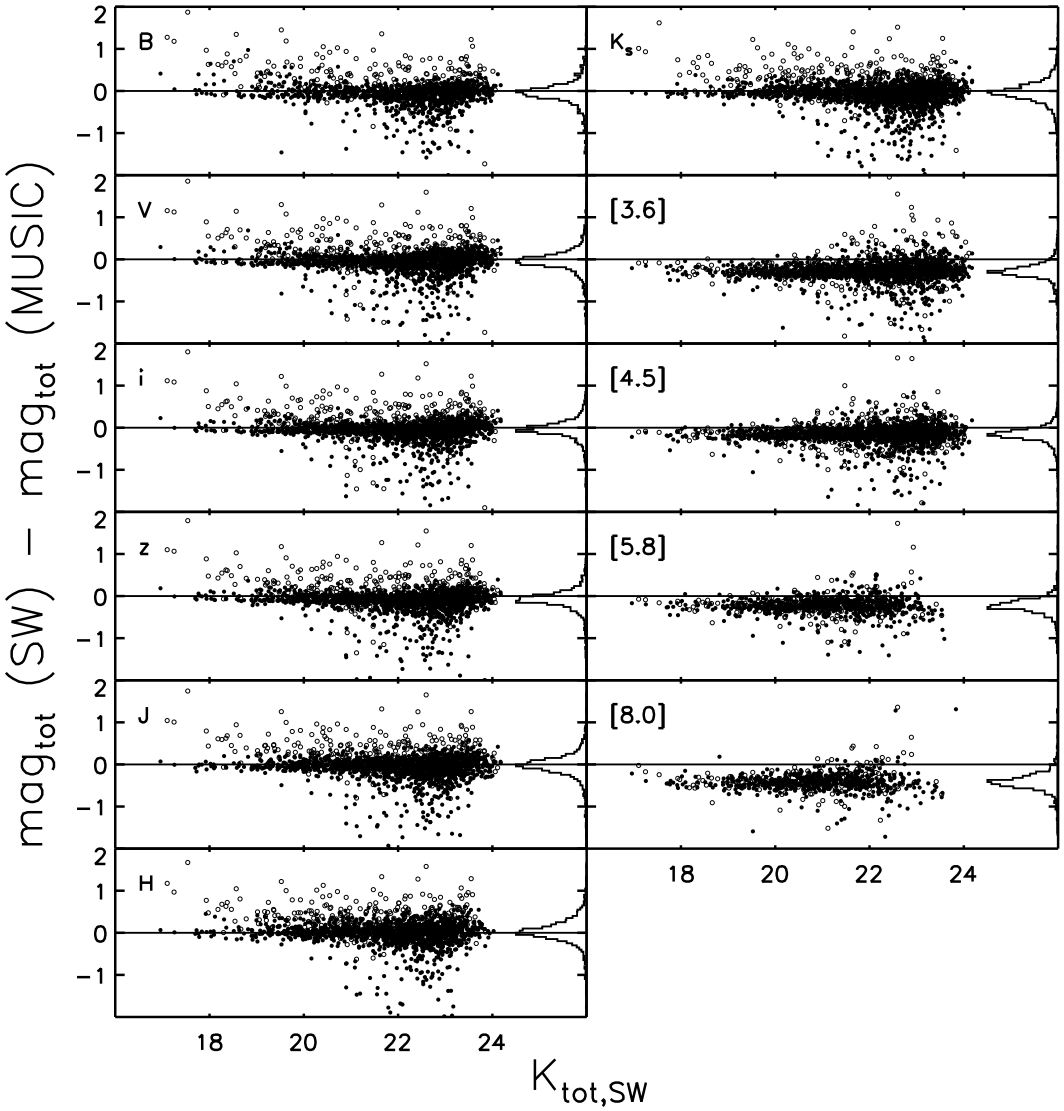

Figure 3.6 — A direct comparison of total magnitudes for sources with $S/N > 10$ in the B-to-8.0 μm bandpasses in common between GOODS-MUSIC and our catalog. Sources that are blended in the K_s-band image are plotted as empty symbols. On the right side of each panel, a histogram shows the distribution of offsets. We find an overall good correspondence in the optical and NIR bands, with offsets of roughly 6% due to aperture corrections. Larger aperture corrections for the IRAC bands lead to offsets up to 0.4 mag.

3.7.2 Comparing photometry

We cross-correlated the two catalogs using a search radius of 1.″2 and in Figure 3.6 present a comparison of the B-to-8.0 μm total magnitudes for objects with $S/N > 10$ in the K_s-band and the band under consideration. Objects that are marked by SExtractor as blended in the K_s-band, are indicated with empty symbols. The overall correspondence in the B-to-K_s bands is good, and offsets can be well understood from the differences in the applied photometric method. We measure a typical median offset for non-blended sources in the optical and NIR bands of $mag_{tot,SW} - mag_{tot,MUSIC} = -0.06$, and a scatter of $\sigma_{NMAD} < 0.2$. Grazian et al. (2006a) based their total magnitudes on SExtractor's "MAG_AUTO" parameter for the z-band detections and on the "MAG_BEST" for the remaining K_s-band detections that were not detected in the z-band. Grazian et al. (2006a) did not apply an aperture correction based on the stellar growth curve to correct for the flux lost because it fell outside the "MAG_AUTO" or "MAG_BEST" aperture. The lack of aperture correction explains at least part of the systematic offset. Sources marked as blended in our K_s-band detection map typically are brighter by 0.2 - 0.4 mag in the MUSIC catalog. This can be explained by the contamination from neighboring sources within the "MAG_AUTO" aperture, which we avoid by using the isophotal aperture in combination with an aperture correction for blended sources.

For the IRAC photometry, the discrepancies are larger, ranging from 0.16 mag in the 4.5 μm band to 0.42 mag at 8.0 μm. Again, aperture corrections (or the lack thereof) are most likely responsible for the offset. Using simple aperture photometry of isolated stars, we find that the GOODS-MUSIC IRAC magnitudes account for the light within an aperture of $2.''0 - 2.''5$. From the growth curves of our constructed IRAC PSFs, we derive that the correction factors needed to account for the light outside this aperture are consistent with the measured offsets between the GOODS-MUSIC and our IRAC magnitudes. Grazian et al. (2006a) apparently did not apply this aperture correction. We stress that, since the aperture correction for the IRAC photometry is considerably larger than for the optical and NIR bands, this not only affects the estimate of total magnitudes and its derived properties such as stellar mass, but also the optical-to-MIR and NIR-to-MIR colors. For example, our $z - [3.6\ \mu\text{m}]$, $z - [4.5\ \mu\text{m}]$, $z - [5.8\ \mu\text{m}]$, and $z - [8.0\ \mu\text{m}]$ colors are redder than the GOODS-MUSIC colors by 0.23, 0.11, 0.17, and 0.37 mag in the median respectively. Similarly, our $K_s - [3.6\ \mu\text{m}]$, $K_s - [4.5\ \mu\text{m}]$, $K_s - [5.8\ \mu\text{m}]$, and $K_s - [8.0\ \mu\text{m}]$ colors are redder in the median by 0.29, 0.16, 0.22, and 0.42 respectively. The scatter in the color differences with respect to GOODS-MUSIC typically amounts to 1.5 times the size of the median offset.

3.7.3 Comparing photometric redshifts

Finally, we compare the photometric redshifts presented in §4.6 with those derived by Grazian et al. (2006a). The numbers quoted in §4.6 and by Grazian et al. (2006a) cannot directly be compared since new spectroscopic redshifts were added, and objects that showed evidence for the presence of an AGN in their optical spectrum were rejected from the GOODS-MUSIC photometric redshift analysis. Nevertheless, when comparing the performance of the z_{phot} estimates for a set of 569 non-AGN with reliable z_{spec} and coverage in all bands in both catalogs, we find a scatter in $\Delta z/(1+z)$

that is nearly 1.5 times smaller for GOODS-MUSIC ($\sigma_{NMAD} = 0.037$) than for our best estimates ($\sigma_{NMAD} = 0.054$). The median $\Delta z/(1+z)$ is 0.009 and -0.003 for the GOODS-MUSIC and our z_{phot} estimates respectively.

Two facts could attribute to the better performance by GOODS-MUSIC. First, an observed U to rest-frame 5.5 μm wavelength baseline was used by GOODS-MUSIC to estimate z_{phot}, whereas our estimate was based on B-to-K_s photometry. A second possible reason, is the difference in template sets. GOODS-MUSIC used PEGASE 2.0 models (Fioc & Rocca-Volmerange 1997), whereas our estimates were based on synthetic models by Bruzual & Charlot (2003). Comparing the photometric redshifts for all our K_s-band detected objects with a cross-identification within 1$''$.2 in the GOODS-MUSIC sample, we find that $\Delta z/(1+z)$ has a median of 0 and σ_{NMAD} of 0.073.

We conclude that there is an overall reasonable agreement between both catalogs with differences that can be understood from the applied method. We therefore proceed with strengthened confidence to exploit our catalog to analyze the colors and total IR energy output of distant galaxies.

3.8 Total IR properties of distant K_s-selected galaxies

With the catalog at hand, we aim to answer the following simple questions: Which K_s-selected ($S/N_{K_s} > 5$, $K^{tot}_{s,AB} \lesssim 24.3$) galaxies at $1.5 < z < 2.5$ have the brightest total IR luminosities, and which contribute most to the integrated total IR luminosity? The answer will be either red or blue galaxies, with the color defined in the rest-frame UV, optical or NIR wavelength regime. We focus on the $1.5 < z < 2.5$ interval, since at those redshifts the observed 24 μm broadly correlates with the total IR luminosity.

3.8.1 Observed 24 μm flux as function of observed colors

We approach the questions raised above by first studying the correlation between purely observational properties: the 24 μm flux as proxy for IR luminosity and the observed $B-V$, $J-K_s$, and $K_s-[4.5\ \mu\text{m}]$ colors as proxy for the rest-frame UV, optical and optical-to-NIR color respectively. Unless the redshift dependence of the conversion from 24 μm to total IR luminosity and of the conversion from observed to rest-frame colors are conspiring, any trend in the directly observable properties should be a signpost for correlations in the rest-frame properties, whose derivation involves significant systematic uncertainties.

Since a large number of K_s-selected galaxies at $1.5 < z < 2.5$ remains undetected in the 24 μm observations ($[24\ \mu\text{m}]_{tot} \sim 16\ \mu$Jy; 5σ), we divide our galaxies in bins of similar color. Each bin contains 80 objects. To start, we leave the origin of the 24 μm emission (dust heated by AGN or star formation) as an open question. We note however that excluding X-ray detected sources each bin would contain 76 objects, and applying such a selection would not affect the results of our stacking analysis. The mean and median stacked 24 μm flux densities of the galaxies in each bin are significantly detected, and plotted in Figure 3.7 versus the observed $B-V$, $J-K_s$, and $K_s-[4.5\ \mu\text{m}]$ color. The mean stack counts has a contribution from all the galaxies in the color bin.

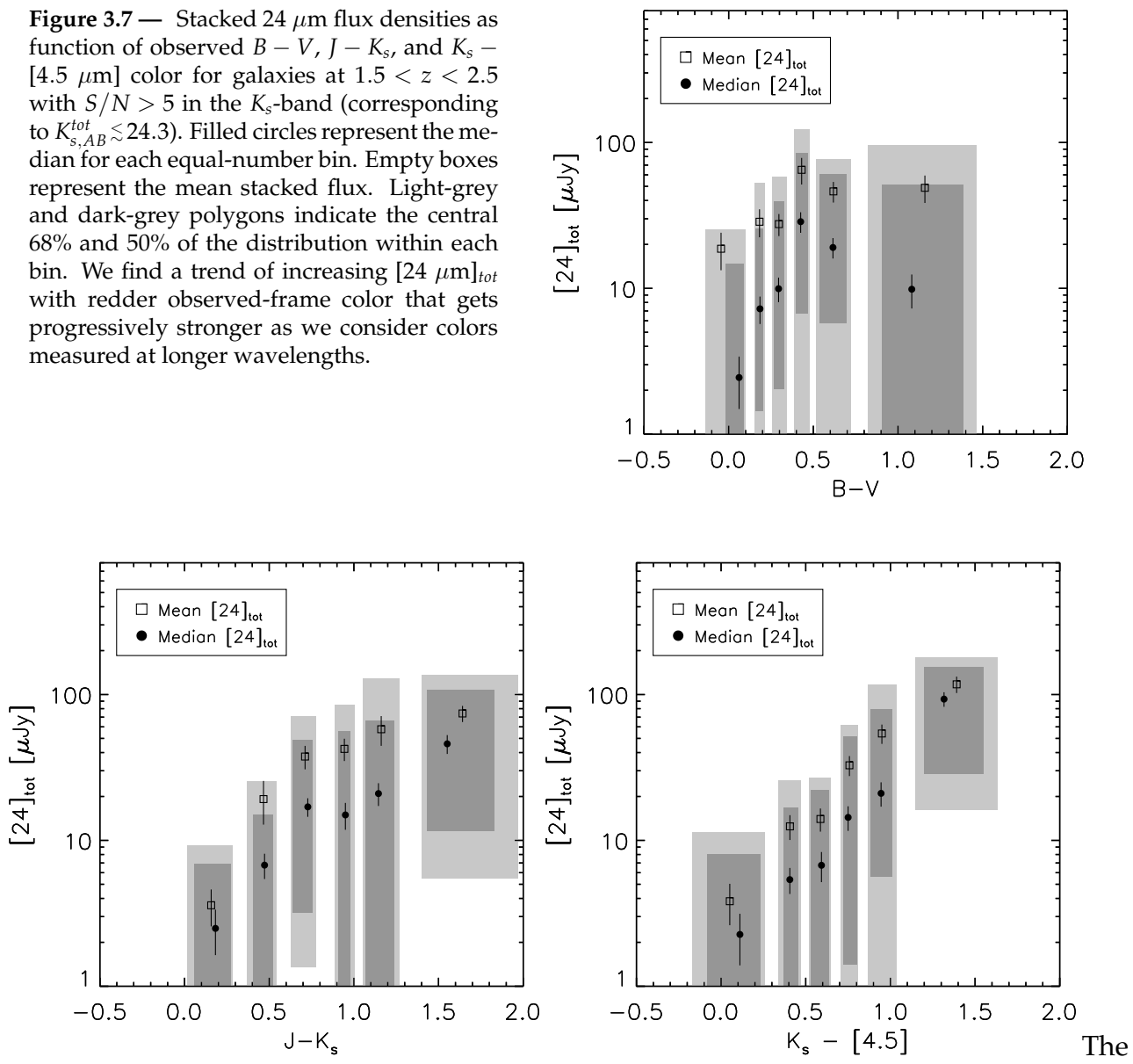

Figure 3.7 — Stacked 24 μm flux densities as function of observed $B-V$, $J-K_s$, and K_s- [4.5 μm] color for galaxies at $1.5 < z < 2.5$ with $S/N > 5$ in the K_s-band (corresponding to $K_{s,AB}^{tot} \lesssim 24.3$). Filled circles represent the median for each equal-number bin. Empty boxes represent the mean stacked flux. Light-grey and dark-grey polygons indicate the central 68% and 50% of the distribution within each bin. We find a trend of increasing [24 μm]$_{tot}$ with redder observed-frame color that gets progressively stronger as we consider colors measured at longer wavelengths.

The median stack is lower since it does not capture the brightest sources, but has the advantage that it is more robust against any residual contamination from bright neighbors. The error bars on the mean flux measurement indicate the errors in the mean ($\sigma([24\ \mu\mathrm{m}]_{tot})/\sqrt{N}$), whereas the error bars on the median flux measurement are computed as $\sigma_{NMAD}([24\ \mu\mathrm{m}]_{tot})/\sqrt{N}$. Furthermore, the light-grey and dark-grey polygons show the range containing 68% and 50% of the binned galaxies. Each color bin contains galaxies with a large spread in 24 μm fluxes. In most bins, at least 16% and often more than 25% of the galaxies are individually undetected at 24 μm.

Figure 3.7 shows that the galaxies in the bluest $B-V$ bins are the faintest 24 μm sources. However, the stacked [24 μm]$_{tot}$ flux is not uniformly increasing over the whole observed optical color range. Considering colors measured at longer wavelengths, we do find a highly significant increase in the stacked [24 μm]$_{tot}$ flux over the

entire $J - K_s$ and $K_s - [4.5\ \mu\mathrm{m}]_{tot}$ color range. The trend is strongest in the observed $K_s - [4.5\ \mu\mathrm{m}]_{tot}$ color, where we find an increase in $[24\ \mu\mathrm{m}]_{tot}$ of factor ~ 30 over a color range of ~ 1.5 mag. Since the bins contain an equal number of objects, it is trivial to see that not only the reddest galaxies in $J - K_s$ and $K_s - [4.5\ \mu\mathrm{m}]$ are brightest at 24 μm, they also contribute the most to the total 24 μm emission integrated over all distant K_s-selected galaxies.

3.8.2 Total IR luminosity as function of rest-frame colors

Although the trend of more 24 μm emission for galaxies with a redder observed color is highly significant for $J - K_s$ and $K_s - [4.5\ \mu\mathrm{m}]$, it could still be contaminated or, alternatively, driven by redshift dependencies within the $1.5 < z < 2.5$ redshift interval under consideration. Now, we will attempt to remove possible redshift dependencies by converting both axes to a rest-frame equivalent. Moreover, instead of converting the measured flux density at 24 μm to a rest-frame flux density at $24\ \mu\mathrm{m}/(1+z)$, we use it as a probe to determine the total IR luminosity $L_{IR} \equiv L(8 - 1000\ \mu\mathrm{m})$. Since this conversion assumes that the 24 μm emission originates from dust heated by star formation, we further reject all X-ray detections from our sample to rule out AGN candidates.

In the following, we first describe the derivation of rest-frame UV to NIR colors. Next, we explain the method to estimate the total IR luminosity. Finally, we repeat the stacking analysis using the derived rest-frame properties.

3.8.2.1 UV slope and rest-frame colors

For each of the galaxies in our sample, we modeled the spectral energy distribution (SED) using the stellar population synthesis code by Bruzual & Charlot (2003). We used an identical approach as Wuyts et al. (2007), assuming a Salpeter IMF and solar metallicity, and fitting three star formation histories: a single stellar population without dust, an exponentially declining model with e-folding time of 300 Myr and allowed dust attenuation in the range $A_V = 0 - 4$, and a constant star formation model with the same freedom in attenuation. We characterize the rest-frame UV part of each SED by fitting the functional form $F_\lambda \sim \lambda^\beta$ to the best-fitting template, using the rest-frame UV bins defined by Calzetti, Kinney,& Storchi-Bergmann (1994). The robustness of this technique is discussed by van Dokkum et al. (2006).

The rest-frame $(U - V)_{rest}$ and $(V - J)_{rest}$ colors were determined by interpolation between the directly observed bands using templates as a guide. For an in-depth discussion of the algorithm, we refer the reader to Rudnick et al. (2001; 2003).

3.8.2.2 Converting 24 μm flux to total IR luminosity

At redshifts $1.5 < z < 2.5$, the 24 μm fluxes trace the rest-frame 7.7 μm emission from polycyclic aromatic hydrocarbons (PAHs). To convert this MIR emission to a total IR luminosity $L_{IR} \equiv L(8 - 1000\ \mu\mathrm{m})$, we use the infrared spectral energy distributions of star-forming galaxies provided by Dale & Helou (2002). The template set allows us to quantify the IR/MIR flux ratio for different heating levels of the interstellar environment, parameterized by $dM(U) \sim U^{-\alpha} dU$ where M(U) represents the dust mass heated

by an intensity U of the interstellar radiation field.

We computed the total infrared luminosity $L_{IR,\alpha}$ for each object for all Dale & Helou (2002) templates within the reasonable range from $\alpha = 1$ for active galaxies to $\alpha = 2.5$ for quiescent galaxies. Following Geach et al. (2006), the mean of all $L_{IR,\alpha}$ was adopted as best estimate for the IR luminosity, and the 0.9 dex variation from $L_{IR,\alpha=2.5}$ to $L_{IR,\alpha=1}$ was taken as a measure for the systematic uncertainty in the conversion.

Apart from the random photometric error and systematic template uncertainty, uncertainties in the photometric redshift contribute to the total error budget. For each galaxy, we calculated the spread in L_{IR} caused by variations of z_{phot} within the 68% confidence interval. Although the uncertainty in photometric redshift is partly random (propagating from photometric uncertainties in the SED), we treat it as purely systematic, originating from template mismatches. This means the error bars related to z_{phot} on the stacked L_{IR} measurements do not scale with $1/\sqrt{N}$. Instead, they range from the stacked L_{IR} based on the lowest $L_{IR,individual}$ estimates allowed for each object within its z_{phot} uncertainty, to the stacked L_{IR} based on the maximum $L_{IR,individual}$ allowed for each object.

3.8.2.3 L_{IR} versus rest-frame color

Having determined the rest-frame colors and total IR luminosities of K_s-selected non-AGN at $1.5 < z < 2.5$, we now proceed to investigate which K_s-selected galaxies contribute most to the IR emission. Again, we make use of a stacking procedure to enhance the robustness of our results. In Figure 3.8, we plot the mean and median stacked total IR luminosities of our sample divided into color bins versus the rest-frame UV slope β, the rest-frame optical color $(U-V)_{rest}$, and the rest-frame optical-to-NIR color $(V-J)_{rest}$. The black error bars indicate the errors in the mean and median. With dotted error bars, we show the systematic variations allowed within the photometric redshift uncertainties. Finally, the error bar in the bottom right corner represents the range from quiescent to active galaxy templates by Dale & Helou (2002). Clearly, systematic uncertainties are dominating the error budget in this analysis.

As in Figure 3.7, we find a large range in IR properties within each bin, illustrated by the light-grey and dark-grey polygons that mark the central 68% and 50% of the distribution of L_{IR} of individual objects respectively. Nevertheless, a general trend is visible of redder colors corresponding to larger IR luminosities. No matter which part of the spectral energy distribution is used to define red or blue galaxies, the redder 2/3 of the galaxies in our sample have stacked IR properties in the LIRG ($L_{IR} = 10^{11} - 10^{12}\ L_\odot$) regime. The trend seems to flatten at the reddest UV slopes, and possibly the contribution to the total IR luminosity even drops for the reddest $(U-V)_{rest}$ bin. In $(V-J)_{rest}$ on the other hand, the increase in L_{IR} with reddening color continues over the entire color range, reaching ULIRG luminosities ($L_{IR} > 10^{12}\ L_\odot$) for the stack of the reddest bin. While Luminous ($10^{11} L_\odot < L_{IR} < 10^{12} L_\odot$) and Ultraluminous ($L_{IR} > 10^{12} L_\odot$) Infrared Galaxies, (U)LIRGS (Sanders & Mirabel 1996), are locally very rare, they are found to be increasingly more common toward higher redshifts (e.g., Caputi et al. 2006). Considering the IR luminosities of individual objects in our high-redshift sample, we find that ULIRGs make up 14% of our K_s-selected sample with $K_{s,AB}^{tot} < 24.3$.

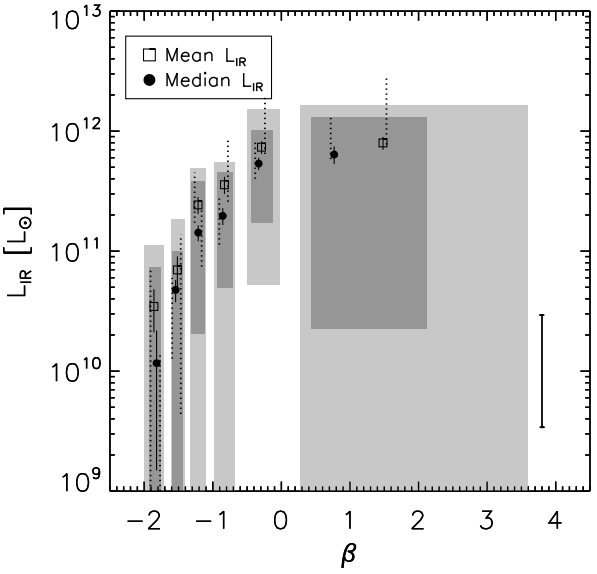

Figure 3.8 — Stacked total IR luminosities as function of rest-frame UV slope, $(U-V)_{rest}$, and $(V-J)_{rest}$ for non-AGN at $1.5 < z < 2.5$ with $S/N > 5$ in the K_s-band ($K^{tot}_{s,AB} \lesssim 24.3$). Filled circles represent the median for each equal-number bin. Empty boxes represent the mean stacked flux. Light-grey and dark-grey polygons indicate the central 68% and 50% of the distribution within each bin. The systematic uncertainty induced by template uncertainties in the conversion to L_{IR} is indicated in the bottom right corner. The dotted error bars indicate the variation in the mean and median stacked L_{IR} by systematic variations in z_{phot}. We find a trend of increasing L_{IR} with redder rest-frame color. Since the bins contain equal numbers of objects, this also means that red galaxies contribute most to the integrated IR emission of distant K_s-selected galaxies.

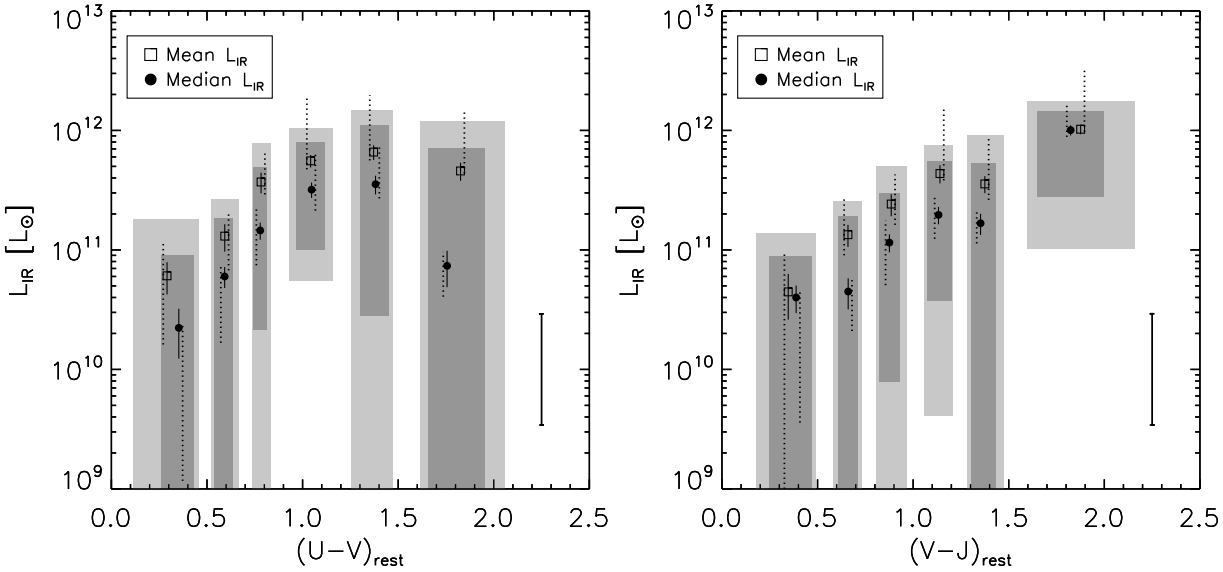

The fraction of ULIRGs increases to 37% when only considering massive ($M > 10^{11}\ M_\odot$) galaxies, with the masses derived from SED modeling as described by Wuyts et al. (2007). A similar fraction was found by Daddi et al. (2007). Although the IR/MIR conversion factor varies by nearly an order of magnitude between the use of quiescent ($\alpha = 2.5$) or active ($\alpha = 1$) galaxy templates, we stress that we conservatively use a mean over all α for each of the galaxies. Using a lower α for brighter galaxies would only increase the correlation between stacked total IR luminosity and rest-frame color.

We thus conclude that amongst distant K_s-selected galaxies that show no sign of AGN at X-ray wavelengths, the redder galaxies have on average larger total IR luminosities. Given that each bin in Figure 3.8 contains an equal number of objects, it is also clear that red galaxies in our sample contribute more to the integrated total IR lumi-

nosity than blue galaxies. We argue that this trend cannot be explained by systematic errors, and tested that this conclusion is robust against the precise choice of redshift interval by varying the lower edge between redshift 1 and 2 and the upper edge between 2 and 3. Likewise, we verified that none of our conclusions critically depend on the number of color bins. Dividing the sample in two equal-number bins according to β, $(U-V)_{rest}$, and $(V-J)_{rest}$, we find that the integrated total IR luminosity of the red half is larger than that of the blue half by a factor 5.3, 2.9, and 4.4 respectively. Imposing a brighter cut in the K_s-band magnitude weakens the correlation of L_{IR} with $(V-J)_{rest}$, and causes the stacked L_{IR} of the reddest UV slopes and $(U-V)_{rest}$ colors to drop. Adopting a $K_{s,AB}^{tot} < 22.86$ cut, as is the case for the NIR-selected sample studied by Reddy et al. (2006), we find that the ratio of the stacked L_{IR} of the red and the blue half of the galaxies in β, $(U-V)_{rest}$, and $(V-J)_{rest}$ amounts to a factor of 2.7, 0.9, and 2.3 respectively. Finally, we note that, although X-ray detections were excluded from our analysis to validate the use of IR templates for starforming galaxies, the stacking results remain nearly unaffected when we treat them as normal galaxies.

It is tempting to elaborate on the physical interpretation in terms of star formation rate (SFR), age, and dust content of the galaxies in our sample implied by the presented results. Colors in different wavelength regimes are to a greater or lesser extent determined by these physical parameters. The UV slope and $(V-J)_{rest}$ color are both sensitive tracers of dust attenuation (Meurer et al. 1999 and Wuyts et al. 2007 respectively). The $(U-V)_{rest}$ color on its behalf is primarily a tracer of stellar age and to lesser extent reddened by dust. The fact that in the reddest $(U-V)_{rest}$ bin the total IR luminosity drops again might therefore indicate an increasing contribution from low L_{IR} galaxies with little dust-obscured star formation. In combination with the fact that rest-frame optically selected galaxies often have faint UV luminosities and thus little unobscured star formation (Förster Schreiber et al. 2004), this suggests that part of the galaxies making up the reddest $(U-V)_{rest}$ bin have a low overall SFR (unobscured + obscured). This is consistent with the spectral evidence for galaxies with quenched star formation at $z \sim 2$ (Kriek et al. 2006). A similar conclusion was drawn by Reddy et al. (2006), who found for a sample of galaxies at similar redshifts selected by optical and NIR color criteria that the IR luminosity of 24 μm detected sources increased toward redder observed $z-K$, but that at the reddest $z-K$ color a population without 24 μm detection exists that satisfies the Distant Red Galaxies (Franx et al. 2003) and/or BzK/PE (Daddi et al. 2004) color criteria. We note that in samples with a brighter magnitude limit, e.g., $K_{s,AB}^{tot} < 22.86$ as for the NIR-selected galaxies studied by Reddy et al. (2006), the population without 24 μm detection is more prominently present among the red galaxies than in our deeper K_s-selected sample, while the overall fraction of galaxies without 24 μm detection is lower by a factor 1.5 in the $K_{s,AB}^{tot} < 22.86$ sample. Based on X-ray stacking in the GOODS-North field, although also probing only to $K_{s,AB}^{tot} < 22.86$, Reddy et al. (2005) found a similar turnover in inferred SFR at $z-K > 3$. Although the observed $z-K$ color is redshift dependent and at $z \sim 2$ spans a somewhat broader wavelength range than $(U-V)_{rest}$, both colors probe the Balmer/4000Åbreak and the observed turnover therefore likely share the same origin. The strength of the Balmer/4000Åbreak correlates with age, and is to a slightly lesser degree also dependent on metallicity and dust (see, e.g., BC03; Worthey 1994;

MacArthur 2005). An in-depth analysis of the mix between dust-obscured starforming systems and evolved red galaxies would require a careful SED modeling, estimating the SFR based on different wavelength tracers from X-ray over UV to the infrared, and a treatment of each object on an individual basis to assess their relative contribution. Such a study is clearly beyond the scope of this chapter, and will be presented by Labbé et al. (in preparation) based on the combined sample of galaxies in the CDFS (this chapter), MS 1054–03 (FS06) and the HDFS (L03).

3.9 Summary

We present a K_s-band selected catalog for the GOODS-CDFS, containing consistent photometry in the B,V,i,z,J,H,K_s,[3.6 μm], [4.5 μm], [5.8 μm], [8.0 μm], and [24 μm] bands. Together with the photometry, we release a list of photometric redshifts with a scatter in $\Delta z/(1+z)$ of 0.053, a cross-correlation with all available spectroscopic redshifts to date, and a cross-correlation with the 1Ms X-ray catalog by Giacconi et al. (2002). After a description of the catalog construction, we discuss the differences with the GOODS-MUSIC '$z + K_s$'-selected catalog by Grazian et al. (2006a). Finally, the catalog, which has been used to estimate stellar mass densities (Rudnick et al. 2006), construct luminosity functions (Marchesini et al. 2006) and study the predominance of red galaxies at the high mass end (van Dokkum et al. 2006), is exploited to answer the following question: Which distant K_s-band selected galaxies are brightest and contribute most to the total IR luminosity?

First, we compared the stacked 24 μm fluxes of galaxies at $1.5 < z < 2.5$ with $K_{s,AB}^{tot} < 24.3$ split in observed color bins. Overall, a large spread in IR properties is found in each color bin. Nevertheless, stacking the fluxes within each bin reveals a clear trend with color. Both in the observed $B-V$, $J-K_s$, and K_s-[4.5 μm] colors, the lowest mean and median [24 μm]$_{tot}$ fluxes are found for the bluest color bin. In $J-K_s$ and $K_s-[4.5\mu m]$, the emission at 24 μm continues to rise toward redder colors.

Second, we use our photometric redshifts to convert the observed spectral energy distributions to rest-frame colors and translate the observed 24 μm flux to the total IR luminosity $L_{IR} \equiv L(8-1000\ \mu\mathrm{m})$. In this procedure, all AGN candidates, selected by their X-ray detection, were rejected from the sample. Removing the redshift dependence and extrapolating from MIR to total IR goes at the cost of systematic uncertainties. We carefully measured the systematic contribution to the total error budget from uncertainties in z_{phot} and from our lack of knowledge about which IR template SED matches best the spectral shape of the objects in our sample. Doing so, we find a continuous increase in L_{IR} with $(V-J)_{rest}$. An increasing L_{IR} is also measured with UV slope β, flattening at the largest β. The rising trend of the stacked L_{IR} luminosity toward redder $(U-V)_{rest}$ seems to reverse in the reddest color bin. The large range of total IR properties in this bin suggests a mixture of galaxies with large amounts of dust emission (LIRGs up to ULIRGs) and objects devoid of it. We note that, if we were to apply a different translation from MIR to total IR luminosity than simply averaging over the conversion factors derived from all reasonable templates, the observed trend would only increase. This is e.g. the case when an SED template corresponding to a larger heating intensity of the interstellar radiation field is used for objects with a

larger rest-frame IR luminosity density, as done by Papovich et al. (2006). Since our stacking analysis divides our K_s-band selected sample in bins containing equal numbers of objects, it is immediately clear that not only do red galaxies have on average the largest total IR luminosities, it is also true that they form the dominant contribution to the overall total IR luminosity emitted by K_s-selected galaxies at $1.5 < z < 2.5$.

Acknowledgments

This research was supported by grants from the Netherlands Foundation for Research (NWO), the Leids Kerkhoven-Bosscha Fonds, and the Lorentz Center.

References

Bertin, E.,& Arnouts, S. 1996, A&AS, 117, 393
Bruzual, G.,& Charlot, S. 2003, MNRAS, 344, 1000 (BC03)
Calzetti, D., Kinney, A. L.,& Storchi-Bergmann, T. 1994, ApJ, 429, 582
Calzetti, D., et al. 2000, ApJ, 533, 682
Caputi, K. I., Dole, H., Lagache, G., McLure, R. J., Dunlop, J. S., Puget, J.-L., Le Floc'h, E.,& Pérez-Gonzaléz, P. G. 2006, A&A, 454, 143
Cristiani, S., et al. 2000, A&A, 359, 489
Croom, S. M., Warren, S. J.,& Glazebrook, K. 2001, MNRAS, 328, 150
Daddi, E., Cimatti, A., Renzini, A., Fontana, A., Mignoli, M., Pozzetti, L., Tozzi, P.,& Zamorani, G. 2004, ApJ, 617, 746
Daddi, E., et al. 2007, submitted to ApJ (astro-ph/07052831)
Dale, D. A.,& Helou, G. 2002, ApJ, 576, 159
Doherty, M., Bunker, A. J., Ellis, R. S.,& McCarthy, P. J. 2005, MNRAS, 361, 525
Fazio, G. G., et al. 2004, ApJS, 154, 10
Fioc, M.,& Rocca-Volmerange, B. 1997, A&A, 326, 950
Förster Schreiber, N. M., et al. 2004, ApJ, 616, 40
Förster Schreiber, N. M., et al. 2006, AJ, 131, 1891
Franx, M., et al. 2003, ApJ, 587, L79
Geach, J. E., et al. 2006, ApJ, 649, 661
Giacconi, R., et al. 2000, A&AS, 197, 9001
Giacconi, R., et al. 2002, ApJS, 139, 369
Giavalisco, M.,& the GOODS Team 2004, ApJ, 600, L93
Grazian, A., et al. 2006a, A&A, 449, 951
Grazian, A., et al. 2006b, A&A, 453, 507
Grazian, A., et al. 2007, A&A, 465, 393
Groenewegen, M. A. T., et al. 2002, A&A, 392, 741
Hopkins, A. M.,& Beacom, J. F. 2006, ApJ, 651, 142
Kriek, M., et al. 2006, ApJ, 645, 44
Kriek, M., et al. 2007, ApJ, astro-ph/0611724
Kriek, M., et al. 2007, submitted to ApJ
Labbé, I., et al. 2003, AJ, 125, 1107
Le Fèvre, O., et al. 2004, A&A, 428, 1043
MacArthur, L. A. 2005, ApJ, 623, 795
Marchesini, D., et al. 2006, 656, 42
Meurer, G., Heckman, T. M.,& Calzetti, D. 1999, ApJ, 521, 64
Mignoli, M., Cimatti, A., Zamorani, G., et al. 2005, A&A, 437, 883
Norman, C., et al. 2002, ApJ, 571, 218
Papovich, C., Dickinson, M., Giavalisco, M., Conselice, C. J.,& Ferguson, H. C. 2005, ApJ, 631, 101
Persson, S. E., Murphy, D. C., Krzeminski, W., Roth, M.,& Rieke, M. J. 1998, AJ, 116, 2475

Ravikumar, C. D., et al. 2007, A&A, 465, 1099
Reddy, N. A., et al. 2005, ApJ, 633, 748
Reddy, N. A., et al. 2006, ApJ, 644, 792
Rieke, G. H., et al. 2004, ApJS, 154, 25
Roche, N. D., Dunlop, J.,& Almaini, O. 2003, MNRAS, 346, 803
Rudnick, G., et al. 2001, AJ, 122, 2205
Rudnick, G., et al. 2003, ApJ, 599, 847
Rudnick, G., et al. 2006, ApJ, 650, 624
Salpeter, E. E. 1955, ApJ, 121, 161
Sanders, D. B.,& Mirabel, I. F. 1996, ARA&A, 34, 749
Smail, I., Ivison, R. J.,& Blain, A. W. 1997, ApJ, 490, L5
Strolger, L.-G., et al. 2004, ApJ, 613, 200
STScI, 2001, VizieR Online Data Catalog, 1271
Szokoly, G. P., et al. 2004, ApJS, 155, 271
Vandame, B. 2002, SPIE, 4847, 123
Vandame, B., et al. 2001, astro-ph/0102300
van der Wel, A., Franx, M., van Dokkum, P. G., Rix, H.-W., Illingworth, G. D.,& Rosati, P. 2005, ApJ, 631, 145
van Dokkum, P. G., et al. 2006, ApJ, 638, 59
Williams, R. E., et al. 1996, AJ, 112, 1335
Worthey, G. 1994, ApJS, 95, 107
Wuyts, S., et al. 2007, ApJ, 655, 51

Chapter 4

Optical spectroscopy of Distant Red Galaxies

Abstract. We present optical spectroscopic follow-up of a sample of Distant Red Galaxies (DRGs) with $K_{s,Vega}^{tot} < 22.5$, selected by $(J-K)_{Vega} > 2.3$, in the Hubble Deep Field South (HDFS), the MS 1054–03 field, and the Chandra Deep Field South (CDFS). Spectroscopic redshifts were obtained for 15 DRGs. Redshifts were measured for an additional 11 objects satisfying the DRG criterion by other surveys in the CDFS. Only 2 out of 15 DRGs are located at $z < 2$, confirming the high efficiency to select high-redshift sources. We use the sample of spectroscopically confirmed DRGs to establish the high quality ($\Delta z/(1+z) \sim 0.06$) of photometric redshifts in the considered deep fields. Photometric redshifts based on a semi-empirical and an entirely synthetic template set are discussed. The combination of spectroscopic and photometric redshifts is used to analyze the distinct intrinsic and observed properties of DRGs at $z < 2$ and $z > 2$. In our photometric sample to $K_{s,Vega}^{tot} < 22.5$, low-redshift DRGs are brighter in K_s than high-redshift DRGs by 0.7 mag, and more extincted by 2 mag in A_V.

S. Wuyts, N. M. Förster Schreiber, M. Franx, G. D. Illingworth,
I. Labbé, G. Rudnick & P. G. van Dokkum

4.1 Introduction

STUDIES of the history of star formation and mass assembly in galaxies requires samples of galaxies over a range of lookback times. Since large spectroscopic surveys of purely magnitude-limited samples (e.g., VVDS, Le Fèvre et al. 2004) become progressively less efficient at probing higher redshifts, a variety of photometric criteria have been developed to efficiently select distant galaxies. The application of one or combination of several of these criteria should allow us to construct samples that are representative for the whole galaxy population at the considered redshift. The Lyman-break technique (Steidel & Hamilton 1993) was the first to be routineously used, identifying relatively unobscured, actively star-forming galaxies at $z \sim 3$ based on their rest-frame UV colors. Similar criteria were designed to probe star-forming galaxies at $z \sim 2.3$ and $z \sim 1.7$, referred to as BX and BM galaxies respectively (Adelberger et al. 2004). Finally, the advent of near-infrared (NIR) instruments on 8-10m class telescopes encouraged the study of NIR-selected galaxies at high redshift. The NIR flux is less affected by dust obscuration and small amounts of recent star formation and is therefore a better tracer of stellar mass than the optical fluxes. The two most commonly used color criteria in the NIR to probe distant galaxies are based on the BzK bands (Daddi et al. 2004, identifying galaxies at $z > 1.4$) and $J - K$ color (Franx et al. 2003, designed to select red galaxies at $z > 2$). The latter class of galaxies, so-called Distant Red Galaxies (DRGs), are characterized by the simple color criterion $J - K > 2.3$. They are found to be massive ($M_* \sim 10^{11}\ M_\odot$ for $K_{s,Vega}^{tot} \lesssim 21.5$) systems (van Dokkum et al. 2004; Förster Schreiber et al. 2004) and range from dusty star-forming to quiescent types (Labbé et al. 2005; Kriek et al. 2006; Wuyts et al. 2007).

In all of the surveys mentioned above, spectroscopic confirmation is indispensable. The high-redshift nature of a color-selected population can only be directly verified by measuring redshifts from their spectra. Apart from establishing the redshift range probed, the presence of emission and/or absorption lines provides valuable information on the nature of the galaxies. Moreover, having a spectroscopic redshift reduces the number of free parameters in Spectral Energy Distribution (SED) modeling by one. Finally, the availability of spectroscopic redshifts allows us to address the quality of photometric redshift estimates, on which many analyses of the high-redshift galaxy population rely.

Large samples of optically selected galaxies have been spectroscopically confirmed and their stellar populations, metallicity and kinematics such as large-scale outflows have been studied extensively based on the obtained optical and NIR spectra (e.g., Steidel et al. 1996; Shapley et al. 2003; Erb et al. 2006). The samples of NIR-selected distant galaxies with spectroscopic confirmation to date are considerably smaller, the reason being twofold. First, their faint nature in the rest-frame UV makes optical spectroscopic follow-up challinging. Second, NIR spectroscopic follow-up (e.g., Kriek et al. 2006) is time-consuming due to the lack of NIR Multi-object spectrographs and the brightness of the night sky at $\lambda \gtrsim 1\ \mu$m.

In this chapter, we report on optical spectroscopic follow-up of DRGs, extending initial results by van Dokkum et al. (2003, hereafter vD03). The sample is defined in §4.2. In §4.3, we give an overview of the observations, followed by a description of

the data reduction in §4.4. Success rate and bias are discussed in §4.5.1. §4.5.3 presents the spectroscopic redshift distribution and §4.6 discusses the quality of photometric redshifts. In §4.7 we consider how the observed broad-band properties of DRGs at $z < 2$ differ from their high-redshift counterparts. Finally, §7.11 summarizes the chapter.

Vega magnitudes are used throughout this chapter.

4.2 Sample selection

4.2.1 Pure J − K selected sample

During 9 observing runs from February 2002 to November 2003 we obtained optical spectra for NIR-selected galaxies in the following three fields: HDFS, MS 1054–03, and CDFS-GOODS. Very deep J_s and K_s imaging of the 2.5'x2.5' HDFS (Labbé et al. 2003) and the 5'x5' field around cluster MS 1054–03 (Förster Schreiber et al. 2006) were obtained as part of the FIRES survey (Franx et al. 2000). A K_s-band selected photometric catalog containing 10'x15' $BVizJHK_s$ imaging of the CDFS-GOODS (Dickinson 2001) is presented in Chapter 3.

Sources for optical spectroscopy were selected with the simple color criterion $J - K > 2.3$ (DRGs) and, with lower priority, galaxies with $I - H > 3.0$ and $J - K < 2.3$ were placed in the masks. The masks were usually shared with other high-redshift candidates and bright fillers. Finally, 11 sources selected by their flux excess in a narrow-band filter centered at 4190 Å were placed in one of the masks targeting the MS 1054–03 field. In some rare cases, targets were selected with $J - K > 2.3$ in an older catalog, and have $J - K < 2.3$ in the final catalog. This explains why objects #1195 and #1458 from vD03 are not part of the DRG sample presented in this chapter.

A total of 64 DRGs was placed in the spectroscopic masks, all of them having $K_{s,tot} < 22.5$. Figure 4.1 illustrates their location (*large symbols*) in a $V_{606} - K$ versus $V_{606,tot}$ color-magnitude diagram with respect to all DRGs with $K_{s,tot} < 22.5$ (*small symbols*) in the three fields. The figure demonstrates that the DRGs selected for optical spectroscopic follow-up span the whole 5 magnitudes in $V_{606} - K$ color occupied by the total DRG sample. Furthermore, they exhibit a similar range of $V_{606,tot}$ magnitudes, with a median $V_{606,tot}$ of 26.3.

4.2.2 DRGs from other surveys

The CDFS-GOODS field is likely the most heavily studied deep field on the sky. Several spectroscopic surveys have been conducted, each with their own selection criteria, resulting in a vast database of spectroscopic redshifts from nearby to the most distant currently attainable. We cross-correlated our K_s-band selected catalog for the CDFS field with an up-to-date list of reliable redshifts, most of which were provided by GOODS-FORS2 (v2.0, Vanzella et al. 2006), the K20 survey (Mignoli et al. 2005), the VVDS survey (Le Fèvre et al. 2004), and the CXO survey (Szokoly et al. 2004). For each DRG with a matching object within a (reasonably large) search radius of 1.″2, we checked both reliability of redshift identification and cross-correlation by eye, resulting in a list of 11 additional DRGs with spectroscopic confirmation (see Table 4.2).

Since different photometric criteria were applied to select these objects (e.g., an X-ray selection for the CXO survey), the spectroscopically confirmed DRGs in the lit-

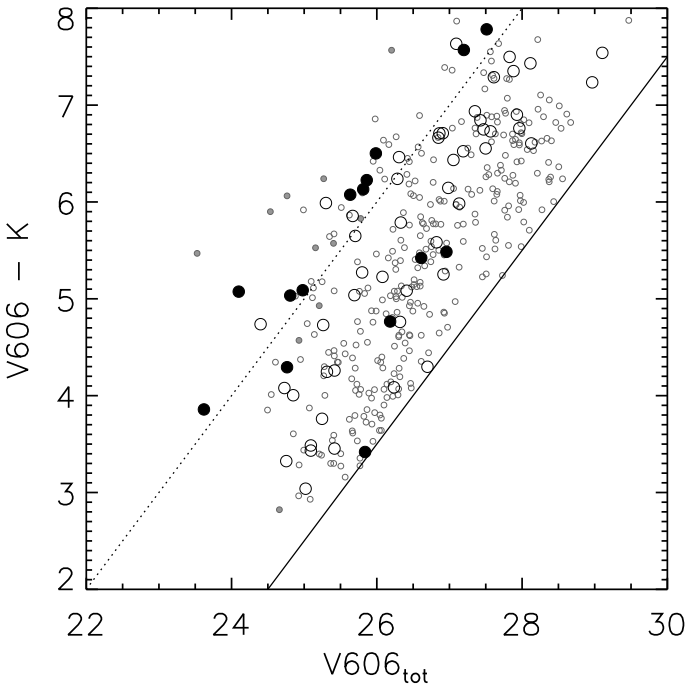

Figure 4.1 — Sample selection for the spectroscopic survey of DRGs. The location of all DRGs with $K_{s,tot} < 22.5$ in the HDFS, MS 1054–03, and CDFS fields is plotted with small circles in the $V_{606} - K_s$ versus $V_{606,tot}$ color-magnitude diagram. Large circles represent DRGs observed during the spectroscopic campaign described in this chapter, with filled black symbols indicating the successful redshift determinations. Filled grey circles are DRGs in the CDFS for which a spectroscopic redshift is available from the literature. Lines of constant $K_{s,tot} = 22.5$ (the magnitude limit of our sample; *solid*) and $K_{s,tot} = 20$ (*dashed*) are plotted to guide the eye. The sample targeted by our survey shows a representative range in $V_{606} - K_s$ and in $V_{606,tot}$. The success rate is biased toward DRGs that are bright in the K_s-band.

erature are not necessarily representative for the whole population of galaxies with $J - K > 2.3$. We therefore decide to mark them throughout the chapter as having spectroscopic redshifts, but treat them as a seperate class, i.e., they are not taken into account to compute the fraction of $z < 2$ interlopers or to estimate the AGN fraction based on the optical spectra.

4.3 Observations

A variety of optical spectrographs on 8-10m class telescopes was used to identify redshifts of the optically very faint DRGs: the Low Resolution Imaging Spectrograph (LRIS, Oke et al. 1995) and DEIMOS (Faber et al. 2003) on the W.M. Keck Telescope, FORS2 (Nicklas et al. 1997) on VLT and GMOS (Hook et al. 2003) on Gemini South. An overview of the spectroscopic observations is presented in Table 4.3.

Specifications for the February 2002 run, targeting the MS 1054–03 field with LRIS, are described by vD03. During the other LRIS runs, the 400 lines mm^{-1} grism (3400 Å blaze) was used on the blue arm and the 400 lines mm^{-1} grating (8500 Å blaze) on the red arm. The D680 dichroic was used in January 2003, whereas in March and November 2003 the D560 dichroic was inserted. The total exposure time with LRIS, spread over 2 masks in MS 1054–03 and one in CDFS, amounted to 30.5 ks. Series of 3 or 4 exposures (typically 1800 s each), dithered in 2″ steps along the slit, enabled a more efficient sky subtraction.

In January 2003, DEIMOS was pointed on MS 1054–03 using a 600 lines mm^{-1} grism in conjunction with the gg495 order-blocking filter. The exposure time was 18 ks. Two other masks, containing a handful of $J - K > 2.3$ objects as fillers, were exposed for 36.24 ks altogether. For the latter the grism was blazed at 7700 Å and the og550 filter was inserted. Similar to the LRIS observations, we dithered along the slit.

FORS2 observations with the grism GRIS_300V, partly in combination with filter gg375, took place in September 2002, December 2002, March 2003 and October 2003. A total of 88.37 ks exposure time was spread over masks in the HDFS, MS 1054–03 and the CDFS. The same dithering strategy as for the LRIS spectroscopy was used. In September 2003 the GMOS spectrograph on Gemini South was targeted on the HDFS. In order to allow for smaller slit lengths and consequently a larger number of objects in the mask, no dithering was applied along the slit. Instead, a 600 lines mm^{-1} grating was blazed at 4500 Å during half of the exposures and at 4530 Å during the second half. For all DRGs we obtained 28.8 ks total exposures. One red galaxy was exposed for an additional 9.6 ks as a filler in a mask with optically brighter objects. Using the described instrument settings, we obtained spectra for a total of 64 DRGs. No slits containing DRGs were lost due to failures in the reduction process or other technical problems. Exposure times per object varied from a minimum of 7.9 ks to a maximum of 75.34 ks. In the course of the 9 observing runs seeing conditions were highly variable, ranging from $0\farcs5$ to $2\farcs0$, with a typical value of $1\farcs0$. The 1 to 1.1″ wide slits gave a typical resolution of 7.5 Å, 3.6 Å, 10.5 Å and 4.6 Å (FWHM) for LRIS, DEIMOS, FORS2, and GMOS respectively.

4.4 Reduction

Multi-object spectroscopic data obtained by LRIS, DEIMOS, FORS2 and GMOS generally undergo the same reduction steps. For a detailed description of the standard LRIS reduction process, we refer the reader to van Dokkum & Stanford (2003). Briefly, the observations were divided in sessions of four dithered exposures. We used standard IRAF tasks to subtract the bias and apply the flatfielding and fringe correction to each of the slit exposures. Next, cosmic rays were cleaned and skylines subtracted. The wavelength calibration was based on arc lamp images, and we used the location of a bright skyline to apply a zero-point correction. Finally, the 4 reduced slit exposures were aligned, averaged, and the s-distortion was removed.

The part of the slit where the target object (and possibly a second object) is located, needs to be masked during several reduction steps. It is of great importance that the correct part of the slit is masked. As the NIR-selected galaxies are extremely faint in the optical, it is impossible to measure their positions in the slit on the raw science frames. We determined the object position in the slit from the mask design and verified the predicted position for bright filler objects on the raw science frames. The maskwidth was set to $\sim 1\farcs9$.

In the case of the GMOS run, where no dithering was applied, the use of 2 gratings blazed at 4500 Å and 4530 Å helped to distinguish hot pixels (at fixed CCD position) from real spectral features (at fixed wavelength). Nevertheless, the lack of dithering resulted in a lower quality of the spectra. Ten out of 64 DRGs targeted by our survey were only placed in the GMOS masks.

4.5 Results from optical spectroscopy of DRGs

4.5.1 Redshift determination, success rate, and bias

Given the faint median $V_{606,tot}$ magnitude of 26.3 for all targeted and 25.8 for all successfully targeted DRGs, it comes as no surprise that continua, if detected, have a too low signal-to-noise ratio to allow for redshift identifications based on absorption lines. Therefore, all spectroscopic redshifts for DRGs in our sample are based on emission lines. In cases where only a single emission line was detected, the presence of a break (lower continuum on the blue side of the spectral feature) and absence of Hβ and [OIII]5007 at the expected wavelength if the emission line were [OII]3727 was used to distinguish Lyα from [OII]3727 as identification.

Out of 64 galaxies satisfying the DRG criterion without further selection bias, the optical spectroscopic follow-up resulted in 14 redshift identifications (a success rate of 22%). Furthermore, NIR spectroscopy with NIRSPEC (McLean et al. 1998) on the W. M. Keck Telescope presented by van Dokkum et al. (2004) provided a redshift for one targeted DRG that did not show emission lines in its optical spectrum. The 15 redshifts for purely $J-K$ selected DRGs are listed in Table 4.4. Spectroscopic redshifts obtained for non-DRGs during our spectroscopic campaign are listed in Table 4.1.

We investigate a possible bias of the subsample of DRGs with a successful redshift determination in Figure 4.1. The 15 spectroscopically confirmed galaxies that were selected purely on the basis of their red ($J-K>2.3$) color are plotted with large filled circles. The other DRGs targeted by our survey are marked with large empty circles. With smaller circles, we plot all other (*small empty circles*) DRGs with $K_{s,tot}<22.5$ in the observed fields and the subsample for which a redshift was obtained by other spectroscopic surveys (*small grey circles*). The successful targets in our spectroscopic campaign of DRGs are biased toward brighter magnitudes in both V_{606} and K_s with respect to both the whole spectroscopically observed sample and the complete sample of DRGs in the three considered fields. One could expect a bias toward brighter magnitudes based on signal-to-noise arguments. However, the possible presence of emission lines makes the relation between success rate and broad-band flux less direct. A redshift may be more easily obtained from a faint emission line spectrum than from a brighter absorption spectrum. We discuss the spectral types in §4.5.2. Remarkably, Figure 4.1 suggests a larger dependence of the success rate on the $K_{s,tot}$ magnitude than on the $V_{606,tot}$ magnitude, even though the spectra were obtained in the optical. Out of the 10 (20) brightest targeted DRGs in $K_{s,tot}$, a redshift was successfully derived from the optical spectra for 60% (45%) of them. Considering the brightest 10 (20) targets in $V_{606,tot}$, the success rates drop to 50% (25%). As noted before, all redshifts were based on the presence of emission lines. Although caution should be taken due to small number statistics and variable seeing conditions between the observing runs, this might hint toward an increasing prevalence of DRGs with Lyα emission with brighter K_s-band flux.

4.5.2 Optical spectra

Figure 4.2 presents the 1D spectra of our successful redshift identifications. Since all spectroscopic redshifts for DRGs in our sample are based on emission lines, we should

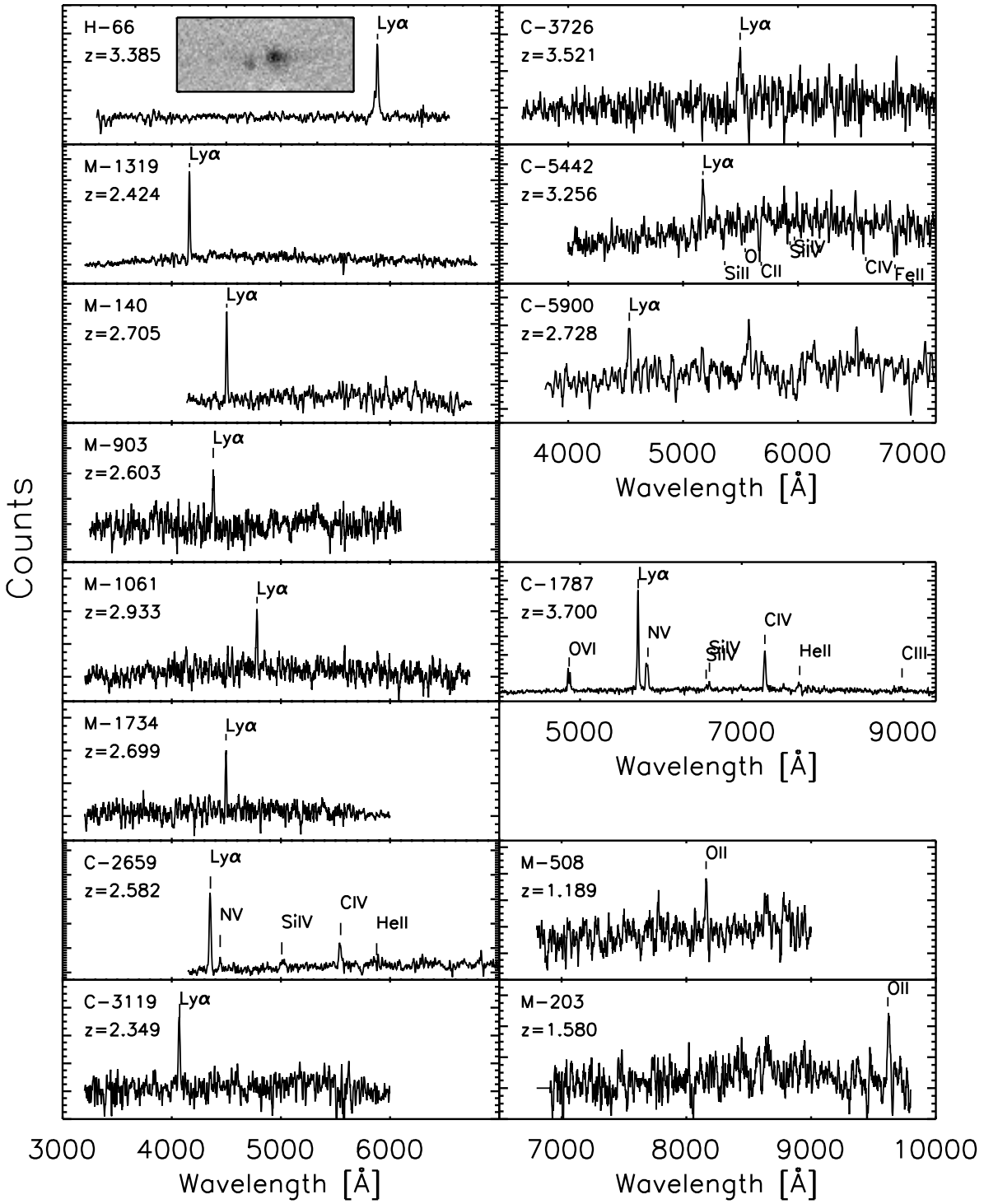

Figure 4.2 — 1D optical spectra of DRGs observed in our survey with successful redshift identification. The presented spectra of DRGs at $z > 2$ show Lyα in emission, possibly in combination with other lines. Two interlopers at $z < 2$ were identified by the presence of [OII]3727 in emission, with the continuum extending blueward of the emission line. Inset for object H-66 is a part of the GMOS 2D spectrum, showing a smaller feature close to the Lyα emission from the target. Galaxies C-1787 and C-2659 show evidence of AGN activity in their optical spectra. Interstellar absorption lines are detected in C-5442.

keep in mind that we are likely dealing with a biased representation of the whole population of galaxies with $J - K > 2.3$. Inverting the success rate, we can place a conservative upper limit of 78% on the fraction of DRGs without emission lines.

Galaxies M-203 and M-508 show [OII]3727 in emission at $z < 2$. All other spectra presented in Figure 4.2 feature Lyα in emission, possibly in combination with interstellar absorption lines (C-5442) or confirmed by NV, SiIV, CIV and other emission lines indicating the presence of an AGN (C-1787, C-2659). The presence of Lyα indicates that at least a quarter of the DRGs must host regions of star formation that are not heavily obscured, complementary to an old underlying or dusty young population that according to SED modeling (e.g., Labbé et al. 2005; Wuyts et al. 2007) is responsible for their red rest-frame optical color. Differences between the rest-frame UV and rest-frame optical morphologies of DRGs also indicate that these galaxies do not have homogeneous stellar populations (Toft et al. 2005).

As illustrated by the inset 2D GMOS spectrum of H-66, a smaller feature is visible near the Lyα emission line of the target, offset from H-66 in the spatial direction by $0\farcs35$ and in the wavelength direction by 13.7 Å. The large dispersion of GMOS allows for an accurate measurement of the emission line centers: 5330.8 Å (H-66) and 5317.1 Å (serendipitous object). Interpreting both lines as Lyα at identical cosmological distance, the shift in wavelength corresponds to a relative velocity of $\Delta v_r = 771$ km s^{-1}. At $z = 3.385$ the projected spatial offset corresponds to 2.6 kpc.

Lyα at 4781 Å was detected in both the LRIS and 2 FORS2 spectra of M-1061. However, the spectrum is offset by $1\farcs5$ from the predicted position in the slit as calculated from the center of the K-band flux. An identical offset is measured between the centers of flux on the B- and K_s-band images. Whether the optical and NIR light correspond to different parts of the same galaxy, or come from physically unrelated sources, remains uncertain. NIR spectroscopy could confirm the redshift of the DRG unambiguously if Hα is detected at 2.5811 μm. At $z = 2.933$ the offset of $1\farcs5$ corresponds to 11.6 kpc. We verified that our results would not be affected by excluding M-1061 from our spectroscopic redshift sample.

C-1787 was also observed by Norman et al. (2002). These authors find that at $z = 3.7$, C-1787 is the most distant type-2 QSO known to date, showing a bright X-ray counterpart in the 1 Ms Chandra imaging of the CDFS. The detection of OVI, Lyα , NV, SiIV, NIV, CIV, HeII, and CIII in our FORS2 spectrum of the source confirms its nature.

Interpreting a detection of CIV in emission as evidence for an AGN, we find active nuclei in 13% of the DRGs with spectroscopic redshifts. Under the assumption that all DRGs without redshift identification lack emission lines in their spectra, the estimated (unobscured) AGN fraction among the observed DRGs could be as low as $\sim 3\%$. For comparison, 4 out of 28 (14%) of our spectroscopically observed DRGs in the CDFS have a X-ray detection in the 1Ms Chandra exposure on that field (Giacconi et al. 2002). The X-ray detected fraction among all DRGs with $K^{tot}_{s,Vega} < 22.5$ in the CDFS amounts to 9%. The estimated AGN fraction based on our optical spectroscopy is surprisingly low compared to the AGN fraction of 20 - 30% implied by recent multi-wavelength studies by Reddy et al. (2005), Papovich et al. (2006), and Daddi et al. (2007). This might imply a prevalence of obscured AGN.

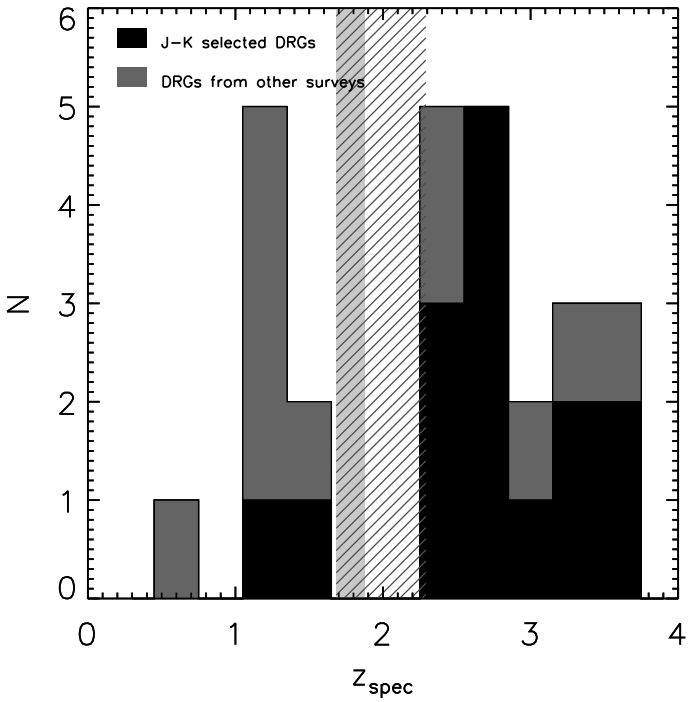

Figure 4.3 — Spectroscopic redshift histogram of DRGs in the HDFS, MS 1054–03, and the CDFS. Redshifts obtained for purely $J-K>2.3$ selected galaxies are presented in black. Additional spectroscopic redshifts of objects from other surveys (with their own selection criteria) satisfying $J-K>2.3$ are indicated in dark grey. The hatched and light-grey regions mark the range in redshifts where [OII]3727 falls redward and Lyα falls blueward of the sensitive part of the FORS2 and LRIS detectors respectively.

4.5.3 Redshift distribution

We next discuss the distribution of spectroscopic redshifts obtained for DRGs. Three questions need to be addressed. How efficient is the DRG selection criterion to isolate galaxies at $z>2$, for which it was designed? What is the typical redshift of DRGs? And to what range of redshifts are they confined?

The solid histogram in Figure 4.3 shows the redshift distribution of spectroscopically confirmed DRGs from our purely $J-K$ selected sample. The vertical bar (*light grey*) at $1.68<z<1.88$ marks the region in redshift space where spectroscopic confirmation with LRIS is complicated because [OII]3727 lies redward of the covered wavelength range while Lyα has not entered the blue sensitive region of the detector yet. The corresponding region for the FORS2 spectrograph, whose sensitivity in the blue reaches down to ~ 4000 Å, is indicated with the shaded area. Two out of 15 sources (13%) are located below $z=2$, at $z=1.580$ and $z=1.189$. The median of the purely $J-K$ selected DRGs lies at $z=2.7$ with a distribution ranging to $z=3.7$.

Considering the DRGs whose redshifts were obtained as part of other surveys, we find that all those with a X-ray detection (Szokoly et al. 2004) lie above $z=2$. Cross-correlation with the K20 survey ($K_s<20$ selected), the VLT/FORS2 survey ($z_{850}<25$ and $i_{775}-z_{850}$ selected) and NIR spectroscopy of K_s-selected galaxies by Kriek et al. (in preparation) added 6 extra low-redshift ($0.6<z<1.7$) interlopers. Combining the spectroscopic redshifts from our and other surveys, we find that DRGs at $z<2$ have a median K_s-band magnitude that is 1 magnitude brighter than those at $z>2$, a difference at the 10σ level. No significant offset in $V_{606,tot}$ is measured. Our result is in qualitative agreement with Conselice et al. (2007) who studied a sample of bright NIR-selected DRGs. Using a combination of photometric redshifts and spectroscopic redshifts from the DEEP2 survey, the latter reaching to $z=1.4$, they conclude that at

the bright end ($K_{s,Vega}^{tot} < 20.5$) 64% of all DRGs are located at $z < 2$. Quadri et al. (2007) also found that their (photometric) redshift distribution of DRGs shifts toward lower redshift when imposing a brighter K_s-band cut.

We note that the two low-redshift interlopers from our survey are the faintest in K_s of all spectroscopically confirmed $z < 2$ DRGs. The suggested K_s-band dependence of the success rate to identify redshifts (see §4.5.1) is thus not trivially related to a redshift dependence of the success rate.

4.6 Photometric redshifts

In order to better address the observed and intrinsic properties, and fraction of low-redshift ($z < 2$) DRGs, we will complement the spectroscopic sample presented above with photometric redshift estimates for the remaining DRGs in the HDFS, MS 1054–03, and the CDFS. We first present the method and templates used to estimate redshifts from broad-band photometry. Next, we analyse the quality of the photometric redshifts by comparison to the available spectroscopic redshifts. In this chapter, we restrict ourselves mainly to the quality and distribution of photometric redshifts of DRGs. For an in-depth discussion of the z_{phot} quality for the whole galaxy population, template mismatch etc., we refer the reader to Förster Schreiber et al. (in preparation).

4.6.1 Method and template sets

Using the algorithm developed by Rudnick et al. (2001, 2003), updated photometric redshifts (z_{phot}) were derived for all K_s-band selected sources in the HDFS, MS 1054–03, and the CDFS, presented in detail by Förster Schreiber et al. (in preparation). Briefly, a linear combination of empirical and/or synthetic templates is fit to the spectral energy distribution of each galaxy. The broad-band photometry used in deriving the photometric redshifts consisted of $U_{300}B_{450}V_{606}I_{814}J_sHK_s$ for the HDFS, $UBVV606I_{814}J_sHK_s$ for MS 1054–03, and $B_{435}V_{606}i_{775}z_{850}JHK_s$ for the CDFS. Uncertainties in z_{phot} are estimated from Monte Carlo simulations, accounting for photometric uncertainties and template mismatch.

We present results obtained with 2 sets of templates, which we refer to as the CWW++ (used previously by e.g., Rudnick et al. 2006; Quadri et al. 2007; Marchesini et al. 2007) and the BC03 template set (Förster Schreiber et al. in preparation).

First, the CWW++ template set consists of 8 templates: the empirical E, Sbc, Scd and Im templates from Coleman, Wu, & Weedman (1980), the two least reddened starburst templates from Kinney et al. (1996) and a 1 Gyr and 10 Myr Bruzual & Charlot (2003; hereafter BC03) single stellar population (SSP) with a Salpeter (1955) initial mass function. The BC03 stellar population synthesis code also provided extensions into the IR for the empirical templates. The empirical templates inherently include some intrinsic reddening, but only a small amount for the Sbc and Scd templates which were constructed from nearby face-on spirals, and reaching up to $E(B-V) \leq 0.21$ for the SB2 template from Kinney et al. (1996).

The second template set, fed to the same algorithm, consists of synthetic templates only. Ten SSP templates with ages evenly spaced in log time between 50 Myr and 10 Gyr were selected from the stellar population synthesis code by BC03. Each of the

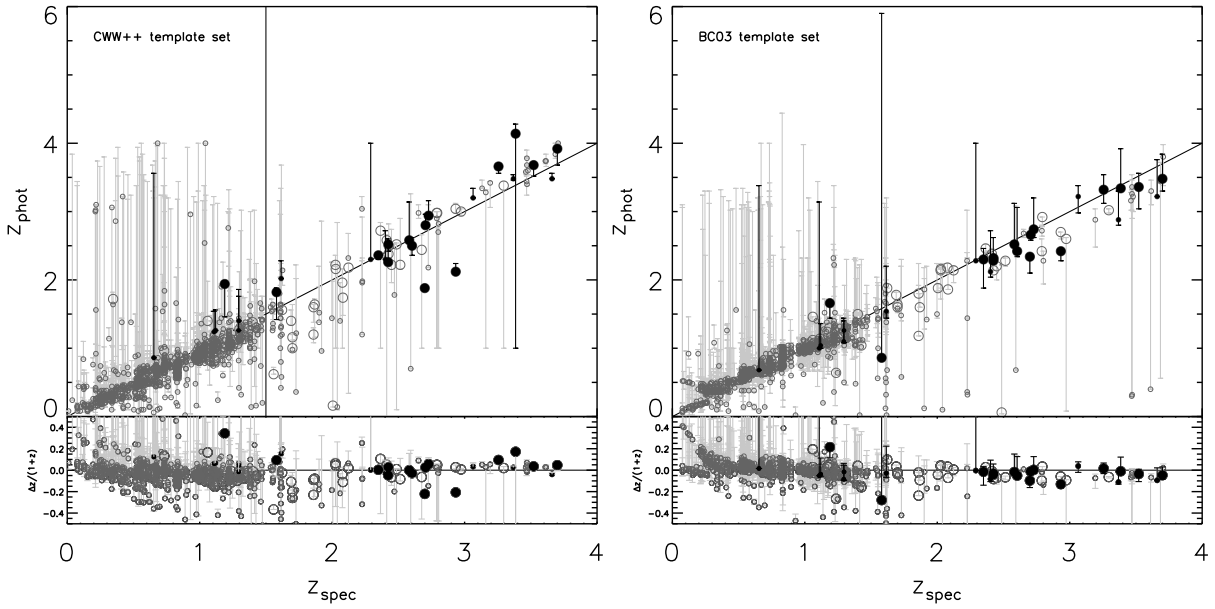

Figure 4.4 — Direct comparison between photometric and spectroscopic redshifts for all sources with $K_{s,tot} < 22.5$ in the HDFS, MS 1054–03, and CDFS fields for which a reliable spectroscopic redshift is available. Distant Red Galaxies are highlighted in black. Large symbols denote redshifts obtained during our spectroscopic survey. (a) z_{phot} based on the CWW++ template set. (b) z_{phot} based on the BC03 template set.

templates was allowed to have $E(B-V)$= 0.0, 0.1, 0.3, or 0.6, applying a Calzetti et al. (2000) attenuation law. The BC03 template set thus effectively contains 40 templates and allows for a larger degree of reddening than the CWW+ template set.

4.6.2 Quality of photometric redshifts

We quantify the performance of the photometric redshift code by Rudnick et al. (2003) by a direct comparison with the available spectroscopic redshifts (see Figure 4.4). DRGs are marked in red, with large symbols representing objects targeted by our spectroscopic survey. Galaxies with $J-K < 2.3$ are plotted in black. Their spectroscopic redshifts are compiled from the literature on the 3 fields, carefully cross-correlating galaxies from the spectroscopic surveys to objects in the K_s-band selected catalogs and conservatively limiting ourselves to high quality flags.

Ideally, one algorithm and set of templates provides simultaneously accurate redshift estimates for galaxies of different types and at a range of cosmological distances. Here, we focus on the z_{phot} quality of DRGs, but place it in context by comparing the distribution of $\Delta z/(1+z) = \frac{(z_{spec}-z_{phot})}{(1+z_{spec})}$ for DRGs to that of the whole population of galaxies and the subsample at $z > 2$.

The results for the CWW++ and BC03 z_{phot} estimates are quantified with 3 statistical measures in Table 4.5: the median of $\Delta z/(1+z)$ quantifies systematic offsets, the normalized median absolute deviation σ_{NMAD} (equal to the rms for a gaussian distribution) is a measure of scatter robust against outliers. The mean absolute deviation (MAD) is sensitive to catastrophic outliers.

We find a tight correlation between z_{phot} and z_{spec} for the DRGs, characterised by a $0.05 < \sigma_{NMAD} < 0.07$ for the two template sets and without serious catastrophic outliers. The scatter for the DRGs is marginally smaller for the BC03 than for the CWW++ template set. We note that whereas the CWW++ template set systematically overpredicts the z_{phot} of DRGs by 0.03, the BC03 template set underpredicts by the same amount. It is reassuring that, despite the lack of AGN templates, both template sets perform equally well for those DRGs with an X-ray detection as for the others. This might mean that the optical-to-NIR SEDs of these DRGs with an X-ray detection is dominated by stellar light, and that the AGN is obscured.

Considering all 1090 galaxies with spectroscopic redshifts, 91% (95%) of which lie below $z = 1.5$ (2), we find that the BC03 template set removes the systematic underprediction of redshifts below $z = 2$ that was present in CWW++. Furthermore, the scatter is reduced to $\sigma_{NMAD} = 0.058$, a similar high quality as that for DRGs. At redshifts above 2, we note that the nature of catastrophic outliers is different for the z_{phot} based on the CWW++ template set than for those based on the BC03 templates. On the one hand, the BC03 template set reduces the contamination by low-redshift galaxies mistakenly placed at high redshift. Such catastrophic outliers will lead to artificially boosted stellar mass and rest-frame luminosity estimates, and may does have a critical impact on studies of the bright end of the high-redshift galaxy population. On the other hand, a larger number of sources at $z > 2$ will be placed at $z < 0.5$, leading to an underprediction of the number density at high redshift. The MAD values in Table 4.5 reflect this effect.

We conclude that a similar high quality of photometric redshifts is reached for the spectroscopically confirmed DRGs as for the total galaxy population. However, as noted earlier, the subsample of DRGs with spectroscopic confirmation is biased toward sources with emission lines. NIR multi-object spectrographs that will come online during the following years will be able to establish the z_{phot} accuracy for the DRG sample as a whole in a time-efficient manner, targeting either rest-frame optical emission lines (e.g., Kriek et al. 2007) or Balmer/4000 Å breaks in the continuum (Kriek et al. 2006). We proceed by using the z_{phot} based on the BC03 template set.

4.7 The nature of low-redshift DRGs

Having established confidence in the z_{phot} estimates for DRGs, we can now revisit the question how efficient the DRG selection criterion is at selecting high-redshift galaxies, and how the low-redshift DRGs stand out with respect to their high-redshift counterparts. To this purpose, we plot the $J - K$ color of all galaxies with $K^{tot}_{s,Vega} < 22.5$ in the considered fields versus z_{phot} (*empty symbols*), or z_{spec} (*filled symbols*) when available (Figure 4.5). The efficiency of the $J - K > 2.3$ criterion in selecting galaxies above $z = 2$ is found to be 68% using the BC03 template set. The efficiency progressively increases with redder $J - K$ color. Only 9% of the galaxies with $J - K > 2.9$ was assigned a redshift below $z = 2$. Less than half of the DRGs at $z < 2$ have a $J - K$ color that is consistent at the 1σ level with being photometrically scattered into the DRG selection window, making it unlikely that all of the low-redshift interlopers are due to photometric uncertainties.

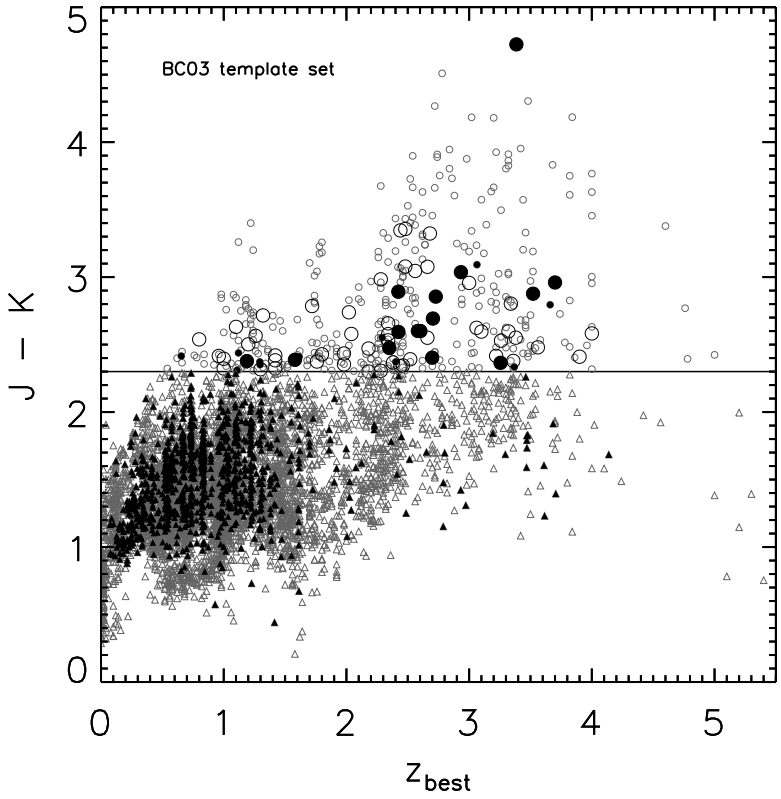

Figure 4.5 — $J - K$ versus redshift for all sources with $K_{s,tot} < 22.5$ in the HDFS, MS 1054–03, and CDFS fields. Filled symbols are used for spectroscopic redshifts. For other sources the photometric redshift estimate based on the BC03 template set is plotted. Large symbols represent galaxies selected for our spectroscopic follow-up. Objects above the horizontal line marking $J - K = 2.3$ satisfy the DRG criterion. Selecting galaxies based on their red $J - K$ color is an efficient means to find $z > 2$ galaxies.

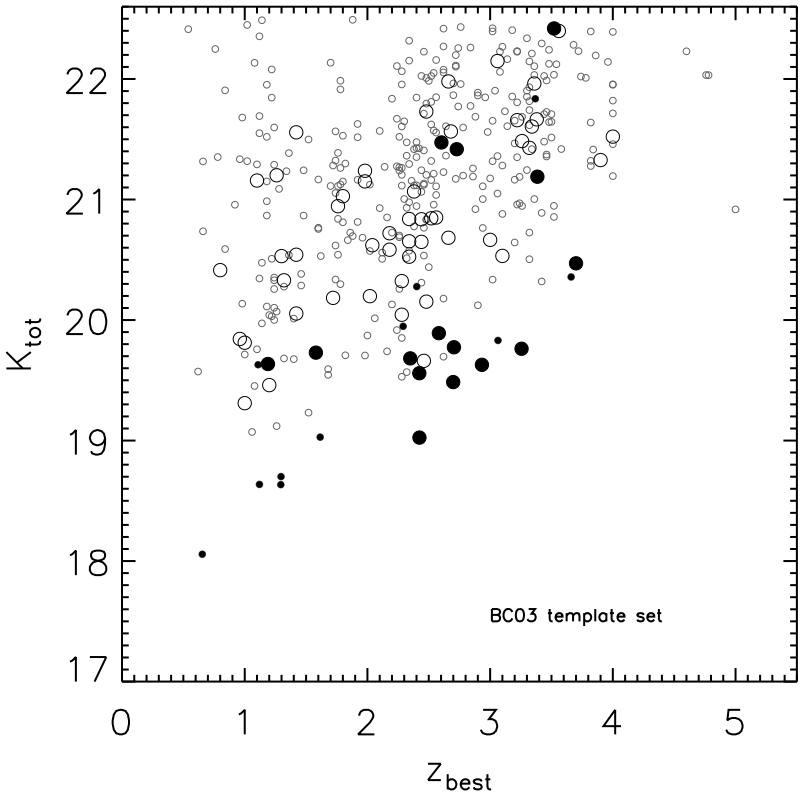

Figure 4.6 — Observed K_s-band magnitude versus redshift for all DRGs with $K_{s,tot} < 22.5$ in the HDFS, MS 1054–03, and CDFS fields. Filled circles are used for DRGs with spectroscopic redshifts. For other DRGs (*empty circles*) the photometric redshift estimate based on the BC03 template set is plotted. Large symbols represent galaxies in our spectroscopic survey. Low-redshift DRGs reach to brighter $K_{s,tot}$ than high-redshift DRGs.

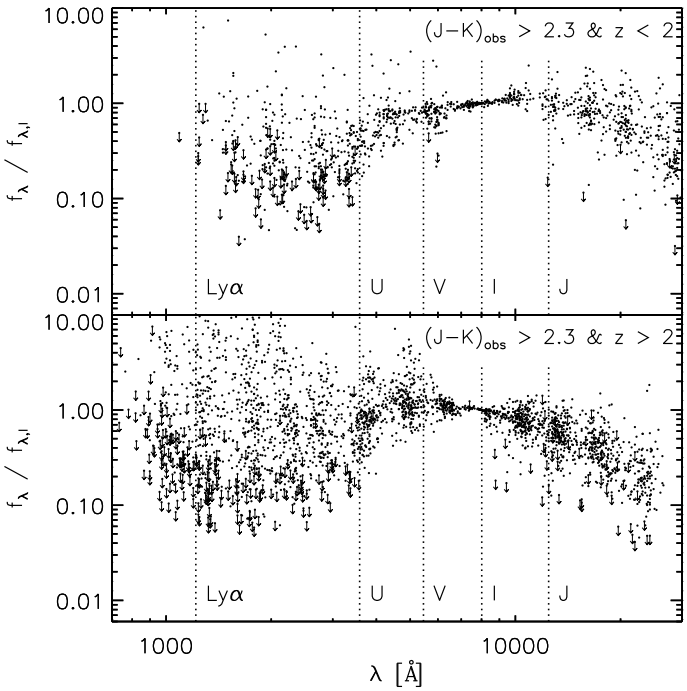

Figure 4.7 — *Top panel:* Rest-frame broad-band SEDs, normalized to the rest-frame I-band flux, of all low-redshift ($z < 2$) DRGs to $K_{s,tot} < 22.5$ in the HDFS, MS 1054–03, and CDFS fields. *Bottom panel:* High-redshift ($z > 2$) DRGs to the same magnitude limit. Upper limits indicate the 1σ confidence levels. Low-redshift DRGs have a red SED shape from the rest-frame UV to the rest-frame J-band, whereas the SEDs of high-redshift DRGs show a wide range in rest-frame UV slopes and are on average declining redward of the rest-frame V-band.

We now proceed to examine the nature of DRGs at $z < 2$. First, we consider the observed K_s-band magnitude of DRGs as a function of redshift (Figure 4.6). Apart from the spectroscopically confirmed redshifts from our (*large filled circles*) and other (*small filled circles*) surveys, we plot the other DRGs (*empty circles*) in the considered fields using their photometric redshift estimates. Both the spectroscopic and the photometric sample of DRGs show a correlation between K_s-band magnitude and redshift. In our sample to $K_{s,tot} < 22.5$, we find a median $K_{s,tot} = 20.5$ for $z < 2$ DRGs, compared to a median $K_{s,tot} = 21.2$ for $z > 2$ DRGs. Consequently, the fraction of low-redshift ($z < 2$) DRGs increases toward brighter K_s-band magnitudes, consistent with Quadri et al. (2007).

In order to investigate the difference in intrinsic properties between low- and high-redshift DRGs, we plot their rest-frame SEDs, normalized to the rest-frame I-band flux, in Figure 4.7. Although satisfying the same observed color criterion ($J - K > 2.3$), the populations at low- and high redshift show a marked difference in rest-frame SED shapes. The low-redshift DRGs show low flux levels in the UV and a positive slope of the SED at the rest-frame I-band. The high-redshift DRGs instead show a wide range in rest-frame UV slopes and have SEDs with a declining slope at the rest-frame I-band (see also Förster Schreiber et al. 2004).

An interpretation of the difference in rest-frame SED shapes is provided by modeling of the optical-to-MIR SEDs using the Bruzual & Charlot (2003) stellar population synthesis code following the procedure described by Wuyts et al. (2007), keeping the redshift fixed to that derived with the BC03 template set. A maximal visual extinction of $A_V = 4$ magnitudes was allowed during the fit, adopting a Calzetti et al. (2000) attenuation law. Figure 4.8 shows that this artificial upper limit is only reached for DRGs with $z_{best,BC03} < 2$. Although DRGs at $z > 2$ with several magnitudes of extinction in the V-band do exist, a trend of A_V with redshift is significant at the 99.9% level, both

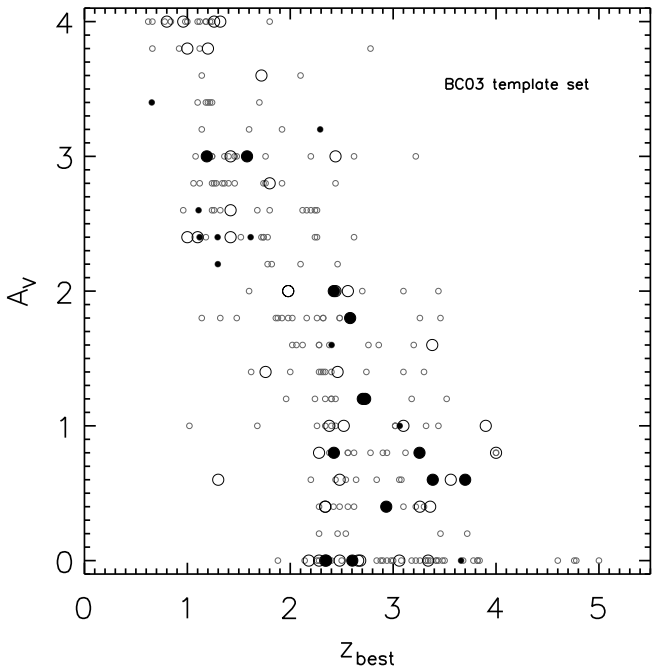

Figure 4.8 — Best-fitted A_V versus redshift ($z_{phot,BC03}$ or z_{spec} when available) for all DRGs with $K_{s,tot} < 22.5$ in the HDFS, MS 1054–03, and CDFS fields. Spectroscopic redshifts are marked with filled symbols. Large symbols indicate galaxies that were part of our spectroscopic follow-up of DRGs. The dust content of DRGs decreases with increasing redshift.

for the total sample and the subsample with spectroscopic redshifts. The median dust extinction of $z < 2$ DRGs is $A_V = 2.8$, compared to a median value of $A_V = 0.8$ for the $z > 2$ DRGs to the same $K_{s,tot} < 22.5$ limit. We note that more than 85% of the DRGs at $z < 2$ would also be picked up by the $I - H > 3$ selection criterion for Extremely Red Objects (EROs, McCarthy et al. 2001). This fraction drops to about 60% for the DRGs at higher redshifts. Based on Keck spectroscopy of $I - H > 3$ selected EROs, Doherty et al. (2005) inferred a dominant old stellar population for 75% of the ERO sample, being responsible for their red color. Based on our SED modeling we conclude that, with the additional constraint of $J - K > 2.3$, one preferentially selects those EROs whose large dust content is responsible for the red slope of the SED over a large wavelength range. The fact that the BC03 template set allows for SED shapes that are more heavily affected by dust obscuration explains the larger fraction of DRGs placed at $z < 2$.

4.8 Summary

In this chapter, we presented optical spectroscopic follow-up for a sample of Distant Red Galaxies with $K^{tot}_{s,Vega} < 25$ in the fields HDFS, MS 1054–03, and CDFS. Redshifts were identified for a total of 15 of the observed DRGs. An additional 11 DRGs, though not necessarily representative for that population, are spectroscopically confirmed by other surveys in the CDFS.

Using 8-10m class telescopes under varying seeing conditions, we obtain a modest success rate of 22% only, increasing toward brighter $V_{606,tot}$ and especially $K_{s,tot}$ magnitude. Emission line spectra are more easily identified, meaning that the spectroscopic

sample is biased toward those sources with at least some unobscured radiating gas present. Apart from Lyα , interstellar absorption lines are detected in one and emission lines typical for AGN activity in two of the high-redshift DRGs. With only 2 objects at $z < 2$ in the purely $J - K$ selected sample, we confirm that the DRG criterion $J - K > 2.3$ is an efficient means to isolate galaxies at $z > 2$, with their redshift distribution peaking around $z \sim 2.7$.

We use the total sample of 26 spectroscopically confirmed DRGs to address the quality of the photometric redshift code developed by Rudnick et al. (2001, 2003). We quantified the deviation between z_{phot} and z_{spec}, $\Delta z/(1+z)$, using two sets of templates. The semi-empirical CWW++ template set was used for several analyses in the literature (e.g., Rudnick et al. 2006; Marchesini et al. 2007). Furthermore, a new synthetic template set is presented, based on models from Bruzual & Charlot (2003) and allowing for a larger impact of dust on the spectral energy distribution (up to $E(B-V) = 0.6$). Although both template sets give significantly different results for the galaxy population as a whole, the $\sigma_{NMAD}(\Delta z/(1+z))$ for the DRGs has an equally small value of 0.05-0.07 (depending on the restriction to $z > 2$ DRGs or not) for both, similar in quality to what is measured for all 1090 galaxies spanning the entire redshift range with spectroscopic confirmation in the considered deep fields.

Including DRGs with photometric redshifts, we find that the median of the predicted redshift distribution is $z = 2.4$, and the efficiency to select galaxies at $z > 2$ is 68%, for the CWW++ and BC03 template sets respectively. DRGs at redshifts below $z = 2$ are significantly more extincted by dust than those at higher redshifts. In observed properties, they are generally characterized by having brighter $K_{s,tot}$ magnitudes (0.7 mag brighter in the median than $z > 2$ DRGs to the same $K_{s,tot} < 22.5$ limit), and $J - K$ colors close to $J - K = 2.3$. SED modeling implies a median dust extinction for $z < 2$ DRGs that is as high as $A_V = 2.8$.

Acknowledgments

SW would like to thank the Yale astronomy department for its hospitality during several working visits. This research was supported by grants from the Netherlands Foundation for Research (NWO), the Leids Kerkhoven-Bosscha Fonds, and the Lorentz Center. Based on observations carried out at the European Southern Observatory, Paranal, Chile. Based on observations obtained at the Gemini Observatory, which is operated by the Association of Universities for Research in Astronomy, Inc., under a cooperative agreement with the NSF on behalf of the Gemini partnership. Also based on data obtained at the W. M. Keck Observatory, which is operated as a scientific partnership among the California Institute of Technology, the University of California and the National Aeronautics and Space Administration. The Observatory was made possible by the generous financial support of the W. M. Keck Foundation. The authors wish to recognize and acknowledge the very significant cultural role and reverence that the summit of Mauna Kea has always had within the indigenous Hawaiian community. We are most fortunate to have the opportunity to conduct observations from this mountain.

Table 4.1. Spectroscopic redshifts for non-DRGs obtained during our spectroscopic survey

ID[a]	ra	dec	z_{spec}	Remark[b]
H-92	338.22568	-60.569154	2.412	$I_{814} - H = 1.84$; $J_s - K_s = 1.54$
H-228	338.21679	-60.561796	3.295	$I_{814} - H = 1.35$; $J_s - K_s = 1.69$
H-245	338.22862	-60.561701	2.676	$I_{814} - H = 0.97$; $J_s - K_s = 1.24$
H-257	338.21121	-60.557914	2.027	$I_{814} - H = 2.19$; $J_s - K_s = 1.49$
H-290	338.26335	-60.558267	2.025	$I_{814} - H = 2.11$; $J_s - K_s = 1.37$
H-294	338.27042	-60.558536	2.365	$I_{814} - H = 1.64$; $J_s - K_s = 1.78$
H-408	338.24993	-60.551115	1.228	$I_{814} - H = 1.80$; $J_s - K_s = 1.29$
H-470	338.22038	-60.554717	1.284	$I_{814} - H = 2.94$; $J_s - K_s = 2.01$
H-565	338.22220	-60.544237	1.114	$I_{814} - H = 2.39$; $J_s - K_s = 1.81$
H-620	338.23714	-60.536690	1.558	$I_{814} - H = 1.58$; $J_s - K_s = 1.26$
H-657	338.20360	-60.531616	2.793	$I_{814} - H = 2.09$; $J_s - K_s = 1.91$
H-806	338.20579	-60.540609	2.789	$I_{814} - H = 1.20$; $J_s - K_s = 1.15$
H-	338.25705	-60.590965	0.695	-
H-	338.27145	-60.577366	0.439	-
H-	338.27145	-60.579903	0.844	-
H-	338.28201	-60.587112	0.344	-
H-	338.25686	-60.59766	2.899	LBG candidate
H-	338.28486	-60.57794	3.190	LBG candidate
M-147	164.23573	-3.6498842	1.265	$I_{814} - H = 2.45$; $J_s - K_s = 1.55$
M-161	164.24502	-3.6475178	1.859	$I_{814} - H = 2.21$; $J_s - K_s = 1.87$
M-266	164.22595	-3.6422003	2.005	$I_{814} - H = 1.57$; $J_s - K_s = 1.08$
M-303	164.21742	-3.6400908	2.486	$I_{814} - H = 2.03$; $J_s - K_s = 1.25$
M-383	164.22318	-3.6365197	2.123	$I_{814} - H = 2.30$; $J_s - K_s = 1.62$
M-450	164.20416	-3.6339978	0.346	no I_{814} coverage; $J_s - K_s = 1.85$
M-713	164.24837	-3.6252800	1.700	$I_{814} - H = 3.67$; $J_s - K_s = 1.75$
M-897	164.24914	-3.6203344	2.973	$I_{814} - H = 1.13$; $J_s - K_s = 1.31$
M-972	164.21320	-3.6176475	2.448	$I_{814} - H = 2.01$; $J_s - K_s = 1.82$
M-1132	164.27260	-3.6095794	1.060	$I_{814} - H = 3.23$; $J_s - K_s = 2.14$
M-1155	164.22757	-3.6094061	1.622	$I_{814} - H = 3.59$; $J_s - K_s = 1.90$
M-1272	164.27786	-3.6050289	0.829	$I_{814} - H = 1.31$; $J_s - K_s = 1.12$
M-1396	164.24016	-3.6010686	2.514	$I_{814} - H = 2.13$; $J_s - K_s = 1.65$
M-1450	164.24319	-3.5979289	0.622	$I_{814} - H = 1.23$; $J_s - K_s = 1.08$
M-1459	164.25297	-3.5974653	2.081	$I_{814} - H = 3.92$; $J_s - K_s = 2.22$
M-1637	164.23843	-3.5876183	1.300	$I_{814} - H = 3.10$; $J_s - K_s = 2.24$
M-1728	164.26288	-3.5815978	2.93200	$I_{814} - H = 1.63$; $J_s - K_s = 1.42$
M-	164.23486	-3.5825150	2.428	NB4190
M-	164.21390	-3.5891633	2.436	NB4190
M-	164.19865	-3.6408465	2.428	NB4190
M-	164.22060	-3.6178541	2.422	NB4190
M-	164.23906	-3.5812418	2.280	NB4190
M-	164.27251	-3.5855079	0.559	NB4190
M-	164.21590	-3.6068938	0.119	NB4190
M-	164.22655	-3.6836915	0.261	-
M-	164.22023	-3.6792324	1.086	-
M-	164.22426	-3.6761484	0.577	-
C-2363	53.082743	-27.831706	0.246	$I_{775} - H = 1.91$; $J - K_s = 1.15$
C-2472	53.093660	-27.826402	0.732	$I_{775} - H = 3.11$; $J - K_s = 2.18$
C-2484	53.092048	-27.827811	0.731	$I_{775} - H = 1.33$; $J - K_s = 0.96$
C-3358	53.178065	-27.792739	1.427	$I_{775} - H = 3.54$; $J - K_s = 2.17$

[a]H- stands for HDFS, M- for MS 1054–03, and C- for CDFS. Objects without ID number are either located outside the area covered by the K_s-selected catalog or are not detected in K_s.

[b]Objects with a narrow-band flux excess at 4190 Å are indicated with NB4190.

Table 4.2. Spectroscopic redshifts for DRGs from cross-correlation with other surveys in the CDFS

ID	ra	dec	z_{spec}	Source[a]
C-1553	53.0784636	-27.8598817	3.660	CXO
C-1957	53.1988252	-27.8438850	1.612	Kriek et al.
C-2482	53.2021505	-27.8263119	1.120	VLT/FORS2
C-2855	53.1652224	-27.8140093	3.064	CXO
C-3129	53.0446457	-27.8019901	0.654	K20
C-3968	53.1729054	-27.7444701	1.296	VLT/FORS2
C-4712	53.0632815	-27.6996566	2.402	CXO
C-5177	53.1070458	-27.7181950	2.291	CXO
C-5605	53.1205657	-27.7365600	3.368	MUSYC IMACS
C-5842	53.0362490	-27.7522039	1.294	K20
C-6132	53.1169241	-27.7684461	1.109	K20

[a]NIR spectroscopy from Kriek et al. and optical IMACS spectroscopy by the MUSYC survey from private communication.

Table 4.3. Spectroscopic observing runs

Date	Telescope	Instrument	Field	Total exposure time s	Instrument settings	Seeing "
February 2002	Keck	LRIS	MS 1054–03	72000	D680 dichroic blue: 300 line mm^{-1} red: 400/8500 Å and 600/1 μm grating	0.8 - 1.5
September 2002	VLT	FORS2	HDFS	19800	GRIS_300V, filter gg375	0.8 - 2.0
December 2002	VLT	FORS2	CDFS	29700	GRIS_300V	1.0 - 2.3
January 2003	Keck	LRIS	MS 1054–03	6800	D680 dichroic blue: 400/3400 Å grism red: 400/8500 Å grating	0.7 - 0.8
		DEIMOS	MS 1054–03	18000	mask1: 600/7300 Å grism, filter gg495	0.8 - 1.0
				36240	mask2,3: 600/7700 Å grism, filter og550	0.7 - 1.4
March 2003	Keck	LRIS	MS 1054–03	14400	D560 dichroic blue: 400/3400 Å grism red: 400/8500 Å grating	0.9 - 1.1
March 2003	VLT	FORS2	MS 1054–03	14400	GRIS_300V, filter gg375	0.6 - 0.9
September 2003	Gemini-South	GMOS	HDFS	38400	B600/4500 Å and B600/4530 Å grating	0.9 - 1.4
October 2003	VLT	FORS2	CDFS	24470	GRIS_300V	0.5 - 2.0
			HDFS	16200	GRIS_300V	0.65 - 1.8
November 2003	Keck	LRIS	CDFS	9300	D560 dichroic blue: 400/3400 Å grism red: 400/8500 Å grating	0.7 - 1.5

Table 4.4. Spectroscopic redshifts from our spectroscopic follow-up of DRGs

ID[a]	ra	dec	z_{spec}	Remark
H-66	338.2713649	-60.5703250	3.385	has close companion at 2.6 kpc
M-140	164.2106125	-3.6508417	2.705	-
M-203	164.2078833	-3.6463678	1.580	-
M-508	164.2299500	-3.6315592	1.189	-
M-903	164.1998917	-3.6207567	2.603	-
M-1061	164.2394875	-3.6131875	2.933	optical and NIR flux offset by $1\farcs5$
M-1319	164.2775375	-3.6010592	2.424	-
M-1383	164.2603167	-3.6006669	2.423	redshift from NIR spectroscopy
M-1734	164.2233917	-3.5811008	2.699	-
C-1787	53.1243363	-27.8516408	3.700	also analysed by Norman et al. (2002)
C-2659	53.1488159	-27.8211517	2.582	-
C-3119	53.1231066	-27.8033550	2.349	-
C-3726	53.0550864	-27.7785031	3.521	-
C-5442	53.1177728	-27.7342424	3.256	-
C-5900	53.1080817	-27.7539822	2.728	-

[a]H- stands for HDFS, M- for MS 1054–03, and C- for CDFS.

Table 4.5. Quality of photometric redshifts: statistical measures of $\Delta z/(1+z)$

	CWW++ template set			BC03 template set		
Sample	Median	σ_{NMAD}	MAD	Median	σ_{NMAD}	MAD
DRGs	0.031	0.068	0.077	-0.033	0.056	0.060
DRGs $z_{spec} > 2$	0.014	0.051	0.061	-0.033	0.055	0.046
All	-0.033	0.079	0.122	0.006	0.058	0.104
All $z_{spec} > 2$	0.021	0.061	0.098	-0.052	0.076	0.145
All $z_{phot} > 2$	0.034	0.070	0.544	-0.027	0.069	0.392

References

Adelberger, K. L., Steidel, C. C., Shapley, A. E., Hunt, M. P., Erb, D. K., Reddy, N. A.,& Pettini, M. 2004, ApJ, 607, 226
Bruzual, G.,& Charlot, S. 2003, MNRAS, 344, 1000 (BC03)
Calzetti, D., et al. 2000, ApJ, 533, 682
Coleman, G. D., Wu, C.-C.,& Weedman, D. W. 1980, ApJS, 43, 393
Conselice, C. J., et al. 2007, ApJ, 660, 55
Daddi, E., Cimatti, A., Renzini, A., Fontana, A., Mignoli, M., Pozzetti, L., Tozzi, P.,& Zamorani, G. 2004, ApJ, 617, 746
Daddi, E., et al. 2007, astro-ph/07052832
Dickinson, M.,& the GOODS Legacy Team 2001, A&AS, 198, 2501
Doherty, M., Bunker, A. J., Ellis, R. S.,& McCarthy, P. J. 2005, MNRAS, 361, 525
Erb, D. K., Shapley, A. E., Pettini, M., Steidel, C. C., Reddy, N. A.,& Adelberger, K. L. 2006, ApJ, 644, 813
Faber, S. M., et al. 2003, in Iye M., Moorwood, A. F. M., eds, Proc. SPIE, Vol. 4841, Instrument Design and Performance for Optical/Infrared Ground-Based Telescopes. p. 1657
Förster Schreiber, N. M., et al. 2004, ApJ, 616, 40
Förster Schreiber, N. M., et al. 2006, AJ, 131, 1891
Franx, M., et al. 2000, The Messenger, 99, 20
Franx, M., et al. 2003, ApJ, 587, L79
Giacconi, R., et al. 2002, ApJS, 139, 369
Hook, I., et al. 2003, SPIE, 4841, 1645
Kinney, A. L., et al. 1996, ApJ, 467, 38
Kriek, M., et al. 2006, ApJ, 645, 44
Kriek, M., et al. 2007, ApJ, astro-ph/0611724
Labbé, I., et al. 2003, AJ, 125, 1107
Labbé, I., et al. 2005, ApJ, 624, L81
Le Fèvre,), O., et al. 2004, A&A, 428, 1043
Marchesini, D., et al. 2007, ApJ, 656, 42
McCarthy, P. J., et al. 2001, ApJ, 560, 131
McLean, I. S., et al. 1998, Proc. SPIE, 3354, 566
Mignoli, M., et al. 2005, A&A, 437, 883
Nicklas, H., Seifert, W., Boehnhardt, H., Kiesewetter-Koebinger, S.& Rupprecht, G. 1997, SPIE, 2871, 1222
Norman, C., et al. 2002, ApJ, 571, 218
Oke, J. B., et al. 1995, PASP, 107, 375
Papovich, C., et al. 2006, ApJ, 640, 29
Quadri, R., et al. 2007, ApJ, 654, 138
Reddy, N. A., Erb, D. K., Steidel, C. C., Shapley, A. E., Adelberger, K. L.,& Pettini, M. 2005, ApJ, 633, 748
Rudnick, G., et al. 2001, AJ, 122, 2205
Rudnick, G., et al. 2003, ApJ, 599, 847
Rudnick, G., et al. 2006, ApJ, 650, 624
Salpeter, E. E. 1955, ApJ, 121, 161
Shapley, A. E., Steidel, C. C., Pettini, M.,& Adelberger, K. L. 2003, ApJ, 588, 65
Steidel, C. C.,& Hamilton, D. 1993, AJ, 105, 2017
Steidel, C. C., Giavalisco, M., Pettini, M., Dickinson, M.,& Adelberger, K. L. 1996, ApJ, 462, L17
Szokoly, G. P., et al. 2004, ApJS, 155, 271
Toft, S., van Dokkum, P. G., Franx, M., Thompson, R. I., Illingworth, G. D., Bouwens, R. J.,& Kriek, M. 2005, ApJ, 624, 9
van Dokkum, P. G., et al. 2003, ApJ, 585, 78
van Dokkum, P. G., et al. 2003, ApJ, 587, L83
van Dokkum, P. G., et al. 2004, ApJ, 611, 703
Vanzella, E., et al. 2006, A&A, 454, 423
Wuyts, S., et al. 2007, ApJ, 655, 51

Chapter 5

What do we learn from IRAC observations of galaxies at $2 < z < 3.5$?

Abstract. We analyze very deep HST, VLT and Spitzer photometry of galaxies at $2 < z < 3.5$ in the Hubble Deep Field South. The sample is selected from the deepest public K-band imaging currently available. We show that the rest-frame $U - V$ vs $V - J$ color-color diagram is a powerful diagnostic of the stellar populations of distant galaxies. Galaxies with red rest-frame $U - V$ colors are generally red in rest-frame $V - J$ as well. However, at a given $U - V$ color a range in $V - J$ colors exists, and we show that this allows us to distinguish young, dusty galaxies from old, passively evolving galaxies. We quantify the effects of IRAC photometry on estimates of masses, ages, and the dust content of $z > 2$ galaxies. The estimated distributions of these properties do not change significantly when adding IRAC data to the $UBVIJHK$ photometry. However, for individual galaxies the addition of IRAC can improve the constraints on the stellar populations, especially for red galaxies: uncertainties in stellar mass decrease by a factor of 2.7 for red $[(U - V)_{rest} > 1]$ galaxies, but only by a factor of 1.3 for blue $[(U - V)_{rest} < 1]$ galaxies. We find a similar color-dependence of the improvement for estimates of age and dust extinction. In addition, the improvement from adding IRAC depends on the availability of full NIR JHK coverage; if only K-band were available, the mass uncertainties of blue galaxies would decrease by a more substantial factor 1.9. Finally, we find that a trend of galaxy color with stellar mass is already present at $z > 2$. The most massive galaxies at high redshift have red rest-frame $U - V$ colors compared to lower mass galaxies even when allowing for complex star formation histories.

S. Wuyts, I. Labbé, M. Franx, G. Rudnick, P. G. van Dokkum, G. G. Fazio,
N. M. Förster Schreiber, J. Huang, A. F. M. Moorwood, H.-W. Rix,
H. Röttgering & P. van der Werf
The Astrophysical Journal, **655**, 51 (2007)

5.1 Introduction

TWO of the major challenges in observational cosmology are understanding the history of star formation in galaxies, and understanding the assembly of mass through cosmic time. In the local universe elaborate surveys mapped the diversity of nearby galaxies (e.g., Blanton et al. 2003) and characterized the dependence of their colors (Baldry et al. 2004) and star formation (Kauffmann et al. 2003) on galaxy mass. The study of their progenitors at $z \gtrsim 2$ is important since it is believed that at this epoch the most massive galaxies formed their stars (Glazebrook et al. 2004; van der Wel et al. 2005; Rudnick et al. 2006).

The first method to efficiently identify distant galaxies was the Lyman-break technique (Steidel et al. 1996). Large samples have been spectroscopically confirmed (Steidel et al. 1999). Their stellar populations have been characterized by means of broad-band photometry (e.g., Papovich, Dickinson, & Ferguson 2001, Shapley et al. 2005), optical spectroscopy (e.g., Shapley et al. 2003) and near-infrared (NIR) spectroscopy (Erb et al. 2003, 2006). Lyman break galaxies (LBGs) have spectral energy distributions similar to nearby starburst galaxies.

In recent years, new selection criteria provided evidence for a variety in color space among high-redshift galaxies as rich as in the local universe. Among the newly discovered populations are submm galaxies (e.g., Smail et al. 2004), "IRAC Extremely Red Objects" (IEROs; Yan et al. 2004), "BzK" objects (Daddi et al. 2004) and distant red galaxies (DRGs; Franx et al. 2003). The latter are selected by the simple color criterion $(J-K)_{Vega} > 2.3$. Their rest-frame UV-to-optical SEDs resemble those of normal nearby galaxies of type Sbc-Scd (Förster Schreiber et al. 2004). NIR spectroscopy of DRGs (Kriek et al. 2006) and extension of the broad-band photometry to mid-infrared wavelengths (Labbé et al. 2005) suggests that evolved stellar populations exist already at $2 < z < 3.5$. Rudnick et al. (2006) showed that DRGs contribute significantly to the mass density in rest-frame optically luminous galaxies. van Dokkum et al. (2006) studied a stellar mass-limited sample of galaxies with $M > 10^{11}\ M_{\odot}$ and found that DRGs, rather than LBGs, are the dominant population at the high mass end at $2 < z < 3$.

In this chapter, we exploit the 3-8 μm imaging of the Hubble Deep Field South by *Spitzer*'s Infrared Array Camera (IRAC; Fazio et al. 2004) to extend the SED analysis of distant galaxies to the rest-frame NIR and constrain their stellar masses and stellar populations. Our sample is complete to $K_{tot,AB} = 25$. No color selection criteria are applied. The depth of our imaging allows us to probe down to stellar masses of a few $10^9\ M_{\odot}$. We investigate whether IRAC helps to study the diversity of galaxies at high redshift and if the addition of IRAC improves the constraints on stellar mass, age and dust content. Finally, we investigate the dependence of galaxy color on stellar mass.

The chapter is structured as follows. In §5.2 we describe the data, IRAC photometry and sample definition. §5.3 explains the modeling of spectral energy distributions (SEDs). The rest-frame optical to NIR color distribution of our *K*-selected sample is discussed in §5.4. §5.5 provides an in-depth discussion of the constraints that IRAC places on estimates of age, dust extinction and stellar mass. First wavelength and model dependence are discussed from a theoretical perspective. Next we discuss results from applying the models to our *U*-to-8 μm spectral energy distributions. In §5.6 we investi-

Table 5.1. Characteristics of the IRAC observations

Filter (μ)	Exposure time (hr)	FWHM ($''$)	Limiting depth (5σ, $3''$ diameter aperture)	Positional Accuracy[a] ($''$)
3.6	3.76	1.95	25.6	0.09
4.5	3.76	1.90	25.6	0.15
5.8	3.76	2.10	23.4	0.14
8.0	3.64	2.15	23.3	0.11

[a]The rms difference between bright star positions in IRAC and K-band image.

Table 5.2. Characteristics of the optical-to-NIR observations (see L03)

Instrument/Telescope	Filter	Exposure time (hr)	FWHM ($''$)	Limiting depth (5σ, $0\farcs7$ diameter aperture)
WFPC2/HST	*F*300*W*	36.8	0.16	27.8
WFPC2/HST	*F*450*W*	28.3	0.14	28.6
WFPC2/HST	*F*606*W*	27.0	0.13	28.9
WFPC2/HST	*F*814*W*	31.2	0.14	28.3
ISAAC/VLT	J_s	33.6	0.45	26.9
ISAAC/VLT	H	32.3	0.48	26.4
ISAAC/VLT	K_s	35.6	0.46	26.4

gate the rest-frame optical colors of high-redshift galaxies as a function of stellar mass. Finally, the conclusions are summarized in §5.7.

Throughout this chapter we adopt a cosmology with $H_0 = 70\ km\ s^{-1}\ Mpc^{-1}$, $\Omega_m = 0.3$, and $\Omega_\Lambda = 0.7$.

5.2 Data, photometry and sample selection

5.2.1 Data

Observations of the HDFS/WFPC2 field were obtained with the IRAC camera (Fazio et al. 2004) on the *Spitzer Space Telescope* (Werner et al. 2004) in June 2004 and June 2005 (GTO program 214). A $5' \times 5'$ field of view was covered by the 4 broadband filters at 3.6, 4.5, 5.8 and 8 microns. The data, reduction and photometry will be described in detail by I. Labbé et al. (in preparation). Briefly, we started with the Basic Calibrated Data (BCD) as provided by the Spitzer Science Center pipeline. We applied a series of procedures to reject cosmic rays and remove artifacts such as column pulldown, muxbleed, and the "first frame effect" (Hora et al. 2004). Finally, the frames were registered to and projected on a 2x2 blocked ($0\farcs2396$ pixel scale) version of an existing ISAAC K-band image (Labbé et al. 2003, hereafter L03)[1], and average-combined. Characteristics such as exposure time, FWHM, limiting depth (5σ, 3" diameter aperture) and positional ac-

[1]NIR data from the FIRES survey of the HDFS is publicly available from http://www.strw.leidenuniv.nl/~fires

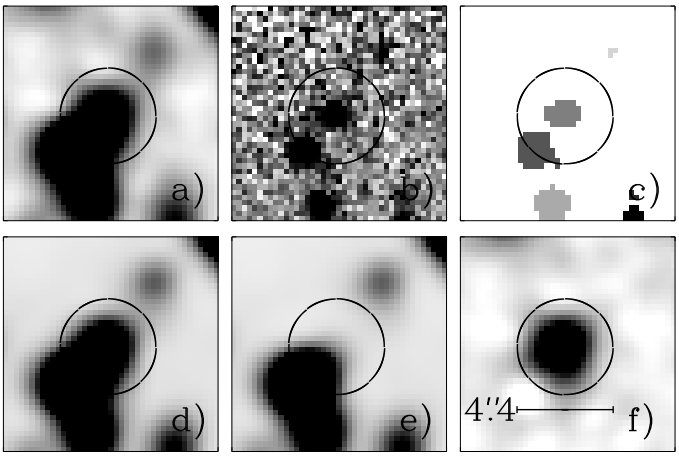

Figure 5.1 — Postage stamps (9.″8 × 9.″8) illustrating the deblending procedure for IRAC photometry. Confusion by nearby neighbors in the original 3.6 μm image (a) is reduced using the higher resolution *K*-band image (b) and its SExtractor segmentation map (c). A model 3.6 μm image (d) is created using information on position and extent of the galaxies from the *K*-band image. The model of the nearby neighbors (e) is subtracted from the original image to obtain a cleaned 3.6 μm image (f).

curacy in each of the 4 IRAC bands are summarized in Table 5.1. A summary of the optical-to-NIR observations by L03 is provided in Table 5.2. All magnitudes quoted in this chapter are in the AB system.

5.2.2 Photometry

In this section we describe the steps to combine the IRAC data and optical-to-NIR data (L03) into one consistent *K*-band selected photometric catalog. In this chapter we limit ourselves to the $2.5' \times 2.5'$ field where very deep *K*-band data is available from L03. The main challenge in doing IRAC photometry is a proper treatment of source confusion and PSF matching of the data. Integrating for nearly 4 hours with IRAC at 3.6 μm and 4.5 μm reaches a depth only 1 mag shallower than 36 hours of ISAAC *K*-band imaging (10σ *limit* $K_{tot,AB} = 25$), but the IRAC images have a 4 times broader PSF causing many sources to be blended. Information on the position and extent of *K*-band detected objects was used to fit and subtract the fluxes of neighbouring sources. Each *K*-band detected source was isolated using the SExtractor "segmentation map" and convolved individually to the considered IRAC PSF. Next, all convolved sources were fitted to the IRAC image, leaving only their fluxes as free parameters. We subsequently subtract the best-fit fluxes of all neighboring sources to remove the contamination. An illustration of this measurement technique is presented in Fig 5.1. The resulting cleaned IRAC images are matched to the broadest PSF (of the 8 μm image). We measured fluxes on the cleaned, PSF-matched images within a fixed 4.″4 diameter circular aperture. The aperture size is a compromise between quality of PSF matching (within 3% as derived from dividing growthcurves) and adding too much noise. Finally, we applied for each source an aperture correction to scale the IRAC fluxes to the "color" apertures defined for the *K*-band catalog by L03. The correction factor is the ratio of the original *K*-band flux in the color aperture and the *K*-band flux in the 8 μm PSF matched image within a 4.″4 diameter aperture. Photometric errors were calculated by taking the rms of fluxes in 4.″4 diameter apertures on empty places in the IRAC image. The end product is a photometric catalog with consistent photometry from optical to MIR wavelengths with 11 filters ($UBVIJHK$+IRAC).

5.2.3 Sample selection

From the catalog described in §5.2.2 we selected all galaxies, well covered by all 11 filters, that have $S/N > 10$ in the K-band. The sample reaches to a limiting total K-band magnitude $K_{tot,AB} = 25$.

Since spectroscopic redshifts are only available for 63 out of 274 objects, we mostly rely on photometric redshift estimates to select high-redshift galaxies and compute rest-frame colors and luminosities. The photometric redshifts and derived rest-frame photometry were calculated as follows. We used an algorithm developed by Rudnick et al. (2001, 2003) to fit a nonnegative linear combination of galaxy templates to the spectral energy distribution of each galaxy. The template set consisted of empirical E, Sbc, Scd and Im templates from Coleman, Wu,& Weedman (1980), the two least reddened starburst templates from Kinney et al. (1996) and two Bruzual & Charlot (2003; hereafter BC03) single stellar populations (SSP) with a Salpeter (1955) stellar initial mass function (IMF), aged 1 Gyr and 10 Myr respectively. The empirical templates were extended into the IR using the BC03 stellar population synthesis code. The derived photometric redshifts show a good agreement with the available spectroscopic redshifts. The average value of $|z_{spec} - z_{phot}|/(1 + z_{spec})$ is 0.06, 0.09 and 0.08 for galaxies at $0 < z < 1$, $1 < z < 2$ and $2 < z < 3.5$ respectively.

Once the redshift was derived, we calculated rest-frame luminosities and colors by interpolating between observed bands using the best-fit templates as a guide. For a detailed description, we refer the reader to Rudnick et al. (2003).

The K-band selected sample contains 121 sources at $0 < z < 1$, 72 at $1 < z < 2$ and 75 at $2 < z < 3.5$. The K+IRAC photometry of the galaxies at $2 < z < 3.5$ is provided in Table 5.3. In §5.4 we study the color-distribution of galaxies with $L_V > 5 \times 10^9 L_\odot$ over the whole redshift range. From that point on we focus on the high-redshift bin. Two commonly color-selected populations at $z > 2$ are highlighted where they are of interest. LBGs are selected from the WFPC2 imaging using the criteria of Madau et al. (1996). DRGs are selected by the simple color criterion $(J - K)_{AB} > 1.34$ (Franx et al. 2003).

5.3 SED modeling

To study physical characteristics of the galaxies such as stellar mass, stellar age and amount of dust extinction, we make use of the evolutionary synthesis code developed by BC03. We fitted the synthetic spectra to our observed SEDs using the publicly available HYPERZ stellar population fitting code, version 1.1 (Bolzonella et al. 2000). Redshifts were fixed to the z_{phot} measurement (see §5.2.3, Rudnick et al. 2003) or z_{spec} when available. A minimum error of 0.08 mag was adopted to avoid the problem of data points with the largest errors being effectively ignored in the SED fits. We fitted three distinct star formation histories: a single stellar population (SSP) without dust, a constant star formation (CSF) history with dust (A_V varying from 0 to 4 in steps of 0.2) and an exponentially declining star formation history with an e-folding timescale of 300 Myr (τ_{300}) and identical range of A_V values. The exponentially declining model allows for quiescent systems that underwent a period of enhanced star formation in their past.

Table 5.3. K+IRAC photometry of HDFS galaxies at $2 < z < 3.5$

Object[a]	$f_{K,tot}$[b]	$f_{K,col}$	$f_{3.6\mu m,col}$	$f_{4.5\mu m,col}$	$f_{5.8\mu m,col}$	$f_{8.0\mu m,col}$
62	1.90 ± 0.33	1.30 ± 0.10	1.85 ± 0.19	1.57 ± 0.21	-2.36 ± 1.46	-3.48 ± 1.73
66	6.03 ± 0.58	4.96 ± 0.22	8.82 ± 0.22	11.15 ± 0.23	14.95 ± 1.63	20.31 ± 1.93
92	3.17 ± 0.13	2.11 ± 0.08	2.29 ± 0.19	2.31 ± 0.20	0.45 ± 1.40	-1.85 ± 1.66
96	4.55 ± 0.62	3.45 ± 0.19	4.45 ± 0.21	4.33 ± 0.23	2.46 ± 1.62	4.72 ± 1.93
114	1.44 ± 0.25	0.99 ± 0.09	1.06 ± 0.18	1.25 ± 0.20	-0.09 ± 1.38	-4.15 ± 1.64
116	1.72 ± 0.27	1.26 ± 0.09	1.75 ± 0.20	2.26 ± 0.21	1.77 ± 1.49	0.52 ± 1.76
130	1.83 ± 0.26	1.71 ± 0.10	2.03 ± 0.20	1.53 ± 0.22	4.50 ± 1.51	2.98 ± 1.79
133	2.44 ± 0.27	1.94 ± 0.10	3.10 ± 0.20	2.64 ± 0.22	3.19 ± 1.52	0.53 ± 1.81
143	4.47 ± 0.15	3.56 ± 0.12	6.16 ± 0.21	6.12 ± 0.23	4.75 ± 1.60	1.18 ± 1.90
158	1.42 ± 0.23	0.79 ± 0.07	0.81 ± 0.16	1.00 ± 0.18	-0.89 ± 1.24	1.93 ± 1.47

Note.– Table 5.3 is published in its entirety in the electronic edition of the *Astrophysical Journal*. A portion is shown here for guidance regarding its form and content.

[a]Object identification number corresponds to that of the *U*-to-*K* catalog by Labbé et al. (2003).

[b]Fluxes in total (tot) and color (col) aperture are scaled to an AB zero point of 25, i.e., $\mathrm{mag}_{AB} = 25 - 2.5 \log f$.

Table 5.4. Modeling results for HDFS galaxies at $2 < z < 3.5$

Object[a]	z	SFH	$\log(M_*)$ ($M_\odot$)	A_V	$\log(Age_w)$ (Gyr)
62	$2.72^{+0.04}_{-0.04}$	CSF	$9.69^{+0.15}_{-0.05}$	$0.4^{+0.0}_{-0.2}$	$-0.75^{+0.45}_{-0.05}$
66	$3.38^{+0.00}_{-0.00}$	τ_{300}	$11.04^{+0.14}_{-0.00}$	$1.6^{+0.0}_{-0.6}$	$-0.50^{+0.37}_{-0.00}$
92	$2.66^{+0.28}_{-0.08}$	SSP	$9.75^{+0.26}_{-0.00}$	$0.0^{+0.4}_{-0.0}$	$-1.09^{+0.54}_{-0.00}$
96	$2.06^{+0.08}_{-0.02}$	CSF	$10.02^{+0.01}_{-0.12}$	$0.2^{+0.0}_{-0.0}$	$-0.30^{+0.00}_{-0.31}$
114	$2.98^{+0.16}_{-0.38}$	τ_{300}	$9.75^{+0.11}_{-0.13}$	$0.2^{+0.2}_{-0.2}$	$-0.50^{+0.12}_{-0.12}$
116	$3.14^{+0.14}_{-0.10}$	CSF	$10.18^{+0.02}_{-0.14}$	$0.4^{+0.0}_{-0.2}$	$-0.10^{+0.00}_{-0.39}$
130	$2.16^{+0.04}_{-0.12}$	SSP	$9.44^{+0.22}_{-0.01}$	$0.0^{+0.4}_{-0.0}$	$-0.84^{+0.47}_{-0.00}$
133	$2.04^{+0.02}_{-0.28}$	τ_{300}	$9.68^{+0.12}_{-0.12}$	$0.6^{+0.2}_{-0.2}$	$-0.73^{+0.43}_{-0.07}$
143	$2.16^{+0.04}_{-0.12}$	τ_{300}	$10.12^{+0.07}_{-0.06}$	$0.8^{+0.0}_{-0.2}$	$-0.67^{+0.18}_{-0.06}$
158	$2.08^{+0.14}_{-0.18}$	CSF	$9.55^{+0.14}_{-0.09}$	$0.2^{+0.0}_{-0.2}$	$-0.20^{+0.33}_{-0.35}$

Note.– Table 5.4 is published in its entirety in the electronic edition of the *Astrophysical Journal*. A portion is shown here for guidance regarding its form and content.

[a]Object identification number corresponds to that of the *U*-to-*K* catalog by Labbé et al. (2003).

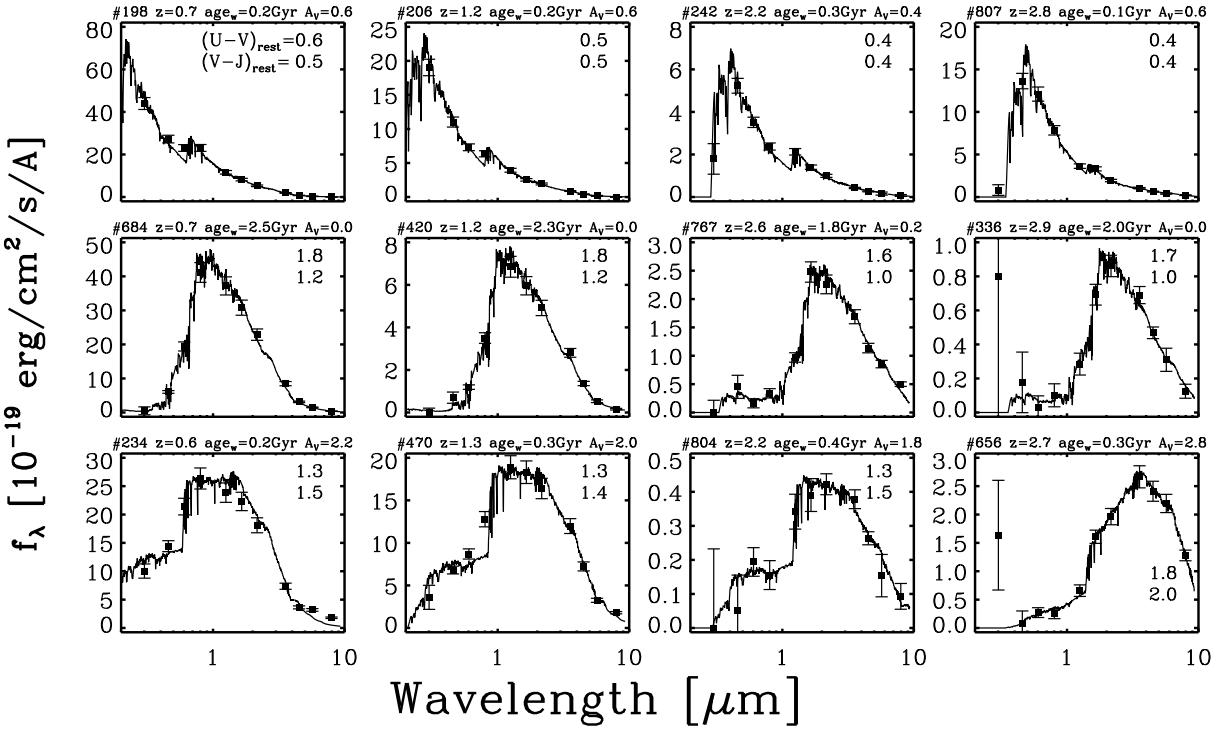

Figure 5.2 — The U-to-8 μm spectral energy distributions of a subset of galaxies occupying different locations in $(U-V)_{rest}$ vs $(V-J)_{rest}$ color-color space. Each row shows observed and BC03 model SEDs for galaxies with redshifts ranging from $z \sim 0.7$ to $z \sim 3$. A broad range of galaxy types is present at all redshifts. Galaxies with blue $(U-V)_{rest}$ colors (*top row*) have young ages and a modest amount of dust obscuration. Objects with red $(U-V)_{rest}$ colors that are on the blue side of the $(V-J)_{rest}$ color distribution (*middle row*) are best fit by old stellar populations with little dust obscuration. The bottom row shows examples of galaxies with red optical and red optical-to-NIR colors. They are consistent with young stellar populations with a large dust reddening.

Förster Schreiber et al. (2004) showed that the estimated extinction values do not vary monotonically with the *e*-folding timescale τ, but reach a minimum around 300 Myr. Including the τ_{300} model thus ensures that the allowed star formation histories encompass the whole region of parameter space that would be occupied when fitting models with different values of τ. For each of the star formation histories (SFHs), we constrained the time elapsed since the onset of star formation to a minimum of 50 Myr, avoiding fit results with improbable young ages. The age of the universe at the observed redshift was set as an upper limit to the ages. Furthermore, we assume a Salpeter (1955) IMF with lower and upper mass cut-offs $0.1M_\odot$ and $100M_\odot$, solar metallicity and we adopt a Calzetti et al. (2000) extinction law. For each object the star formation history resulting in the lowest χ^2 of the fit was selected and corresponding model quantities such as age, mass and dust extinction were adopted as the best-fit value. We calculated the mass-weighted age for each galaxy by integrating over the different ages of SSPs that build up the SFH, weighting with their mass fraction. We use this measure since it is more robust with respect to degeneracies in SFH than the time passed since the onset of star formation; it describes the age of the bulk of the stars. See Table 5.4 for a summary of the results of our SED modeling for the subsample of

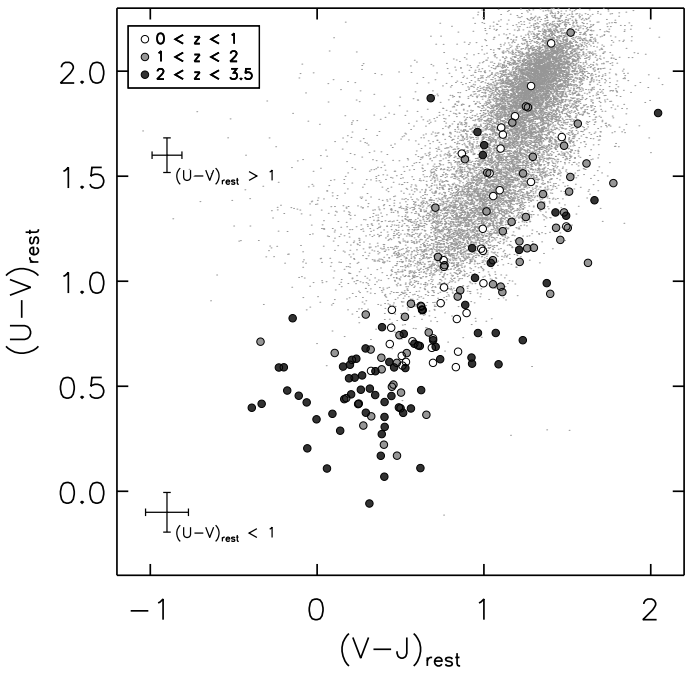

Figure 5.3 — Rest-Frame $U-V$ versus $V-J$ color-color diagram of all galaxies with $L_V > 5 \times 10^9 L_\odot$. SDSS+2MASS galaxies (*small grey dots*) are plotted as a local reference. Greyscale coding refers to the redshift bin. Galaxies with red $U-V$ colors are also red in $V-J$. Compared to the local SDSS galaxies the high-redshift color distribution extends to bluer $U-V$ colors (where Lyman-break galaxies are located) and for the same $U-V$ color to redder $V-J$ colors.

galaxies at $2 < z < 3.5$. In Figure 5.2 we show example U-to-8 μm SEDs with best-fit BC03 models of galaxies over the whole redshift range, illustrating that at all epochs a large variety of galaxy types is present.

We fitted all objects in our sample twice, once with and once without IRAC photometry. We repeated the SED modeling with the same parameter settings using the models by Maraston (2005; hereafter M05). The results are discussed in §5.5.2.2. Variations in modeled parameters due to a different metallicity are addressed in §5.5.2.3. The effects of adopting a different extinction law are discussed in §5.5.2.4. Unless noted otherwise, we refer to stellar mass, mass-weighted age and dust extinction values derived from the U-to-8 μm SEDs with BC03 models.

5.4 Rest-frame optical to near-infrared color distribution

At redshifts above 1 all rest-frame NIR bands have shifted redward of observed K, and mid-infrared photometry is needed to compute rest-frame NIR fluxes from interpolation between observed bands. It has only been with the advent of IRAC on the *Spitzer Space Telescope* that the rest-frame NIR opened up for the study of high-redshift galaxies. As the 3.6 μm and 4.5 μm images are much deeper than the 5.8 μm and 8.0 μm images (see Table 5.1), we focus on the rest-frame J band (J_{rest}).

Several studies have focussed on the optical to NIR colors and inferred stellar populations of particular color-selected samples (e.g., Shapley et al. 2005, Labbé et al. 2005). In this section we take advantage of the multiwavelength data and the very deep K-band selection to study the rest-frame optical to NIR colors of all galaxies up to $z = 3.5$ without color bias. For the first time we can therefore investigate what range in optical to NIR colors high-redshift galaxies occupy, how their optical to NIR colors relate to pure optical colors, and what this tells us about the nature of their stellar populations.

In Figure 5.3 we present a color-color diagram of $(U-V)_{rest}$ versus $(V-J)_{rest}$ for the

redshift bins $0 < z < 1$, $1 < z < 2$ and $2 < z < 3.5$. A clear correlation of $(U-V)_{rest}$ with $(V-J)_{rest}$ is observed at all redshifts. The $(U-V)_{rest}$ color samples the Balmer/4000$\AA$ break. The large wavelength range spanned by $(U-V)_{rest}$ and $(V-J)_{rest}$ together is useful to probe reddening by dust.

To study how the color distribution compares to that in the local universe, we indicate the colors of galaxies in the low-redshift New York University Value-Added Galaxy Catalog (NYU_VAGC; Blanton et al. 2005) with small grey dots. The low-z NYU_VAGC is a sample of nearly 50000 galaxies at $0.0033 < z < 0.05$ extracted from the Sloan Digital Sky Survey (SDSS data release 4; Adelman-McCarthy et al. 2006). It is designed to serve as a reliable reference for the local galaxy population and contains matches to the Two Micron All Sky Survey Point Source Catalog and Extended Source Catalog (2MASS; Cutri et al. 2000). Only the subsample of 20180 sources that are detected in the 2MASS J-band are plotted in Figure 5.3. This results effectively in a reduction of the blue peak of the bimodal $U-V$ distribution. We only show those galaxies (both for the local sample and for our sample of HDFS galaxies) with a rest-frame V-band luminosity $L_V > 5 \times 10^9 L_\odot$. At this luminosity the distribution of low-z NYU_VAGC galaxies with SDSS and 2MASS detections starts falling off. From the much deeper HDFS imaging the luminosity cut weeds out low- to intermediate-redshift dwarf galaxies.

The same trend of optically red galaxies being red in optical to NIR wavelengths that we found for galaxies up to $z = 3.5$ is observed in the local universe. However, there are two notable differences in the color distribution between distant and local galaxies. First, a population of luminous high-redshift galaxies with very blue $(U-V)_{rest}$ and $(V-J)_{rest}$ exists without an abundant counterpart in the local universe. The 2MASS observations are not deep enough to probe very blue $V-J$ colors, but we can ascertain that 95% of all low-z NYU_VAGC sources with $L_V > 5 \times 10^9 L_\odot$ lie in the range $0.73 < U-V < 2.24$. About half of the blue galaxies at $z > 2$ with $(U-V)_{rest} < 0.73$ and $L_V > 5 \times 10^9 L_\odot$ satisfy the Lyman-break criterion. Their stellar populations have been extensively studied (e.g., Papovich et al. 2001; Shapley et al. 2001; among many others) and their blue SEDs (see e.g., object #242 and #807 in Figure 5.2) are found to be well described by relatively unobscured star formation. The rest-frame optical bluing with increasing redshift of galaxies down to a fixed L_V is thoroughly discussed by Rudnick et al. (2003).

A second notable difference with respect to the color distribution of nearby galaxies is present at $(U-V)_{rest} > 1$, where most local galaxies reside. Our sample of HDFS galaxies has a median offset with respect to the SDSS+2MASS galaxies of 0.22 ± 0.04 mag toward redder $(V-J)_{rest}$ at a given $(U-V)_{rest}$. Furthermore, the spread in $(V-J)_{rest}$ is larger, extending from colors similar to that of local galaxies to $(V-J)_{rest}$ colors up to a magnitude redder. The larger spread in $(V-J)_{rest}$ colors at a given $(U-V)_{rest}$ is not caused by photometric uncertainties. After subtraction in quadrature of the scatter expected from measurement errors (0.05 mag) we obtain an intrinsic scatter of 0.3 mag, significantly larger than that for SDSS+2MASS galaxies (0.19 mag) at a 4.5σ level.

In order to understand the nature of galaxies with similar or redder $(V-J)_{rest}$ than the bulk of nearby galaxies, we make use of stellar population synthesis models by BC03. In Figure 5.4 we draw age tracks for three different dust-free star formation

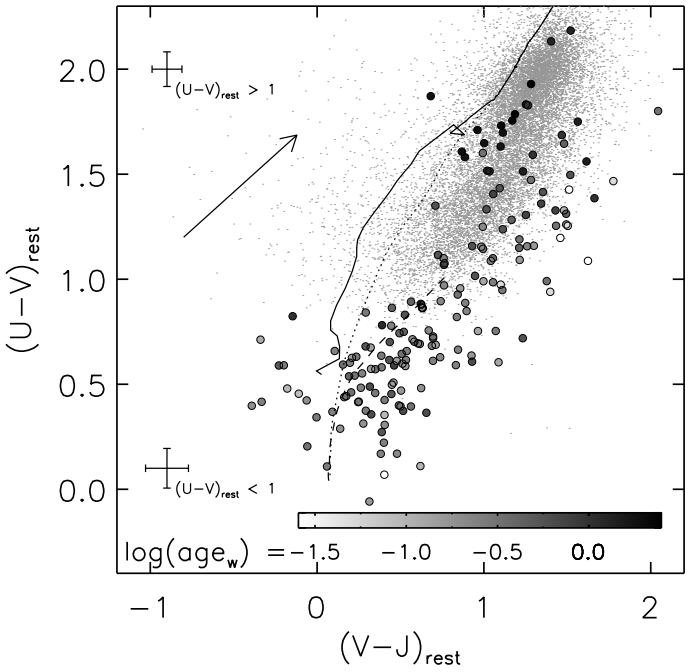

Figure 5.4 — Rest-Frame $U-V$ versus $V-J$ color-color diagram of all galaxies with $L_V > 5 \times 10^9 L_\odot$. SDSS+2MASS galaxies (*small grey dots*) are plotted as a local reference. The dust vector indicates an extinction of $A_V = 1$ mag. Color evolution tracks of (unreddened) Bruzual & Charlot (2003) models are overplotted: a simple stellar population (SSP, *solid line*), an exponentially declining (τ_{300}, *dotted line*) and constant (CSF, *dashed line*) star formation model. Galaxies are greyscale-coded by best-fit mass-weighted age. The tracks show an increase toward redder $U-V$ and slightly redder $V-J$ with age. At a given $U-V$ color redder than 1 galaxies that are red in $V-J$ have the youngest best-fit mass-weighted ages.

histories in the $(U-V)_{rest}$ vs $(V-J)_{rest}$ color-color diagram. The solid line represents a single stellar population (SSP), the dashed line a continuous star formation model (CSF) and the dotted line an exponentially declining star formation model with an *e*-folding timescale of 300 Myr (τ_{300}). All star formation histories show an evolution to redder $(U-V)_{rest}$ and $(V-J)_{rest}$ with age. The τ_{300} model first has similar colors as a CSF model and eventually moves to the same region in color space as an evolved SSP, namely where the red peak of the SDSS bimodal $U-V$ distribution is located. In the absence of dust a population with a constant star formation history only reaches $U-V=1$ in a Hubble time.

We now investigate how the location in this color plane is related to stellar populations. Using the best-fit model parameters (see §5.3) we plot the mass-weighted ages for the galaxies with $L_V > 5 \times 10^9 L_\odot$ with greyscale-coding on Figure 5.4. Galaxies with blue optical colors are indeed found to be young, the median mass-weighted age for galaxies at $(U-V)_{rest} < 1$ being 250 Myr. At $(U-V)_{rest} > 1$ galaxies with a wide range of stellar ages are found. The oldest stellar populations show the bluest $(V-J)_{rest}$ colors at a given $(U-V)_{rest}$. Over the whole redshift range galaxies are present that have red optical colors and whose SEDs are consistent with evolved stellar populations and low dust content. According to their best-fit model, three of them started forming stars less than 0.5 Gyr after the big bang and already at $z > 2.5$ have star formation rates less than a percent of the past-averaged value. We note that in the Chandra Deep Field South Papovich et al. (2006) find a number density of passively evolving galaxies at high redshift that is nearly an order of magnitude lower than in the HDFS, possibly owing to the fact that the HDFS observations probe to fainter K-band magnitudes. The red $(V-J)_{rest}$ side of the color distribution is made up of galaxies that are best fitted by young stellar populations. Since the age tracks alone cannot explain the presence of galaxies with such red SEDs from the optical throughout the NIR, we investigate the

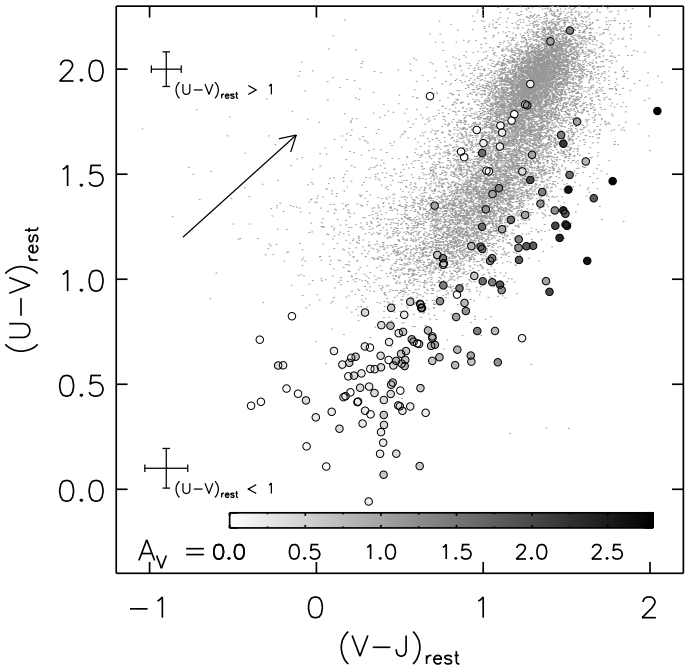

Figure 5.5 — Rest-Frame $U-V$ versus $V-J$ color-color diagram of all galaxies with $L_V > 5 \times 10^9 L_\odot$. SDSS+2MASS galaxies (*small grey dots*) are plotted as a local reference. The vector indicates a dust extinction of $A_V = 1$ mag. Galaxies are greyscale-coded by best-fit A_V. The presence of dust moves galaxies to redder $U-V$ and $V-J$ colors. Galaxies falling redward in $V-J$ of the distribution of local galaxies are best described by dusty stellar populations.

role of dust in shaping the galaxy color distribution.

Figure 5.5 shows again the $(U-V)_{rest}$ versus $(V-J)_{rest}$ color-color diagram, now greyscale-coded by best-fit dust extinction, expressed in A_V. The arrow indicates an A_V of 1 magnitude using a Calzetti et al. (2000) extinction law. It is immediately apparent that the optical to NIR color-color diagram is a useful diagnostic for distinguishing stellar populations with various amounts of dust extinction. At the bluest $(U-V)_{rest}$ colors there is little evidence for dust obscuration. The degree of dust extinction increases as we move along the dust vector to redder colors.

Independent constraints on dust-enshrouded activity in distant galaxies can be derived from MIPS 24 μm imaging (Webb et al. 2006; Papovich et al. 2006). The mid-infrared emission is usually thought to be powered by a dusty starburst in which PAH features are produced or by an active galactic nucleus (AGN). Of the area with very deep U-to-8 μm in the HDFS 95% is covered by a 1 hr MIPS pointing. We performed the same photometric procedure to reduce confusion as for the IRAC photometry (see §5.2.2). Fluxes were measured within a 6″ diameter aperture and then scaled to total using the growthcurve of the 24 μm PSF.

In Figure 5.6 we plot the $(U-V)_{rest}$ versus $(V-J)_{rest}$ color-color diagram of all objects in the redshift interval $1.5 < z < 3.5$ with $L_V > 5 \times 10^9 L_\odot$ that are covered by MIPS (*empty circles*). At these redshifts, strong PAH features, if present, move through the MIPS 24 μm passband. Six sources have a MIPS 24 μm detection above 28 μJy (3σ). Their 24 μm flux is indicated by the filled circles. Object #767 is well detected with $F_{24\mu m} = 95$ μJy. As noted by Labbé et al. (2005) its SED shows an $8\mu m$ excess with respect to the best-fitting template. The combination of 8 μm excess and 24 μm detection suggests that this galaxy hosts an AGN whose power law SED dominates throughout the mid-infrared. All other 24 μm detections are located in the part of the diagram where our U-to-8 μm SED modeling found dusty young populations. None

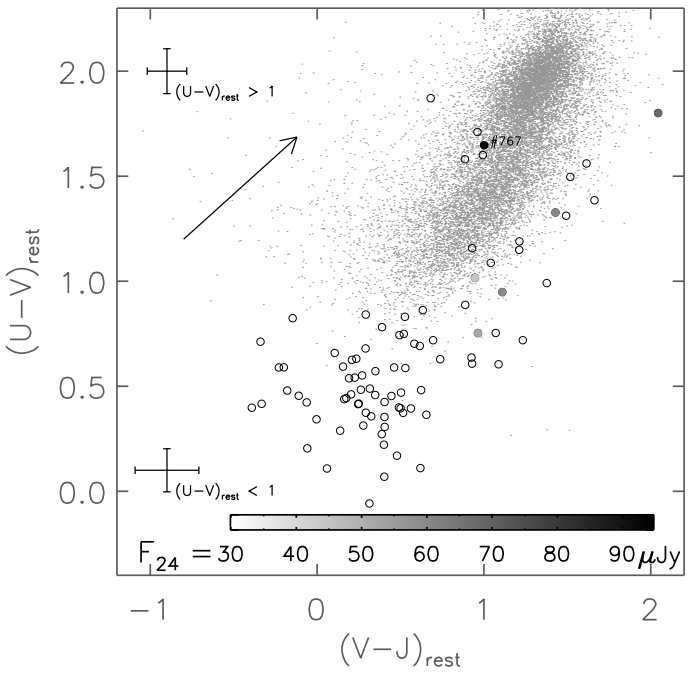

Figure 5.6 — Rest-Frame $U-V$ versus $V-J$ color-color diagram of galaxies at $1.5 < z < 3$ with $L_V > 5 \times 10^9 L_\odot$ with MIPS 24 μm coverage. SDSS+2MASS galaxies (*small grey dots*) are plotted as a local reference. Filled circles represent MIPS 24 μm detections above a 28 μJy (3σ) threshold. #767 is detected at 24 μm and has an excess of 8 μm flux compared to the best-fitting template SED, suggesting the presence of an obscured AGN. All other 24 μm detections lie in the $U-V$, $V-J$ region populated by galaxies with dusty stellar populations. Assuming the 24 micron flux originates from PAH emission produced by dust-enshrouded star formation, the MIPS observations confirm the diagnostic power of this color combination.

of the blue relatively unobscured star-forming galaxies or red evolved galaxies show evidence of PAH emission from the observed 24 μm flux. There are various reasons why not all star-forming dusty galaxies have a 24 μm detection. The density of the UV radiation field exciting the PAHs may vary among galaxies. Furthermore, the narrow PAH features with respect to the width of the 24 μm passband make the 24 μm flux very sensitive to redshift. Overall, MIPS observations agree well with SED modeling and rest-frame optical-NIR color characterization.

We conclude that over the whole redshift range from $z = 0$ to $z = 3.5$ a trend is visible of galaxies with redder optical colors showing redder optical to NIR colors. However, at a given optical color, a spread in optical to NIR colors is observed that is larger than for nearby galaxies. At $(U-V)_{rest} > 1$ evolved galaxies with little dust extinction are found at the bluest $(V-J)_{rest}$. Dusty young star-forming galaxies occupy the reddest $(V-J)_{rest}$ colors. This is once more illustrated by the SEDs of galaxies with $(U-V)_{rest} > 1$ presented in Figure 5.7. The top row shows SEDs of objects at the blue side of the $(V-J)_{rest}$ color distribution. The bottom panels show SEDs of galaxies matched in $(U-V)_{rest}$, but with comparatively redder $(V-J)_{rest}$ colors. The latter galaxies have comparatively younger ages and a larger dust content. Since this distinction could not be made on the basis of $(U-V)_{rest}$ color alone, the addition of IRAC 3.6 - 8 μm photometry to our U-to-K SEDs proves very valuable for the understanding of stellar populations at high redshift.

We verified that no substantial changes occur to the rest-frame optical-to-NIR color distribution and its interpretation in terms of age and dust content of the galaxies when we derive photometric redshifts by running HYPERZ with redshift as free parameter instead of using the algorithm developed by Rudnick et al. (2003; see §5.2.3).

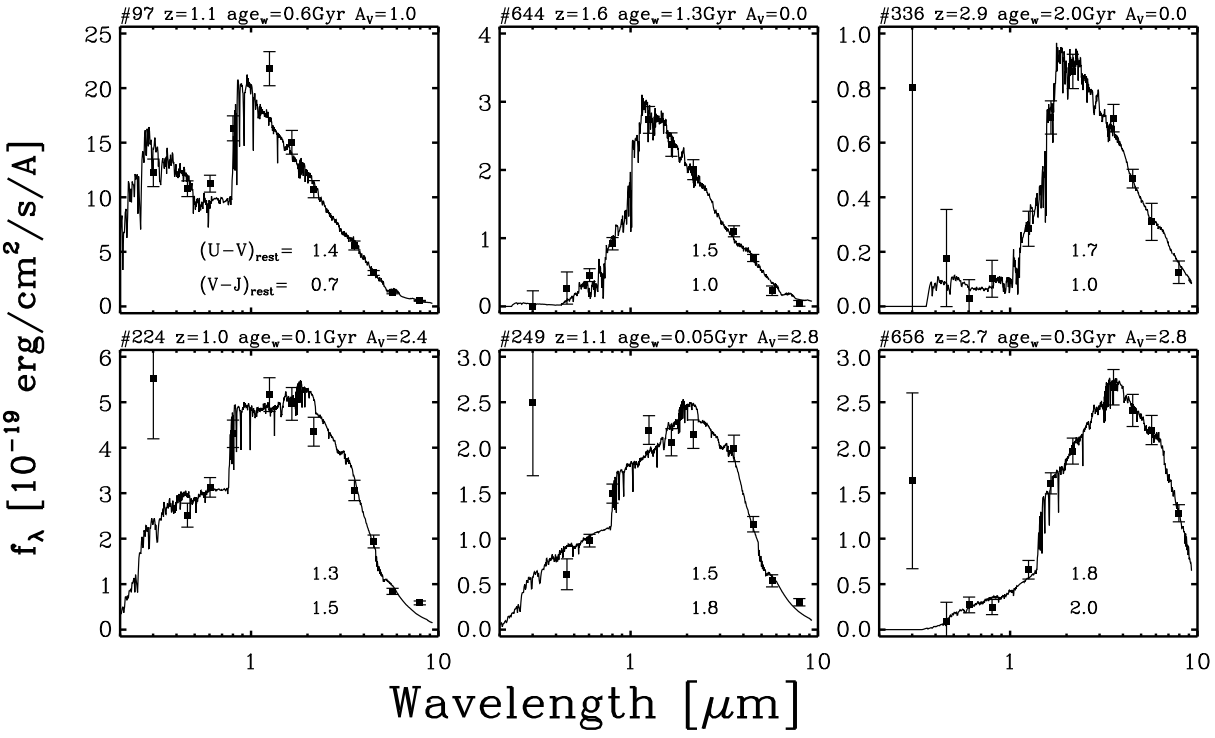

Figure 5.7 — Comparison of galaxies with similar $(U-V)_{rest}$ color but different $(V-J)_{rest}$ color. The top row shows the galaxies with blue $(V-J)_{rest}$ colors, and the bottom row shows galaxies with matching $(U-V)_{rest}$ color but much redder $(V-J)_{rest}$ color. The systematic difference in the SEDs of the two rows is striking. Fits indicate old bursts of star formation with little dust in the top row, and dusty young galaxies in the bottom row. This demonstrates the power of $(V-J)_{rest}$ in separating these classes. Note that the U-band photometry for objects #224 and #249 deviates by more than 2σ from the predicted U-band flux of the best-fit template.

5.5 Constraints on stellar population properties at $2 < z < 3.5$: age, dust and mass

We now proceed to analyze in more detail the constraints that IRAC places on the stellar populations of the subsample of galaxies at $2 < z < 3.5$ (75 galaxies). In particular we will focus on stellar mass, which likely plays a key role in galaxy evolution at all redshifts (e.g., Kauffmann et al. 2003; Bundy et al. 2005; Drory et al. 2005; Rudnick et al. 2006). Fortunately, estimates of stellar mass from modeling the broad-band SEDs are generally more robust than estimates of dust content and stellar age (Bell& de Jong 2001; Shapley et al. 2001; Papovich et al. 2001; Förster Schreiber et al. 2004). Nevertheless, translating colors to mass-to-light ratios and subsequently stellar masses requires a good understanding of the effects of age and dust.

5.5.1 Predictions from stellar population synthesis models

5.5.1.1 Wavelength dependence: optical versus near-infrared

In its simplest form the stellar mass of a galaxy can be estimated from one color (see, e.g., Bell & de Jong 2001). To illustrate this process, we present the evolutionary track of a dust-free BC03 model in a M/L_V versus $U-V$ diagram (Fig. 5.8). Up to 2.5 Gyr

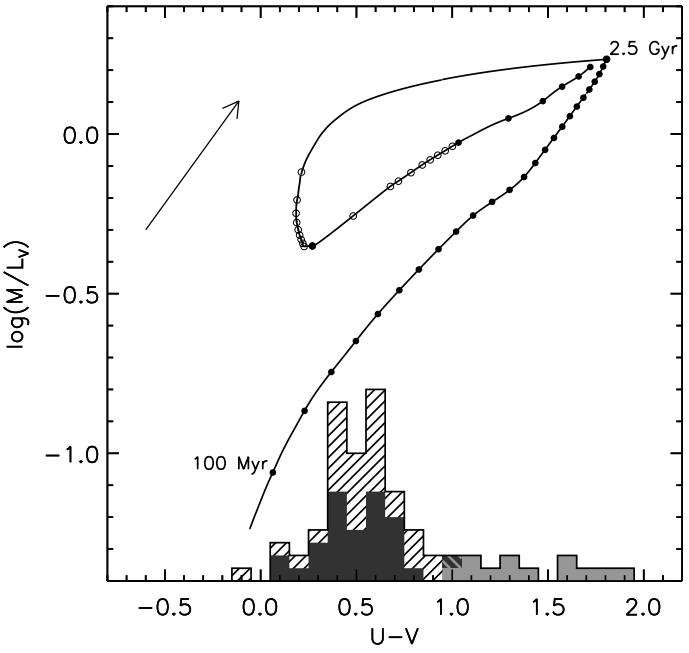

Figure 5.8 — Evolutionary track of a two-component stellar population in the M/L_V versus $U-V$ plane. Filled circles mark age steps of 100 Myr. Open circles represent 10 Myr age steps. The dust vector, indicating an extinction of $A_V = 1$ mag, lies parallel to the age track. The histogram represents the color distribution of galaxies at $2 < z < 3.5$, with DRGs highlighted in solid light-grey, LBGs in solid dark-grey. The age track starts as an exponentially declining star formation model ($\tau = 300$ Myr, BC03). At 2.5 Gyr a new burst of star formation is introduced, lasting 100 Myr and contributing 20% to the mass. Translating $U-V$ into M/L_V assuming one-component models can lead to underestimates of M/L_V and thus stellar mass. The possible underestimate is largest for blue galaxies.

after the onset of star formation (Fig. 5.8, *top right corner*) the track represents a one-component population with a star formation history that is exponentially declining, with an *e*-folding timescale of 300 Myr. For most of the galaxies in our sample this was the best-fitting star formation history. For more extreme star formation histories such as an SSP or CSF the process of estimating M/L values follows similar arguments. The filled circles on Figure 5.8 represent age steps of 100 Myr. As the stellar population ages, its V-band luminosity fades with only a small decrease in stellar mass from mass loss, moving the galaxy up in M/L_V. Simultaneously the $U-V$ color reddens as the hot early-type stars with short lifetimes die. The dust vector indicating a reddening of $A_V = 1$ mag runs parallel to the age track of the one-component model. Ironically, the mass estimate benefits greatly from this degeneracy between age and dust in the optical. Under the assumption of a monotonic star formation history $(U-V)_{rest}$ can uniquely be translated to M/L_V, regardless of the precise role of dust or age. Only a normalization with L_V is needed to derive the stellar mass. A similar relation was used by Rudnick et al. (2003) to translate the integrated $(U-V)_{rest}$ color of high-redshift galaxies into a global M/L_V and stellar mass density ρ_*. They found that the conversion to mass-to-light ratio is more robust from the $(U-V)_{rest}$ color than from the $(U-B)_{rest}$ or $(B-V)_{rest}$ color.

What if the actual star formation history is more complex? What effect does it have on the derived stellar mass? There is ample evidence from local fossil records (e.g., Trager et al. 2000; Lancon et al. 2001; Freeman & Bland-Hawthorn 2002; Förster Schreiber et al. 2003; Angeretti et al. 2005) and high-redshift studies (e.g., Papovich et al. 2001; Ferguson et al. 2002; Papovich et al. 2005) that galaxies of various types have complex and diverse star formation histories, often with multiple or recurrent episodes of intense star formation . Such a scenario is also predicted by cold dark matter models (e.g., Somerville, Primack,& Faber 2001; Nagamine et al. 2005; De Lucia

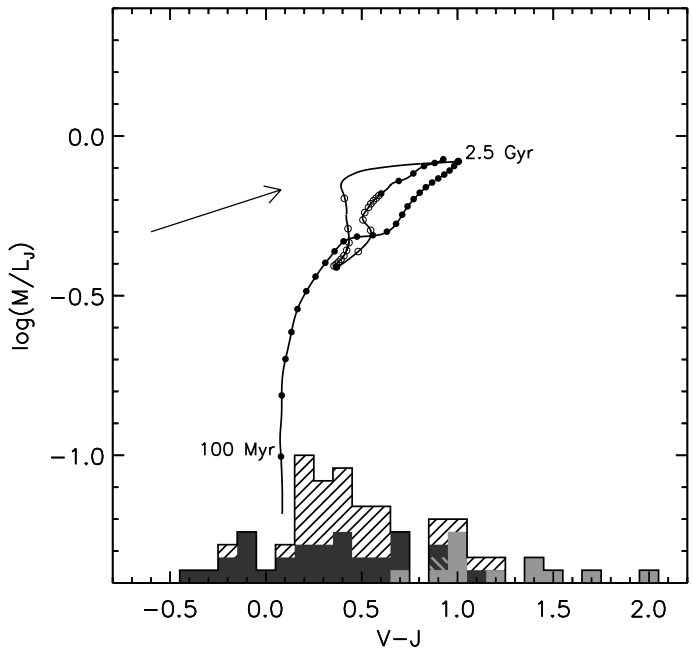

Figure 5.9 — Evolutionary track of a two-component stellar population in the M/L_J versus $V-J$ plane. A τ_{300} model from BC03 is shown. At 2.5 Gyr a 100 Myr burst is added , contributing 20% to the mass. Age marks represent 100 Myr (*filled circles*) and 10 Myr (*open circles*) respectively. The histogram shows the color distribution of our sample at $2 < z < 3.5$, with DRGs in solid light-grey and LBGs in solid dark-grey. For blue galaxies the $V-J$ color is insensitive to M/L_J, further complicated by the dust vector ($A_V = 1$ mag) that lies nearly orthogonal to the age track meaning blue galaxies can have a range of masses for the same $V-J$ color. On the other hand, the introduction of a second burst only causes a small offset in M/L_J from the single-component track, showing that the inclusion of a rest-frame NIR band reduces the uncertainties in stellar M/L caused by poor knowledge of the star formation history.

et al. 2005). In order to address this question qualitatively, we consider the case of a two-component population. At $t = 2.5$ Gyr we added a burst of star formation to the τ_{300} model, lasting 100 Myr and contributing 20% to the mass. To follow the evolution of the two-component population closely, we mark 10 Myr timesteps with open circles. Over a timespan of only 10 Myr the galaxy color shifts by 1.6 mag toward the blue, while the M/L_V value stays well above the one-component M/L_V corresponding to that color. As the newly formed stars grow older, the galaxy moves toward the upper right corner of the diagram again. The offset of M/L_V with respect to the one-component model is a decreasing function of $U-V$. This means that if a bursty star formation is mistakenly fit with a one-component model the mass and mass-to-light ratio are underestimated more for blue than for red galaxies, confirming what Shapley et al. (2005) found for a sample of star-forming galaxies at $z > 2$.

The histogram at the bottom of Figure 5.8 indicates the $(U-V)_{rest}$ color distribution of galaxies in the HDFS at $2 < z < 3.5$. The population of Lyman-break galaxies (LBGs) is marked in blue, Distant Red Galaxies (DRGs) in red. The possible underestimate in mass-to-light ratio and thus mass is largest for blue galaxies, up to a factor of 3 for $(U-V)_{rest} = 0.2$, the bluest color reached by this two-component model. For DRGs only a modest amount of mass can be hidden under the glare of a young burst of star formation. The exact error that bursts cause depends on the form of the bursty star formation history (see, e.g., Fig. 6 in Rudnick et al. 2003 for a different example).

We can now test whether rest-frame NIR photometry, as provided by IRAC, improves the constraints on the SED-based stellar mass estimates of high-redshift galaxies. Labbé et al. (2005) found that the range in M/L_K for DRGs and LBGs together is as

large as a factor 6, meaning that a Spitzer 8 μm-selected sample would be very different from a mass-selected sample. However, if a similar relation between mass-to-light ratio and color exists in the rest-frame NIR as in the rest-frame optical, this does not mean that the stellar mass estimate is uncertain by the same amount (a factor of 6). Here we consider whether the mass-to-light ratio can robustly be derived from a given rest-frame NIR color. We discuss only the rest-frame J-band but note that the results for rest-frame K are similar. In Figure 5.9 we repeat the same exercise of drawing a M/L versus color evolutionary track for the rest-frame NIR. The burst that we superposed on the τ_{300} model after 2.5 Gyr is again contributing 20% to the mass over a period of 100 Myr. Note that the scale is identical to that of Figure 5.8. The $(V-J)_{rest}$ histogram of sources at $2 < z < 3.5$ is derived from observed near- to mid-infrared wavelengths. During the first gigayear, the $V-J$ color hardly changes whereas M/L_J does by a factor of 7. As an immediate consequence, the translation of $V-J$ into M/L_J is highly uncertain for the blue galaxies in our sample and the additional IRAC observations do not improve the constraints on the mass-to-light ratio. The situation is further complicated by the effect of dust. $V-J$ is a lot more sensitive to dust than M/L_J, illustrated by the dust vector of $A_V = 1$ mag. The effects of dust and age no longer conspire to give robust mass estimates at a given $V-J$ color. At redder $V-J$ the situation improves as the slope of the age track flattens. Here the inclusion of a rest-frame NIR color clearly reduces the uncertainty in stellar M/L that stems from the poor knowledge of the star formation history. The loop toward bluer colors is a magnitude smaller in size and we see no large offsets in M/L between the one- and two-component modeling.

We have discussed the different behavior of dust and age in simplified one- and two-component models and have investigated the improvements expected from the inclusion of the rest-frame NIR with respect to the rest-frame optical. While additional rest-frame NIR data can lead to better M/L estimates, in particular for redder galaxies ($U-V > 1$; $V-J > 0.4$), it is clear that we need to take advantage of the full U-to-8 μm SED information to derive reliable estimates of stellar mass, stellar age and dust content.

5.5.1.2 Model dependence: Bruzual & Charlot vs Maraston

It is important to note that different stellar population synthesis models do not paint a consistent picture of evolution in the rest-frame NIR. To illustrate, we compare BC03 models to M05 models under the same assumption of Salpeter initial mass function and solar metallicity.

Whereas the age track in a M/L_V versus $U-V$ diagram behaves similarly for M05 and BC03, the NIR evolution of a τ_{300} model looks very different (see Fig. 5.10). The grey dashed line represents the age track of a BC03 τ_{300} model with superposed burst at 2.5 Gyr as described in §5.5.1.1. In black we overplot the age track of a two-component model with identical parameters by M05. In the $0.2-2$ Gyr age range the two models look strikingly different. At the same $V-J$ color the M05 model predicts M/L_J values that are up to a factor 2.5 smaller than those of the BC03 model. The offset between M/L_J as predicted from one- and two-component modeling is also larger by a similar factor. The BC03 and M05 models differ in several aspects: the stellar evolutionary tracks adopted to construct the isochrones, the synthesis technique and the

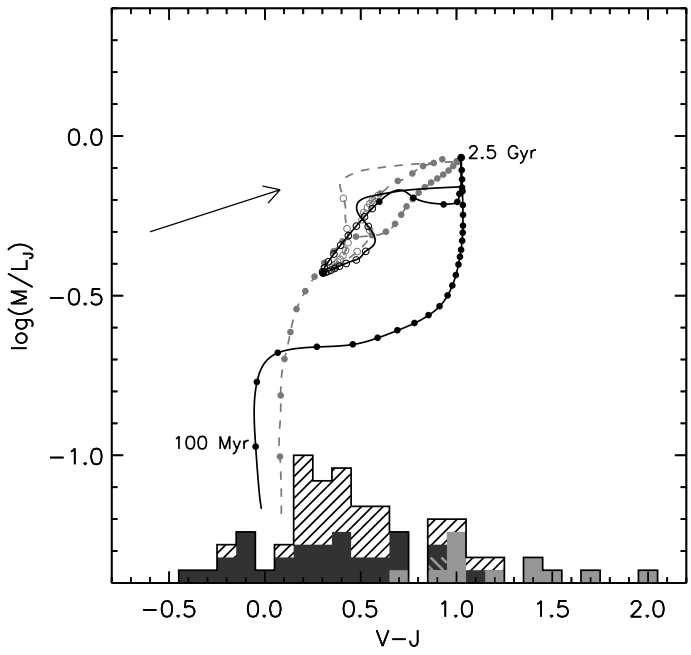

Figure 5.10 — Evolutionary track of two-component stellar populations in the M/L_J vs $V-J$ plane based on BC03 (*grey dashed line*) and M05 (*black solid line*) models. For ages between 0.2 and 2 Gyr, the M05 model predicts much lower M/L_J values than the BC03 model. The underestimate of M/L_J as derived from one-component modeling is therefore much more severe for the M05 model than for the BC03 model, and the inclusion of rest-frame NIR data does not necessarily improve constraints on stellar M/L.

treatment of the thermally pulsating Asymptotic Giant Branch (TP-AGB) phase. The Padova stellar tracks (Fagotto et al. 1994) used by BC03 include a certain amount of convective-core overshooting whereas the Frascati tracks (Cassisi et al. 1997) do not. The two stellar evolutionary models also differ for the temperature distribution of the red giant branch phase. The higher NIR luminosity originates mainly from a different implementation of the Thermally Pulsating Asymptotic Giant Branch (TP-AGB) phase (M05). Following the fuel consumption approach, M05 finds that this phase in stellar evolution has a substantial impact on the NIR luminosity at ages between 0.2 and 2 Gyr. BC03 follow the isochrone synthesis approach, characterizing properties of the stellar population per mass bin. The latter method leads to smaller luminosity contributions by TP-AGB stars. We refer the reader to recent studies from M05, van der Wel et al. (2006) and Maraston et al. (2006) for discussions of the model differences in greater detail.

For our purpose it is sufficient to state that a given $V-J$ color corresponds to younger ages, lower mass-to-light ratios and thus lower masses for the M05 model than for the BC03 model. Most importantly, we note that for M05 models inclusion of NIR data does not reduce stellar mass uncertainties caused by the unknown star formation history.

5.5.2 Constraints on mass, dust and age from modeling our observed galaxies

5.5.2.1 Wavelength dependence: optical versus near-infrared

Having investigated the qualitative relationship between M/L and the rest-frame optical-to-NIR color in §5.5.1.1, we now quantify the effect of inclusion of IRAC MIR photometry on the stellar population constraints of galaxies at $2 < z < 3.5$. Our goal is to investigate whether and how the addition of IRAC imaging changes our best estimate of the stellar population properties and their confidence intervals.

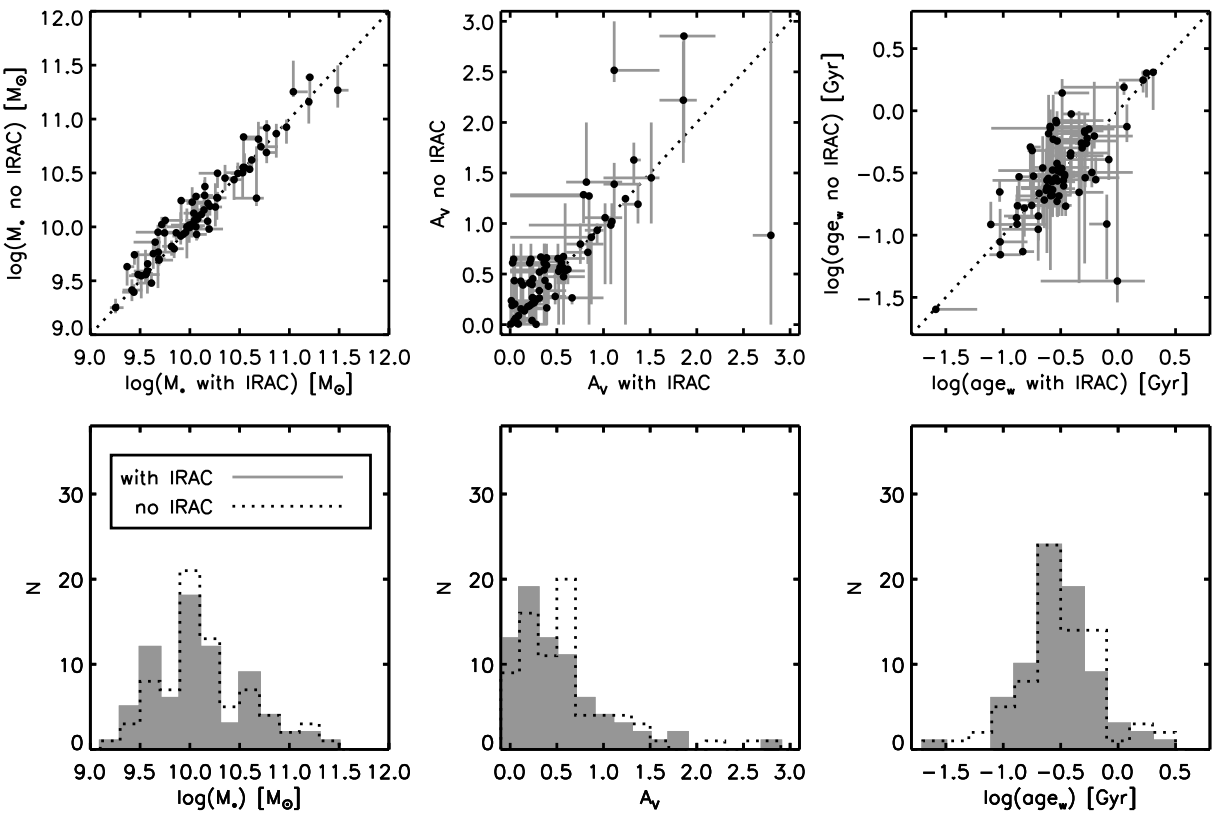

Figure 5.11 — *Top row:* Comparison of best-fit stellar masses, dust extinctions and mass-weighted ages for galaxies at $2 < z < 3.5$ when fit with IRAC photometry or without. The error bars are based on Monte Carlo simulations given the photometric errors. *Bottom row:* Corresponding histograms with IRAC photometry (*filled*) or without (*dashed*). No significant change in the overall distributions is observed, but the best-fit properties of individual galaxies may change substantially.

First we compare the distribution of stellar mass, dust content and mass-weighted stellar age as fit with or without IRAC. The top row of Figure 5.11 shows a direct comparison of the inferred model parameters with or without IRAC photometry for all galaxies at $2 < z < 3.5$. The filled histogram in the bottom row of Figure 5.11 shows the distribution of mass, dust extinction and age derived from the full U-to-8 μm SED. The dotted line indicates the distribution of best-fitting parameters from modeling the U-to-K photometry. Both the median and the width of the distribution stays the same for all three parameters. Defining the difference between mass, mass-weighted age, and A_V as $\Delta\log(M) = \log(M_{withIRAC}) - \log(M_{noIRAC})$, $\Delta A_V = A_{V,withIRAC} - A_{V,noIRAC}$, and $\Delta\log(age_w) = \log(age_{w,withIRAC}) - \log(age_{w,noIRAC})$ we find a median and normalized median absolute deviation (equal to the rms for a gaussian distribution) $[\hat{x}, \sigma_{NMAD}(x)]$ of $(-0.007 \pm 0.009,\ 0.07)$, $(0.00 \pm 0.03,\ 0.30)$, and $(0.00 \pm 0.02,\ 0.16)$ respectively. The average and standard deviation $[\langle x\rangle; \sigma(x)]$ of $\Delta\log(M)$, ΔA_V and $\Delta\log(age_w)$ are $(-0.04 \pm 0.02; 0.13)$, $(-0.08 \pm 0.04; 0.36)$ and $(-0.02 \pm 0.03; 0.28)$ respectively. Thus the differences for the galaxy sample as a whole after including IRAC are very small. The results for stellar mass are similar to what Shapley et al. (2005) found for a more specific sample of optically selected star-forming galaxies at $z \sim 2$.

Having determined that the overall distribution of best-fit age, dust content and

stellar mass does not change after including IRAC, the question remains whether IRAC helps to improve the constraints on the stellar population characeristics for individual galaxies. We address this question using the measure $\sigma_{noIRAC}/\sigma_{withIRAC}$, defined as the ratio of confidence intervals without and with IRAC. The 1σ confidence intervals, representing random uncertainties propagating from photometric errors, are derived from Monte Carlo simulations. For each galaxy SED we create 100 mock SEDs where the flux-point in each band is randomly drawn from a Gaussian with the measured flux as the mean, and its error as the standard deviation. Next, each SED was fitted with the same fitting procedure as the observed version. As we want to isolate the effect of including IRAC observations on the confidence intervals we fix the redshift to z_{phot} (or z_{spec} where available). In calculating $\sigma_{noIRAC}/\sigma_{withIRAC}$ we measure the confidence interval in log-space for stellar mass and mass-weighted age and in magnitude for A_V. Furthermore we set a lower limit to the confidence intervals to account for the discreteness of our models, i.e., age and A_V steps.

Figure 5.12 shows the values of $\sigma_{noIRAC}/\sigma_{withIRAC}$ for mass, age and dust content as a function of rest-frame $(U-V)_{rest}$ color for the galaxies at $2 < z < 3.5$. We divide the sample into a blue and red bin and indicate the median reduction of confidence intervals for each bin with dashed lines. The separation between blue and red is chosen to be $(U-V)_{rest} = 1$, corresponding to the oberved $(J-K)_{Vega} > 2.3$ color cut for Distant Red Galaxies at the median redshift of our sample $z = 2.66$. We find that the typical improvement of confidence intervals is dependent on galaxy color for all considered stellar population parameters. For red galaxies, the reduction amounts to a median factor of 2.7, 1.7 and 2.9 in the case of stellar mass, A_V and age respectively. For blue galaxies the reduction of the mass confidence interval is only a factor 1.3, though with a large scatter, while for A_V and age no median reduction is found. With the color tracks of the stellar population models in mind (see Figs. 5.8-5.9) this color dependence should come as no surprise. We demonstrated in §5.5.1.1 that for blue galaxies optical to NIR colors are degenerate with the mass-to-light ratio. Hence, the IRAC bands of blue galaxies contribute little information about their mass.

For a sample of (generally blue) optically selected star-forming galaxies at $z \sim 2$ Shapley et al. (2005) found a reduction in stellar mass uncertainties by a factor $1.5-2$ due to the addition of IRAC photometry, which seems like a contradiction. However, the distribution of observed $R-K$ color of their galaxies extends toward redder colors than the Lyman-break galaxies (LBGs) in our sample, which may partly explain the larger improvement than we find for blue LBGs. Another important difference is that Shapley et al. (2005) lacked J and H images and hence did not probe rest-frame $U-B$ or $U-V$ for their galaxies. It is possible that the lack of the near infrared J and H bands in Shapley et al. (2005) is the main reason for the discrepancy. We simulated this effect by omitting J and H and repeating the Monte Carlo simulations with and without IRAC. The median reduction of the 1σ mass confidence interval now increases to a factor 1.9 when including IRAC.

We conclude that, in the presence of very deep observed J, H, and K photometry, inclusion of mid-infrared data places little extra constraints on the stellar populations of blue galaxies. However, for galaxies redder than $(U-V)_{rest} = 1$, IRAC reduces the confidence interval by a substantial factor $2.5-3$.

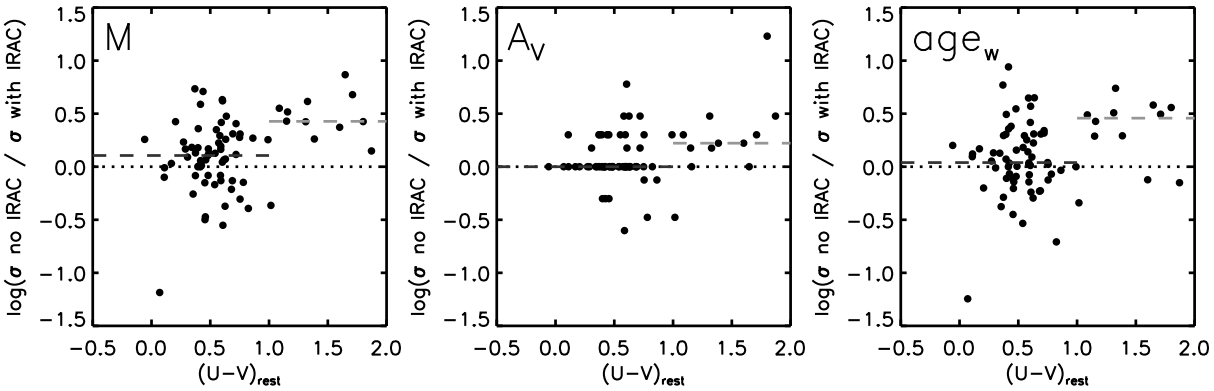

Figure 5.12 — Tightening of the confidence interval around best-fit stellar mass, age and dust extinction as a function of rest-frame $U-V$ color for galaxies at $2 < z < 3.5$. The median improvement after including the IRAC photometry is a factor 2.7 for red galaxies [$(U-V)_{rest} > 1$], significantly larger than the factor 1.3 for blue galaxies [$(U-V)_{rest} < 1$]. A similar color-dependence is found for constraints on age and dust extinction.

Table 5.5. Differences between stellar population properties derived from BC03 and M05

	median(Δ_{BC03_M05})	$\sigma_{NMAD}(\Delta_{BC03\_M05})$	mean(Δ_{BC03_M05})	$\sigma(\Delta_{BC03\_M05})$
$\log(M_*)$	0.14 ± 0.01	0.06	0.15 ± 0.01	0.08
A_V	-0.20 ± 0.00	0.00	-0.18 ± 0.02	0.19
$\log(Age_w)$	0.29 ± 0.02	0.17	0.34 ± 0.02	0.18

5.5.2.2 Model dependence: Bruzual & Charlot vs Maraston

In §5.5.1.2 we pointed out strong differences in the rest-frame optical-to-NIR colors between the BC03 and M05 models. In this paragraph we quantify how our results change if we use M05 models. The median and normalized median absolute deviation, average and standard deviation of the differences between BC03 fits and M05 fits [$\Delta\log(M)_{BC03\_M05}$, $\Delta A_{V,BC03\_M05}$ and $\Delta\log(age_w)_{BC03\_M05}$] are summarized in Table 5.5.

As expected, the BC03 models predict older ages and thus higher stellar masses than the M05 models for our $z = 2 - 3.5$ galaxies. The estimated mass for the M05 models is systematically lower by a factor 1.4. Maraston et al. (2006) found a similar discrepancy for a sample of 7 galaxies in the Hubble Ultra Deep Field that satisfy the BzK criterion (Daddi et al. 2004) for $z > 1.4$ passively evolving galaxies. Apart from a systematic shift a scatter of 0.1 in dex is found in $\Delta\log(M)_{BC03\_M05}$, meaning the choice of stellar population synthesis model introduces a considerable systematic uncertainty.

It is of great importance to test whether $\Delta\log(M)_{BC03\_M05} = \log(M_{BC03}) - \log(M_{M05})$ correlates with redshift, color or stellar mass, since such dependencies, if present, could bias studies of galaxy evolution or trends with mass. In Figure 5.13 we plot $\Delta\log(M)_{BC03\_M05}$ versus redshift, $(U-V)_{rest}$ color, and stellar mass (the latter derived from BC03 models). We show galaxies with $L_V > 5 \times 10^9 L_\odot$ at $1 < z < 2$ (*open symbols*) and at $2 < z < 3.5$ (*filled symbols*); no evidence for a redshift dependence is found.

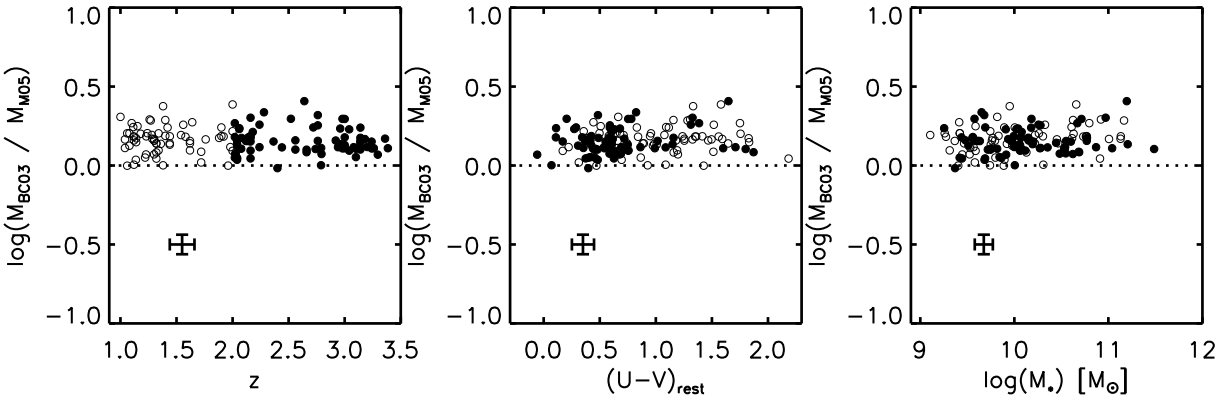

Figure 5.13 — Difference between best-fit stellar mass as derived from BC03 and M05 models as a function of redshift, $(U-V)_{rest}$ color and BC03 stellar mass for galaxies with $L_V > 5 \times 10^9 L_\odot$ at $1 < z < 2$ (*open symbols*) and $2 < z < 3.5$ (*filled symbols*). The stellar masses derived from BC03 models are systematically higher than those derived from M05 models by a factor 1.4. The scatter in $\log(M_{BC03}/M_{M05})$ is 0.1 in dex. No significant dependence of $\log(M_{BC03}/M_{M05})$ on redshift, $(U-V)_{rest}$ color or stellar mass is found. The bias introduced by the choice of stellar population synthesis model amounts to a maximum of 15% over the whole $(U-V)_{rest}$ color or stellar mass range of our sample.

For the $(U-V)_{rest}$ (*middle panel*) and stellar mass (*right*) panel, the p-values for statistical significance from the Spearman rank order correlation test are also larger than 0.05, meaning no significant correlation is found. Fitting a line to the points in the $\Delta\log(M)_{BC03\_M05}$ versus $(U-V)_{rest}$ diagram, a difference of 0.06 dex in $\Delta\log(M)_{BC03\_M05}$ is found over the 2 mag range in $(U-V)_{rest}$ color spanned by the galaxies in our sample. Even if a trend of increasing $\Delta\log(M)_{BC03\_M05}$ with redder $(U-V)_{rest}$ color is real, it only introduces a small bias of the order of 15%. A similar conclusion can be drawn for the dependence on stellar mass.

5.5.2.3 Metallicity dependence

We test how variations from solar metallicity affect the estimates of stellar mass, mass-weighted age and dust extinction. We study the effect of a different metal abundance by fitting BC03 templates with metallicity $Z = 0.2\ Z_\odot$ to the observed SEDs, leaving the extinction law to Calzetti et al. (2000). NIR spectroscopy of DRGs (van Dokkum et al. 2004) and LBGs (Erb et al. 2006a) indicates that a range of $Z = 0.2 - 1\ Z_\odot$ is appropriate for galaxies at $2 < z < 3.5$. Furthermore, at metallicities below $Z = 0.2\ Z_\odot$ the tracks and spectral libraries used to build the BC03 templates become more uncertain by lack of observational constraints. Decreasing the metallicity from $Z = Z_\odot$ to $Z = 0.2\ Z_\odot$ lowers the estimated stellar masses of galaxies at $2 < z < 3.5$ by 0.1 dex, leads to a mass-weighted age that is typically lower by 0.2 dex, and is compensated by an average increase in A_V of 0.2 mag. The fact that age estimates are more strongly affected than estimates of stellar mass when changing the assumed metallicity was demonstrated in detail by Worthey (1994). While absolute values of ages and dust extinctions may be biased as just described, the relative age and dust trends within the galaxy population as discussed in §5.4 based on the standard SED modeling (see §5.3) are robust.

5.5.2.4 Dependence on extinction law

The Calzetti et al. (2000) extinction law was empirically derived from observations of local starburst galaxies. We quantify the variations in stellar population properties due to the adopted extinction law by comparing our modeling results with a Calzetti et al. (2000) law to those obtained with reddening laws from Fitzpatrick (1986) for the Large Magellanic Cloud (LMC) and Prévot et al. (1984) for the Small Magellanic Cloud (SMC), leaving the metallicity to solar. Stellar masses, mass-weighted ages and A_V values of galaxies at $2 < z < 3.5$ derived with the LMC law models are similar to those obtained with the Calzetti et al. (2000) law. The SMC law, which rises more steeply toward shorter wavelengths in the near-UV, gives similar mass estimates, A_V values that are on average smaller by 0.3 mag and mass-weighted stellar ages that are older by 0.23 dex, with the ages of the oldest galaxies being limited by the age of the universe constraint. As for metallicity, we conclude that using a different extinction law has a larger impact on the age estimates than on estimates of stellar mass.

5.6 Stellar mass - optical color relation

In this section we study the relation between the rest-frame optical color of high-redshift galaxies and their stellar mass. We start with a model-independent approach in Figure 5.14, plotting rest-frame $(U-V)_{rest}$ versus rest-frame J_{rest} magnitude for all galaxies at $2 < z < 3.5$. The emission of low mass long-lived stars that make up the bulk of the mass in a galaxy peaks in the rest-frame NIR. J_{rest} is therefore expected to be a reasonably good tracer of stellar mass. The galaxies that satisfy the DRG selection criterion (*light-grey circles*) are found at redder $(U-V)_{rest}$ than the Lyman-break galaxies (*dark-grey circles*). The reddest $(U-V)_{rest}$ colors are found at the brightest J_{rest} magnitudes. Note however that the observed trend is partially driven by the K-band selection of our sample. The line on Figure 5.14 indicates at which magnitude a galaxy with identical colors to our observed galaxies would fall out of the sample. Even if we only consider galaxies brighter than the limiting $J_{rest} = -21.5$ to which we are complete over the whole $(U-V)_{rest}$ color range, we find that galaxies redder than $(U-V)_{rest} = 1$ are 1 mag brighter than galaxies with $(U-V)_{rest} < 1$, significant at the 3σ level. Studying a sample without color bias (as advocated by van Dokkum et al. 2006) proves crucial to pick up the trend of $(U-V)_{rest}$ with J_{rest}. We note that Meurer et al. (1999) found that LBGs with higher rest-frame UV luminosities tend to have redder rest-frame UV colors, illustrating that, while trends of color with luminosity are most notable in samples without color bias, they are still present in at least some color selected samples.

If J_{rest} is a reasonable tracer of stellar mass, we expect to see a similar or stronger trend of $(U-V)_{rest}$ with the stellar mass. This is shown in Figure 5.15. The plotted mass is derived from one-component SED modeling of the U-to-8 μm SED as described in §5.3. The typical error bar is indicated in the bottom left corner. The depth of our K detection band allows us to probe stellar masses from $3 \times 10^{11}\ M_\odot$ down to $2 \times 10^{9}\ M_\odot$. A correlation of $(U-V)_{rest}$ with stellar mass is clearly visible. The most massive galaxies have a red optical color. LBGs and other blue galaxies at high redshift contain typically 5 times less stellar mass than the DRGs in our sample. Again the K-band

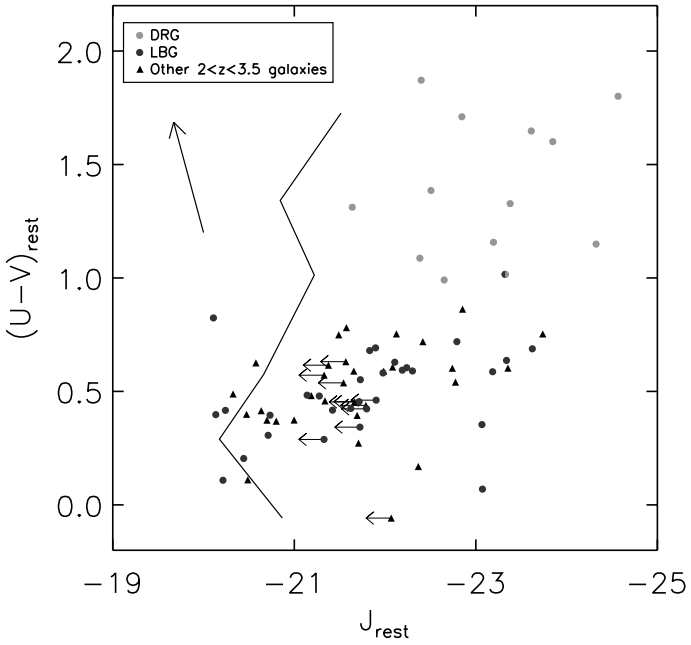

Figure 5.14 — Rest-Frame $U - V$ color versus absolute J magnitude for galaxies at $2 < z < 3.5$. Lyman-break galaxies are plotted with dark-grey circles. DRGs (*light-grey circles*) populate the red side of the $U - V$ color distribution. Black symbols denote those objects that do not meet either criteria. The solid line marks the K-band selection of our sample. The dust vector indicates an extinction of $A_V = 1$ mag. The most luminous galaxies in the rest-frame NIR have redder rest-frame optical colors than fainter galaxies.

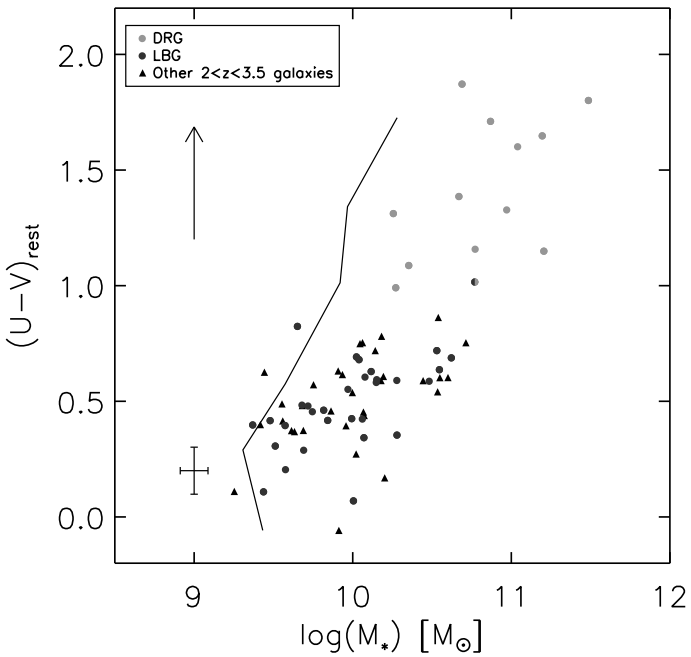

Figure 5.15 — Rest-Frame $U - V$ color versus stellar mass for galaxies at $2 < z < 3.5$. DRGs are marked with light-grey circles, LBGs with dark-grey circles. The K-band selection of our sample is indicated by the solid line. The dust vector indicates an extinction of $A_V = 1$ mag. Low-mass galaxies with red colors might exist, but would not enter the sample. The most massive galaxies have redder $U - V$ colors than less massive galaxies; notice the striking absence of massive blue galaxies.

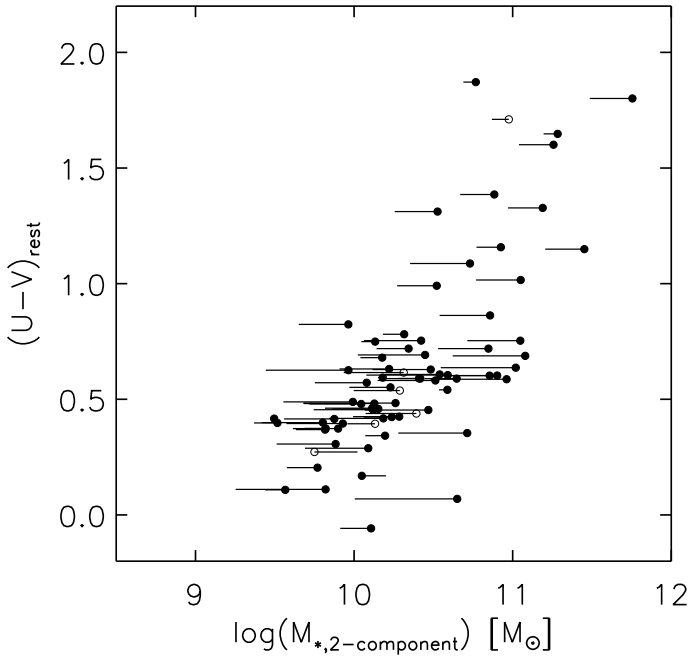

Figure 5.16 — Rest-Frame $U - V$ color versus stellar mass for galaxies at $2 < z < 3.5$ with complex star formation histories. For each object a vector starts at the best-fit mass from one-component SED modeling. The vector ends at an upper limit for the stellar mass as obtained by fitting two-component models. The two-component model is composed of a maximally old stellar population with a second burst of star formation during the last 100 Myr superposed. Empty symbols refer to objects for which $\chi^2_{red,two-component} - \chi^2_{red,one-component} > 2$ for all considered burst fractions. The mass that is plotted here corresponds to the burstfraction that gave the lowest χ^2_{red}. The typical amount of mass that can be hidden under the glare of a young secondary burst is on average larger for blue than for red galaxies. Nevertheless, even allowing for more complex star formation histories than one-component models a lack of massive blue galaxies remains visible.

selection of our sample (*solid line*) limits our ability to detect faint red galaxies. Therefore we can not exclude the presence of low-mass red galaxies. The lack of massive blue galaxies seems to be real. Rigopoulou et al. (2006) find a co-moving density of $\Phi = (1.6 \pm 0.5) \times 10^{-5}\, Mpc^{-3}$ for LBGs with $M > 10^{11} M_{\odot}$ at an average redshift $\langle z \rangle \simeq 3$, consistent with the absence of such massive but rare LBGs in our sample.

However, the lack of massive blue galaxies could be an artifact of our choice of simple star formation histories. As demonstrated in §5.5.1.1 a severe underestimate of the stellar mass is possible when the true star formation history is more complex than that of the modeled one-component stellar population. When a young burst of star formation is superposed on a maximally old population, its blue light will dominate the $(U - V)_{rest}$ color and the mass from the underlying population will be hidden. In order to constrain the possible underestimate in mass, we fit two-component models to our SEDs. Erb et al. (2006b) describe a procedure to achieve this in two steps, where first a maximally old population is fit to the K(+IRAC) data and subsequently a young population is fit to the (primarily UV) residual. However, this procedure does not guarantee a good fit in the χ^2 sense. Instead, we decided to perform a simultaneous fit of both old and young components. We constructed template SEDs consisting of

a maximally old single stellar population with a recent burst of star formation that started 100 Myr ago and lasted till the moment of observation superposed. We made templates where the mass fraction created in the burst is 2^x with x going from -6 to 2 in steps of 1. We assume that the same reddening by dust applies to the old and the young population, with A_V ranging from 0 to 3 in steps of 0.2. Without this assumption, one could in principle hide an infinite amount of mass in an old population as long as an optically thick medium is shielding it from our sight. However, such a scenario is physically implausible. Since we are interested in an upper limit on the mass, as opposed to the most likely value, we do not search for the least-squares solution over all x. Instead we perform the fit for every burst fraction and select the highest mass that still has $\Delta\chi^2_{red} = \chi^2_{red,two-component} - \chi^2_{red,min,one-component} < 2$.

Fitting the two-component models to the U-to- 8 μm SEDs of our galaxy sample at $2 < z < 3.5$, we indeed see that a higher stellar mass is allowed when more complex star formation histories are adopted (Fig. 5.16). The upper bound on stellar mass that we derive from this particular two-burst model is in the median a factor 1.7 higher than the one-component estimate for galaxies redder than $(U-V)_{rest} = 1$. For blue galaxies the median increase is a factor 2.1. Despite the fact that more mass can be hidden in blue galaxies, a trend of optical color with stellar mass remains visible. We performed a Mann-Whitney U-test to compare the $(U-V)_{rest}$ colors of galaxies with different stellar mass. We conservatively adopted the one-component stellar mass for galaxies with $(U-V)_{rest} > 1$ and the two-component upper limit for objects with $(U-V)_{rest} < 1$. To avoid selection effects we only consider galaxies more massive than $M = 10^{10}\ M_\odot$. Dividing them in two mass bins with an equal number of objects the Mann-Whitney U-test (Walpole & Myers 1985) confirms at a 99% significance level that the mean of the $(U-V)_{rest}$ distributions differs. Applying the same two-component models to the U-to-K SEDs (omitting IRAC), the median upper mass estimate increases to a factor 2.3 above the one-component estimate for red objects and a factor 3.7 for blue objects. We conclude that, as expected from §5.5.1.1, more mass can be hidden in blue than in red galaxies, but this effect is insufficient to remove the trend of stellar mass with color. Furthermore, the amount of mass that can be hidden is constrained by addition of IRAC photometry.

The color dependence that we derive for the amount of mass that can be hidden in an underlying old population confirms findings from Shapley et al. (2005) based on a sample of star-forming galaxies at $z \sim 2$. The predominance of distant red galaxies at the high-mass end was illustrated recently by van Dokkum et al. (2006) using a mass-selected sample of galaxies at $2 < z < 3$ with $M > 10^{11}\ M_\odot$. Only with very deep imaging such as that of the HDFS analyzed in this chapter it is possible to probe down to lower masses and prove that the most massive galaxies have red $(U-V)_{rest}$ colors compared to lower mass galaxies.

5.7 Summary

We investigated the rest-frame optical to NIR color distribution of galaxies up to $2 < z < 3.5$ in the Hubble Deep Field South. At all redshifts, galaxies with redder $(U-V)_{rest}$ tend to have redder $(V-J)_{rest}$, as is the case in the local universe. At $(U-V)_{rest}$ colors

comparable to that of local galaxies, the color distribution of distant galaxies extends to redder $(V-J)_{rest}$. At $(U-V)_{rest} > 1$ the population of galaxies at the red $(V-J)_{rest}$ end is well described by dust-enshrouded star-forming models, whereas galaxies with $(V-J)_{rest}$ similar to that of local galaxies are consistent with old passively evolving systems. We conclude that $(U-V)_{rest}$ alone allows us to isolate blue relatively unobscured star-forming galaxies, but addition of $(V-J)_{rest}$ is necessary to distinguish young dusty from old passively evolved systems. At redshifts above $z = 1$, this means IRAC observations are crucial in understanding the wide variety in stellar populations. We note that our analysis is not subject to uncertainties due to field-to-field variations, but surveys over much larger areas are needed to study the relative contributions of galaxies with different stellar populations.

We analyzed the constraints that IRAC places on stellar mass, stellar age and dust content of galaxies at $2 < z < 3.5$. No evidence is found for systematic offsets when determining the stellar population characteristics with or without IRAC. However, the ratio of confidence intervals on stellar mass, mass-weighted age and dust extinction is typically reduced by a factor 2.7, 2.9 and 1.7 respectively for red $[(U-V)_{rest} > 1]$ galaxies. In general, IRAC does not provide stronger constraints for blue galaxies $[(U-V)_{rest} < 1]$ when very deep NIR imaging is available (as is the case for the HDFS).

We caution that, in characterizing the stellar populations using M05 models, we find stellar masses that are typically a factor 1.4 lower than for BC03 models with a scatter of 0.1 in dex.

A trend of brighter J_{rest} with redder $(U-V)_{rest}$ is observed for galaxies at $2 < z < 3.5$, where the NIR luminosity serves as a (imperfect but model-independent) tracer for stellar mass. Plotting $(U-V)_{rest}$ versus modeled stellar mass, we arrive at a similar conclusion: the most massive galaxies in our sample have red rest-frame optical colors. A possible concern is that this trend with mass is caused by our simplistic choice of star formation histories. When we allow for more complex star formation histories, more mass can be hidden than in the case of a one-component stellar population and the amount depends on the color of the galaxy. We used two-component stellar populations, consisting of a maximally old population with a young population superposed, to set an upper bound on the stellar mass present. Even though relatively more mass can be hidden in blue galaxies compared to red galaxies, under the assumption of an equal dust reddening of the young and old component, a trend of $(U-V)_{rest}$ increasing to redder colors with stellar mass remains visible.

Acknowledgments

This research was supported by a grant from the Netherlands Foundation for Research (NWO), and the Leids Kerkhoven-Bosscha Fonds. The authors would like to thank Carnegie Observatories and the Lorentz Center for its hospitality during working visits and workshops. Support from NASA LTSA grant NNG04GE12G is gratefully acknowledged.

References

Adelman-McCarthy, J. K. et al. 2006, ApJS, 162, 38
Angeretti, L., Tosi, M., Greggio, L., Sabbi, E., Aloisi, A.,& Leitherer, Claus 2005, AJ, 129, 2203
Baldry, I. K., Glazebrook, K., Brinkmann, J., Ivezić, Ž., Lupton, R. H., Nichol, R. C.,& Szalay, A. S. 2004, ApJ, 600, 681
Bell, E. F.,& de Jong, R. S. 2001, ApJ, 550, 212
Blanton, M. R., et al. 2003, ApJ, 594, 186
Blanton, M. R., et al. 2005, AJ, 129, 2562
Bolzonella, M., Miralles, J.-M.,& Pelló, R. 2000, A&A, 363, 476
Bruzual, G.,& Charlot, S. 2003, MNRAS, 344, 1000 (BC03)
Bundy, K., Ellis, R. S.,& Conselice, C. J. 2005, ApJ, 625, 621
Calzetti, D., et al. 2000, ApJ, 533, 682
Cassisi, S., Castellani, M.,& Castellani, V. 1997, A&A, 317, 108
Coleman, G. D., Wu, C.-C.,& Weedman, D. W. 1980, ApJS, 43, 393
Cutri, R. M., et al. 2000, The 2MASS Explanatory Supplement (Pasadena: IPAC), http://www.ipac.caltech.edu/2mass/releases/allsky/doc/explsup.html
Daddi, E., Cimatti, A., Renzini, A., Fontana, A., Mignoli, M., Pozzetti, L., Tozzi, P.,& Zamorani, G. 2004, ApJ, 617, 746
De Lucia, G., Springel, V., White, S. D. M., Croton, D.,& Kauffmann, G. K. 2006, MNRAS, 366, 499
Drory, N., Salvato, M., Gabasch, A., Bender, R., Hopp, U., Feulner, G.,& Pannella, M. 2005, ApJ, 619, 131
Erb, D. K., et al. 2003, ApJ, 591, 101
Erb, D. K., Shapley, A. E., Pettini, M., Steidel, C. C., Reddy, N. A.,& Adelberger, K. L. 2006a, ApJ, 644, 813
Erb, D. K., Steidel, C. C., Shapley, A. E., Pettini, M., Reddy, N. A.,& Adelberger, K. L. 2006b, ApJ, 646, 107
Fagotto, F., Bressan, A., Bertelli, G.,& Chiosi, C. 1994, A&AS, 104, 365
Fazio, G. G., et al. 2004, ApJS, 154, 10
Ferguson, H. C., Dickinson, M., Papovich, C. 2002, ApJ, 569, 65
Fitzpatrick, E. L. 1986, AJ, 92, 1068
Förster Schreiber, N. M., et al. 2003, ApJ, 599, 193
Förster Schreiber, N. M., et al. 2004, ApJ, 616, 40
Franx, M., et al. 2003, ApJ, 587, L79
Freeman, K.,& Bland-Hawthorn, J., 2002, ARA&A, 40, 487
Glazebrook, K., et al. 2004, Nature, 430, 181
Hora, J. L., et al. 2004, Proc. SPIE, 5487, 77
Kauffmann, G., et al. 2003, MNRAS, 341, 54
Kriek, M., et al. 2006, ApJ, 645, 44
Kinney, A. L., et al. 1996, ApJ, 467, 38
Labbé, I., et al. 2003, AJ, 125, 1107
Labbé, I., et al. 2005, ApJ, 624, L81
Lancon, A., et al. 2001, ApJ, 552, 150
Madau, P., et al. 1996, MNRAS, 283, 1388
Maraston, C. 2005, MNRAS, 362, 799
Maraston, C., et al. 2006, ApJ, 652, 85
Meurer, G. R., Heckman, T. M.,& Calzetti, D. 1999, ApJ, 521, 64
Nagamine, K., Cen, R., Hernquist, L., Ostriker, J. P.,& Springel, V. 2005, ApJ, 627, 608
Papovich, C., Dickinson, M., & Ferguson, H. C. 2001, ApJ, 559, 620
Papovich, C., Dickinson, M., Giavalisco, M., Conselice, C. J.,& Ferguson, H. C. 2005, ApJ, 631, 101
Papovich, C., et al. 2006, ApJ, 640, 29
Prévot, M. L., Lequeux, J., Prévot, L., Maurice, E.,& Rocca-Volmerange, B. 1984, A&A, 132, 389
Rigopoulou, D., et al. 2006, ApJ, 648, 81
Rudnick, G., et al. 2001, AJ, 122, 2205
Rudnick, G., et al. 2003, ApJ, 599, 847
Rudnick, G., et al. 2006, ApJ, 650, 624

Salpeter, E. E. 1955, ApJ, 121, 161
Shapley, A. E., et al. 2001, ApJ, 562, 95
Shapley, A. E., et al. 2003, ApJ, 588, 65
Shapley, A. E., et al. 2005, ApJ, 626, 698
Smail, I., Chapman, S. C., Blain, A. W.,& Ivison, R. J. 2004, ApJ, 616,71
Somerville, R. S., Primack, J. R.,& Faber, S. M. 2001, MNRAS, 320, 504
Steidel, C. C., et al. 1996, ApJ, 462, L17
Steidel, C. C., et al. 1999, ApJ, 519, 1
Trager, S. C., Faber, S. M., Worthey, G.,& González, J. J. 2000, AJ, 120, 165
van der Wel, A., Franx, M., van Dokkum, P. G., Rix, H.-W., Illingworth, G. D.,& Rosati, P. 2005, ApJ, 631, 145
van der Wel, A., et al. 2006, ApJ, 652, 97
van Dokkum, P. G., et al. 2006, ApJ, 638, 59
Walpole, R. E.,& Myers, R. H. 1985, Probability and Statistics for Engineers and Scientists, 3^{rd} edition (Macmillan Publishing Company)
Webb, T. M., et al. 2006, ApJ, 636, 17
Werner, M. W., et al. 2004, ApJS, 154, 1
Worthey, G. 1994, ApJS, 95, 107
Yan, H., et al. 2004, ApJ, 616,63

Chapter 6

Recovering Stellar Population Properties and Redshifts from Broad-Band Photometry of Simulated Galaxies: Lessons for SED Modeling

Abstract. We present a detailed analysis of our ability to determine stellar masses, ages, reddening and extinction values of high-redshift galaxies by modeling broad-band SEDs with stellar population synthesis. In order to do so, we computed synthetic optical-to-NIR SEDs for model galaxies taken from hydrodynamical merger simulations placed at redshifts $1.5 \leq z \leq 2.9$. Viewed under different angles and during different evolutionary phases, the simulations represent a wide variety of galaxy types (disks, mergers, spheroids). The broad-band SEDs were then fed to a standard SED modeling procedure and resulting stellar population parameters were compared to their true values. We specifically analyze how well the SED modeling reproduces masses, ages, and extinction. Disk galaxies generally show a decent median correspondence between the true and estimated mass and age, albeit with a significant scatter ($\Delta \log M = -0.05^{+0.06}_{-0.13}$, $\Delta \log age_w = -0.04^{+0.26}_{-0.27}$). During the merger itself, we find larger offsets: $\Delta \log M = -0.11^{+0.09}_{-0.14}$ and $\Delta \log age_w = -0.11^{+0.34}_{-0.25}$. $E(B-V)$ values are generally recovered well, but the estimated total visual absorption A_V is consistently too low, increasingly so for larger optical depths ($\Delta A_V = -0.48^{+0.42}_{-0.45}$ in the merger regime). The masses, ages, $E(B-V)$, and A_V of simulated ellipticals are very well reproduced.

We discuss possible biases in SED modeling results caused by mismatch between the true and template star formation history, dust distribution, metallicity variations and AGN contribution. Mismatch between the real and template star formation history, as is the case during the merging event, drives the age, and consequently mass estimate, down with respect to the true age and mass. However, the larger optical depth toward young stars during this phase reduces the effect considerably. Finally, we tested the photometric redshift code EAZY on the simulated galaxies placed at high redshift. We find a small scatter in $\Delta z/(1+z)$ of 0.030 to 0.054, depending on the template set used.

S. Wuyts, T. J. Cox, N. M. Förster Schreiber, M. Franx,
P. F. Hopkins, L. Hernquist, B. Robertson & P. G. van Dokkum

6.1 Introduction

UNDERSTANDING the growth and aging of galaxies over cosmic time requires reliable estimates of their mass, formation epoch and star formation history. With the current generation of telescopes, stellar velocity dispersion measurements can probe the gravitational potential in which the baryonic galaxy content resides out to $z \sim 1.3$ (van Dokkum & Stanford 2003; Holden et al. 2005). Beyond this redshift, gas velocity dispersions can be measured from emission lines, but do not always trace the potential due to outflows (Franx et al. 1997; Pettini et al. 1998, 2001; Shapley et al. 2003), and would lead to biased samples missing quiescent galaxies lacking emission lines in their spectra (Kriek et al. 2006). For these reasons, most studies of high-redshift galaxies have used stellar mass estimates derived by modeling of the broad-band stellar energy distribution to characterize the mass.

Since age estimates from $H\alpha$ equivalent widths (van Dokkum et al. 2004; Erb et al. 2006c) or Balmer/4000Å break strengths (Kriek et al. 2006) are very demanding in terms of telescope time and only attainable for the brightest galaxies, stellar ages as well are commonly derived from broad-band photometry.

Over the past few years, SED modeling has been proven extremely valuable in characterizing the galaxy population in the early universe (e.g. Papovich et al. 2001; Shapley et al. 2001, 2005; Förster Schreiber et al. 2004). Nevertheless, a number of assumptions are required for the limited number of datapoints (11 passbands in our case, but often less) to lead to a single solution in terms of physical properties such as stellar mass, stellar age, dust extinction, and often redshift.

First, the star formation history (SFH) is generally modelled by a simple functional form: a single burst, constant star formation, or an exponentially declining model. In reality, high-redshift galaxies show evidence of more complex SFHs, often with brief recurrent episodes of star formation (e.g. Papovich et al. 2001; Ferguson et al. 2002; Papovich et al. 2005). Second, we use the approximation of a single foreground screen of dust in accounting for the attenuation, even though in reality the dust will be distributed in between the stars. Third, we fit solar metallicity models. Although consistent with the current metallicity estimates from near-infrared (NIR) spectroscopy of high-redshift galaxies (van Dokkum et al. 2004; Erb et al. 2006a), it must be kept in mind that these measurements are currently limited to the bright end of the galaxy population. Fourth, SED modeling generally assumes a purely stellar origin of the light, while observational evidence for a substantial fraction of low luminosity AGN at high redshift has been accumulating (van Dokkum et al. 2004; Reddy et al. 2005; Papovich et al. 2006; Kriek et al. 2006; Daddi et al. 2007). They may contribute to the optical SEDs.

Finally, one adopts a certain attenuation law, initial mass function (IMF), and stellar population synthesis code. Their appropriateness at low and high redshifts is much debated.

In this chapter, we address the impact of the first four assumptions (related to SFH, dust attenuation, metallicity, and AGN) using hydrodynamical simulations of merging galaxies (see Robertson et al. 2006; Cox et al. 2006). The SPH simulations follow the star formation on a physical basis, resulting in more complex SFHs than are allowed

in typical SED modeling. They keep track of the distribution and metallicity of gas and stellar particles, allowing a determination of the line-of-sight dependent extinction toward each stellar particle seperately and a knowledge of the stellar metallicity as a function of time. Here, we apply the same SED modeling that we use for observed galaxies to broad-band photometry extracted from the simulation outputs, and study how well the mass, age, and dust content of the simulated galaxies can be recovered.

The reason we use merger simulations for this exercise is threefold. First, galaxy mergers are believed to play an important role in galaxy evolution (see, e.g., Holmberg 1941; Zwicky 1956; Toomre & Toomre 1972; Toomre 1977), increasingly so at high redshift (see, e.g., Glazebrook et al. 1995; Driver, Windhorst,& Griffiths 1995; Abraham et al. 1996). Moreover, along their evolutionary path they are visible as vastly different galaxy types, allowing to test the recovery of stellar population parameters under a wide range of conditions: gas-rich star-forming disks, dust-obscured mergers, and quiescent spheroids. Finally, in Chapter 7 we will compare predictions of the color distribution and mass density of high-redshift galaxies derived from these simulations with the observed galaxy population in deep fields. A good understanding of what it is we measure with SED modeling is crucial in order to compare identical mass-limited samples of observed and simulated galaxies.

We start with a description of the simulations in §6.2. Next, we explain the methodology of our SED modeling in §6.3. §6.4 discusses how well we can measure stellar population properties when a spectroscopic redshift is available. §6.5 repeats the analysis, now leaving the redshift as an extra free parameter (i.e., fitting for the photometric redshift). Finally, we summarize the results in §7.11.

6.2 The simulations

6.2.1 Main characteristics

The simulations on which we test our SED modeling were performed by Robertson et al. (2006). We refer the reader to that paper for a detailed description of the simulations. Briefly, the simulations were performed with the parallel TreeSPH code GADGET-2 (Springel 2005). The code uses an entropy-conserving formulation of smoothed particle hydrodynamics (Springel & Hernquist 2002), and includes gas cooling, a multiphase model for the interstellar medium (ISM) to describe star formation and supernova feedback (Springel & Hernquist 2003), and a prescription for supermassive black hole growth and feedback (Springel et al. 2005b).

At the start, each simulation consists of 120000 dark matter particles, 80000 gas particles, and 80000 stellar particles. They represent two stable, co-planar disk galaxies, each embedded in an extended dark matter halo with Hernquist (1990) profile. We have realisations where the disks start with a gas fraction of 40% and 80%. Stellar masses at the start of the simulation varied from 7.0×10^9 $M_\odot$ to 2.3×10^{11} $M_\odot$ per disk galaxy. For a given virial velocity, the halo concentration, virial mass and virial radius were scaled following Robertson et al. (2006) to approximate the structure of disk galaxies at redshift $z = 3$. In practice, this means that the mass- and redshift-

dependent halo concentration measured by Bullock et al. (2001) was adopted:

$$C_{vir}(M_{vir}, z) \approx 9 \left(\frac{M_{vir}}{M_{coll,0}} \right)^{-0.13} (1+z)^{-1}, \tag{6.1}$$

where $M_{coll,0} \sim 8 \times 10^{12}\, h^{-1}\, M_{\odot}$ is the linear collapse mass at z=0, and that the following scaling relations were used for the virial mass and virial radius of the progenitors:

$$M_{vir} = \frac{V_{vir}^3}{10GH(z)} \tag{6.2}$$

$$R_{vir} = \frac{V_{vir}}{10H(z)}, \tag{6.3}$$

where V_{vir} is the virial velocity and $H(z)$ is the Hubble parameter.

We set the ages of the stars existing at the start of the simulation such as to represent a constant star formation history prior to the start of the simulation at a star formation rate (SFR) equal to that calculated in the first phases of the simulation. The corresponding stellar metallicities were then set according to the closed box model: $Z(t) = -y \ln[f_{gas}(t)]$, where $Z(t)$ is the metallicity of a stellar particle formed at time t, the yield y=0.02 and $f_{gas}(t)$ is the gas fraction of the system at the considered time. Similarly, the gas at the start of the simulation was assigned a uniform metallicity $Z_{gas}(t_S) = -y \ln[f_{gas}(t_S)]$ where t_S represents the start of the simulation, and $f_{gas}(t_S) = 0.4$ or 0.8 respectively for our 2 gas fraction runs. The closed box model represents an upper limit on the allowed enrichment by heavy elements, which in reality may be reduced by outflows or infall of metal-poor gas (Edmunds 1990). The fact that we consider 2 gas fractions guarantees a wide range of progenitor types, with ages of a few 100 Myr and $Z_{gas} = 0.004$ for $f_{gas} = 0.8$ to typical stellar ages of a Gyr and nearly solar gas metallicity for $f_{gas} = 0.4$.

The overall timespan covered by each simulation was 2 Gyr. Figure 6.1(a) illustrates a typical star formation history of one of the merger simulations. Figure 6.1(b) illustrates the build-up of stellar mass and Figure 6.1(c) presents the accretion history onto the black hole(s). We draw the time axis relative to the actual moment of merging, defined as the timestep when the two black hole particles become one, coinciding with the peak in the accretion history. Cross symbols indicate the snapshots, separated by 70 Myr, when all physical information was stored to disk.

As time progresses, the orderly rotation and star formation in the disks is disturbed by each others gravitational pull. The star formation history shows a first, but rather shallow, bump during the first passage of the disks. Next, gravitational torques enable the gas to loose angular momentum and flow to the centers where it triggers a starburst (Larson & Tinsley 1978; Noguchi 1988; Hernquist 1989; Barnes & Hernquist 1991, 1996; Mihos & Hernquist 1994, 1996). Meanwhile, part of the inflowing gas is fed to the central supermassive black holes (SMBHs). Once the SMBHs grow massive enough, they produce a luminous quasar (Sanders et al. 1988a,b; Hernquist 1989; Sanders & Mirabel 1996; Genzel et al. 1998) whose feedback halts subsequent star formation (Di Matteo et al. 2005; Springel et al 2005a), leaving a red spheroid galaxy as remnant (Robertson et al. 2006; Cox et al. 2006).

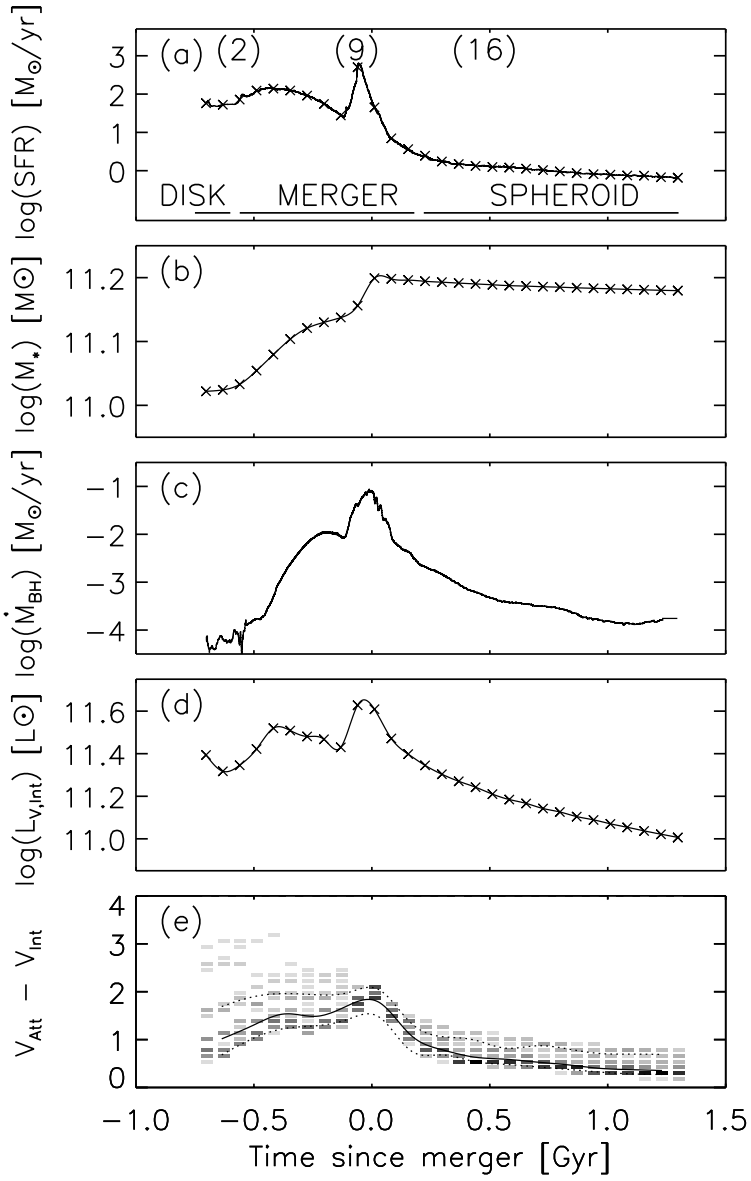

Figure 6.1 — Evolution of a typical merger simulation. (a) The star formation history, (b) the mass build-up, (c) the accretion rate history onto the black hole(s), (d) the evolution of the intrinsic (i.e., unattenuated) V-band luminosity, and (e) the binned distribution of effective visual extinctions (attenuated minus intrinsic V-band magnitude) corresponding to different viewing angles. A darker intensity indicates a larger number of viewing angles. The solid line represents the median evolution which peaks at the moment of actual merging. The dotted lines indicate the interval containing the central 68% of the viewing angles. The cross symbols in panels (a), (b) and (d) mark the sampling of snapshots when the full physical information of all SPH particles was stored to disk. After a first bump in the star formation rate during the first passage of the progenitors, a peak in star formation is reached for a brief period during which several hundreds of solar masses of gas are converted into stars. The typical extinction for a random line of sight is peaking around the same time. Shortly after, the accretion onto the supermassive black hole is maximal, coinciding with the merger between the two progenitor black holes.

6.2.2 Extracting photometry from the simulation output

The evolutionary path as outlined in §6.2.1 is followed by the GADGET-2 code at a fine time resolution ($\Delta t \sim 10^4$ *yr*). At sparser timesteps (70 Myr apart), the positions, masses, ages, and metallicities of all particles were stored. It is from these simulation snapshots that we derive the observed SEDs of the merger as a function of time.

The light a virtual observer would receive from the simulated merger, is composed of stellar and AGN emission, the latter only contributing significantly during a brief period of time. We ignore any contribution from emission lines produced by the gas content of the galaxies, possibly contributing on the order of 0.1 mag in the optical. Furthermore, we account for attenuation by interstellar dust and Lyman forest attenuation by the intervening medium between the redshifted galaxy and the observer following Madau (1995). The combination of these steps, described in this section, leads to observables that are similar to the real observations that we model with stellar population synthesis codes.

First, we focus on the computation of intrinsic (i.e., unattenuated) magnitudes from the stellar component. Each of the stellar particles is treated as a single stellar population characterized by its mass, age, and metallicity. We choose to use the Salpeter (1955) IMF, as was done in previous observational work (e.g. Förster Schreiber et al. 2004; Wuyts et al. 2007). We then interpolate the corresponding luminosity for each stellar particle from a grid of SSP templates with different ages and metallicities from the stellar population synthesis code by Bruzual & Charlot (2003, hereafter BC03). Figure 6.1(d) illustrates the evolution of the intrinsic rest-frame V-band luminosity for one of the simulations.

For the AGN emission, we scale a template SED by the bolometric black hole luminosity given by the simulation. The template SED was derived from the optically blue (i.e., unreddened) quasar sample by Richards et al. (2006) with locally attenuated light being reprocessed as an IR bump longward of $\lambda > 1$ μm. A full discussion of the AGN template is presented by Hopkins, Richards,& Hernquist (2007). In most of our analysis, we will consider the stellar light only. §6.4.4 addresses the impact AGN can have on the outcome of SED modeling during the brief period when its contribution to the total light is significant.

Galaxies, certainly in their actively star-forming phases, are not devoid of gas and dust. It is therefore crucial to account for the obscuring and reddening effect dust has on the stellar and AGN emission. We compute the optical depth along the line of sight toward each stellar particle. To do so, we compute the local gas density on a fine grid derived from the SPH formalism and the particle distribution (Hopkins et al. 2005a) and integrate out from each particle along the line of sight to large distance. The simulations are based on the GADGET multi-phase ISM model developed by Springel & Hernquist (2003). This model calculates the local mass fraction in the hot ($T = 10^5 - 10^7$ *K*, diffuse, partially ionized) and cold ($T = 10^3$ *K*, molecular and HI cloud core) phases of dense gas, assuming pressure equilibrium between the two phases. Following Hopkins et al. (2005b), the attenuation along the line of sight is then derived from the density of the hot-phase component only. The assumption that most of the lines of sight only pass through the hot-phase component provides effec-

tively a lower limit on the optical depths. We use a gas-to-dust ratio equal to that of the Milky Way, $(A_B/N_{HI})_{MW} = 8.47 \times 10^{-22}\ cm^2$, with a linear scaling factor accounting for gas metallicities deviating from solar: $A_B/N_{HI} = (Z/0.02)(A_B/N_{HI})_{MW}$. As default, we adopt the Calzetti et al. (2000) attenuation law for the wavelength dependence of the optical depth. Changes in the synthetic photometry when adopting a SMC-like or Milky Way-like attenuation law from Pei (1992) will be discussed in due time. The computation of optical depths was repeated for 30 viewing angles, uniformly spaced in solid angle $d\cos\theta d\phi$. Figure 6.1(e) presents the distribution of effective visual extinction values (attenuated minus intrinsic V-band magnitude) as a function of time since the merger. The extinction varies in the following way. In the early stages typical extinction values are modest, with the exception for a few lines-of-sights were the disks are seen edge-on. The overall extinction along all lines-of-sight reaches a peak during the merger-triggered starburst and drops to very low values after star formation has ceased.

Finally, in computing the observer-frame apparent magnitudes, we redshift the attenuated SED and convolve it with the same set of filtercurves that we have observations for in the Chandra Deep Field South (CDFS; Chapter 3). Here, we apply the depression factors $D_A(z)$ and $D_B(z)$ given by Madau (1995) for the Lyman forest attenuation of the continuum between Lyα and Lyβ and between Lyβ and the Lyman limit respectively. The flux blueward of the Lyman limit ($\lambda_L = 912$Å) was set to 0, as is done by the HYPERZ code (v1.1, Bolzonella et al. 2000) that we use for SED modeling.

In practice, it is computationally more convenient to interpolate the apparent magnitudes in a given passband for all stellar particles on a precompiled grid of BC03 apparent magnitudes at the redshift of interest. The internal dust attenuation is then applied using the value of the Calzetti et al. (2000) attenuation law at the effective wavelength for that passband. We tested that this method, as opposed to attenuating the full resolution BC03 spectrum and then convolving with the filtercurve, leads to photometric differences of at most a few percent.

We note that we never attempt to separate the light into the contribution from the two progenitors. Instead, we always study the total photometry, as if the merging system were unresolved.

6.2.3 The colors and SEDs of simulated and observed galaxies

Prior to analyzing the performance of our SED modeling procedure, it is important to confirm that the simulated galaxies have spectral shapes resembling those of real high-redshift galaxies in observed deep fields, thus validating their role as test objects. To this end, we indicate the binned color distribution of simulated galaxies, viewed from different angles and during different phases of their evolution, in a rest-frame $U-V$ versus $V-J$ color-color diagram. Labbé et al. (2005) first introduced the observed-frame equivalent of this diagram to illustrate the wide range of galaxy types at high redshift ranging from blue, relatively unobscured star-forming systems to dusty starbursts to quiescent red galaxies. Plus symbols show the location of observed galaxies in the HDFS (Labbé et al. 2003), MS 1054–03 (Förster Schreiber et al. 2006), and the CDFS (Chapter 3) selected by their photometric redshift (or spectroscopic when available) to lie in the same redshift range ($1.5 < z < 3.0$). We also applied a stellar mass

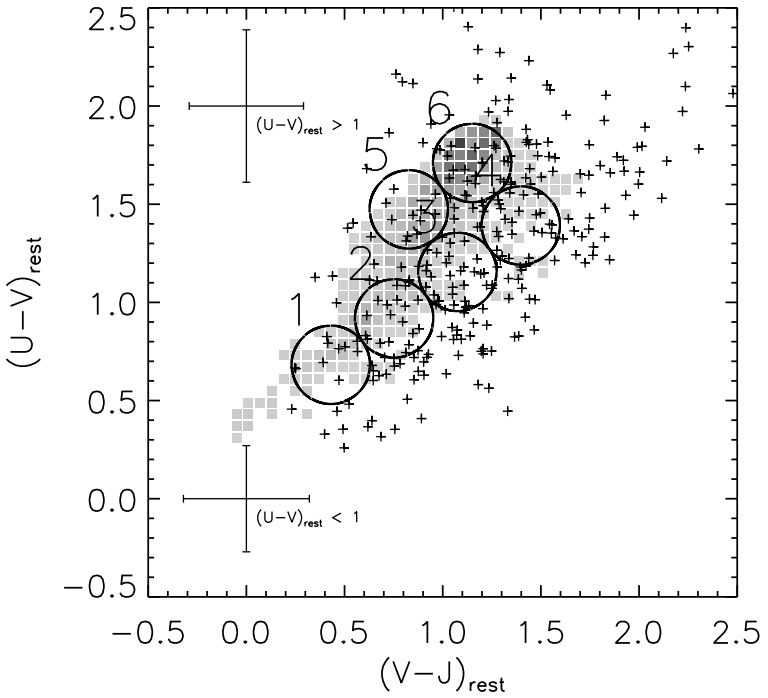

Figure 6.2 — Rest-frame $U-V$ versus $V-J$ color-color diagram showing the binned color distribution of the simulations seen under different viewing angles and at different epochs. Overplotted (*plus symbols*) are the rest-frame colors of observed galaxies with $M_* > 1.4 \times 10^{10}\ M_\odot$ at $1.5 < z < 3$ in the HDFS, MS 1054–03, and the CDFS. Observed galaxies with matching colors are found for all simulated galaxies. The reddest observed sources in $U-V$ and $V-J$ are not reproduced by the considered set of simulations. Rest-frame SEDs for sources in regions 1-6 are displayed in Figure 6.3.

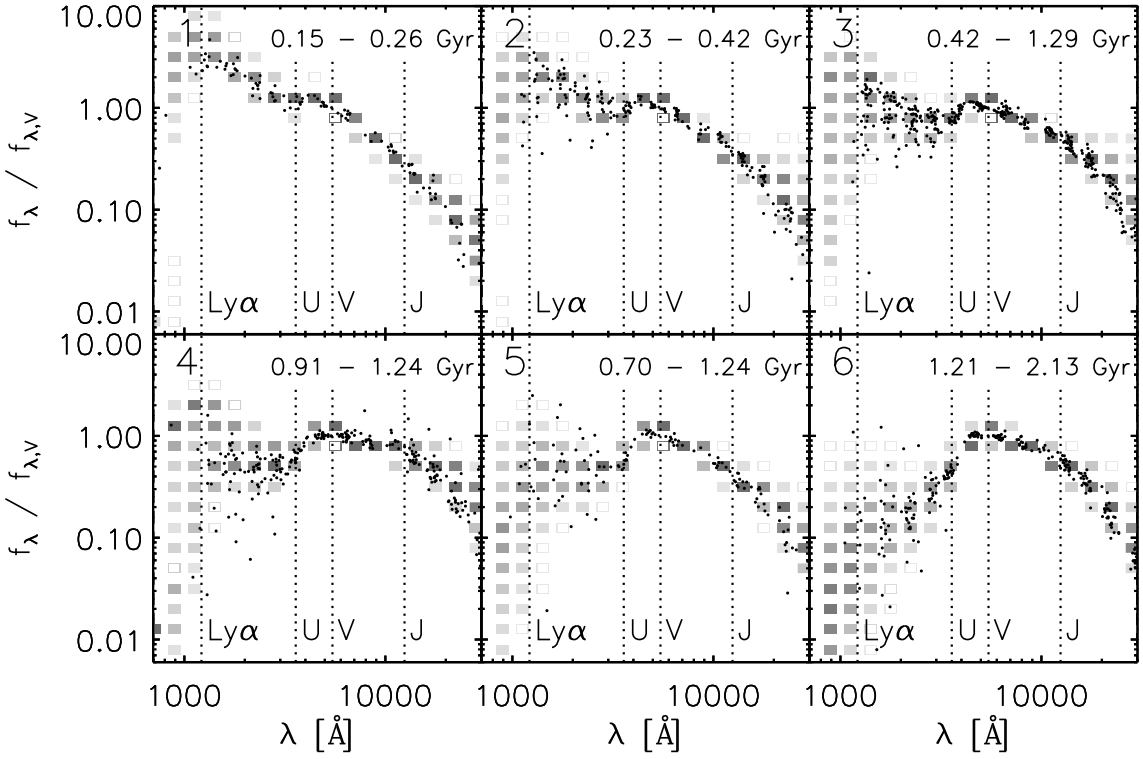

Figure 6.3 — Rest-frame SEDs of simulated galaxies in regions 1-6 of Figure 6.2. A darker intensity of the binned representation indicates a larger density of simulated galaxies with that flux level. In each panel, the central 68% interval of the age distribution of simulated galaxies in the respective region is given. Overplotted (*black dots*) are the rest-frame broad-band SEDs of observed $1.5 < z < 3$ galaxies with $M_* > 1.4 \times 10^{10}\ M_\odot$ in the HDFS, MS 1054–03, and the CDFS. A general agreement between observed and simulated spectral shapes is observed, also outside the U-to-J range where the correspondence was not imposed by selection.

cut at $M_* > 1.4 \times 10^{10}\ M_\odot$ for the observed sample; the lowest initial stellar mass for the considered set of simulations. Here, we do not attempt to statistically compare the two samples. The abundances of different types of galaxies as predicted from the simulations will be addressed in Chapter 7. For our current purpose of analyzing the effects from star formation history, dust, metallicity and AGN on SED modeling, it is sufficient to note that there is a large overlap between the color-color space spanned by the simulated and observed galaxies. However, the observed distribution extends to redder colors by a few 0.1 mag, both in $U-V$ and in $V-J$. Given the one-sided nature of the different color spread, it is unlikely that this can be attributed to photometric uncertainties alone. Therefore, we caution that our results may not necessarily be extrapolated to the reddest galaxies present in observed samples.

To ascertain that observed and simulated galaxies with similar $U-V$ and $V-J$ colors have similar SEDs over the whole spectral range, Figure 6.3 presents the rest-frame SEDs of objects in region 1-6 of Figure 6.2. Again, the binned distribution represents the simulations, with the grayscale indicating a larger number of objects. Overplotted with black dots is the broad-band photometry of our observed sample within the same region of color-color space, placed at the respective rest-frame wavelength. The SEDs are normalized to the rest-frame V-band. By selection, the observed and simulated photometry matches well at rest-frame U and J. In between the UVJ filters, and outside the U-to-J range, no correspondence was imposed. The fact that the UV spectral shape and the NIR tail of the observed and simulated SEDs show a general agreement, is encouraging. We conclude that the simulated photometry can be adopted as a realistic input to our SED modeling procedure. The results of our analysis will be applicable to observed galaxies with similar colors.

6.3 SED modeling: methodology

We characterize physical parameters such as stellar mass, stellar age, and dust attenuation by matching the observed-frame broad-band photometry to synthetic templates from the stellar population synthesis code by BC03. We use the HYPERZ stellar population fitting code, version 1.1 (Bolzonella et al. 2000) and fit the SED twice: first fixing the redshift to the true value (for which we computed the simulated photometry), next adopting a photometric redshift estimate obtained from the EAZY version 0.5 photometric redshift code (Brammer et al. in preparation). In each case, the full B-to-8 μm SED, sampled with identical passbands as available for the GOODS-CDFS (B_{435}, V_{606}, i_{775}, z_{850}, J, H, K_s, [3.6 μm], [4.5 μm], [5.8 μm], [8.0 μm]), was fed to HYPERZ. Random photometric uncertainties were assigned as to mimic real observations in the CDFS, and fluxes in each band were perturbed accordingly. Precisely, for each of the 5400 SEDs corresponding to a simulated galaxy observed during a certain phase of its evolution, placed at a certain redshift, and observed along a certain line-of-sight, we compute 5 realizations of the SED by introducing a gaussian perturbation in all bands with the amplitude derived from the depth of GOODS-CDFS observations in the respective bands. A minimum error of 0.08 mag was adopted for all bands, preventing small errors from dominating the fit.

As in Wuyts et al. (2007), we selected the least χ^2 solution out of three possible

star formation histories: a single stellar population (SSP) without dust, a constant star formation (CSF) history with dust (A_V varying from 0 to 4 in steps of 0.2), and an exponentially declining star formation history with an *e*-folding timescale of 300 Myr (τ300) and identical range of A_V values. Ages were constrained to be larger than 50 Myr, to prevent imporbably young ages, and smaller than the age of the universe at the observed redshift. We used a Calzetti et al. (2000) attenuation law, and assumed solar metallicity and a Salpeter (1955) IMF with lower and upper mass cut-offs $0.1M_{\odot}$ and $100M_{\odot}$.

When refering to the age derived from SED modeling, we mean the age obtained by integrating over the different ages of SSPs that build up the best-fit SFH, weighted with their mass fraction. This measure aims to quantify the age of the bulk of the stars. For an SSP, it equals the time passed since the single burst. For a CSF history, it is essentially half the time passed since the onset of star formation. The τ300 SFH represents an intermediate case.

6.4 Results from SED modeling at fixed redshift

In order to isolate effects from star formation history (§6.4.1), dust attenuation (§6.4.2), metallicity variations (§6.4.3), and AGN contribution (§6.4.4), we computed the photometry for each snapshot with and without attenuation, with and without AGN contribution, and using solar metallicity, or the metallicity as computed by the simulation for each stellar particle. To each of these sets of SEDs, we applied the modeling described in §6.3. In §6.4.1 - §6.4.4, we build up the analysis step by step adding one aspect at a time. The overall performance of the standard SED modeling applied to the 'full' photometry, taking into account the effects of both attenuation, metallicity, and AGN contribution as realistically as possible, is discussed in §6.4.5.

6.4.1 Impact of mismatch between true and template SFH

The contribution of massive O and B stars makes young stellar populations brighter than older stellar populations, giving them more weight in the integrated SED. Consequently, the light-weighted stellar age will be younger than the mass-weighted stellar age. This is always the case, but provided we have a template representing the correct SFH, it is possible to account for this effect and still find the correct age of the bulk of the stars. Our three allowed SFHs are an SSP, where all stars formed in a single burst, a model with $SFR \propto e^{-t/\tau}$ with τ = 300 Myr, and a constant star formation history. These are standard choices in analyses of distant galaxies. However, they do not encompass a star formation history where the rate of star formation was lower in the past than it is now, as is the case during first passage and during the actual merger-triggered starburst (see Figure 6.1). In general, fitting a template SFH that has $\left[\frac{dSFR}{dt}\right]_{template} < \left[\frac{dSFR}{dt}\right]_{true}$, the older population will be lost to some degree under the glare of newly formed stars, leading to an underestimate of the age. Since one tends to count the young light only, mass will be underestimated as well. For the same reason, models allowing for a secondary burst of star formation on top of an older stellar population were found to reveal larger total stellar masses, in particular for blue objects (Papovich et al. 2006; Erb et al. 2006b; Wuyts et al. 2007).

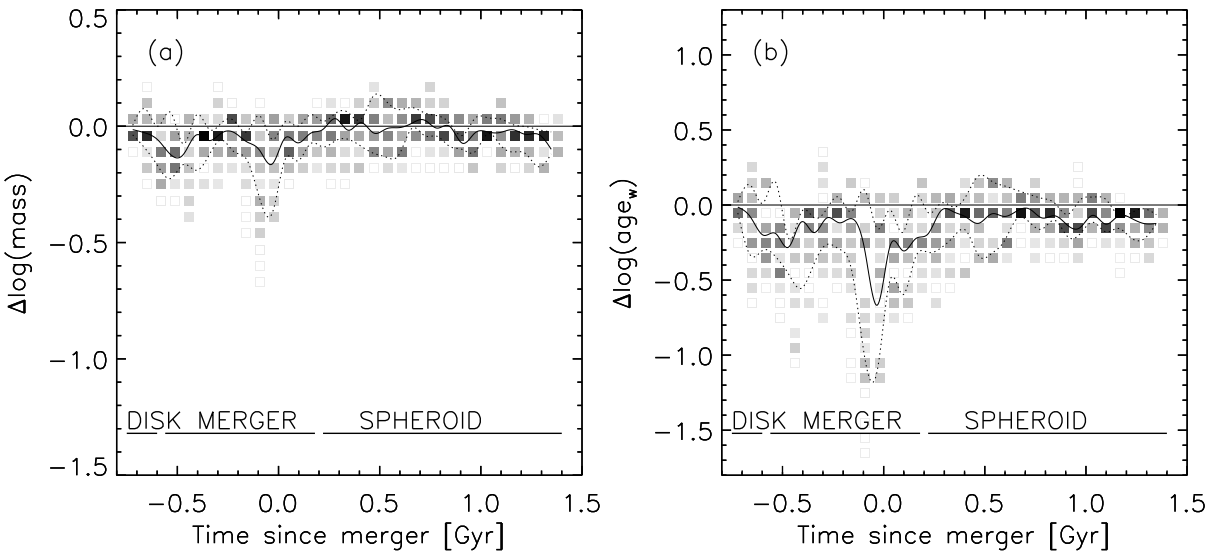

Figure 6.4 — Impact of star formation history. The difference between estimated and true (a) mass and (b) mass-weighted age as a function of time for all simulations, with the SED modeling performed on the intrinsic (i.e., unattenuated) stellar photometry with all stars set to solar metallicity. The solid line indicates the median. The dotted lines contain the central 68% of the distribution. Deviations from 0 (negative indicating an underestimate) are due to mismatch between the actual star formation history and the histories allowed in our SED modeling (SSP/CSF+dust/τ300+dust). Maximal underestimates of mass and age are reached during the merger itself. A secondary minimum is reached during first passage of the progenitors, 0.3 to 0.4 Gyr before.

We demonstrate that the underestimate of mass and age takes place by considering the performance of our SED modeling procedure as applied on intrinsic stellar photometry with all stars set to solar metallicity. Here, we define $\Delta log(age_w)$ as $log(age_{w,recovered}) - log(age_{w,simulation})$. Hereafter, similar definitions will be used to quantify the offset in mass, reddening and extinction, always indicating an underestimate with a negative value of Δ. Figure 6.4 shows $\Delta log(age_w)$ as a function of time with respect to the merger between the supermassive black holes. We bin the distribution of points for different initial conditions, timesteps and lines-of-sight. Darker intensities represent a higher density in the bin. Empty boxes contain less than 1% of the total number of SEDs at that timestep. The solid line represents the median of the distribution and the dotted curves mark the central 68% interval. During the first snapshot, when the star formation history matches (by construction) our CSF template, we find no systematic offset and a low scatter, purely resulting from photometric uncertainties. Soon after, we start to underestimate the age and mass, with minima coinciding with the moment of first passage (500 Myr before the actual merger) and that of the actual merger-triggered starburst. It is precisely at these moments that the real SFH deviates most from the allowed template SFHs. During the starburst phase itself, the median offset of true mass-weighted age versus recovered age exceeds 0.5 dex, with a large scatter due to differences in the SFH for different initial conditions. For example, the ratio of SFR at first passage over SFR during the central starburst increases with gas fraction. After all activity has quieted down, the derived ages and masses lie within 0.1 dex of their true value.

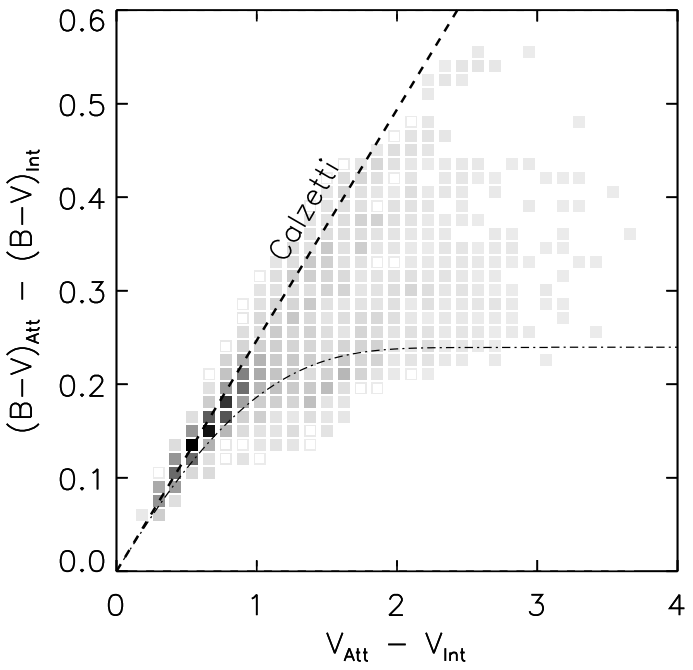

Figure 6.5 — The effective reddening (attenuated minus intrinsic $B-V$ color) versus total absorption in the V-band for all timesteps, viewing angles and initial conditions. The intensity of the binned distribution indicates the number of simulations in the respective part of the diagram. A ratio of total to selective absorption $R_V = 4.05$ as by Calzetti et al. (2000) is plotted with the thick dashed line. The dot-dashed curve indicates a toy model where the distribution of A_V values is uniform between 0 and a maximum value, and all emitting sources are identical. Stellar particles individually have $R_V = 4.05$, but in the case of a non-uniform dust distribution the sum of all stellar particles has an effective $R_V > 4.05$.

6.4.2 Impact of attenuation

As described in §6.3, we use the approach of a foreground screen to account for the attenuation by dust in our SED modeling. Figure 6.1(e), illustrating the range of effective visual extinction values (attenuated minus intrinsic V-band magnitude) for a random simulation depending on the viewing angle, proves that such a representation is not valid. Here we address the impact that a non-uniform distribution of the dust will have when modeled by a foreground screen.

First, we consider a situation where the optical depth to the stellar particles is not constant, but the variations are uncorrelated with the intrinsic properties of the stellar particles. Such a scenario is by construction the case at the start of the simulation. For each stellar particle individually the ratio of total to selective absorption,

$$R_V = \frac{A_V}{E(B-V)} = 4.05, \tag{6.4}$$

was taken from Calzetti et al. (2000). Since less extincted regions are also less reddened and have a larger weight in the integrated SED, the effective extinction $A_{V,eff} \equiv V_{Att} - V_{Int}$ and effective reddening $E(B-V)_{eff} \equiv (B-V)_{Att} - (B-V)_{Int}$ of the galaxy as a whole will not be related by the same factor 4.05 as for the individual particles. Instead, the overall reddening for a given A_V will be smaller than predicted by Calzetti (i.e., the extinction is greyer). This is illustrated in Figure 6.5 where the dashed line represents the $A_V = 4.05 \times E(B-V)$ scaling by Calzetti et al. (2000) and the dotted line represents a toy model with a uniform distribution of A_V values between 0 and A_{Vmax} to stellar particles that all emit at identical intrinsic luminosities:

$$A_{V,eff} = -2.5 \log \left[\frac{10^{-0.4 A_{Vmax}} - 1}{-0.4 A_{Vmax} ln(10)} \right] \tag{6.5}$$

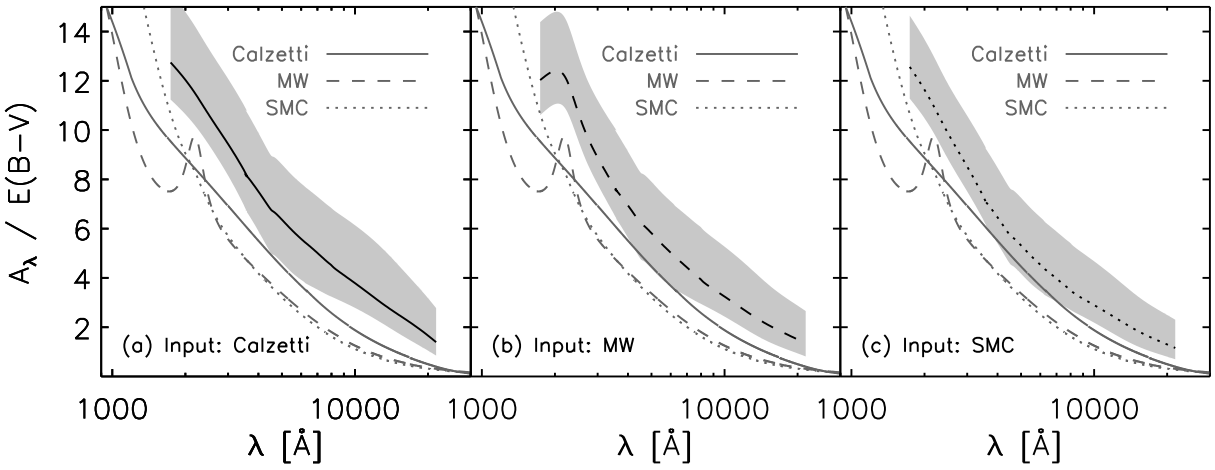

Figure 6.6 — Effective extinction curves of simulated galaxies with $A_{V,eff} > 1$ for different input attenuation laws: (a) the Calzetti et al. (2000) law, MW-like reddening from Pei (1992), and (c) SMC-like reddening from Pei (1992). The black curve indicates the median over all snapshots and viewing angles with $A_{V,eff} > 1$. The light grey polygon indicates the central 68% interval. The Calzetti, MW, and SMC attenuation laws are plotted in grey. In all cases, the effective extinction of simulated galaxies with large $A_{V,eff}$ is greyer than the Calzetti et al. (2000) law that is used in standard SED modeling. The offset is smallest when each stellar particle is attenuated according to the SMC-like law.

$$E(B-V)_{eff} = 2.5 \log \left[\frac{\left(1 + \frac{1}{4.05}\right) \left[10^{-0.4 A_{Vmax}} - 1\right]}{10^{-0.4\left(1+\frac{1}{4.05}\right) A_{Vmax}} - 1} \right]. \tag{6.6}$$

Since the Calzetti et al. (2000) attenuation law was derived empirically for galaxies as a whole, it is arguably not the appropriate law to apply to the individual stellar particles, i.e., the smallest stellar populations that our simulation can resolve, typically $10^5 - 10^6\ M_\odot$. We investigated the changes in photometry when adopting a MW and SMC-like reddening curve by Pei (1992), which were derived in a more bottom-up fashion from the physics of interstellar dust grains. Again, we scaled the optical depth with the metallicity along the line of sight. For the SMC reddening curve, the resulting colors become redder by up to 0.05, 0.1, and 0.2 mag in rest-frame $B-V$, $U-V$, and $V-J$ respectively. The MW-like attenuation law is also less grey than Calzetti, thus producing slightly redder colors, though less so than for the SMC law. The effective extinction curve, expressed as $\frac{A_\lambda}{E(B-V)}$ as a function of wavelength, of snapshots and viewing angles with large optical depths ($A_{V,eff} > 1$) is presented for different input attenuation laws in Figure 6.6.

Not only does non-uniform extinction change the reddening ($\frac{dA_\lambda}{d\lambda}$) at a given A_V, it also affects the dependence of the reddening on wavelength ($\frac{d^2A_\lambda}{d\lambda^2}$). For extinction that is uncorrelated to the properties of the emitting sources, this gives the dust vector in the $U-V$ versus $V-J$ color-color diagram a shallower slope, i.e., for a given reddening in $V-J$, the reddening in $U-V$ is smaller than predicted by the Calzetti et al. (2000) law. The consequence of a different $\frac{d^2A_\lambda}{d\lambda^2}$ than Calzetti is clarified in Figure 6.7. The solid line represents the evolutionary track of a stellar population following a CSF history. The track starts 50 Myr after the onset of star formation and ends 2 Gyr later. Suppose different parts of a galaxy all contain a 1 Gyr old CSF population whose

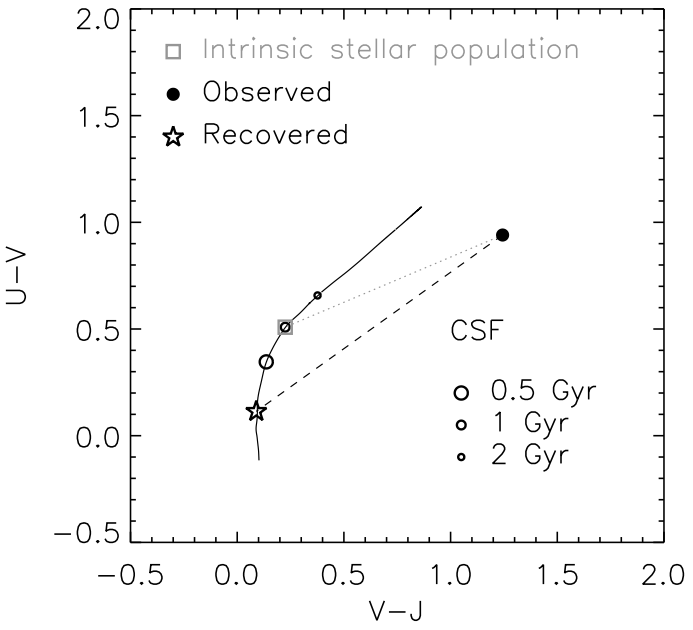

Figure 6.7 — Rest-frame $U-V$ versus $V-J$ color-color diagram illustrating the effect of a non-uniform distribution of A_V values that is uncorrelated with the intrinsic properties of the emitting sources. The black curve indicates a CSF population with age between 50 Myr and 2 Gyr. Suppose an intrinsic population (*box symbol*) is reddened by such a dust distribution to the location in color-color space of the filled circle. Under the assumption of a uniform foreground screen of dust, the observed colors will then be traced back along the Calzetti et al. (2000) reddening vector (*dashed black line*), resulting in an artificially young age (*star symbol*).

intrinsic location in color-color space is marked by the empty grey box. A distribution of dust as described by the above mentioned toy model will redden the galaxy along the dotted line. Interpreting the observed colors (*filled circle*) as a CSF population attenuated by a foreground screen according to the Calzetti et al. (2000) law, will lead to a best-fit age (*star symbol*) that is too young and reddening that is too large.

Since in our simulations the ages of the stellar particles (that are each treated as SSPs) present at the start of the simulation were drawn randomly from a uniform distribution, the system has a CSF history in the earliest snapshots without a correlation between the optical depth and intrinsic light of the stellar particles. Therefore, it comes as no surprise that, when looking at the attenuated stellar photometry in Figure 6.8 (for now all stars still set to solar metallicity), the central 68% interval in $\Delta \log age_w$ reaches to more negative values (to -0.5 dex) during the earliest phases than was the case for the unattenuated photometry (Figure 6.4). The estimated reddening is slightly larger than the true value, but nevertheless the use of Eq. 6.4 still causes an underestimated A_V, as can be understood from Figure 6.5. The systematic underestimate in age and A_V combined cause the evaluation of the stellar mass during the first snapshots, when template mismatch due to the SFH is still negligible, to be too small by ~ 0.12 dex.

After a few 100 Myr after the beginning of the simulation however, Figure 6.8 reveals an improved recovery of the mass-weighted stellar age compared to that obtained by SED modeling of the intrinsic light (Figure 6.4). Clearly, the assumption of a non-uniform dust distribution that is uncorrelated with the intrinsic properties of the emitting sources breaks down.

Figure 6.9 demonstrates the occurence of preferential extinction toward young star forming regions in one of our simulations. The three panels indicate the binned distribution of the metallicity-scaled hydrogen column density measured along various lines-of-sight versus the age of the stellar particle to which the column density was computed for the 3 epochs marked in the star formation history panel of Figure 6.1.

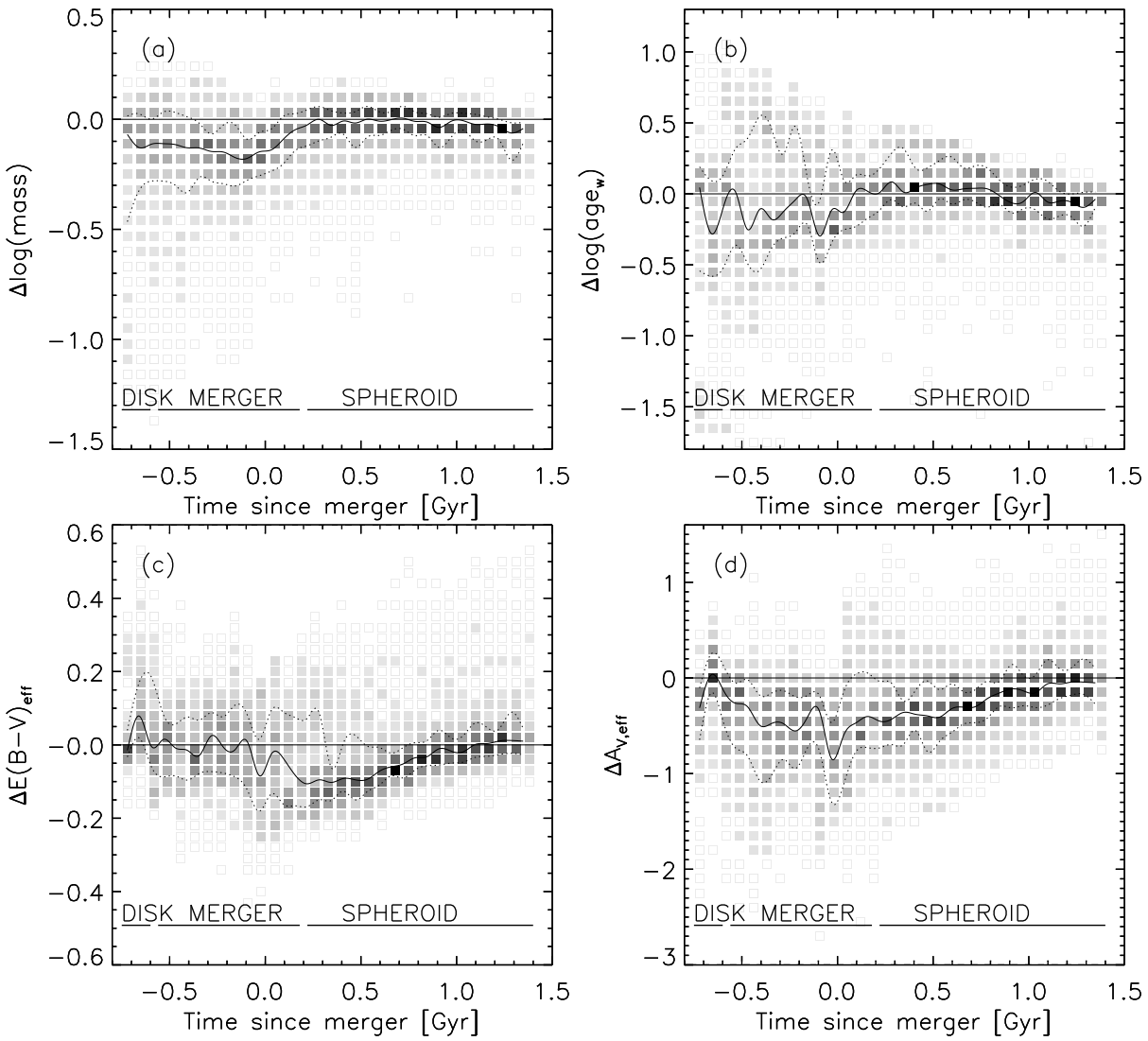

Figure 6.8 — Effect of extinction. The difference between estimated and true (a) stellar mass, (b) mass-weighted age, (c) effective reddening, and (d) effective visual extinction as a function of time since the merger. The SED modeling was performed on the attenuated stellar photometry with all stars set to solar metallicity. The solid line indicates the median and dotted lines comprise the central 68% of the distribution. Ages are still underestimated for the first 0.8 Gyr of the evolution, but to a lesser degree than estimates based on the intrinsic light. Added to the underestimated A_V, this leads to a characterization of the stellar mass that is too low by 0.1 - 0.15 dex.

The vertical arrow indicates the start of the simulation. All stellar ages older than this value (cut off for illustrational purposes) were set by hand as explained in §6.2.1. As we already pointed out in the A_V history panel of Figure 6.1, the typical column densities are higher during the merger (panel b) than before (a) or after (c). Moreover, Figure 6.9 shows that the ratio of column densities toward ongoing star formation over column densities toward older populations reaches a maximum during the merger (b). Using sticky particle simulations of dusty starburst mergers, Bekki & Shioya (2001) found a similar age-dependent extinction, confirming that this is a generic feature of merging systems and not determined by the method used to model dissipative processes.

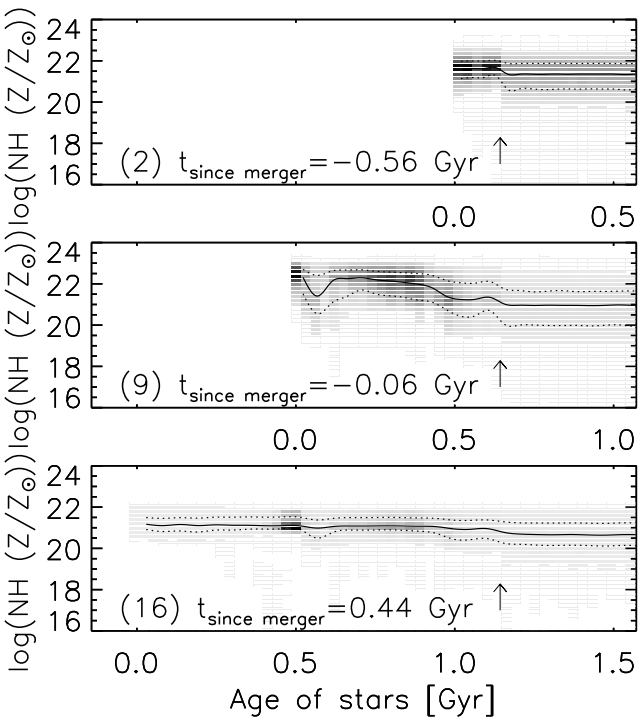

Figure 6.9 — Distribution of hydrogen column densities, linearly scaled with the metallicity of the gas along different lines-of-sight to the stellar particles versus the age of the respective stellar particle. The relation between column density and stellar age is plotted for 3 snapshots: before (2), during (9), and after (16) the merger (see Figure 6.1). The solid and dotted lines indicate the median and 68% interval of the distribution respectively. Darker intensity means a larger number of stars is present with that age. All stellar ages rightward of the arrow correspond to initial stars and were set by hand. The optical depth, which is proportional to the metallicity-scaled gas density, is larger toward newly formed stars during the merger-triggered starburst. The signature of this age-dependent extinction weakens during more quiescent episodes of star formation.

Poggianti & Wu (2000) inferred age-dependent extinction during a starburst to explain the nature of so-called e(a) galaxies: galaxies with [OII] in emission and strong Balmer absorption lines, frequently associated with merger morphologies.

From a physical perspective, it is expected that during the merging process hydrodynamical and gravitational forces channel gas and dust to the central regions where it triggers a starburst. Once started, supernovae going of on a few 10^7 yr timescale further increase the dust content of the regions where newly formed stars reside. The fact that the distribution of younger (and thus intrinsically bluer) stellar populations does not trace that of the older populations of stars and that it is intimately correlated with the dust distribution leads to an overestimate in age. In analogy to Figure 6.7, the effective $\frac{d^2A_\lambda}{d\lambda^2}$ is such that the galaxy is reddened along a steeper vector in the $U-V$ versus $V-J$ diagram than is the case for the Calzetti curve. Since an observer will mistakenly model the galaxy with an intrinsically redder template, the reddening by dust $E(B-V)$ will be underestimated. Although a given total absorption corresponds to a stronger reddening in the presence of age-dependent extinction compared to uncorrelated non-uniform extinction, the Calzetti et al. (2000) relation between $E(B-V)$ and A_V given by Eq. 6.4 can still be considered as an upper limit. Therefore, the total absorption will be underestimated. This is illustrated in Figure 6.5 where we plot the binned distribution of true $E(B-V)$ versus true A_V for all of our simulation snapshots, viewed under a range of viewing angles. Finally, the derived stellar mass owes its more robust character to the compensating effects of systematic offsets in age and absorption.

The effect of the larger extinction toward young stars will in practice be superposed on the effect of mismatch between template and true SFH, that prevents us from fully accounting for the difference between light- and mass-weighted stellar age (see §6.4.1).

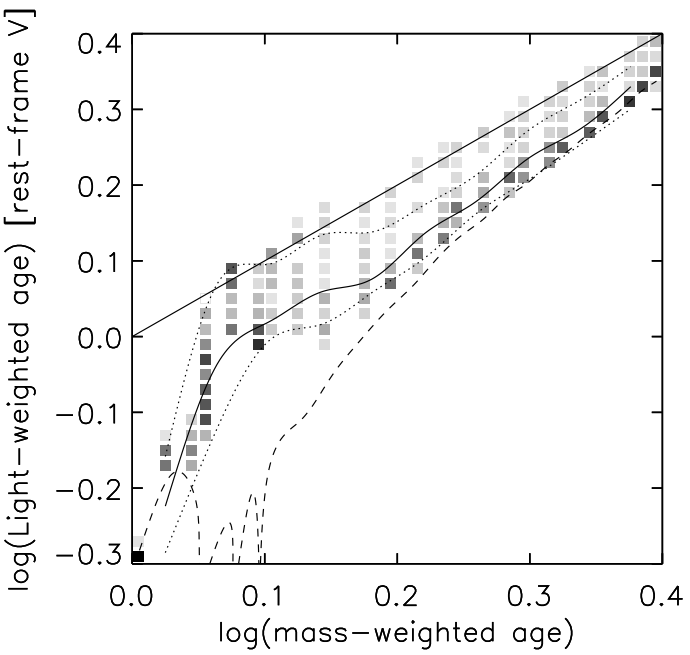

Figure 6.10 — Rest-frame V-band light-weighted age versus mass-weighted age for an initially 40% gas fraction simulation. The boxes mark the mean age weighted with the attenuated V-band light. Darker intensities indicate a larger number of viewing angles. The solid and dotted curves mark the median and central 68% interval respectively. The dashed line indicates the mean age weighted with the intrinsic V-band light (no attenuation). The attenuated light-weighted age is a better approximation of the mass-weighted age than the intrinsic light-weighted age, increasingly so for younger stellar populations. Larger optical depths to young than to old stars are responsible for this effect.

Figure 6.10 illustrates how an increased extinction toward young stars reduces the difference between the light-weighted and mass-weighted measure of age. We conclude that the SED modeling on galaxies with solar metallicity stars and dust distributed in between still underestimates the age, but adding dust has improved our best guess to an overall median offset of -0.04 dex (compare Figure 6.8(b) to Figure 6.4(b)). Similar conclusions were drawn by Bell & de Jong (2001) who examine the reddening and dimming effects of dust and its impact on estimating stellar mass-to-light ratios.

6.4.3 Impact of stellar metallicity

So far, we tested our SED modeling on synthetic photometry that was computed assuming a solar metallicity for all emitting sources. In reality, stars with a range of metallicities will be present, reflecting the level of enrichment in the gas at the epoch of their formation. Before we repeat our analysis now setting the stellar metallicities to their appropriate value calculated by the GADGET-2 code, we anticipate the effect using the diagnostic $U-V$ versus $V-J$ color-color diagram in Figure 6.11.

The tracks represent exponentially declining SFHs for metallicities of Z=0.008 (*grey*) and 0.02 (solar, in *black*). Both evolutionary tracks are drawn from 50 Myr to 2 Gyr after the onset of star formation. The classic age-metallicity degeneracy states that the optical broad-band colors of a young stellar population are nearly indistinguishable from that of an older, more metal-poor population (O'Connell 1986). For the τ300 star formation history drawn here, this effect gets only notable at later times: 2 Gyr after the onset of star formation the sub-solar metallicity track has the same $U-V$ color as a solar metallicity population that started forming stars 1.8 Gyr ago. On the one hand, the addition of dust will complicate the age-metallicity degeneracy. On the other hand, the addition of NIR photometry helps to separate the evolutionary tracks for different metallicities. A galaxy whose attenuated light has colors marked by the filled circle may correspond with one of the intrinsic colors indicated by the grey boxes depend-

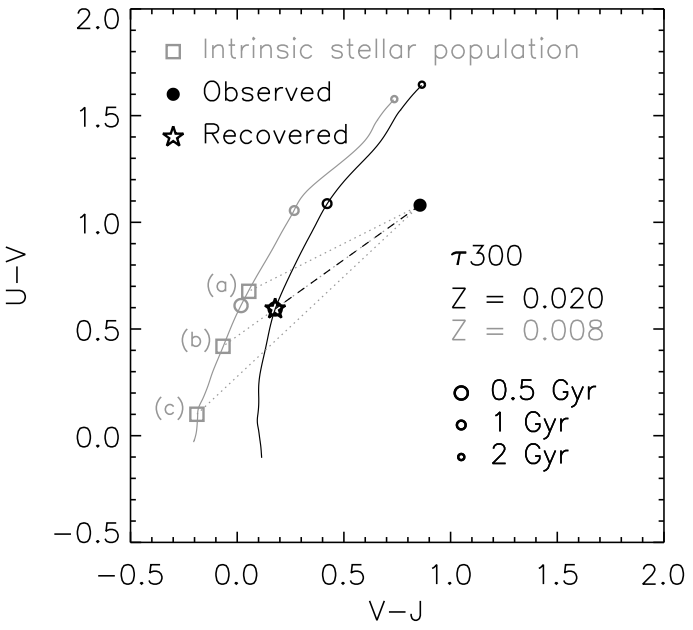

Figure 6.11 — Rest-frame $U-V$ versus $V-J$ color-color diagram illustrating the effect of fitting solar metallicity templates to stellar populations of sub-solar metallicity. The black and grey curves represent evolutionary tracks for an exponentially declining star formation history with e-folding time of 300 Myr for solar ($Z = 0.02$) and sub-solar ($Z = 0.008$) metallicity respectively, each starting at 50 Myr. Stellar population with intrinsic colors indicated by the grey boxes will be reddened to the location in color-space marked by the filled circle in the case of (a) non-uniform age-independent extinction, (b) extinction by a uniform foreground screen, and (c) age-dependent extinction. In all three cases, the assumption of solar metallicity and Calzetti attenuation will lead to the conclusion that the stellar population formed its first stars 0.5 Gyr ago. This is an underestimate (a) or overestimate (b, c) respectively. The reddening is always underestimated.

ing on the kind of extinction: (a) for non-uniform age-independent extinction, (b) for a foreground screen of dust, and (c) for age-dependent extinction. In case (a), the assumption of Calzetti attenuation and solar metallicity in our SED modeling leads to a recovered evolutionary stage that is too young, marked with the star symbol on the solar metallicity track. In case (b) and (c), the same recovered evolutionary stage is too old. In all cases, the determination of the reddening will be too low, as will consequently be the case for the A_V and the stellar mass, and increasingly so for lower metallicities. Obviously, the effects described will again be superposed on the previously discussed effects of star formation history and dust. It is also noteworthy that following the enrichment by heavy elements reduces the effect of age-dependent extinction. Young stellar populations are still intrinsically bluer than old populations, but to a lesser degree since they have formed at later times from gas that was more enriched.

In our recovery analysis of stellar population properties, we find that at metallicities of a quarter solar and below, the age is overestimated by 0 to 0.5 dex (central 68% interval of $\Delta \log age_w$). However, the underestimate in reddening and therefore extinction for these low-metallicity galaxies is such that the mass estimate (which is dependent on both age and A_V) stays within ± 0.1 dex of its true value for 68% of the cases.

6.4.4 Impact of AGN contribution

Since the merger simulations described in this chapter take into account the role of supermassive black holes on its environment (see e.g. Di Matteo et al. 2005; Springel

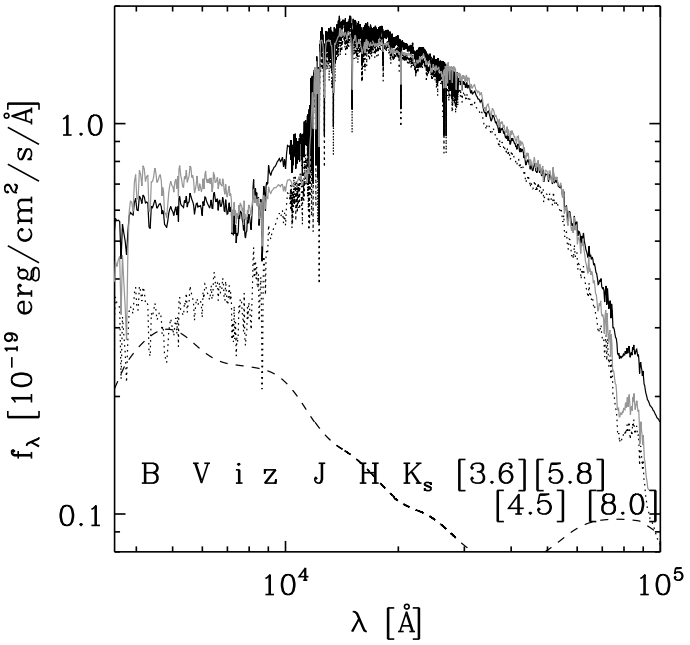

Figure 6.12 — Attenuated spectrum of a simulated merger placed at $z = 2.1$ during the peak of AGN activity. The total attenuated light (*black solid line*) is decomposed into a contribution from stars (*dotted line*) and AGN (dashed line). An observer who samples the total attenuated light with an identical set of broad-band filters as available for GOODS-CDFS and models the SED using stellar population synthesis only, will find as best-fitting model the spectrum in grey. Its age is too young by $\Delta \log age_w = -0.4$. The reddening $E(B-V)$ and absorption A_V are overestimated by 0.1 and 0.4 mag respectively. The opposite sign of offsets in age and A_V leads to a mass recovery that is only 0.05 dex below its true value.

et al. 2005b), it is straightforward to include its contribution to the integrated galaxy SED. We note that only during a timespan of the order of a Salpeter time, a few 10^7 to 10^8 year, the AGN emission amounts to a significant fraction of the stellar emission. Admittedly, the peak of AGN activity can be missed by the time sampling of our snapshots. Nevertheless, the current dataset provides a useful insight on its impact on the SED modeling.

We illustrate the typical behavior in Figure 6.12 showing the photometry computed at the time of merging when the accretion onto the supermassive black hole is maximal. Here, the solid black curve represents the light received by an observer. We break down the attenuated SED in a stellar (*dotted line*) and AGN contribution (*dashed line*). Finally, the best-fit model (in this case an exponentially declining star formation history that started 0.8 Gyr ago) is plotted in grey. Although resulting in a low $\chi^2_{reduced} \sim 1$, the SED modeling is mislead by a degeneracy between the stellar+AGN light and the stellar light of a younger population obscured by large columns of dust. The addition of AGN light, when exceeding 10% of the total emission, adds another -0.1 to -0.15 dex to $\Delta \log age_w$, +0.05 to +0.1 mag to $\Delta E(B-V)$, and +0.3 to +0.5 mag to ΔA_V. These cases typically show a larger $\chi^2_{reduced}$ (70% have $\chi^2_{reduced} > 5$).

6.4.5 Overall performance

Our analysis was performed on synthetic photometry of galaxies placed at redshifts $z = 1.5$ to $z = 2.9$. The results do not show a trend with redshift. This indicates that the details of the filterset play no role. Our study only focuses on continuum shape and in the presence of spectral lines, a higher wavelength sampling in the form of spectroscopic studies will obviously provide valuable extra information. The trends described in this section are all systematic and cannot be attributed to signal-to-noise effects (e.g. more extincted galaxies at the highest redshifts being fainter and therefore less well recovered). We tested this in two ways: first by omitting the perturbation of

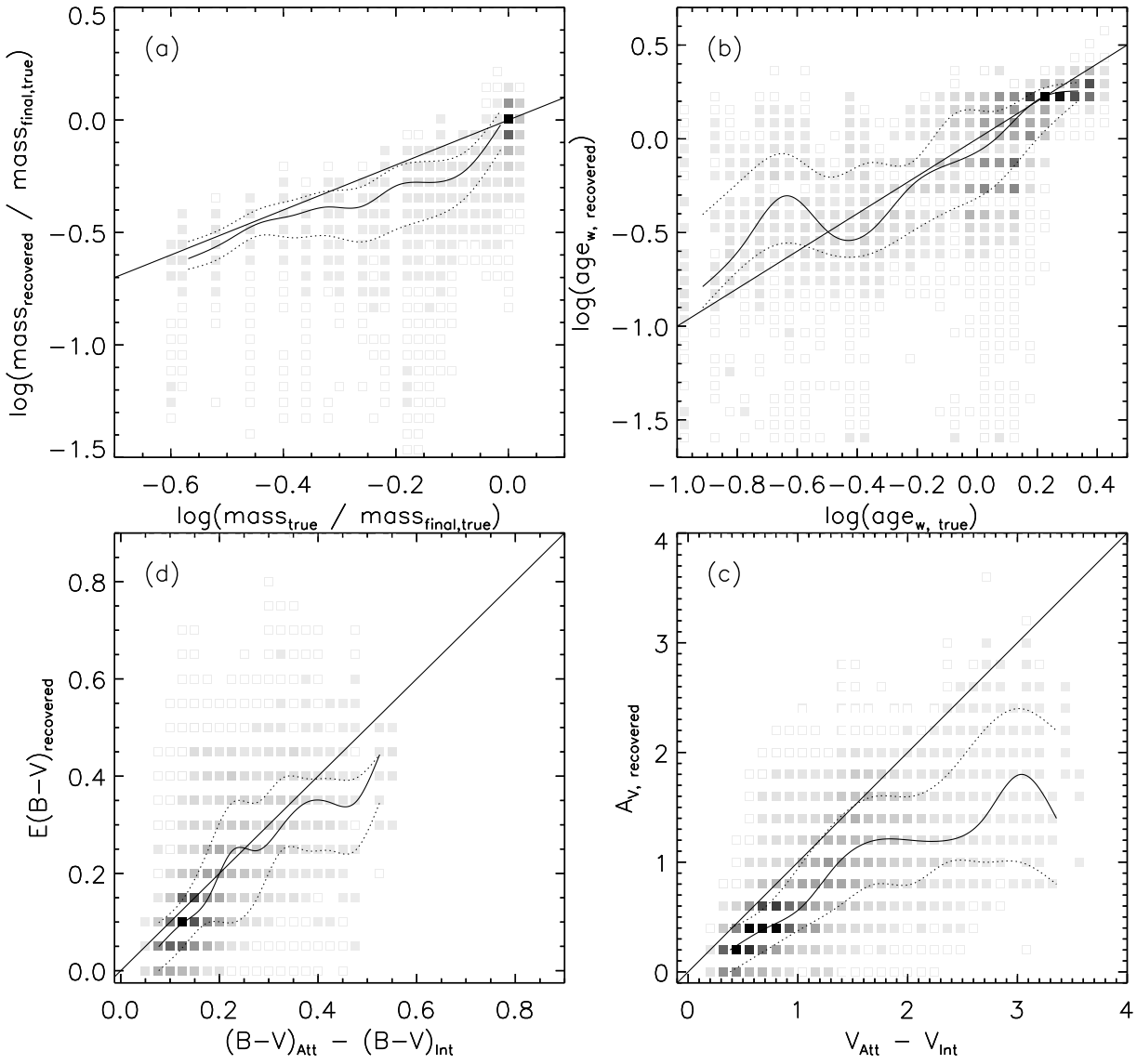

Figure 6.13 — Overall performance of the SED modeling. Recovered versus true (a) ratio of current to final stellar mass, (b) mass-weighted stellar age, (c) effective reddening (i.e., attenuated minus intrinsic $B-V$ color), and (d) effective visual extinction (i.e., attenuated minus intrinsic V-band magnitude). The SED modeling was performed on the total (stellar+AGN) attenuated photometry. The solid line indicates the median and dotted lines comprise the central 68% of the distribution. The total visual extinction A_V is the least constrained of the four studied parameters. In particular for heavily extincted galaxies the A_V is greatly underestimated.

the synthetic fluxes, second by applying a conservative cut in the observed K_s-band magnitude: $K_{s,obs} < 23.6$, corresponding to $S/N_{K_s} > 10$. In both cases, the same trends described in this Section are still present.

The combined effects of mismatch in SFH, attenuation by dust, metallicity variations and AGN activity on our ability to characterize the mass, age, reddening and extinction of a galaxy is summarized in Figure 6.13. Figure 6.14 presents the performance of the SED modeling on the full photometry (including dust, metallicity variations, and

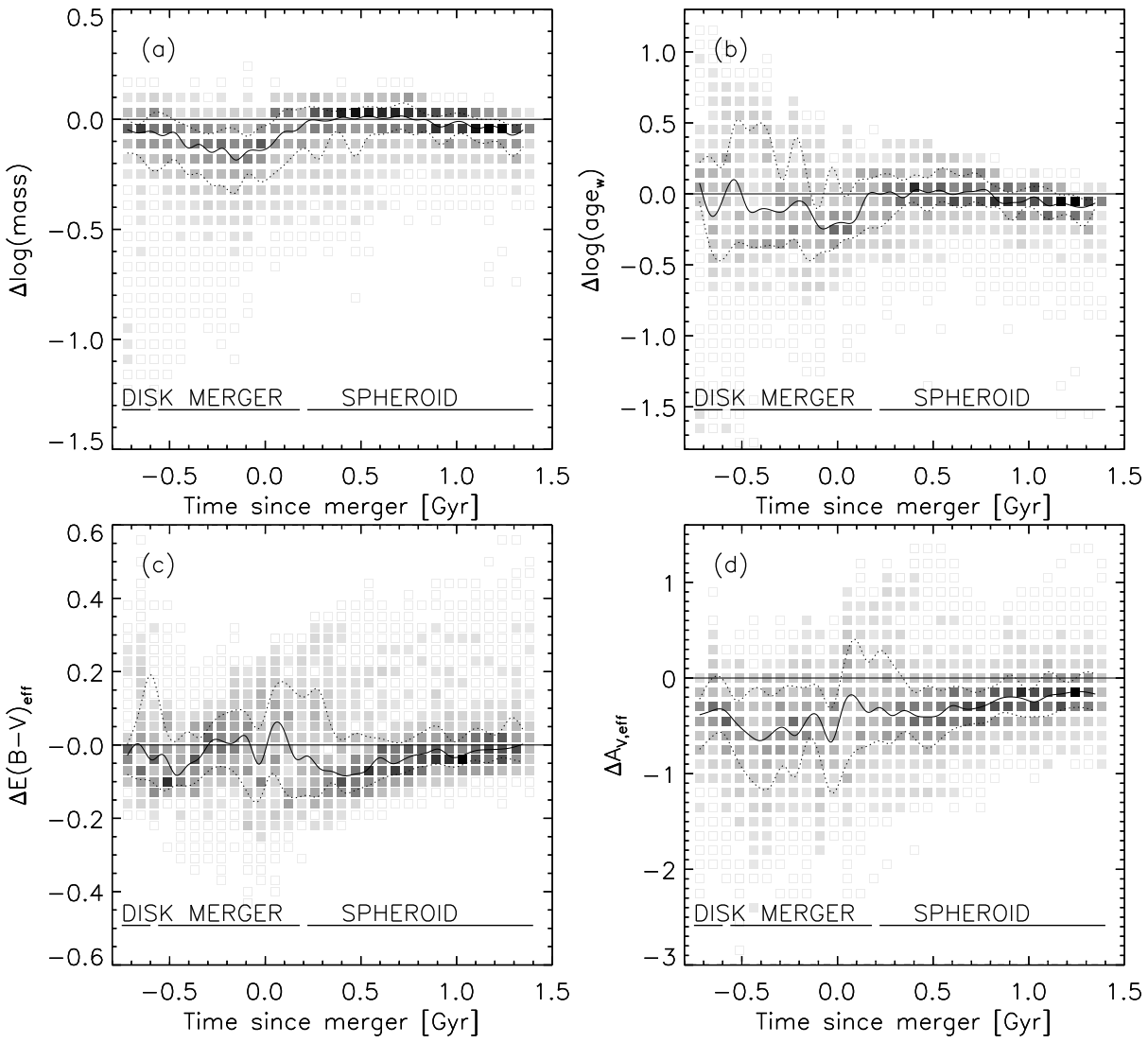

Figure 6.14 — Overall performance of the SED modeling. The difference between estimated and true (a) stellar mass, (b) mass-weighted age, (c) effective reddening, and (d) effective visual extinction as a function of time since the merger. The SED modeling was performed on the total (stellar+AGN) attenuated photometry. The solid line indicates the median and dotted lines comprise the central 68% of the distribution. The properties of merger remnants are well reproduced. The results for star-forming galaxies, especially for those in the phase of merging, show underestimates in both age, extinction, and mass.

AGN) in a different manner, as a function of time since the merger. Figure 6.13(a) compares the recovered and true stellar mass, normalized to the final stellar mass of the simulation. At low M/M_{final} ratios, i.e., at the start of the high gas fraction simulations, the mass estimates agree well with the true values. The largest systematic underestimates occur at intermediate M/M_{final}, during the merger-triggered star-forming phases of the simulation. Finally, the correspondence is best at $\log(M/M_{final}) \sim 0$, where the merger remnants reside. The same scenario is visible in Figure 6.14(a). We quantify the performance of the SED modeling separately for galaxies in the 'disk', 'merger', and 'spheroid' regime by averaging the solid (median $\Delta \log M$ as a function

of time) and dotted (central 68% interval) lines over the respective time interval indicated in Figure 6.14(a). We find $\Delta \log M_{disk} = -0.05^{+0.06}_{-0.13}$, $\Delta \log M_{merger} = -0.11^{+0.09}_{-0.14}$, and $\Delta \log M_{spheroid} = -0.01^{+0.04}_{-0.09}$. The errors indicate the range around the typical offset comprising 68% of the simulations.

Quantifying the quality of age estimates (Figure 6.13(b), Figure 6.14(b)), we find $\Delta \log age_{w,disk} = -0.04^{+0.26}_{-0.27}$, $\Delta \log age_{w,merger} = -0.11^{+0.34}_{-0.25}$, $\Delta \log age_{w,spheroid} = -0.03^{+0.10}_{-0.10}$. Again, the underestimate and scatter is largest for the phases of merger-triggered star formation. The overestimate of the youngest ages shown in Figure 6.13(b) concerns the 80% gas fraction simulations in their earliest phases, when the metallicity is low and the results from §6.4.3 apply.

The reddening (Figure 6.13(c), Figure 6.14(c)) is overall well reproduced: $\Delta E(B-V)_{disk} = -0.02^{+0.12}_{-0.07}$, $\Delta E(B-V)_{merger} = -0.01^{+0.09}_{-0.09}$, and $\Delta E(B-V)_{spheroid} = -0.04^{+0.08}_{-0.04}$. Only at the highest reddening levels, the agreement deteriorates. The latter correspond to the times when and viewing angles under which the effect of increased extinction toward young stars is maximal (see §6.4.2).

As opposed to the reddening, however, the extinction (Figure 6.13(d), Figure 6.14(d)) shows large systematic underestimates, in particular during the star-forming (disk and merger) phases. Using an R_V of 4.05 to translate the selective absorption $E(B-V)$ into a total visual absorption A_V results in an underestimate over the whole range of A_V values, particularly during the highly obscured phases. The sum of emitting sources that are each attenuated according to Calzetti et al. (2000) does not follow that same reddening law. An observer is limited by the light that he/she receives. These results are quantified as follows: $\Delta A_{V,disk} = -0.35^{+0.27}_{-0.29}$, $\Delta A_{V,merger} = -0.48^{+0.42}_{-0.45}$, and $\Delta A_{V,spheroid} = -0.27^{+0.25}_{-0.21}$.

6.4.6 Lessons for SED modeling

How can the modeling of real high-redshift galaxies benefit from our analysis of merger simulations? In order to answer this question, we need to translate the mechanisms described above in terms of the physical properties of stars and dust into their combined effect as a function of observables, such as color.

Since the results of our SED modeling showed no trend with redshift for which the synthetic photometry was computed, we can describe the quality of recovering stellar population properties in terms of rest-frame colors. Although not true observables, their computation as described by Rudnick et al. (2003) suffers from only a minor template dependence compared to parameters such as mass, age, and dust content. In Figure 6.15, we present the performance of our SED modeling as a function of location in the rest-frame $U-V$ versus $V-J$ color-color diagram. Simulations with initial gas fractions of 40% and 80% are shown separately. The SED modeling was based on the full (stellar+AGN) photometry in both cases. Downward triangles indicate a median value of $\Delta parameter$ that is negative for simulations with the respective colors. Upward triangles represent an overprediction of the true value. Lighter symbols are used for a better correspondence between the true and modeled parameter value. The different initial stellar ages and lower metallicities for $f_{gas} = 80\%$ runs explain why they extend to bluer $U-V$ colors. At blue optical colors ($U-V<1$), the attenuation is seriously underestimated. An overestimate of the age by a similar order of magnitude

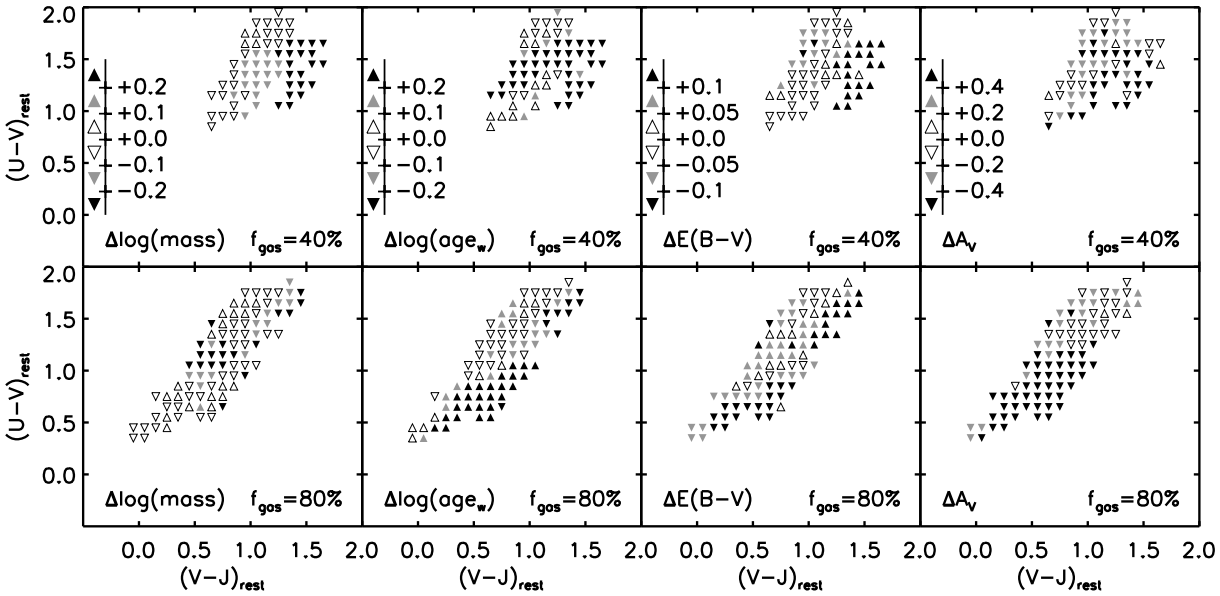

Figure 6.15 — Median quality of recovered stellar population properties for simulations with a gas fraction of 40% and 80% as a function of rest-frame optical and optical-to-NIR color. Downward triangles indicate underestimates with respect to the true value. Upward triangles mark overpredictions. Galaxies in regions with white triangles are characterized most accurately. Simulations with $f_{gas} = 80\%$ reach bluer colors in $(U-V)_{rest}$ than those with $f_{gas} = 40\%$ since their initial stars were set to younger ages (see §6.2.1). At red optical colors [$(U-V)_{rest} > 1$], galaxies with relatively blue $(V-J)_{rest}$ colors are better recovered than those at the red $(V-J)_{rest}$ end. The former are older, less obscured systems, while the latter have a young and dusty nature. At blue optical colors [$(U-V)_{rest} < 1$], large systematics in the determination of age and A_V occur. Their opposite signs cancel out in the derivation of stellar mass.

(at $U-V < 0.65$ mostly due to the lower metallicity and at $0.65 < U-V < 1$ due to age-dependent extinction) leads to a relatively robust estimate of the mass.

At red optical colors ($U-V > 1$), sources with relatively blue $V-J$ colors are generally better modeled than those with the reddest $V-J$ colors in our sample. In the $1 < U-V < 1.8$ color regime, the effects of dust attenuation play an important role. Here we find objects that are heavily extincted during the merger-triggered starburst, but also disk galaxies seen edge-on during the earliest phases of the simulation. All sources with $V-J > 1.5$ in our sample belong the latter category. Since we did not impose an age gradient for the initial stars, the dust distribution in thoses cases is non-uniform but uncorrelated with intrinsic color of the stellar particles. This explains why they have the strongest overestimate in $E(B-V)$. The upper part of the color-color distribution ($U-V > 1.8$) is where each galaxy ends up by aging without further inflow of gas. In such a system, the A_V values are modest to low and the lack of a template exactly matching the SFH is less problematic as the epoch of major star formation lies further back in time.

6.5 Results from SED modeling with free redshift

In practice, complete spectroscopic surveys of mass-limited samples of high-redshift galaxies are rare. Consequently, we often are not able to fix the redshift in the SED

modeling procedure to its exact true value. Over the past few years, several codes have improved on estimating the redshift based on the broad-band SED, by experimenting with different template sets and fitting algorithms. In this section, we will use the new photometric redshift code EAZY (Brammer et al. in preparation) to establish the quality of photometric redshift (z_{phot}) estimates derived from our synthetic photometry and analyze the impact of z_{phot} uncertainties on the derived stellar population properties.

6.5.1 The photometric redshift code EAZY

Here, we summarize the main characteristics of the EAZY photometric redshift code. A full description of the algorithm and template sets will be presented by Brammer et al. (in preparation). We test our ability to recover the redshifts using two template sets. The first template set is based on the same BC03 code from which the broad-band photometry of our simulations was derived (§ 6.2.2). This set consists of 10 SSP templates with a Salpeter (1955) IMF, solar metallicity, and ages logarithmically spaced between 50 Myr and 10 Gyr. Each template is allowed to have an attenuation of A_V=0.0, 0.1, 0.3, or 0.6, applied according to the Calzetti et al. (2000) law. We fit a non-negative superposition of what are effectively 40 different templates to the B-to-K_s band photometry, using a template error function that effectively downweights the rest-frame UV portion of the templates in the fit. The maximum likelihood solution is then adopted as best z_{phot} estimate.
The second setup relies on a set of hundreds of PEGASE 2.0 (Fioc & Rocca-Volmerange 1997) templates, closely matching those described by Grazian et al. (2006). The template set includes Calzetti et al. (2000) reddened CSF models to account for the presence of dusty star-forming sources. Since it is completely independent from the photometry of our simulations, it provides a check of robustness against choice of stellar population synthesis code. Given the large number of templates, we now match each template individually to the B-to-K_s band photometry, using the same template error function as for the BC03 templates.

EAZY allows for the use of a magnitude prior function, constructed from observed or simulated number counts as a function of apparent magnitude and redshift. However, since we shift each simulation over the entire redshift range $1.5 \leq z \leq 2.9$, our methodology does not allow to test this feature.

6.5.2 Recovering redshifts and stellar population properties from broad-band photometry

6.5.2.1 Recovering redshifts

In Figure 6.16, we compare the photometric redshifts obtained with EAZY+BC03 and EAZY+Pegase with the input redshifts for which the synthetic broad-band SEDs were computed. The measure commonly used to quantify the photometric redshift quality is $\Delta z/(1+z)$. Its normalized median absolute deviation is 0.030 using the BC03 template set and 0.054 using the Pegase template set. Even when using the Pegase templates, whose population synthesis is largely independent of the input photometry, the performance of EAZY is very good and competitive with that of other codes presented in

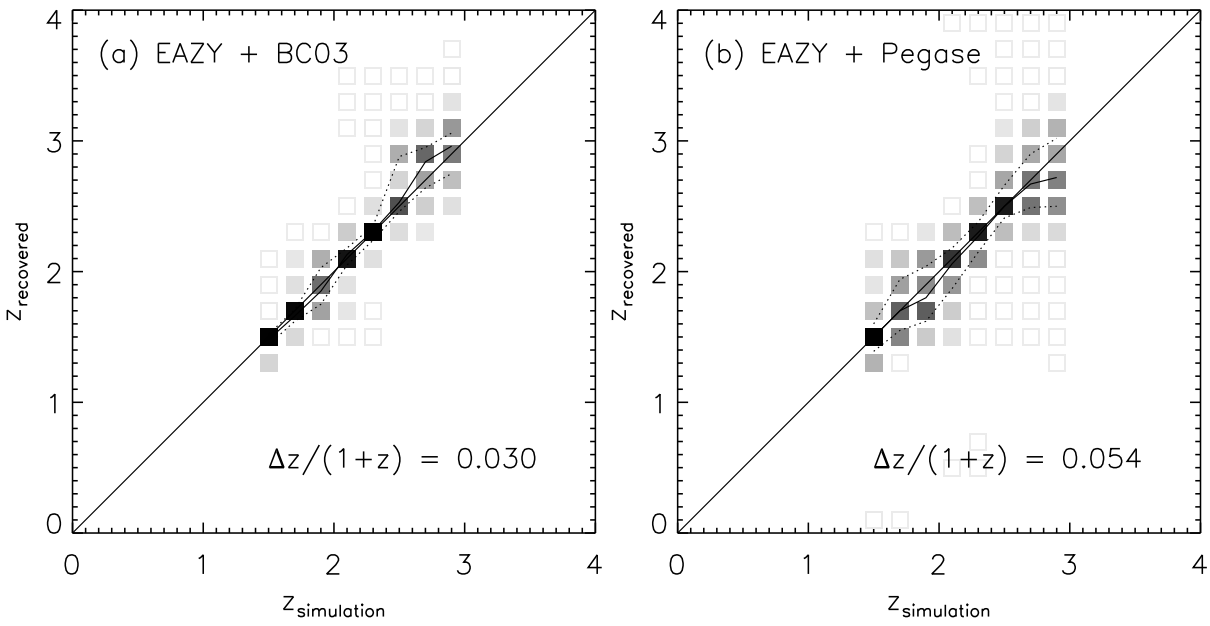

Figure 6.16 — Comparison of photometric redshifts z_{phot} by EAZY versus true redshift for a template set based on (a) the BC03 and (b) the Pegase stellar population synthesis code. The correspondence is good in both cases ($\sigma_{NMAD}(\Delta z/(1+z)) < 0.06$), without significant systematic offsets. The lower scatter for EAZY+BC03 with respect to EAZY+Pegase is likely due to the fact that the input photometry is essentially a function of BC03 single stellar population templates.

the literature.

We find a correlation between $\Delta z/(1+z)$ and the time since (or before) the merger, with opposite sign for the two template sets. For EAZY+BC03, the median $\Delta z/(1+z)$ increases from -0.01 at the start of the simulation to +0.01 at the end 2 Gyr later. For EAZY+Pegase, the median $\Delta z/(1+z)$ drops from +0.02 to -0.02 over the same timespan. The correlation is with time relative to the merger (i.e., phase in star formation history) and not the stellar age. We can tell this by considering separately the 40% and 80% gas fraction simulations, which differ by their initial conditions in mass-weighted age, but show a similar dependence of the z_{phot} accuracy on time relative to the merger. No trend with A_V was found except for the reflection of the correlation with evolutionary time, i.e., the attenuation history is correlated with the star formation history (see Figure 6.1).

This exercise offers a valuable complementary test to the empirical comparison with spectroscopic samples of high-redshift galaxies. The latter are direct measurements and therefore insensitive to our knowledge of stellar tracks and population synthesis. On the other hand, spectroscopic samples of high-redshift galaxies often suffer from selection biases, especially against galaxies lacking emission lines.

6.5.2.2 Impact of z_{phot} uncertainties

Having quantified the quality of photometric redshifts, we now repeat the SED modeling fixing the redshift to its best-fit value (EAZY+BC03). The same mechanisms as discussed in §6.4 are still influencing the recovery of physical parameters. Given the

partially random nature of the z_{phot} uncertainties, it comes as no suprise that the central 68% interval broadens with respect to the SED modeling at fixed redshift. Averaged over time, the broadening amounts to 25%, 10%, 11%, and 15% in $\Delta \log M$, $\Delta \log age_w$, $\Delta E(B-V)_{eff}$, and $\Delta A_{V,eff}$ respectively.

The systematic part of the z_{phot} uncertainty translates into additional but small systematic offsets in the stellar population properties. Qualitatively, when a source is mistakenly placed at higher redshift, a larger mass estimate and lower dust reddening are required to match the observed SED. In numbers, the median of $\log M_{fixz} - \log M_{EAZY+BC03}$ evolves from -0.015 to +0.01 over the timespan of the simulation. $A_{V,fixz} - A_{V,EAZY+BC03}$ evolves from ~ 0 to -0.1 mag, and $E(B-V)_{fixz} - E(B-V)_{EAZY+BC03}$ from +0.01 to -0.02 mag. We find no systematic propagation of the z_{phot} uncertainty in the stellar age. Note that the impact of z_{phot} uncertainties is highly dependent on the template set used, e.g., the systematic dependence on time has the opposite sign when using Pegase templates.

6.6 Summary

We analyzed the performance of a simple SED modeling procedure applied to synthetic optical-to-NIR broad-band SEDs of merger simulations placed at redshifts z=1.5, 1.7, ..., 2.9. First, we modeled the SEDs assuming the redshift was known. The masses, ages, $E(B-V)$, and A_V of simulated ellipticals are very well reproduced, with an average value of $\Delta \log M = -0.01^{+0.04}_{-0.09}$, $\Delta \log age_w = -0.03^{+0.10}_{-0.10}$, $\Delta E(B-V) = -0.04^{+0.08}_{-0.04}$, and $\Delta A_V = -0.27^{+0.25}_{-0.21}$. Here the errors indicate the central 68% interval of the distribution of $\Delta parameter$ values of all the simulations (different masses, gas fractions, viewing angles) in the spheroid regime. In earlier, actively star-forming, phases, the scatter in recovered stellar population properties with respect to the true value increases, and larger systematic underestimates of age, mass, and extinction occur. This is particularly the case for the simulation snapshots of phases with merger-triggered star formation, where we find the following offsets and scatter (averaged over the merger regime indicated in Figure 6.1): $\Delta \log M = -0.11^{+0.09}_{-0.14}$, $\Delta \log age_w = -0.11^{+0.34}_{-0.25}$, $\Delta E(B-V) = -0.01^{+0.09}_{-0.09}$, and $\Delta A_V = -0.48^{+0.42}_{-0.45}$. The SED modeling performs better on regular star-forming disks than on galaxies during the merging event. Compared to spheroids however, the results of the SED modeling on disks show a larger scatter and larger systematic underestimates: $\Delta \log M = -0.05^{+0.06}_{-0.13}$, $\Delta \log age_w = -0.04^{+0.26}_{-0.27}$, $\Delta E(B-V) = -0.02^{+0.12}_{-0.07}$, and $\Delta A_V = -0.35^{+0.27}_{-0.29}$.

By adding the effects of dust attenuation, metallicity variations and AGN step by step to the basic intrinsic photometry, we were able to disentangle the different mechanisms at play and their impact on the estimation of the mass, age, reddening, and extinction of the galaxy. The qualitative impact on the SED modeling results by different aspects of the galaxy content is summarized in Table 6.1.

A mismatch between the real SFH and the allowed template SFHs leads to an inability to account for the difference between light-weighted and mass-weighted properties such as stellar age and mass. If the optical depth toward intrinsically bluer emitting sources is larger than to intrinsically redder stellar populations, the netto effect of the age and mass underestimate due to mismatch between true and template SFH is less

severe. We find proof of such an increased extinction toward younger stars during the merger-triggered starburst. Applying the Calzetti et al. (2000) reddening law toward each stellar particle, we find that the overall reddening for a given A_V is less than predicted by the Calzetti et al. (2000) law, particularly when the optical depth is uncorrelated with the intrinsic colors of the sources it is hiding. In the latter case, the dust vector has a shallower slope in the $U-V$ versus $V-J$ color-color diagram than the Calzetti et al. (2000) vector. In the case of larger optical depths toward young (blue) stellar populations, there is relatively more reddening in $U-V$ for a given reddening in $V-J$. Applying a MW or SMC-like attenuation law to the individual stellar particles in the simulation increases the reddening, but the effective extinction is still greyer than the Calzetti et al. (2000) law.

All other properties remaining the same, the effect of applying our SED modeling to stellar populations with sub-solar metallicities is that one would underpredict the reddening. For the young ages where such sub-solar metallicities could be expected, interpreting the light as coming from a solar-metallicity population will lead to an overestimate of the stellar age.

Finally, our SED modeling is based on purely stellar emission. During the brief period when the AGN contribution is significant, the addition of its light will make the galaxy look younger and dustier.

We next repeated our analysis adopting the best-fit photometric redshift estimate. Using the photometric redshift code EAZY (Brammer et al. in preparation) in combination with a set of BC03 templates or Pegase templates, we obtain a median normalized absolute deviation $\sigma_{NMAD}(\Delta z/(1+z)) = 0.030$ or 0.054 respectively. The random uncertainty in z_{phot} boosts the scatter in the quality measures $\Delta \log M$, $\Delta \log age_w$, $\Delta E(B-V)$, and ΔA_V, by 10-25% in the case of EAZY+BC03. A slight dependence on time with respect to the merger (opposite in sign for the two template sets) propagates into systematic differences in the estimated stellar mass, on the 6% level for EAZY+BC03 between the start and end of the simulation 2 Gyr later. Offsets in reddening and visual extinction A_V are anti-correlated with $\Delta z/(1+z)$.

Acknowledgments

We thank Eric Bell, Yuexing Li and Sukanya Chakrabarti for useful discussions in the process of writing this chapter. The hospitality of the Institute for Theory and Computation during several working visits is gratefully acknowledged. This work was supported by the Netherlans Foundation for Research (NWO), the Leids Kerkhoven-Bosscha Fonds, and the Lorentz Center.

Table 6.1. Qualitative summary of systematic trends in recovering stellar population properties.

Effect	on age	on $E(B-V)$	on A_V	on mass
SFH mismatch (higher SFR than in the past)	-	+	-	-
Non-uniform extinction (uncorrelated with intrinsic colors of emitters)	-	+	-	-
Age-dependent extinction (more extinction toward young stars)	+	-	-	-[a]
$Z < Z_\odot$	+	-	-	+[b]
AGN	-	+	+	+[c]

[a]The overestimated age and underestimated A_V compete in the determination of stellar mass. Since in practise we find this effect to be most outspoken in phases where the SFH mismatch is largest, the stellar mass will effectively be underestimated.

[b]Here too, the systematic offsets in age and A_V have an opposite sign. From comparison of mass estimates based on the full attenuated photometry and its equivalent with all stars fixed to $Z_\odot$, we find the effective $\Delta \log M$ is positive.

[c]Similar to (b), we compared the results from SED modeling with/out AGN contribution and find that in the median the addition of AGN light increases the mass estimate slightly.

References

Barnes, J. E.,& Hernquist, L. 1996, ApJ, 471, 115
Barnes, J. E.,& Hernquist, L. 1991, ApJ, 370, L65
Bell, E. F.,& de Jong, R. S. 2001, ApJ, 550, 212
Bolzonella, M., Miralles, J.-M.,& Pelló, R. 2000, A&A, 363, 476
Bruzual, G.,& Charlot, S. 2003, MNRAS, 344, 1000 (BC03)
Bullock, J. S., Kolatt, T. S., Sigad, Y., Somerville, R. S., Kravtsov, A. V., Klypin, A. A., Primack, J. R.,& Dekel, A. 2001, MNRAS, 321, 559
Calzetti, D., et al. 2000, ApJ, 533, 682
Cox, T. J., Dutta, S. N., Di Matteo, T., Hernquist, L., Hopkins, P. F., Robertson, B.,& Springel, V. 2006, ApJ, 650, 791
Daddi, E., et al. 2007, astro-ph/07052832
Di Matteo, T., Springel, V.,& Hernquist, L. 2005, Nature, 433, 604
Driver, S. P., Windhorst, R. A.,& Griffiths, R. E. 1995, ApJ, 453, 48
Edmunds, M. G. 1990, MNRAS, 246, 678
Erb, D. K., Shapley, A. E., Pettini, M., Steidel, C. C., Reddy, N. A.,& Adelberger, K. L. 2006a, ApJ, 644, 813
Erb, D. K., Steidel, C. C., Shapley, A. E., Pettini, M., Reddy, N. A.,& Adelberger, K. L. 2006b, ApJ, 646, 107
Erb, D. K., Steidel, C. C., Shapley, A. E., Pettini, M., Reddy, N. A.,& Adelberger, K. L. 2006c, ApJ, 647, 128
Ferguson, H. C., Dickinson, M., Papovich, C. 2002, ApJ, 569, 65
Fioc, M.,& Rocca-Volmerange, B. 1997, A&A, 326, 950
Förster Schreiber, N. M., et al. 2004, ApJ, 616, 40
Förster Schreiber, N. M., et al. 2006, AJ, 131, 1891
Franx, M., Illingworth, G. D., Kelson, D. D., van Dokkum, P. G.,& Tran, K. 1997, ApJ, 486, L75
Genzel, R., et al. 1998, ApJ, 498, 579
Glazebrook, K., Ellis, R. S., Santiago, B.,& Griffiths, R. 1995, MNRAS, 275, L19
Grazian, A., et al. 2006a, A&A, 449, 951
Hernquist, L. 1989, Nature, 340, 687
Holden, B. P., et al. 2005, ApJ, 620, 83
Holmberg, E. 1941, ApJ, 94, 385
Hopkins, P. F., Hernquist, L., Martini, P., Cox, T. J., Robertson, B., Di Matteo, T.,& Springel, V. 2005a, ApJ, 625, L71
Hopkins, P. F., Hernquist, L., Cox, T. J., Di Matteo, T., Martini, P., Robertson, B.,& Springel, V. 2005b, ApJ, 630, 705
Hopkins, P. F., Richards, G. T.,& Hernquist, L. 2007, ApJ, 654, 731
Kriek, M., et al. 2006, ApJ, 645, 44
Kriek, M., et al. 2006, astro-ph/0611724
Labbé, I., et al. 2003, AJ, 125, 1107
Larson, R. B.,& Tinsley, B. M. 1978, ApJ, 219, 46
Mihos, J. C.,& Hernquist, L. 1994, ApJ, 431, L9
Mihos, J. C.,& Hernquist, L. 1996, ApJ, 464, 641
Noguchi, M. 1988, A&A, 203, 259
O'Connell, R. W. 1986, in Stellar Populations, ed. C. Norman, A. Renzini,& M. Tosi (Cambridge: Cambridge Univ. Press), 213
Panuzzo, P., Granato, G. L., Buat, V., Inoue, A. K., Silva, L., Iglesias-Páramo, J.,& Bressan, A. 2007, MNRAS, 375, 640
Papovich, C., Dickinson, M., & Ferguson, H. C. 2001, ApJ, 559, 620
Papovich, C., Dickinson, M., Giavalisco, M., Conselice, C. J.,& Ferguson, H. C. 2005, ApJ, 631, 101
Papovich, C., et al. 2006, ApJ, 640, 92
Pei, Y. C. 1992, ApJ, 395, 130
Pettini, M., Kellogg, M., Steidel, C. C., Dickinson, M., Adelberger, K. L.,& Giavalisco, M. 1998, ApJ, 508, 539

Pettini, M., et al. 2001, ApJ, 554, 981
Reddy, N. A., Erb, D. K., Steidel, C. C., Shapley, A. E., Adelberger, K. L,& Pettini, M. 2005, ApJ, 633, 748
Richards, G. T., et al. 2006, ApJS, 166, 470
Robertson, B., Cox, T. J., Hernquist, L., Franx, M., Hopkins, P. F., Martini, P.,& Springel, V. 2006, ApJ, 641, 21
Sanders, D. B., Soifer, B. T., Elias, J. H., Madore, B. F., Matthews, K., Neugebauer, G.,& Scoville, N. Z. 1988a, ApJ, 325, 74
Sanders, D. B., Soifer, B. T., Elias, J. H., Neugebauer, G.,& Matthews, K. 1988b, ApJ, 328, L35
Sanders, D. B.,& Mirabel, I. F. 1996, ARA&A, 34, 749
Shapley, A. E., Steidel, C. C., Adelberger, K. L., Dickinson, M., Giavalisco, M.,& Pettini, M. 2001, ApJ, 562, 95
Shapley, A. E., Steidel, C. C., Pettini, M.,& Adelberger, K. L. 2003, ApJ, 588, 65
Shapley, A. E., Steidel, C. C., Erb, D. K., Reddy, N. A., Adelberger, K. L., Pettini, M., Barmby, P.,& Jiasheng, H. 2005, ApJ, 626, 698
Springel, V.,& Hernquist, L. 2003, MNRAS, 339, 289
Springel, V., Di Matteo, T.,& Hernquist, L. 2005a, ApJ, 620, L79
Springel, V., Di Matteo, T.,& Hernquist, L. 2005b, MNRAS, 361, 776
Toomre, A.,& Toomre, J. 1972, ApJ, 178, 623
Toomre, A. 1977, in Evolution of Galaxies and Stellar Populations, 401, Yale Univ. Obs: New Haven
van Dokkum, P. G.,& Stanford, S. A. 2003, ApJ, 585, 78
van Dokkum, P. G., et al. 2004, ApJ, 611, 703
Wuyts, S., et al. 2007, ApJ, 655, 51
Zwicky, F. 1956, Ergebnisse der Exakten Naturwissenschaften, 29, 344

Chapter 7

Color distributions, number and mass densities of massive galaxies at $1.5 < z < 3$: comparing observations with merger simulations

Abstract. We present a comparison between the observed color distribution, number and mass density of massive galaxies at $1.5 < z < 3$ and a model by Hopkins et al. that relates the quasar and galaxy population on the basis of gas-rich mergers. In order to test the hypothesis that quiescent red galaxies are formed after a gas-rich merger involving quasar activity, we confront photometry of massive ($M > 4 \times 10^{10}\ M_{\odot}$) galaxies extracted from the FIRES, GOODS-South, and MUSYC surveys, together spanning an area of 430 arcmin^2, with synthetic photometry from hydrodynamical merger simulations. The merger simulations are placed in a cosmological context using the observed quasar luminosity function. We find that the synthetic $U - V$ and $V - J$ colors of galaxies that had a quasar phase in their past match the colors of observed galaxies that are best characterized by a quiescent stellar population. The model predicts a number density of quiescent red galaxies with $M > 4 \times 10^{10}\ M_{\odot}$ of $3.6 \pm 0.6 \times 10^{-4}\ Mpc^{-3}$ at $z \sim 1.9$ and $1.0 \pm 0.2 \times 10^{-4}\ Mpc^{-3}$ at $z \sim 2.6$, while the observations amount to $2.3^{+0.8}_{-0.6} \times 10^{-4}\ Mpc^{-3}$ at $z \sim 1.9$ and $1.3^{+0.6}_{-0.4} \times 10^{-4}\ Mpc^{-3}$. The corresponding mass densities are $4.4 \pm 0.6 \times 10^{7}\ M_{\odot}\ Mpc^{-3}$ at $z \sim 1.9$ and $1.3 \pm 0.3 \times 10^{7}\ M_{\odot}\ Mpc^{-3}$ at $z \sim 2.6$ for the model against $2.9^{+1.0}_{-0.7} \times 10^{7}\ M_{\odot}\ Mpc^{-3}$ at $z \sim 1.9$ and $2.0^{+0.9}_{-0.6} \times 10^{7}\ M_{\odot}\ Mpc^{-3}$ for the observations. Hence, the data are consistent with the models in which every quiescent massive galaxy underwent a quasar phase in the past. The merger model also predicts a large number and mass density of galaxies undergoing star formation driven by the merger. We find that the number and mass density is consistent with the observations of star-forming galaxies. However, their colors do not match those of observed star-forming galaxies. In particular, the colors of dusty red galaxies are not reproduced by the simulations. Several possible origins of this discrepancy are discussed, ranging from the method to compute the model predictions to the validity of the model assumptions to physical mechanisms such as a large-scale wind producing a foreground screen of obscuring material and thus leading to more efficient reddening

S. Wuyts, T. J. Cox, N. M. Förster Schreiber, M. Franx, L. Hernquist,
P. F. Hopkins, I. Labbé, B. Robertson, G. Rudnick, S. Toft & P. G. van Dokkum

7.1 Introduction

In recent years, deep near- and mid-infrared observations have revealed significant populations of red galaxies at redshifts $z \sim 2$ and above (Franx et al. 2003; Daddi et al. 2004; Yan et al. 2004). The population of Distant Red Galaxies (DRGs), selected by the simple observed color criterion $J - K > 2.3$, makes up 66% in number and 73% in mass of the $2 < z < 3$ galaxy population at the high mass end ($M > 10^{11}\ M_{\odot}$, van Dokkum et al. 2006). Probing to lower masses, Wuyts et al. (2007) found that the lower mass galaxies at redshifts $2 < z < 3.5$ have bluer rest-frame $U - V$ colors compared to the most massive galaxies. A substantial fraction of the massive red galaxies at high redshift are best characterized by a quiescent stellar population on the basis of their broad-band SEDs (Labbé et al. 2005; Wuyts et al. 2007) and the presence of a Balmer/4000Å break and absence of emission lines in their rest-frame optical spectra (Kriek et al. 2006).

Any satisfying theory of galaxy formation has to account for the presence and abundance of these massive red galaxies in the early universe, a condition that was by no means met by the state-of-the-art hierarchical galaxy formation models at the time of their discovery (Somerville 2004).

In the meantime, merger scenarios involving AGN activity have been invoked by semi-analytic models (Granato et al. 2004; Croton et al. 2006; Bower et al. 2006; De Lucia & Blaizot 2007) and hydrodynamical simulations (Springel et al. 2005a; Di Matteo et al. 2005) to explain simultaneously the mass build-up of galaxies and the shutdown of star formation. Such an evolutionary scenario predicts an obscured (and thus red) star-burst phase and ends with a quiescent (and thus red) remnant galaxy (e.g., Hopkins et al. 2006a). Observational support for the connection between dust-enshrouded starbursts, merging, and AGN activity from samples of nearby Ultra-Luminous Infrared Galaxies (ULIRGs) dates from as early as Sanders et al. (1988). Furthermore, the observed relation between the supermassive black hole (SMBH) mass and the mass (Magorrian et al. 1998) or the velocity dispersion (Ferrarese & Merritt 2000; Gebhardt et al. 2000) of their host suggests that black hole and galaxy growth are intimately connected. This scaling relation can be reproduced by merger simulations with implemented AGN feedback (Robertson et al. 2006).

Motivated by the observed and simulated correlations between the properties of SMBHs and their hosts, Hopkins et al. (2006b) used the observed quasar luminosity function to derive the galaxy merger rate as a function of mass. This chapter uses the merger rate function derived by this model in combination with hydrodynamical SPH simulations to predict the color distribution, number and mass density of massive galaxies in the redshift range $1.5 < z < 3$ under the assumption that each galaxy once had or will undergo a quasar phase. We discuss the systematics involved and compare the results to mass-limited samples in the same redshift interval, extracted from the multi-wavelength surveys FIRES (Franx et al. 2000; Labbé et al. 2003; Förster Schreiber et al. 2006), GOODS-South (Giavalisco et al. 2004; Chapter 3), and MUSYC (Quadri et al. 2006).

We give an overview of the observations and simulations in §7.2 and §7.3 respectively. Next, the sample selection is explained in §7.4. §7.5 addresses the methodology

to place the binary merger simulations in a cosmological context. We compare the predicted abundance of massive galaxies by the model to the observations in §7.6. The optical and optical-to-NIR color distribution of observed and simulated massive galaxies will be addressed in §7.7, followed by a discussion of their specific star formation rates (§7.8) and of the number and mass density of quiescent and star-forming massive galaxies in §7.9. We briefly compare observed and modeled pair statistics and address a few caveats on the observational and modeling results in §7.10. Finally, we summarize results in §7.11.

We work in the AB magnitude system throughout the chapter and adopt a $H0 = 70\ km\ s^{-1}\ Mpc^{-1}$, $\Omega_M = 0.3$, $\Omega_\Lambda = 0.7$ cosmology.

7.2 Overview of the observations

7.2.1 Fields, coverage, and depth

We combine K_s-band selected catalogs of three different surveys: FIRES, GOODS-South, and MUSYC. The reduction and photometry of the FIRES observations of the Hubble Deep Field South (HDFS) is presented by Labbé et al. (2003) and was later augmented with IRAC data. The field reaches a K_s-band depth of 25.6 mag (AB, 5σ for point sources) and covers 5 arcmin^2. It was exposed in the WFPC2 U_{300}, B_{450}, V_{606}, I_{814} passbands, the ISAAC J_s, H, and K_s bands, and the 4 IRAC channels. Following similar procedures, a K_s-band selected catalog for the FIRES MS 1054–03 field was constructed by Förster Schreiber et al. (2006). The field, covering 24 arcmin^2, has a K_s-band depth of 25 mag (AB, 5σ for point sources). The catalog comprises FORS1 U, B, and V, WFPC2 V_{606}, and I_{814}, ISAAC J, H, and K_s, and IRAC 3.6 μm - 8.0 μm photometry.

Over a significantly larger area (113 arcmin^2), but to a shallower depth, a K_s-band selected catalog was constructed based on the publicly available GOODS-South data (Chapter 3). The variations in exposure time and observing conditions between the different ISAAC pointings lead to an inhomogeneous depth over the whole GOODS-South field. The 90% completeness level in the K_s-band mosaic is reached at an AB magnitude of $K_{tot,AB} = 23.7$. The photometry was performed in an identical way to that of the FIRES fields, allowing a straightforward combination of the three fields. The included passbands are the ACS B_{435}, V_{606}, i_{775}, and z_{850} bands, the ISAAC J, H, and K_s bands, and the 4 IRAC channels. We also use the ultradeep MIPS 24 μm (20 μJy, 5σ) imaging of the GOODS-South field. As for the IRAC bands, we used the information on position and extent of the sources from the higher resolution K_s-band image to reduce confusion effects on the 24 μm photometry (Labbé et al. in preparation).

Finally, we complement the FIRES and GOODS-South imaging with optical-to-NIR observations of the MUSYC HDFS1, HDFS2, and 1030 fields for parts of our analysis. The K_s-band selected catalogs are presented by Quadri et al. (2006). Together, the MUSYC fields span an area of 291 arcmin^2. They reach the 90% completeness level at $K_{tot,AB} = 22.7$. Given the current lack of IRAC data for the MUSYC fields and their shallower depth, they will only be used in the analysis of the rest-frame $U - V$ color distribution of the most massive ($M > 10^{11}\ M_\odot$) high-redshift galaxies.

7.2.2 Redshifts and rest-frame photometry

Despite the large number of spectroscopic campaigns in the GOODS-South and FIRES fields, the fraction of K_s-selected $1.5 < z < 3$ galaxies that is spectroscopically confirmed is only 7%. The fraction drops to 3% when the MUSYC fields are included. Therefore, a reliable estimate of the photometric redshift is crucial in defining robust samples of massive high-redshift galaxies.

Förster Schreiber et al. (in preparation) used the algorithm developed by Rudnick et al. (2001, 2003) to fit a nonnegative linear combination of galaxy templates to the optical-to-NIR spectral energy distribution of each galaxy. The template set used for the FIRES and GOODS-South fields consisted of 10 Single Stellar Population (SSP) templates with a Salpeter (1955) initial mass function and solar metallicity from the Bruzual & Charlot (2003, hereafter BC03) stellar population synthesis code, with ages logarithmically spaced between 50 Myr and 10 Gyr. Each of the templates was allowed to be attenuated according to the Calzetti et al. (2000) law by $E(B-V) = 0.0$, 0.1, 0.3, or 0.6.

The uncertainties in the photometric redshifts were determined from Monte Carlo simulations. For each galaxy, a set of 100 mock SEDs was created by perturbing each flux point according to its formal error bar, and repeating the z_{phot} computation. The lower and upper error on z_{phot} comprise the central 68% of the Monte Carlo distribution.

We tested the quality of the photometric redshifts in two ways. First we compare them to the available spectroscopic redshifts in the $1.5 < z < 3$ interval, resulting in a normalized median absolute deviation $\sigma_{NMAD}\left(\frac{z_{phot}-z_{spec}}{1+z_{spec}}\right) = 0.10$. The quality measure σ_{NMAD} remains the same when the spectroscopic redshifts in the MUSYC fields are included or excluded. Second we tested how well we could recover the redshift from synthetic broad-band photometry of simulated SPH galaxies placed at redshifts 1.5 to 3. We found that the considered template set performed very well ($\sigma_{NMAD}(\Delta z/(1+z)) = 0.03$). The scatter in the comparison to spectroscopically confirmed galaxies is larger than that derived from the simulations. This is likely due to the fact that the synthetic photometry is based on the same stellar population synthesis code as the template set used to recover the redshifts. Therefore, the second test only studies the impact of an unknown star formation history, dust and metallicity distribution on the derived z_{phot}.

We computed the rest-frame photometry by interpolating between observed bands using the best-fit templates as a guide. Uncertainties in the rest-frame colors were derived from the same Monte Carlo simulations mentioned above, and comprise both a contribution from photometric uncertainties and from z_{phot} uncertainties. For a detailed description, we refer the reader to Rudnick et al. (2003).

7.2.3 Stellar masses

Förster Schreiber et al. (in preparation) derived stellar masses of the observed galaxies following the procedure described by Wuyts et al. (2007). Briefly, we fit BC03 templates to the optical-to-8 μm SED with the HYPERZ stellar population fitting code, version 1.1 (Bolzonella et al. 2000). We allow the following star formation histories: a single stellar

population (SSP) without dust, a constant star formation history (CSF) with dust, and an exponentially declining star formation history with an *e*-folding timescale of 300 Myr (τ_{300}) with dust. The allowed A_V values ranged from 0 to 4 in step of 0.2, and the attenuation law applied was taken from Calzetti et al. (2000). We constrain the time since the onset of star formation to lie between 50 Myr and the age of the universe at the respective redshift. Finally, a Salpeter (1955) IMF was assumed with lower and upper mass cut-offs of 0.1 $M_\odot$ and 100 $M_\odot$. For consistency, the same IMF was adopted by the simulations.

7.2.4 Star formation rates

We derived estimates of the total (unobscured plus obscured) star formation rate of the observed galaxies by adding the UV and IR light, scaled by the calibrations for the local universe (Kennicutt 1998):

$$SFR\ [M_\odot\ yr^{-1}] = 1.8 \times 10^{-10} \left(L_{IR} + 3.3 L_{2800}\right) / L_\odot \tag{7.1}$$

where the rest-frame luminosity $L_{2800} \equiv \nu L_\nu(2800\mathring{A})$ was derived from the observed photometry with the algorithm by Rudnick et al. (2003). The total IR luminosity $L_{IR} \equiv L(8 - 1000\ \mu\mathrm{m})$ was derived from the observed 24 μm flux density in combination with the photometric redshift estimate (spectroscopic when available) following the prescription of Dale & Helou (2002). As best estimate, we adopt the mean conversion factor of all Dale & Helou (2002) IR spectral energy distributions within the range $\alpha = 1 - 2.5$, where α parameterizes the heating intensity level from active ($\alpha = 1$) to quiescent ($\alpha = 2.5$) galaxies. The variation from $L_{IR,\alpha=2.5}$ to $L_{IR,\alpha=1}$ is 0.9 dex in the redshift interval $1.5 < z < 3$. Where relevant, we indicate this systematic uncertainty in the conversion from 24 μm to L_{IR} and eventually star formation rate in the plots.

7.3 Overview of the simulations

We use a set of smoothed particle hydrodynamics (SPH, Lucy 1977; Gingold & Monaghan 1977) simulations performed by Robertson et al. (2006) of co-planar, equal-mass, gas-rich ($f_{gas} = 0.8$) mergers over a range of galaxy masses. A description of the GADGET-2 code used to run the simulations is given by Springel (2005b). Springel & Hernquist (2003) describe the prescriptions for star formation and supernova feedback. The interplay between the supermassive black hole(s) and the environment is discussed by Springel et al. (2005b). We refer the reader to Robertson et al. (2006) for specifications on this particular set of simulations and an explanation of how the progenitors were scaled to approximate the structure of disk galaxies at redshift $z = 3$. The photometry of the snapshots was derived in post-processing as described in Chapter 6.

Briefly, the total attenuated spectral energy distribution (SED) for a given snapshot consisting of N stellar particles is computed as follows:

$$\begin{aligned} L_{Att,tot}(\lambda) \ &= \sum_{i=1}^{N} \ m_i \cdot L_{Int}(age_i, Z_i, \lambda) \\ &\quad \cdot \exp\left[-NH_{i,los} \cdot \frac{Z_{i,los}}{Z_\odot} \cdot \sigma(\lambda)\right] \end{aligned} \tag{7.2}$$

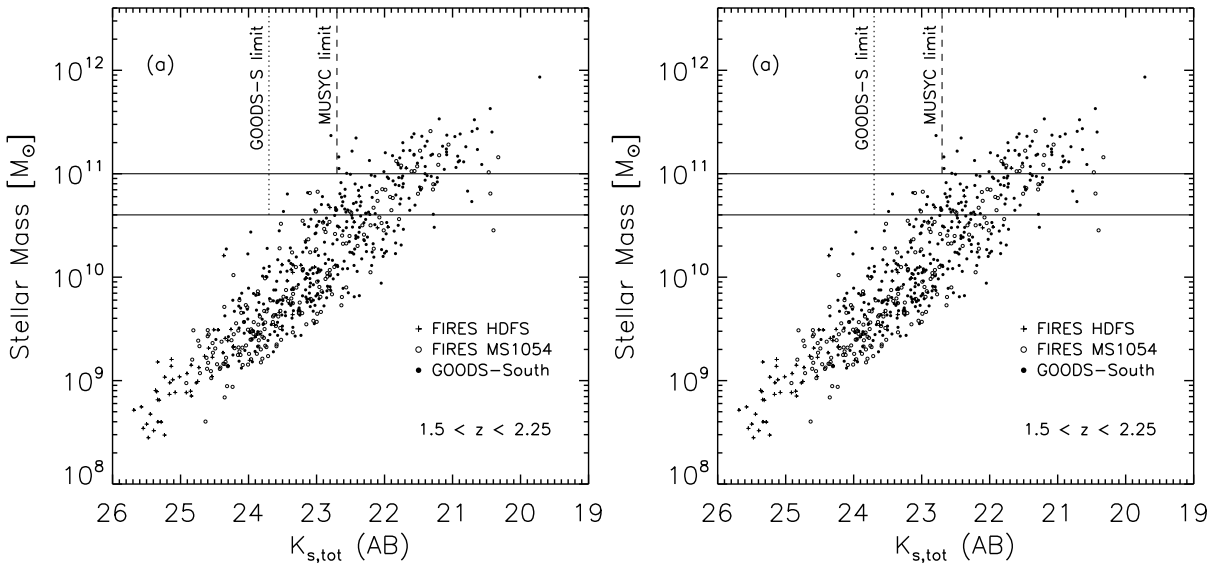

Figure 7.1 — The relation between stellar mass and observed total K_s magnitude for galaxies in the FIRES and GOODS-South fields at (a) $1.5 < z < 2.25$ and (b) $2.25 < z < 3$. The solid lines show the adopted $\log M > 10.6$ (FIRES+GOODS-South) and $\log M > 11$ (FIRES+GOODS-South+MUSYC) mass limits. The dotted line indicates the photometric limit of the GOODS-South imaging. The dashed line indicates the approximate limit for the MUSYC fields. There are few galaxies with $\log M > 10.6$ and $K_{s,tot} > 23.7$, or $\log M > 11$ and $K_{s,tot} > 22.7$. The largest incompleteness correction is needed for the highest redshift bin in the MUSYC fields. A third of the $\log M > 11$ galaxies would be undetected by MUSYC, as estimated from the deeper FIRES+GOODS fields.

where m_i, age_i, and Z_i are, respectively, the mass, age, and metallicity of stellar particle i that is treated as a single stellar population. L_{Int} is the intrinsic (unattenuated) SED interpolated from a grid of templates from a stellar population synthesis code. Here, we use SSP templates from BC03 as default. Results obtained when using a grid of Maraston (2005, hereafter M05) SSP templates for different ages and metallicities will be addressed as well. Parameters in Eq. 7.2 that are dependent on the line of sight are subscripted with "los". To each stellar particle, the column density of hydrogen and the average metallicity along the line of sight was computed for 100 viewing angles, uniformly spaced on a sphere. The optical depth is proportional to this metallicity-scaled column density, with the wavelength dependence adopted from an attenuation law (parameterized by the cross section $\sigma(\lambda)$). We use the Calzetti et al. (2000) reddening curve unless mentioned otherwise. The change in predicted colors when adopting the SMC-like attenuation law from Pei (1992) will be discussed as well.

7.4 Sample selection

Our aim is to compare the color distribution, number and mass density of mass-limited samples of observed and simulated galaxies. We choose the mass-limit such that the observed sample is reasonably complete in the considered redshift interval, even for the field with the shallowest K_s-band depth from which the sample was drawn. In order to optimally exploit the range in area and depth of the considered surveys, we define two mass-limited samples and divide each in two redshift bins: $1.5 < z < 2.25$

and $2.25 < z < 3$, probing a similar comoving volume. The first sample contains galaxies more massive than $\log M = 10.6$ ($M \simeq 4 \times 10^{10}\ M_{\odot}$) in the FIRES and GOODS-South fields. It contains 152 and 84 objects in the low- and high-redshift bin respectively. We present the sample in Figure 7.1, where we plot the stellar mass of all FIRES and GOODS-South sources that are detected above the 5σ level in the respective redshift bin against their total observed K_s-band magnitude. The stellar mass correlates with the K_s-band magnitude, but a scatter of an order of magnitude is present due to the range in redshifts and spectral types of the galaxies. The 90% completeness limit ($K_{s,tot} = 23.7$) for the GOODS-South field , which is shallower than the FIRES fields, is indicated with the dotted line. At $1.5 < z < 2.25$, no massive ($\log M > 10.6$) galaxies fainter than $K_{s,tot} = 23.7$ are found in the FIRES fields and deeper parts of the GOODS-South mosaic. The lowest K_s-band signal-to-noise ratio in the massive galaxy sample is $S/N_{K_s} \simeq 12$, strongly suggesting that no incompleteness correction is needed to compute the number and mass density in the $1.5 < z < 2.25$ redshift bin. In the $2.25 < z < 3$ redshift bin, we find four well-detected massive ($\log M > 10.6$) galaxies fainter than the 90% completeness limit of GOODS-South. Three out of 4 have $6.4 < S/N_{K_s} < 10$, whereas all other massive galaxies are detected above the 10σ level. Evaluating the fraction of massive galaxies fainter than $K_{s,tot} = 23.7$ in the area that is sufficiently deep to detect these sources, we estimate the completeness in the high-redshift bin to be $\sim 95\%$.

In order to reduce the uncertainty from cosmic variance in the derived number and mass densities, we also compose a sample including the MUSYC fields, increasing the sampled area by roughly a factor of 3. The shallower depth forces us to restrict the mass limit to $M > 10^{11}\ M_{\odot}$. We derive the completeness in the two redshift intervals using the deeper FIRES and GOODS-South fields in Figure 7.1. The dashed line marks the approximate depth (90% completeness) for the MUSYC fields. 1.5% of the $1.5 < z < 2.25$ galaxies with $\log M > 11$ in the deeper FIRES and GOODS-South fields are fainter than this limit. For the $2.25 < z < 3$ bin, the fraction of massive galaxies that would be missed by MUSYC increases to 33%. In our analysis, we will mention both the directly measured number and mass densities and those obtained after the incompleteness correction.

7.5 Methodology for cosmological context

To date, hydrodynamical simulations including a self-consistent treatment of SMBH growth have only been run with adequate resolution on binary merger systems (Springel et al. 2005a; Di Matteo et al. 2005; Robertson et al. 2006; Cox et al. 2006) or as zoom-in on overdense regions of cosmological N-body simulations at very high redshift $z \sim 6$ (Li et al. 2006). In order to confront observations of $1.5 < z < 3$ galaxies with the hydrodynamical simulations, we place the binary mergers in a cosmological context using the observed quasar luminosity function following the prescription by Hopkins et al. (2006b).

Briefly, the conversion from quasar demographics to galaxy demographics goes as follows. From a large set of binary merger simulations, Hopkins et al. (2006a) determined the distribution of quasar lifetimes, describing the time $\frac{dt(L,L_{peak})}{d\log(L)}$ spent by a

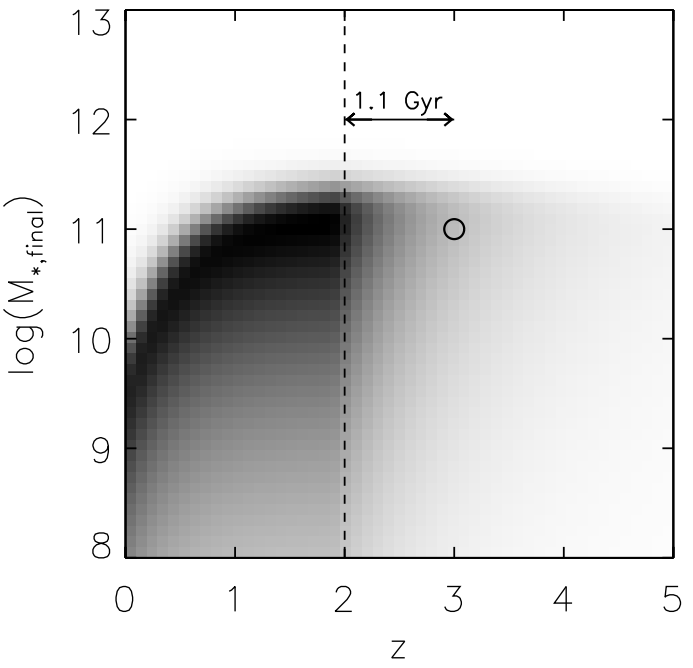

Figure 7.2 — The birth rate of spheroids (in greyscale) as a function of redshift and final stellar mass as derived from the observed quasar luminosity function. The meaning of the time scale arrow and the open circle is described in the text. The model by Hopkins et al. (2006b) assumes that this birth rate equals the merger rate of galaxies. The birth rate (i.e., merger rate) reaches a maximum of 4.5×10^{-4} $\log M^{-1}$ Mpc^{-3} Gyr^{-1} at $z \sim 2$. As time evolves, the peak of the merger rate function shifts toward lower mass galaxies.

quasar of peak luminosity L_{peak} in the luminosity interval $d\log(L)$. The observed quasar luminosity function simply corresponds to the convolution of this differential quasar lifetime with the birth rate $\dot{n}(L_{peak})$ of quasars with peak luminosity L_{peak}:

$$\Phi(L) = \int \frac{dt(L, L_{peak})}{d\log(L)}\, \dot{n}(L_{peak})\, d\log L_{peak} \tag{7.3}$$

Using a compilation of observed quasar luminosity functions in the hard X-rays (Ueda et al. 2003), soft X-rays (Hasinger, Miyaji,& Schmidt 2005), and optical (Richards et al. 2005), Eq. 7.3 was then de-convolved to solve for $\dot{n}(L_{peak})$. The relation between peak luminosity of the quasar and the final black hole mass, derived from the same simulations, was then adopted to calculate the birth rate of black holes of a certain final mass $\dot{n}(M_{BH})$. This function was on its turn converted to a birth rate of spheroids $\dot{n}(M_{sph})$ as a function of their final stellar mass using the SMBH-host connection $M_{BH} = 0.0012\, \frac{(1+z^{2.5})}{\left(1+\left(\frac{z}{1.775}\right)^{2.5}\right)}\, M_{sph}$ (Hopkins et al. 2007).

The model by Hopkins et al. (2006b) assumes that the birth rate of spheroids equals the major merger rate of galaxies. The resulting merger rate as a function of stellar mass is displayed with greyscales in Figure 7.2 (darker meaning a higher merger rate). Its redshift-dependence was derived by considering observed quasar luminosity functions at a range of redshifts. The peak of the merger rate at $z \sim 2$ has a value of 4.5×10^{-4} $\log M^{-1}$ Mpc^{-3} Gyr^{-1}. A clear trend is visible of mergers occuring in lower mass systems as we proceed in time (i.e., to lower redshifts) after this peak. If mergers are responsible for a significant part of the growth in stellar mass, this trend explains at least qualitatively the observed downsizing of star formation over cosmic time (Cowie et al. 1996).

To evaluate the post-merger (i.e., post-quasar, since the merging event triggers

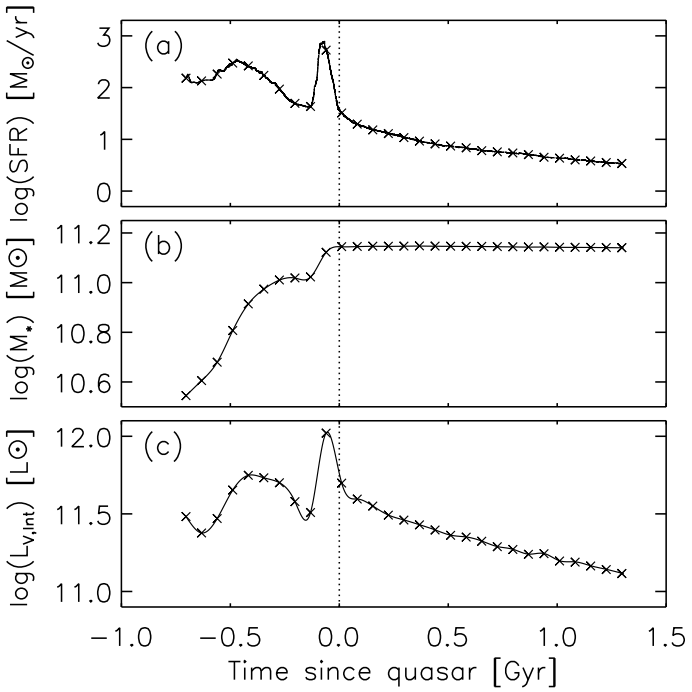

Figure 7.3 — Typical evolution of a merger simulation: (a) star formation history, (b) history of the mass build-up, and (c) evolution of the rest-frame V-band luminosity. The dotted line indicates when the peak in quasar luminosity is reached. For a detailed description of the time evolution in these and other parameters (e.g., accretion rate, quasar luminosity, extinction) we refer the reader to Hopkins et al. (2006a) and Chapter 6.

quasar activity in the simulations) galaxy population at $z \sim 2$, we integrate the merger rate function from $z = \infty$ to 2 and over the whole stellar mass range. For example, when the integration reaches ($M_{*,final} = 10^{11}\ M_{\odot}$; $z = 3$), marked by the circle in Figure 7.2, we compute the photometry of a merger simulation with a final stellar mass of $10^{11}\ M_{\odot}$ at 1.1 Gyr after the peak of quasar luminosity (the time elapsed between $z = 3$ and $z = 2$). As explained in §7.3, we compute the synthetic photometry along 100 lines-of-sight, uniformly spaced on a sphere. The number density of galaxies at $z = 2$ with colors corresponding to the 100 lines-of-sight is then scaled according to the value of the merger rate function at ($M_{*,final} = 10^{11}\ M_{\odot}$; $z = 3$). Finally, a mass cut is applied to guarantee an identical selection of observed and simulated galaxies.

In order to predict the abundance and properties of galaxies at $z \sim 2$ that have yet to reach their peak in quasar luminosity or did not even start merging at the evaluated epoch, one can in principle integrate the merger rate function down to lower and lower redshifts. How far one integrates beyond the evaluated redshift is a rather arbitrary choice. We caution that counting galaxies long before they will contribute to the quasar luminosity function will lead to large uncertainties given their unconstrained pre-merger history. The typical evolution of a merger simulation is illustrated in Figure 7.3 where we plot the star formation rate, stellar mass, and rest-frame V-band luminosity as a function of time since the peak in quasar luminosity. We decide to integrate 700 Myr beyond the evaluated redshift, thus counting both the galaxies that are undergoing a merger-induced nuclear starburst (sometime between 0 and 200 Myr before the quasar phase) and those with star formation triggered by the first passage (sometime between 200 and 700 Myr before the quasar phase). Hereafter, we will refer to all galaxies in an evolutionary stage between 0 and 700 Myr before the quasar phase as merging galaxies. Such a prediction only counts those galaxies that will later merge and produce a quasar. Apart from predicting the abundance and properties of

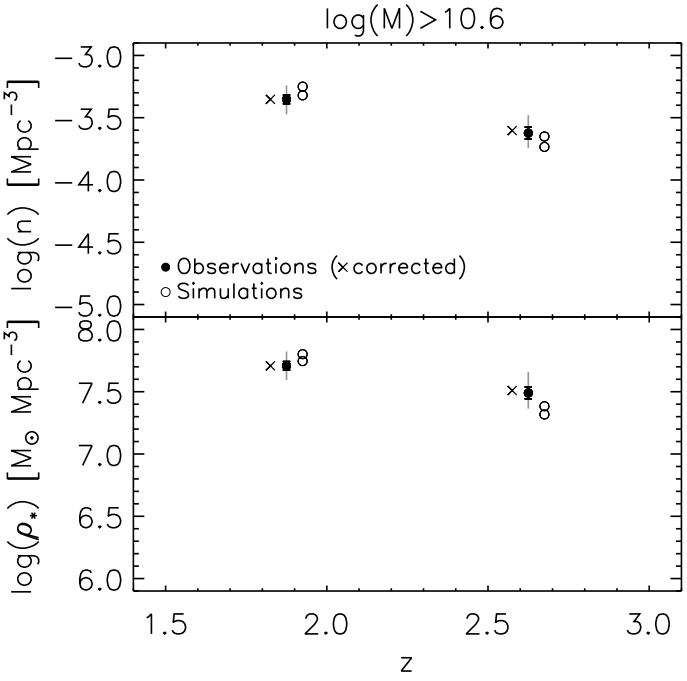

Figure 7.4 — The number and mass density of observed (*filled symbols*; FIRES + GOODS-S) and modeled (*empty symbols*) galaxies with $\log M > 10.6$ as a function of redshift. The cross symbols indicate the observed number and mass density after a correction for incompleteness. The black error bar represents the Poisson shot noise solely. The grey error bar accounts for uncertainties in redshift and mass, and a (dominating) contribution from cosmic variance. We find that both the predicted number and mass densities agree within the error bars with the observed values.

the post-quasar population, we will thus be able to constrain how much of the massive star-forming galaxies can be accounted for by merger-induced star formation.

Provided the assumption of a one-to-one correspondence between quasars and major mergers is valid, the formal uncertainty in the merger rate function presented in Figure 7.2 originates mostly from the weakly constrained faint end of the observed quasar luminosity function, where one can assume a pure luminosity evolution or also a slope evolution. At the bright end, and therefore for our massive galaxy samples, the predictions are robust, as will be indicated in due time.

7.6 The number density, mass density and mass function of galaxies with $\log \mathbf{M} > 10.6$ at $1.5 < \mathbf{z} < 3$

Before analyzing the observed and modeled massive galaxy sample as a function of color and galaxy type, we consider the overall abundance of galaxies above $\log M > 10.6$. We computed the model number and mass density by integrating the merger rate function to 700 Myr beyond the evaluated redshift, i.e., including galaxies up to 700 Myr before the quasar phase. The number and mass densities of galaxies with $\log M > 10.6$ predicted by the model (*empty symbols*) are compared against the abundance of observed galaxies (*filled symbols*) above the same mass limit in Figure 7.4. The results are listed in Table 7.1. The spread of the empty circles indicates the freedom allowed by the model due to the weakly constrained faint end of the quasar luminosity function.

The cross symbols represent the observed number and mass density after applying a 0% and 5% correction for incompleteness in the low- and high-redshift bin respectively. We considered three sources of error in the observations: Poisson shot noise, cosmic variance and selection uncertainties stemming from uncertainties in the redshift and the mass of individual galaxies. The black error bars in Figure 7.4 indicate

the contribution from Poisson noise, ranging from 8 to 10%. We are more severely limited by cosmic variance. We follow the method outlined by Somerville et al. (2004) to calculate the cosmic variance as predicted from cold dark matter theory for a population with unknown clustering as a function of its number density and the probed comoving volume of the sample. The resulting contribution to the error budget is 28% for the $1.5 < z < 2.25$ and 29% for the $2.25 < z < 3$ redshift bin. Finally, the uncertainties in the individual redshift and mass determinations propagate into the number and mass density of quiescent red galaxies. We estimate the contribution to the total error budget from Monte Carlo simulations. We constructed 1000 mock catalogs for the FIRES and GOODS-South fields by perturbing the redshift, rest-frame colors, and stellar masses so that 68% of the perturbed values lie within the formal 1σ lower and upper limits. The uncertainties in the photometric redshift and the rest-frame colors were derived as explained in §7.2.2. For the mass estimates, we adopt a lower error bar of -0.1 dex and upper error bar of +0.04 dex for all merger remnants. This corresponds to the quality with which stellar masses were recovered from synthetic photometry of simulated merger remnants when applying the same SED modeling procedure as we use for our observations (Chapter 6). The median recovered mass was only 0.01 dex lower than the true stellar mass of the simulated merger remnants, suggesting that systematic offsets are negligible for this type of galaxies. For star-forming galaxies that have yet to reach their quasar phase we found a typical mass underestimate of -0.1 dex, with the central 68% interval of $\Delta \log M \equiv \log M_{recovered} - \log M_{true}$ ranging from -0.25 to 0 dex. We should keep in mind however that the input photometry for this test and the templates used to recover the masses are based on the same stellar population synthesis code. It has been noted by several authors (Maraston et al. 2006; van der Wel et al. 2006; Wuyts et al. 2007) that the use of M05 templates instead of BC03 templates leads to stellar mass estimates that are lower by a factor 1.5.

After we constructed the 1000 mock catalogs, we apply the same sample selection (redshift interval, $\log M > 10.6$) and compute the number and mass density for each of them. The lower and upper limits comprising 68% of the distribution of mock number and mass densities were added in quadrature to the uncertainty from Poisson shot noise and cosmic variance, shown with the grey error bar in Figure 7.4. The uncertainty in the number density propagating from redshift and mass uncertainties for individual objects amounts to 5% and 10% for the low and high-redshift bin. The contribution to the uncertainty in the mass density is 6% and 14% for the low- and high-redshift bin respectively. We conclude that, even with the 142 arcmin^2 area of our combined deep fields, cosmic variance is still the limiting factor for the determination of the number and mass density of quiescent red galaxies.

Figure 7.4 shows that the model number and mass density for the population of massive ($\log M > 10.6$) galaxies as a whole agrees within the error bars with the observations. Plotting the mass function for the observations (*black histogram*) and the model (*dark-grey polygon*) in Figure 7.5, we find that the comparable abundance of observed and modeled galaxies still holds when studied as a function of galaxy mass. With lighter grey polygons, we illustrate the model prediction when including only galaxies up to 200 Myr before the merger ($t >$ -200 Myr) or only merger remnants ($t > t_{QSO}$). The width of the polygons reflects the uncertainty in the merger rate func-

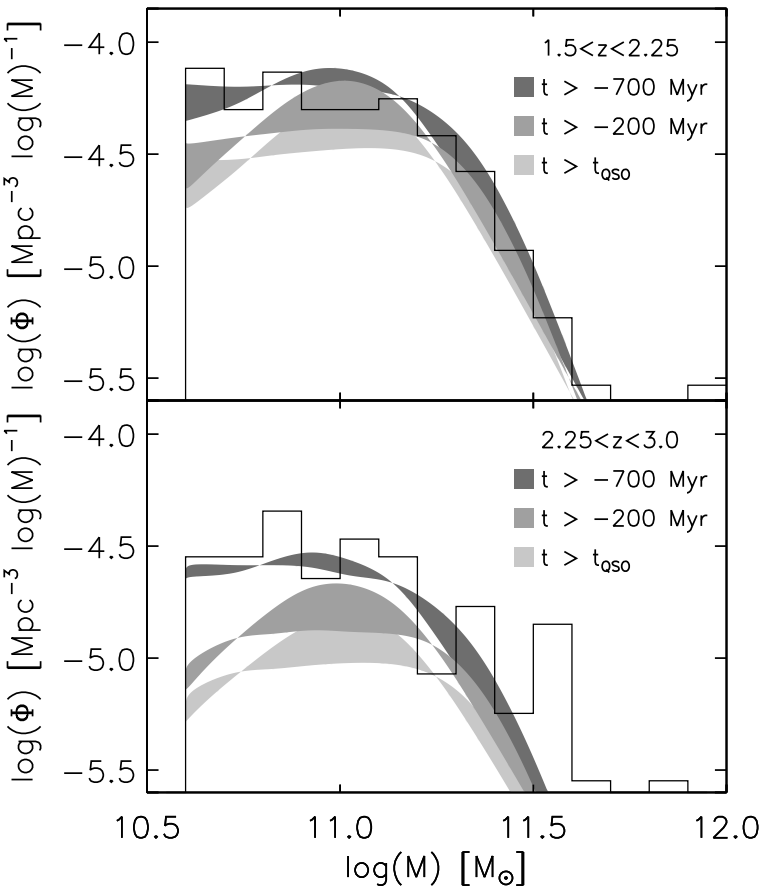

Figure 7.5 — The mass function of observed (*black histogram*; FIRES + GOODS-S) and modeled (*grey polygons*) galaxies with $\log M > 10.6$ at redshift $1.5 < z < 2.25$ (*top panel*) and $2.25 < z < 3.0$ (*bottom panel*). Merger remnants alone ($t > t_{QSO}$) cannot account for the total population of observed galaxies above the same mass limit. Integrating the merger rate function to include galaxies up to 700 Myr before the quasar phase results in a mass function that is consistent with the observations.

tion. We conclude that merger remnants alone cannot account for the entire observed massive galaxy population. However, including galaxies with merger-triggered star formation, the mass function predicted by the model is in good agreement with the observations. This results strengthens the idea that the model fairly reflects reality and encourages a more detailed investigation of the properties of observed and simulated massive galaxies.

7.7 The color distribution of galaxies with $\log \mathbf{M} > 10.6$ at $1.5 < \mathbf{z} < 3$

7.7.1 The U − V color distribution

First, we consider the optical color distribution of our sample of FIRES and GOODS-South galaxies with $M > 4 \times 10^{10}\ M_{\odot}$. A histogram of their rest-frame $U - V$ colors is plotted with a solid line in Figure 7.6(a) and Figure 7.6(b) for the low- and high-redshift bin respectively. No corrections for incompleteness were applied here, but we remind the reader that those are negligible for the low-redshift bin and of the order of 5% only for the high-redshift bin. The total number of massive galaxies is 152 and 85 in the low- and high-redshift bin respectively. They span a broad $U - V$ color range. In both cases, the median color is $U - V = 1.5$ and 68% of the galaxies in each redshift bin lie within the $1.1 < U - V < 1.9$ interval.

It is interesting to consider whether the descendants and progenitors of quasars (or rather quasar hosts) above the same mass limit show colors that are similar and

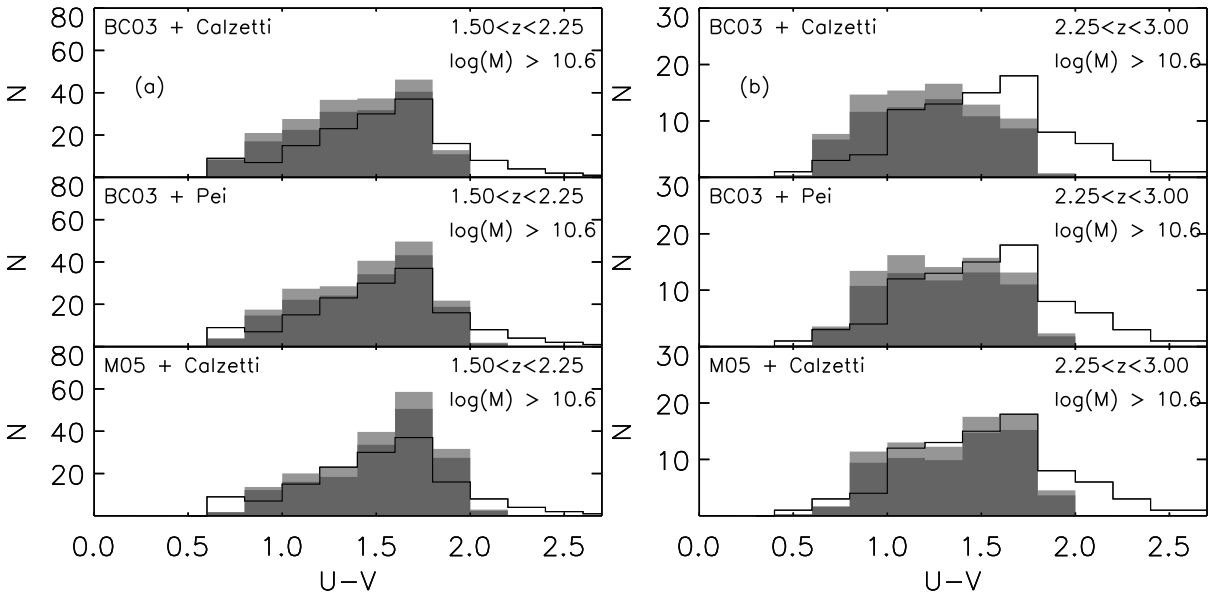

Figure 7.6 — The rest-frame $U - V$ color distribution of observed galaxies with masses above $\log M = 10.6$ in the FIRES and GOODS-South fields (*solid line*) for the redshift intervals (a) $1.5 < z < 2.25$ and (b) $2.25 < z < 3$. With filled histograms, we overplot the predicted $U - V$ color distribution of merging and post-quasar galaxies, scaled to the same solid angle as the observations. The light grey top of the model histogram indicates the uncertainty in the merger rate function used to place the simulated mergers in a cosmological context. For a given redshift interval, the model predictions in the three panels give an indication of the uncertainty in the synthetic photometry induced by the choice of attenuation law (Calzetti et al. 2000 versus the SMC curve from Pei 1992) and the choice of stellar population synthesis code (BC03 versus M05). Overall, the predicted color distribution coincides with that of the observed massive galaxy sample, with roughly equal numbers. The model distribution in the high-redshift bin (b) shows a slight excess at blue $U - V$ colors. The red tail of the observed color distribution is not reproduced by the modeled merger and post-quasar population.

come in numbers comparable to those of the observed massive galaxy sample. In this section, we focus mainly on the first question, but note in passing that we show the predicted color distribution scaled to the same solid angle as probed by the FIRES and GOODS-South observations. The filled grey histograms show the synthetic photometry of merger simulations in either their post-quasar phase or in a phase of at most 700 Myr before their peak in quasar luminosity. The numbers at each color are derived from the observed quasar luminosity function by integrating the merger rate function from $z = \infty$ to 700 Myr beyond the evaluated redshift as described in §7.5. The colors of different evolutionary phases will be discussed seperately in due time. The difference between the dark and light grey histogram reflects the uncertainty in the merger rate function, itself due to uncertainties in the observed quasar luminosity function. Apart from uncertainties in the merger rate function, uncertainties in the synthetic photometry for a given simulation snapshot contribute to the total error budget of the model predictions. To translate the simulated properties such as age, mass, and metallicity of the stellar particles to observables, we make use of a stellar population synthesis code to compute the intrinsic colors and assume an attenuation law to calculate the dimming and reddening by dust. We investigate the dependence on attenuation law

empirically by computing the synthetic photometry using a Calzetti et al. (2000) reddening curve and the SMC-like reddening curve from Pei (1992). We note that the synthetic colors derived with the Milky Way-like attenuation curve by Pei (1992) lie in between those produced by the two reddening curves considerd here. This is demonstrated in Chapter 6. Similarly, we test the dependence on adopted stellar population synthesis templates empirically by computing the synthetic photometry based on a grid of BC03 single stellar populations (SSPs) and based on a grid of SSPs by M05.

We note that the choice of attenuation law has a minor effect only on the $U - V$ color. The use of M05 templates gives the simulated galaxies a slightly redder color. Overall, the same conclusion can be drawn independent of the way the model color distribution was computed. Namely, the simulated galaxies with $\log M > 10.6$ span a color range that reaches from the bluest observed $U - V$ colors to $U - V \sim 2$. At $1.5 < z < 2.25$, the color distribution resembles remarkably well that of the bulk of the observed massive galaxies, both in shape and numbers. At $2.25 < z < 3$, the predicted model colors show a slight excess at blue $U - V$ colors. In both redshift bins, the modeled color distribution does not reach the reddest $U - V$ colors of observed galaxies above the same mass limit. The good overall correspondence between the observed and modeled optical color distributions gives a first indication that the number of massive post-quasar galaxies plus the number of galaxies in the process of merging at $1.5 < z < 3$ as expected from the observed quasar luminosity function may account for a large fraction of the observed massive galaxy population at $1.5 < z < 3$.

7.7.2 The V − J color distribution

Turning to longer wavelengths, we now compare the $V - J$ colors predicted for mergers and merger remnants (i.e., post-quasars) with masses above $\log M = 10.6$ to the color distribution of observed galaxies in the same redshift interval and above the same mass limit (Figure 7.7).

Again, the color distribution of our observed massive galaxy sample has a large range of colors, reaching from $V - J = 0.5$ to $V - J = 2.5$ and peaking centrally at $V - J = 1.3$ and 1.2 for the low- and high-redshift bin respectively. The central 68% interval is $1.0 < V - J < 1.8$ and $0.8 < V - J < 1.8$ for the low- and high-redshift bin respectively.

As for the $U - V$ color distribution, we find that the adopted attenuation law has only a minor influence on the color distribution, reaching at most shifts of 0.2 mag toward redder $V - J$ colors when the SMC-like reddening curve from Pei (1992) is used instead of the Calzetti et al. (2000) attenuation law. Comparing the model $V - J$ color distribution derived from BC03 or M05 templates immediately shows that the predictive power of the merger model is strongly hampered by the uncertainties in the rest-frame NIR wavelength regime that today's stellar population synthesis codes are facing. In the low- and high-redshift bin, the median $V - J$ color of the model distribution is 0.4 and 0.5 mag redder when using M05 than when using BC03. One of the main differences between the BC03 and M05 templates is the treatment of thermally pulsating AGB stars. Using the fuel consumption approach as M05 does instead of the isochrone synthesis approach that BC03 follow, one finds significantly larger NIR luminosities for SSPs at ages between 0.2 and 2 Gyr. For an in-depth discussion of

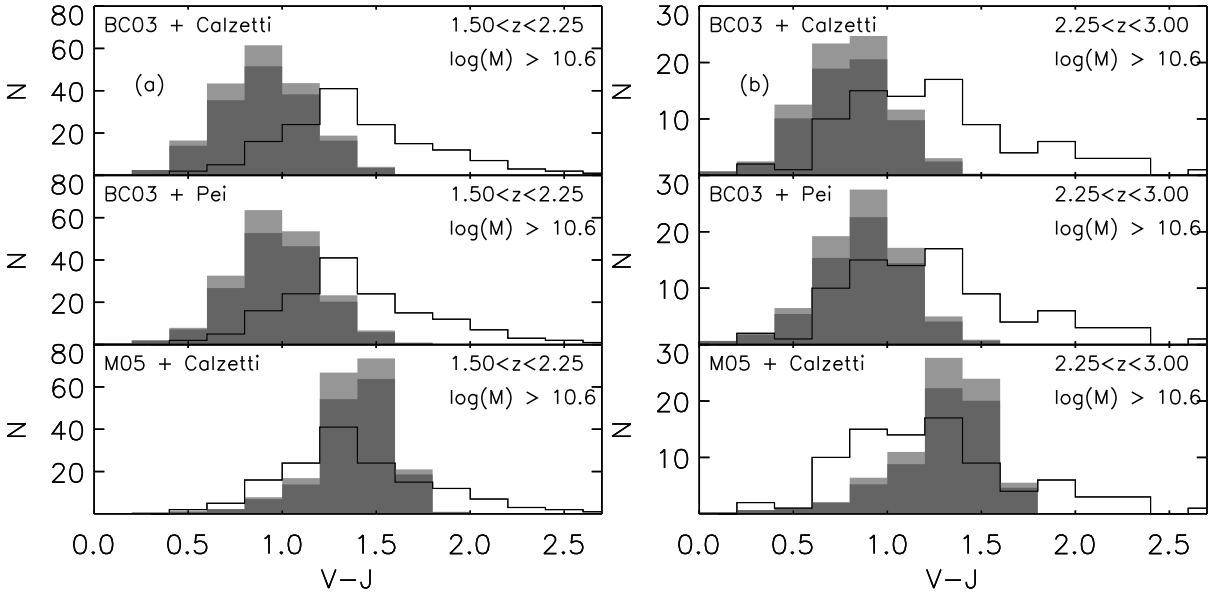

Figure 7.7 — The rest-frame $V - J$ color distribution of observed galaxies with masses above $\log M = 10.6$ in the FIRES and GOODS-South fields (*solid line*) for the redshift intervals (a) $1.5 < z < 2.25$ and (b) $2.25 < z < 3$. With filled histograms, we overplot the predicted $V - J$ color distribution of merging and post-quasar galaxies, scaled to the same solid angle as the observations. The light grey top of the model histogram indicates the uncertainty in the merger rate function used to place the simulated mergers in a cosmological context. For a given redshift interval, the model predictions in the three panels give an indication of the uncertainty in the synthetic photometry induced by the choice of attenuation law (Calzetti et al. 2000 versus the SMC curve from Pei 1992) and the choice of stellar population synthesis code (BC03 versus M05). The model $V - J$ color distribution is weakly constrained by the uncertainties at NIR wavelengths in the stellar population synthesis codes. Nevertheless, we can conclude that there exist massive galaxies with redder $V - J$ colors than those of modeled merging and post-quasar galaxies.

the differences between the two codes, we refer the reader to Maraston (2005) and Maraston et al. (2006). It is worth stressing that, irrespective of whether the BC03 or M05 stellar population synthesis code is used, the red ($V - J > 1.8$) tail of the observed distribution has no counterparts in the modeled color distribution of merging and post-merger galaxies. Conversely, an excess of galaxies is found at blue ($V - J \sim 0.9$) or intermediate ($V - J \sim 1.4$) optical-to-NIR colors for the BC03 and M05 model color distributions respectively.

7.7.3 U − V versus V − J color-color distribution

7.7.3.1 Quiescent red galaxies

Recently, a diagnostic color-color diagram of observer-frame $I - K$ versus K-[4.5 μm] has been proposed by Labbé et al. (2005) to distinguish three basic types of $z > 2$ galaxies. The rest-frame equivalent of this diagram, $U - V$ versus $V - J$, was presented by Wuyts et al. (2007), allowing a comparison of galaxies over a wider redshift range. First, there are galaxies with relatively unobscured star formation, such as Lyman break galaxies (Steidel et al. 2003) and their lower redshift BX/BM analogs (Adelberger et al. 2004). Their young ages and low reddening values result in blue colors, both in the

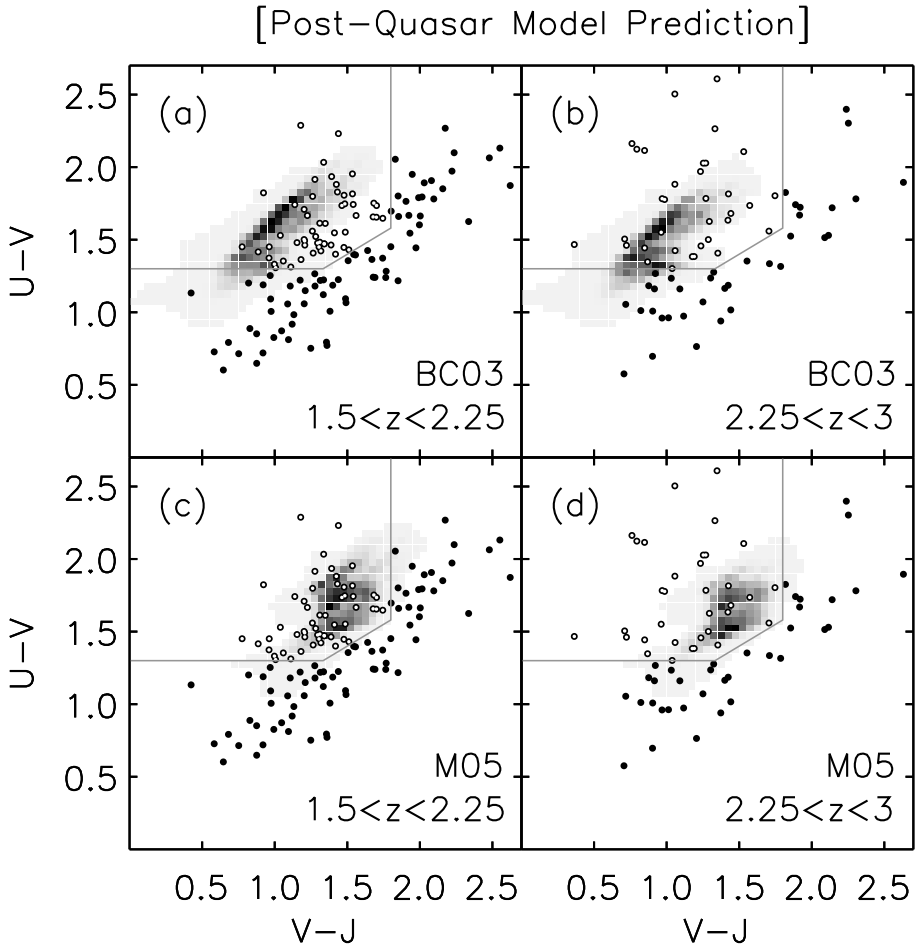

Figure 7.8 — Model $U - V$ versus $V - J$ color-color distribution of simulated galaxies with $\log M > 10.6$ that have had a merger and quasar phase in their past (*greyscales*), with a darker intensity indicating a larger number of post-quasars. Observed galaxies above the same mass limit in the FIRES and GOODS-South fields are overplotted. Empty symbols mark the galaxies that satisfy the quiescent galaxy criterion, whose selection window is marked by the grey wedge. A notable difference between the synthetic photometry derived using the BC03 and M05 stellar population synthesis code is the redder $V - J$ color in the latter case. Recognizing this uncertainty in the model prediction, we can still conclude that the predicted color distribution of post-quasars roughly coincides with that of quiescent red galaxies.

rest-frame optical and in the rest-frame optical-to-NIR. Second, there is a population of star-forming galaxies with much redder colors, due to the presence of dust. Their intrinsic (unobscured) colors are similar to those of Lyman break galaxies, but they are driven along the dust vector toward redder $U - V$ and redder $V - J$ colors. Finally, a population of galaxies with red $U - V$ colors is present at $z \sim 2$ whose SED is well matched by that of a passive or quiescently star-forming galaxy at an older age. Their $V - J$ colors are relatively blue compared to those of dusty starbursts at the same optical color.

Labbé et al. (in preparation) designed a color criterion to select the quiescent red galaxies based on their rest-frame U, V, and J photometry. The selection window is defined as follows:

$$U - V > 1.3 \;\&\; V - J < 1.8 \;\&\; U - V > 0.6(V - J) + 0.5 \tag{7.4}$$

The validity of this selection criterion was confirmed by the fact that quiescent $z \sim 2$ galaxies with a prominent Balmer/4000Å break in their rest-frame optical spectra mostly lie within the wedge. Conversely, MIPS detected galaxies at $z \sim 2$, suggesting dust-enshrouded star formation, tend to lie redward of the wedge. We draw the wedge in Figure 7.8 and indicate the location of all galaxies with $\log M > 10.6$ in the FIRES and GOODS-South fields in the color-color diagram. Empty circles mark the objects that satisfy Eq. 7.4.

We also present a binned representation of the model color-color distribution of post-quasar galaxies only in Figure 7.8. The panels correspond to the $1.5 < z < 2.25$ and $2.25 < z < 3$ redshift bins, and model photometry derived from BC03 and M05 templates respectively. The color-color distribution computed with the SMC-like reddening curve from Pei (1992) instead of the Calzetti et al. (2000) law is not plotted, but looks very similar.

We conclude that in all realizations of the synthetic photometry, the predicted color-color distribution of the post-quasar population coincides more or less with the region of color-color space selected by the quiescent galaxy criterion.

7.7.3.2 Star-forming galaxies

A significant fraction ($\sim 50\%$) of the observed massive galaxy population at $1.5 < z < 3$ has colors located outside the quiescent red galaxy wedge. These objects reach from blue $U - V$ colors typical for Lyman break galaxies, which are known to host relatively unobscured star formation, up to the redder optical and optical-to-NIR colors from galaxies that are believed to host heavily obscured star formation. Here, we investigate whether the predicted color-color distribution for merging galaxies that will undergo a quasar phase in less than 700 Myr can reproduce the color range of observed star-forming galaxies. Figure 7.9 compares the model prediction (*greyscales*) to the observed massive galaxy colors (*empty circles* for star-forming galaxies).

As could be anticipated from §7.7.2, the model photometry does not reproduce the colors of observed dusty star-forming galaxies ($U - V > 1.3$ and outside the quiescent red galaxy wedge).

At bluer $U - V$, the synthetic photometry based on M05 templates gives a decent match to the observations, whereas the BC03 colors in combination with a Calzetti et al. (2000) attenuation law are offset by a few 0.1 mag toward bluer $V - J$.

7.8 Specific star formation rate as a function of stellar mass

So far, we have compared the synthetic colors of merging and post-quasar galaxies with those of observed star-forming and quiescent galaxies respectively. The separation between star-forming and quiescent galaxies for our observed galaxies was based on their broad-band optical-to-NIR colors. As an independent check, we now use the UV + 24 μm derived star formation rates to compare the observed distribution of specific star formation rates as a function stellar mass with the distribution predicted by

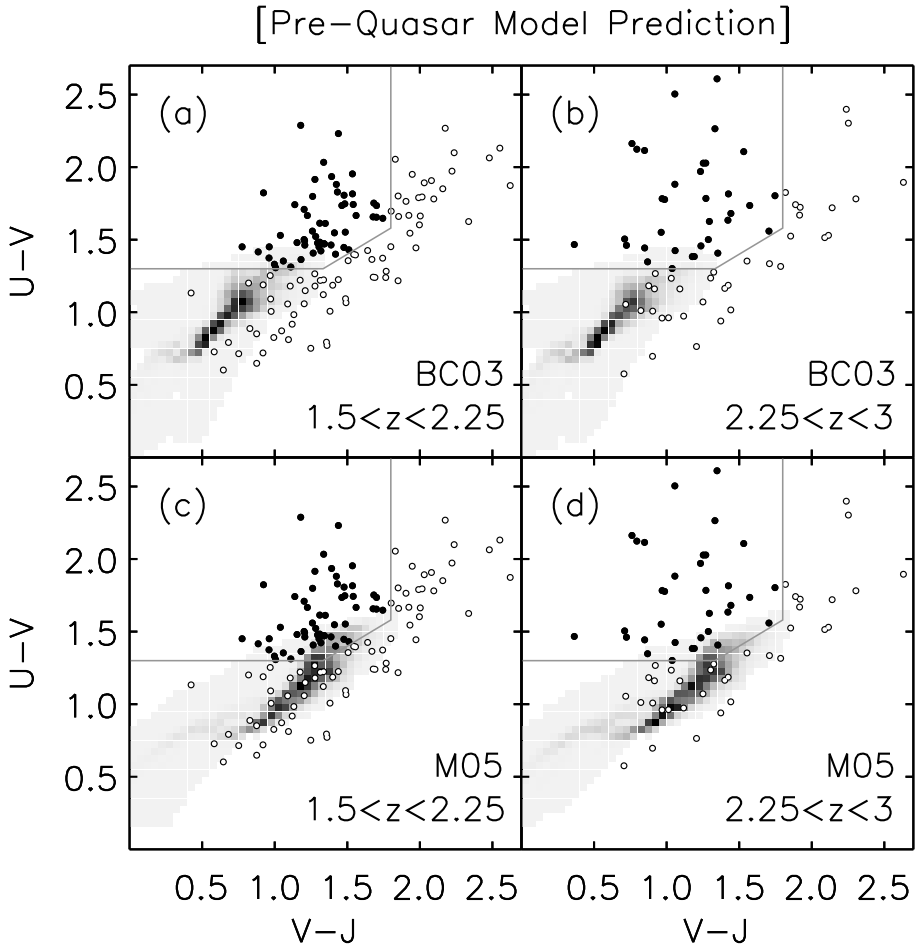

Figure 7.9 — Model $U - V$ versus $V - J$ color-color distribution of simulated galaxies with $\log M > 10.6$ that will undergo a quasar phase in less than 700 Myr (*greyscales*), with a darker intensity indicating a larger number of galaxies. Observed galaxies above the same mass limit in the FIRES and GOODS-South fields are overplotted. Empty symbols mark the galaxies that fall outside the quiescent galaxy criterion (*grey wedge*). A notable difference between the synthetic photometry derived using the BC03 and M05 stellar population synthesis code is the redder $V - J$ color in the latter case. (a) and (b) The model colors based on BC03 are a poor match to the observed star-forming galaxies (*empty symbols*). The $V - J$ colors fall blueward of the observed distribution, and only the lower half of the observed $U - V$ distribution of star-forming galaxies is reproduced. (c) and (d) The model colors based on M05 give a better match in the blue $U - V$ regime, but objects with $V - J \gtrsim 2$ are missing.

the merger model. The specific star formation rate is defined as the ratio of the star formation rate over the stellar mass. It equals the inverse of a mass-doubling time in the case of constant star formation. Here, we limit our sample to the GOODS-South field, where the 24 μm imaging is sufficiently deep (20 μJy, 5σ) to obtain useful constraints on the star formation rates.

Figure 7.10 shows the binned model distribution in greyscales and overplotted are the observed massive galaxies that fall inside (*empty symbols*) and outside (*filled symbols*) the quiescent red galaxy wedge. Upper limits are drawn for objects that were undetected by MIPS. Cross symbols mark those objects that are detected in the 1 Ms Chandra X-ray exposure (Giacconi et al. 2001). We caution that the 24 μm flux of these

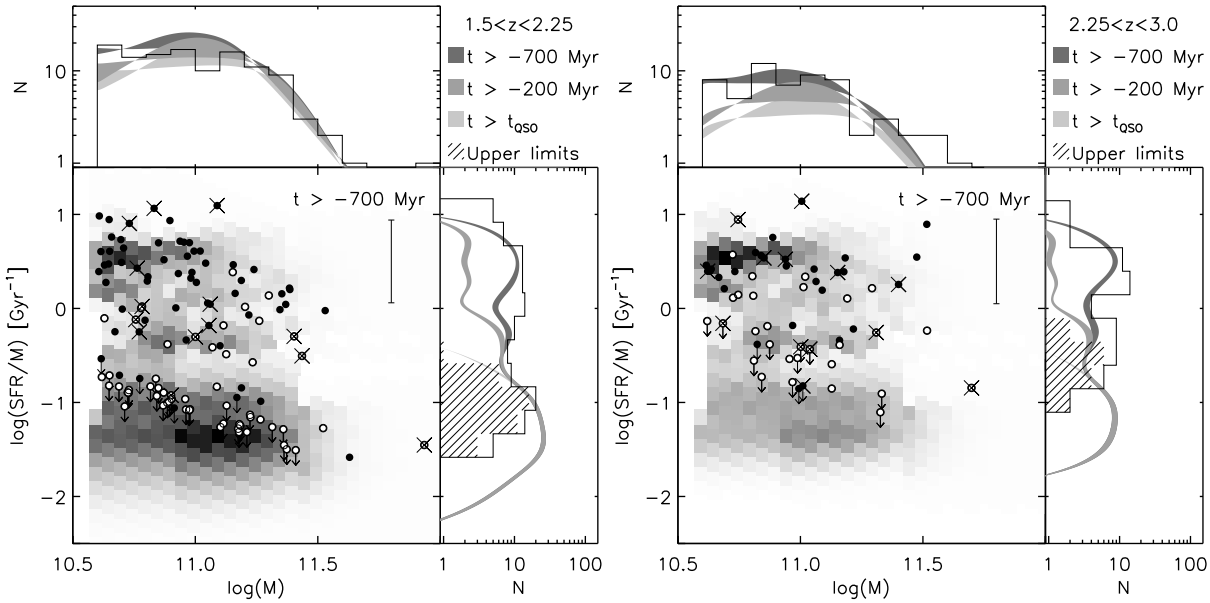

Figure 7.10 — Specific star formation rate as a function of stellar mass for massive galaxies at $1.5 < z < 3$ in the GOODS-South field with colors falling inside (*empty circles*) or outside (*filled circles*) the selection window for quiescent red galaxies. Cross symbols indicate which sources are detected in X-rays. The vertical error bar indicates the systematic error in SFR/M. The model predictions are plotted with greyscales. The top and side panels show the mass and SFR/M distribution, with the black histogram representing the observed sample, and the greyscaled curves showing the model predictions for post-quasars and merging galaxies up to 700, 200, and 0 Myr before the quasar phase. When integrating down to 700 Myr before the quasar phase, the predicted number density of galaxies with $SFR/M > 1$ Gyr^{-1} is 1.6 times smaller than observed, possibly due to AGN contribution to the 24 μm emission from which the observed SFR were derived.

objects could have an AGN contribution. Moreover, Daddi et al. (2007b) recently found that a significant fraction (20-30% to $K^{tot}_{Vega} < 22$, and up to $\sim 50-60\%$ for $M \sim 10^{11}\ M_{\odot}$) of star-forming galaxies that are not individually detected in the X-rays show evidence for heavily obscured AGN by the presence of a mid-IR flux excess. The vertical error bar indicates the systematic uncertainty in the conversion from 24 μm flux to the obscured part of the star formation rate. The top and side panels show the distribution of masses and specific star formation rates separately. With lighter polygons, we illustrate how the predicted distribution changes when integrating the merger rate function only to the evaluated redshift or 200 Myr past the evaluated redshift. The latter case includes the nuclear starburst phase, but not earlier star-forming phases.

We conclude that at $1.5 < z < 2.25$ the broad-band color criterion is efficient in distinguishing quiescent from star-forming galaxies with high specific star formation rates. In the higher redshift bin, we are more limited by upper limits on the 24 μm flux. The bulk of broad-band selected quiescent galaxies shows smaller specific star formation rates than their counterparts outside the broad-band selection window, although some reach values above $SFR/M = 1$ Gyr^{-1}.

As in the observations, in particular at $1.5 < z < 2.25$, there is a slight hint that the most heavily star-forming objects reside primarily at the lower masses within our mass-limited sample. Papovich et al. (2006) and Reddy et al. (2006) find that the

specific star formation rate is inversely proportional to mass, implying that the ongoing star formation at $z \sim 2$ contributes more significantly to the mass buildup of low-mass galaxies than to high-mass galaxies.

The predicted abundance of merger-triggered nuclear starbursts, occuring between 0 and 200 Myr before the quasar phase, seems to be insufficient to account for all observed massive galaxies with high specific star formation rates ($SFR/M > 1$ Gyr^{-1}). However, when we include earlier phases of star formation induced by the merging event (up to 700 Myr before the quasar phase), we find that the observed number density of galaxies with $SFR/M > 1$ Gyr^{-1} is only a factor 1.6 larger than predicted by the model. Such an offset might be expected from possible AGN contributions to the 24 μm emission from which the star formation rates were derived (see, e.g., Daddi et al. 2007b).

7.9 The abundance of massive galaxies at $1.5 < z < 3$: analysis by type

We now proceed to quantify the observed and modeled number and mass densities of massive galaxies at $1.5 < z < 3$. As before, the model prediction was derived by integrating the merger rate function to include all galaxies that once contributed to the observed quasar luminosity function or will do so in less than 700 Myr. From this, we extracted 4 samples using the tools discussed in §7.7.3 and §7.8: galaxies above $\log M > 10.6$ with broad-band colors satisfying the quiescent red galaxy criterion (Eq. 7.4, §7.9.1), galaxies above $\log M > 10.6$ that do not satisfy Eq. 7.4 (§7.9.2), galaxies with $\log M > 10.6$ and $SFR/M > 1$ Gyr^{-1} (§7.9.3), and finally a sample of galaxies more massive than 10^{11} $M_{\odot}$ with red ($U - V > 1.3$) optical colors (§7.9.4). The last sample allows us to include the larger area MUSYC survey in the comparison, for which no IRAC or MIPS imaging is currently available. In each case, we impose an identical selection criterion on the observed sample of galaxies.

7.9.1 The number and mass density of massive ($\log \mathbf{M > 10.6}$) quiescent red galaxies

Having established the similarity in colors of the model post-quasar population and the observed quiescent red galaxy population above a same mass limit, we now turn to a comparison of their number and mass densities. Our aim is to constrain the fraction (in number and mass) of massive quiescent red galaxies at redshifts $1.5 < z < 3$ that descendants of merger-triggered quasars can account for. In order to do this, we selected the observed and modeled galaxies with $\log M > 10.6$ that lie inside the wedge defined by Eq. 7.4 and compute the number and mass density for the probed comoving volume of $\sim 3.5 \times 10^5$ Mpc^3 in each redshift bin. The resulting number and mass densities are plotted as a function of central redshift of the redshift bin in Figure 7.11(a). The filled circles indicate the observed number and mass density of quiescent red galaxies above $\log M = 10.6$. Their values and corresponding uncertainties are listed in Table 7.1.

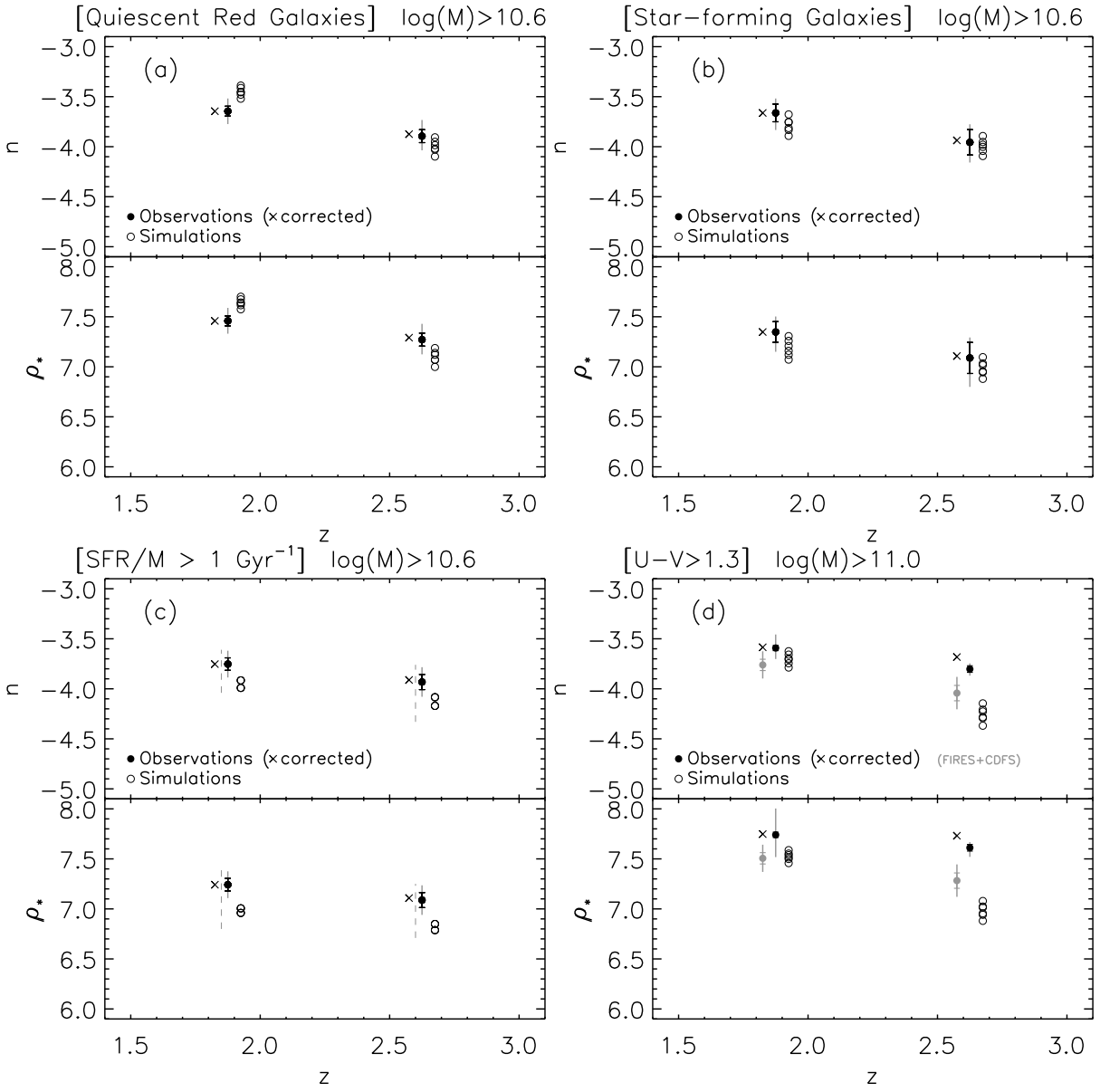

Figure 7.11 — The number and mass density of observed (*filled symbols*) and modeled (*empty symbols*) massive galaxies as a function of redshift above the same mass limit and satisfying the same selection criterion. The cross symbols indicate the observed number and mass density after a correction for incompleteness (which is negligible except for the MUSYC fields). The black error bar represents the Poisson shot noise solely. The grey error bar accounts for uncertainties in redshift, mass, and rest-frame colors and a (mostly dominating) contribution from cosmic variance. The dashed error bar in panel (c) reflects the systematic uncertainty in the SFR. We consider 4 samples: (a) Quiescent red galaxies with $\log M > 10.6$ in FIRES+GOODS-S, (b) Star-forming (non-quiescent) galaxies with $\log M > 10.6$ in FIRES+GOODS-S, (c) galaxies with $SFR/M > 1$ Gyr^{-1} with $\log M > 10.6$ in GOODS-S, and (d) galaxies with $U - V > 1.3$ and $\log M > 11$ in FIRES+GOODS-S+MUSYC. The model predictions were derived by integrating the merger rate function to 700 Myr beyond the evaluated redshift. Changing this value only alters the predictions for panels (b) and (c). We find that both the predicted number and mass densities agree within the error bars with the observed values.

Table 7.1. Number and mass densities for massive galaxies

Type	Mass limit $M_\odot$	Redshift	Observations[a] n $10^{-4}\ Mpc^{-3}$	Observations[a] ρ_* $10^7\ M_\odot\ Mpc^{-3}$	Model Prediction[b] n $10^{-4}\ Mpc^{-3}$	Model Prediction[b] ρ_* $10^7\ M_\odot\ Mpc^{-3}$
All	4×10^{10}	$1.5 < z < 2.25$	$4.4^{+1.3}_{-1.0}$	$5.1^{+1.6}_{-1.2}$	$4.8 - 5.6$	$5.6 - 6.3$
All	4×10^{10}	$2.25 < z < 3$	$2.5^{+1.0}_{-0.6}$	$3.2^{+1.5}_{-0.8}$	$1.8 - 2.2$	$2.1 - 2.4$
Quiescent	4×10^{10}	$1.5 < z < 2.25$	$2.3^{+0.8}_{-0.6}$	$2.9^{+1.0}_{-0.7}$	$3.0 - 4.1$	$3.8 - 5.0$
Quiescent	4×10^{10}	$2.25 < z < 3$	$1.3^{+0.6}_{-0.4}$	$2.0^{+0.9}_{-0.6}$	$0.8 - 1.2$	$1.0 - 1.5$
Star-forming	4×10^{10}	$1.5 < z < 2.25$	$2.2^{+0.9}_{-0.7}$	$2.2^{+0.9}_{-0.8}$	$1.3 - 2.1$	$1.2 - 2.0$
Star-forming	4×10^{10}	$2.25 < z < 3$	$1.2^{+0.6}_{-0.4}$	$1.3^{+0.8}_{-0.6}$	$0.8 - 1.3$	$0.8 - 1.2$
$SFR/M > 1\ \mathrm{Gyr}^{-1}$	4×10^{10}	$1.5 < z < 2.25$	$1.8^{+0.6}_{-0.5}$	$1.7^{+0.6}_{-0.5}$	$1.0 - 1.2$	$0.9 - 1.0$
$SFR/M > 1\ \mathrm{Gyr}^{-1}$	4×10^{10}	$2.25 < z < 3$	$1.2^{+0.5}_{-0.4}$	$1.3^{+0.5}_{-0.4}$	$0.7 - 0.8$	$0.6 - 0.7$
$U - V > 1.3$	10^{11}	$1.5 < z < 2.25$	$2.6^{+0.9}_{-0.6}$	$5.6^{+4.6}_{-2.2}$	$1.6 - 2.4$	$2.9 - 3.9$
$U - V > 1.3$	10^{11}	$2.25 < z < 3$	$2.1^{+0.3}_{-0.3}$	$5.4^{+0.8}_{-1.0}$	$0.4 - 0.7$	$0.8 - 1.2$

[a]The error bars in the observed densities account for Poisson noise, cosmic variance, and the uncertainties in redshift, rest-frame color and mass of the individual galaxies. They do not account for the systematic dependence on the stellar population synthesis code used to derive the stellar masses, nor was the systematic uncertainty in the conversion from 24 μm to SFR (of the order of 1 dex) included in the results for the sample selected on SFR/M.

[b]The range in model densities indicates a crude estimate of the size of uncertainties in the merger rate function and the dependence on choice of attenuation law and stellar population synthesis code to compute the synthetic photometry.

The cross symbols represent the observed number and mass density after applying a 0% and 5% correction for incompleteness in the low- and high-redshift bin respectively. As in §7.6, the black error bars account for Poisson shot noise. The grey error bars also include selection uncertainties stemming from uncertainties in the redshift, mass, and rest-frame colors of individual galaxies, and a dominating contribution from cosmic variance.

The empty symbols on Figure 7.11(a) indicate the predicted number and mass density of galaxies with $\log M > 10.6$ at $1.5 < z < 2.25$ and $2.25 < z < 3$ whose synthetic photometry places them within the selection wedge for quiescent red galaxies. 95% of these modeled galaxies are in a post-quasar phase of their evolution. The different empty circles represent predictions derived with the BC03 and M05 stellar population synthesis codes, with the Calzetti et al. (2000) attenuation law and the SMC-like attenuation law from Pei (1992). Their spread gives a crude indication of the freedom allowed by the model. It also takes into account the uncertainty in the merger rate function used to place the binary merger simulations in a cosmological context.

We find that in both redshift bins, the observed number and mass density of massive quiescent red galaxies agrees within the error bars with the predicted number and mass density of simulated galaxies satisfying the same selection criterion. In other words, assuming a one-to-one correspondence between quasars and gas-rich mergers, the model by Hopkins et al. (2006b) predicts an abundance of merger remnants (i.e., post-quasar galaxies) that is similar to the observed abundance of quiescent red galaxies. The model predicts an increase by a factor 3.5 in the number and mass density for massive post-quasar galaxies in the 1 Gyr that passed between $z = 2.6$ and $z = 1.9$. The observed sample seems to suggest less evolution (a factor 1.8 in number density and 1.5 in mass density), but is formally consistent with both the factor 3.5 and a non-evolving number and mass density over the considered redshift range.

7.9.2 The number and mass density of massive ($\log \mathbf{M} > \mathbf{10.6}$) star-forming galaxies

Following identical procedures as outlined above, we analyze the number and mass density of massive galaxies with colors outside the quiescent red galaxy wedge in Figure 7.11(b). Again, we used a Monte Carlo simulation to determine how many galaxies moved into or out of the selection window when perturbing their properties within the error bars. We took into account the fact that the mass estimates of star-forming galaxies are less robust than for quiescent galaxies. In Chapter 6 we found a typical mass underestimate of -0.1 dex for star-forming galaxies, with the central 68% interval of $\Delta \log M \equiv \log M_{recovered} - \log M_{true}$ ranging from -0.25 to 0 dex.

We find a similar number density of massive quiescent and massive star-forming galaxies in the observed fields. The mass density of the observed star-forming galaxies is lower than that for the quiescent ones above the same mass limit by a factor 1.3 at $z = 1.9$ and 1.5 at $z = 2.6$. We find that the abundances of star-forming galaxies, both in number and mass, as predicted by the merger model agree within the error bars with the observed values. The ratio of quiescent to star-forming galaxies as predicted by the model amounts to 2 (1) for the number density and 2.8 (1.2) for the mass density in the low (high) redshift bin. A more robust model prediction of the pre-quasar number and mass density would also require a careful simulation of the evolutionary stages

during which and viewing angles under which the binary merger would be detected as two separate galaxies, thus contributing twice to the number density, but with half the mass and therefore possibly dropping out of the mass-limited sample.

7.9.3 The number and mass density of massive ($\log \mathbf{M} > 10.6$) galaxies with $\mathbf{SFR/M} > 1$ $\mathbf{Gyr^{-1}}$

Selecting galaxies with specific star formation rates above $SFR/M > 1$ Gyr^{-1}, we find an observed number density of 1.8×10^{-4} Mpc^{-3} and 1.2×10^{-4} Mpc^{-3} at $1.5 < z < 2.25$ and $2.25 < z < 3$ respectively (Figure 7.11(c)). Since we interpreted all the 24 μm emission as dust re-emission from star formation, the true number density can be lower depending on the contribution from AGN (see, e.g., Reddy et al. 2005; Papovich et al. 2006; Daddi et al. 2007b). The merger model predicts an abundance of galaxies with high specific star formation rates that is a factor 1.6 smaller than observed. Given the possible AGN contribution to the 24 μm emission and the large systematic uncertainty in the conversion from 24 μm to the dust-obscured contribution to the star formation rate (*dashed line* in Figure 7.11(c)), the model and observational results are formally consistent.

7.9.4 The number and mass density of galaxies with $\mathbf{M > 10^{11}\ M_\odot}$ and $\mathbf{U - V > 1.3}$

In order to reduce the effect of cosmic variance, we now include the MUSYC fields in our analysis, increasing the area by a factor 3 and reducing the cosmic variance with a similar factor. This goes at the cost of depth (the 90% completeness limit for the MUSYC fields is 1 magnitude shallower than for GOODS-South) and wavelength coverage (no IRAC photometry is currently available for the MUSYC fields). Consequently, we are restricted to a sample limited at $M > 10^{11}$ $M_\odot$, even then requiring a 33% correction for incompleteness in the $2.25 < z < 3$ bin. Moreover, the lack of IRAC observations prevents us from selecting galaxies that fall inside the selection window for quiescent red galaxies. We therefore compare the number and mass density of all $M > 10^{11}$ $M_\odot$ galaxies with $U - V > 1.3$ (the lower edge of the quiescent red galaxy wedge), knowing from §7.7 that a significant fraction of the observed galaxies will fall outside the quiescent red galaxy wedge.

Figure 7.11(d) shows their number and mass density as a function of redshift for the combined FIRES, GOODS-South, and MUSYC surveys (*black symbols*). Poisson noise is negligible for this sample. The grey error bars again account for cosmic variance and the uncertainties in redshift, rest-frame color, and mass of the individual galaxies making up the sample. For the MUSYC survey, we assumed an increase in the mass uncertainty by a factor of 3 with respect to the FIRES and GOODS-South samples due to the lack of IRAC photometry (see Wuyts et al. 2007). In contrast to the FIRES + GOODS-South sample discussed above, the total error budget is not always dominated by cosmic variance. The large uncertainty in the mass density at $z \sim 1.9$ for example is mostly attributed to errors in the properties of individual galaxies as derived from the mock catalogs. Seperately, we indicate the results obtained from the deeper FIRES and GOODS-South surveys (*grey symbols*, dominated in area by GOODS-South). We conclude that the GOODS-South field is significantly underdense in terms

of the highest mass ($M > 10^{11}\ M_{\odot}$) galaxies, in particular in the $2.25 < z < 3$ redshift bin. Our analysis shows an agreement between the observed abundance (in number and mass) of red ($U - V > 1.3$) massive ($M > 10^{11}\ M_{\odot}$) galaxies at $1.5 < z < 3$ on the one hand, and the model prediction of galaxies satisfying the same criteria that either had a merger-triggered quasar phase in their past lifetime or will undergo such a phase within 700 Myr on the other hand. In fact, the vast majority of massive red galaxies predicted by the merger model are post-quasar galaxies (see §7.7.3). At $2.25 < z < 3$, the predicted massive post-quasar population can account for at least 25% in number and 20% in mass of the observed massive red galaxy population.

Assuming that the ratio of massive red galaxies ($M > 10^{11}\ M_{\odot}$ & $U - V > 1.3$) falling inside and outside the quiescent red galaxy selection window in the MUSYC fields equals that in the FIRES and GOODS-South fields, we find that the merger model can account for 70% of the number density and 30% of the mass density of massive quiescent red galaxies at $2.25 < z < 3$ and is consistent with forming all of the massive quiescent red galaxies at $1.5 < z < 2.25$ through mergers involving AGN activity. A recent discussion on the importance of AGN activity at high redshift is provided by Daddi et al. (2007b).

7.10 Comments and caveats

In this Section, we list a number of caveats, and indicate prospects for improvements on both the model and observational side. We list a number of possible reasons for the discrepancy between the synthetic and observed colors of massive star-forming galaxies in §7.10.3.

7.10.1 Pair statistics

In this chapter, we used the integrated properties (color, mass, SFR) for the merging pair to predict number and mass densities for different samples of massive galaxies. In other words, we made the approximation that the merging pair is never detected as two separate galaxies. As suggested in §7.9.2, a more detailed modeling should take into account that, depending on the orbital configuration and the viewing angle, this may not always be the case.

The post-quasar predictions are robust, since by that time the two progenitors have formed one galaxy. If at earlier times some of the progenitor pairs are resolved as two separate objects, this will decrease the mass density of massive galaxies since galaxies will drop out of the sample. The effect on the number density is less trivial. On the one hand, galaxies will drop out of the mass-limited sample. On the other hand, some merging pairs will contribute twice. We leave such an extension of the merger model for later work.

Here, we focus on an additional test of the merger model allowed by the fact that some of the pairs will be resolved into two objects. If a large fraction of the massive galaxy population at $1.5 < z < 3$ is indeed related to merging events, as our analysis suggests, we expect to see an excess in the pair statistics with respect to a random distribution of galaxies on the sky.

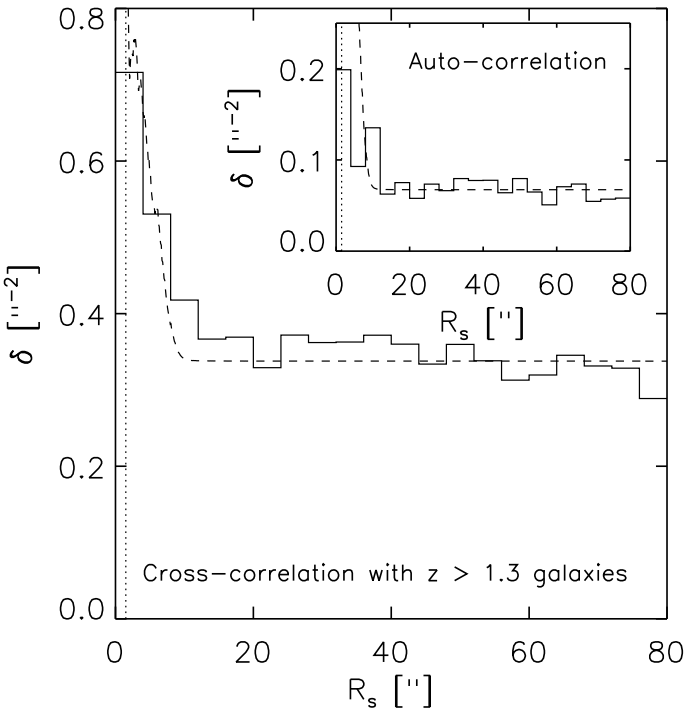

Figure 7.12 — Relative galaxy density (δ) as a function of massive ($\log M > 10.6$) $1.5 < z < 3$ galaxy to $z > 1.3$ galaxy separation (R_s) in the GOODS-South field. The distribution predicted by the merger model is indicated with the dashed line. At separations smaller than $1\farcs5$ (*dotted line*) an increasing number of galaxy pairs, if present, will be missed because they would be detected as a single object. We find a clear excess at small pair separations ($R_s < 8''$), as predicted by the merger model. A weak pair excess is also visible when only considering the distribution of separations between massive $1.5 < z < 3$ galaxies (*inset panel*), but the excess is much below the prediction.

We present the distribution of galaxy-galaxy separations in the GOODS-South field in Figure 7.12 (*solid histogram*). We decide not to include the other fields, to prevent differences in depth from influencing the pair excess signal. The main panel shows the results from a cross-correlation of our massive ($\log M > 10.6$) galaxy sample at $1.5 < z < 3$ with the sample of all galaxies above $z > 1.3$ in the GOODS-South field, thus avoiding the risk of losing pair members that by a typical photometric redshift error were placed at some lower redshift. For each massive galaxy at $1.5 < z < 3$, we measure the distance to all $z > 1.3$ galaxies. We compute the statistic

$$\delta(R_s) = \frac{\sum_{i=1}^{j} N_i(R_s)}{\pi\left((R_s+\epsilon)^2 + (R_s-\epsilon)^2\right)} \tag{7.5}$$

where j is the total number of objects in our massive galaxy sample and $N_i(R_s)$ is the number of $z > 1.3$ galaxies that lie between a distance $R_s - \epsilon$ and $R_s + \epsilon$ from galaxy i. For a random uniform distribution of galaxies, $\delta(R_s)$ will be flat. Figure 7.12 shows that for our sample of massive galaxies at $1.5 < z < 3$, this is clearly not the case. An excess of pairs at $R_s < 8''$ is visible, also when we consider the distribution of separations between members of the massive galaxy sample at $1.5 < z < 3$ only (*inset panel*).

From the simulations, we measured the physical separations between the 2 merging galaxies and computed the distribution of separation angles in arcseconds on the sky using the merger rate function (see §7.5). Adding the mean value of δ as measured in the interval $30'' < R_s < 80''$, we obtain a model prediction (*dashed line*) that is in qualitative agreement with the cross-correlation results, but larger than the weak pair

excess seen in the auto-correlation. Admittedly, the predicted distribution is subject to the orbital configuration set at the start of the simulation, an effect that is not explored in this Chapter.

7.10.2 Dependence on stellar population synthesis code

As pointed out in §7.9.1, the predicted rest-frame NIR luminosities for a single stellar population of a given mass are brighter for the M05 than for the BC03 stellar population synthesis code. Consequently, the mass estimates for observed galaxies with ages between 0.2 and 2 Gyr are lower by about a factor 1.5 when modeled with M05 instead of BC03 templates. We indicated the resulting systematic uncertainties in the number and mass densities of the modeled post-quasar galaxy population. This systematic uncertainty is also present in the estimates of number and mass density for the observations, for which so far we only included the formal uncertainties in mass obtained with BC03 SED modeling. To quantify the impact on the derived number and mass densities, we simply divide all stellar masses by 1.5 and repeat the selection procedure and the calculation of the densities. Using this crude approach, we find number densities for all samples discussed in this chapter to be 50-80% and mass densities to be 40-60% of the value obtained with BC03 masses. Although a significant source of uncertainty, we find that for most samples discussed in this Chapter (except for the quiescent red galaxy sample at $z \sim 1.9$) adopting the M05 mass estimates would only improve the agreement between data and model. Finally, deviations from a Salpeter (1955) IMF would change our results on number and mass densities of massive galaxies, but in a similar manner for the observations and the simulations, thus keeping intact the relative trends.

7.10.3 Reproducing dusty red starbursts

As discussed in §7.7.3.2, the synthetic colors during the star-forming phases of the merger do not reproduce the red optical and optical-to-NIR colors observed for dusty starbursts. If the lack of model colors redder than $V - J > 1.8$ could be fixed, the statistics based on the merger model, when compared to the observed abundances of massive galaxies, strengthen the idea that the model gives a valid representation of galaxy evolution in the real universe. Here we list a number of possible origins for the discrepancy in colors. Future investigations along these lines will help to further test the merger model.

7.10.3.1 Simulating the observing procedure

First, it is possible that the colors of observed and modeled galaxies are in fact in agreement, but that a discrepancy was found because we did not simulate the whole observing procedure. The observed colors are measured on PSF-matched images within apertures of size 1″ to 2″, whereas the synthetic colors were based on integrated photometry of all stellar particles, irrespective of their location. The presence of a color gradient with redder emission in the central regions of the galaxies could therefore induce an offset in colors in the observed direction.

7.10.3.2 Stellar population synthesis

Second, the discrepancy in colors could be real, but due to an incorrect modeling of the stellar populations, rather than invalid assumptions at the basis of the model (i.e., the one-to-one correspondence between quasars and gas-rich mergers). Apart from the choice of stellar population synthesis code (see §7.10.2), the synthetic photometry depends on the attenuation law applied to each of the stellar particles. We note however that the use of a Milky Way-like attenuation law from Pei (1992) leads to colors intermediate between those based on the Calzetti et al. (2000) and SMC-like (Pei 1992) attenuation laws presented in this Chapter. An attenuation law that is less grey than that of the SMC would be required to reproduce the red colors of dusty starburst galaxies.

Another stellar population parameter influencing the synthetic colors is the metallicity of the gas and the stars. In this Chapter, we adopted initial gas metallicities derived from the closed box model (Talbot & Arnett 1971) for the 80% gas fraction (f_{gas}) at the start of the simulation:

$$Z_{init} = -y \ln(f_{gas}) \tag{7.6}$$

where $y = 0.02$ is the yield. The simulation keeps track of the subsequent evolution in the gas metallicity, and stellar metallicities are based on the metallicity of the gas out of which they form. If the gas was pre-enriched, this would boost the optical depths and redden the colors. Evidence of high ($\sim Z_{\odot}$) metallicities of massive high-redshift galaxies with red colors is given by van Dokkum et al. (2004). Repeating the post-processing of simulation snapshots with $1Z_{\odot}$ added to the gas and stellar metallicities, we obtain colors that are 0.2 to 0.5 mag redder in $U - V$ and 0.3 to 1.1 mag redder in $V - J$. We note however that in $V - J$ the largest increase occurs for blue galaxies and the color distribution based on BC03 does not reach beyond $V - J \sim 2$.

7.10.3.3 Merger parameters

Third, the discrepancy in colors might imply that the simulations are not characteristic for the merger activity occuring in the real universe. Hopkins et al. (2006b) confirmed the robustness of the model for quasar lifetimes and the derived merger rate function against changes in various parameters of the merging galaxies, such as gas fraction, orbital parameters and changes in the mass ratio of the progenitors (considering 1:1, 2:1, 3:1, and 5:1 mass ratios). All of the simulations used in this work are equal-mass gas-rich ($f_{gas} = 0.8$) mergers. A smaller initial gas fraction would mean that a larger fraction of the stars was already formed before the merger-triggered starburst. This leads to slightly redder $U - V$ colors. Considering earlier stages in the evolutionary scenario, Dasyra et al. (2006) find for a population of local ULIRGs that still have 2 distinct nuclei that the typical mass fraction is 1.5:1, close to equal-mass mergers. In order to extend the model predictions to lower masses, a detailed study of minor merger simulations will be required to determine the minimum mass ratio required to trigger a (low-luminosity) quasar phase.

7.10.3.4 Evolutionary history

Fourth, it is possible that dusty starburst galaxies are not triggered by mergers, but had a different evolutionary history. Daddi et al. (2007a) make this claim based on the long star formation timescales of ULIRGs at high redshift.

7.10.3.5 Mass loss and intergalactic environment

Fifth, gas replenishment from mass loss and infall of gas from the intergalactic environment could change the optical depths and thus the reddening factors. The simulations only take into account a small amount of mass loss: 10% of the gas mass converted into stars is instantaneously returned to the interstellar medium, accounting for short-lived stars that die as supernovae (Springel & Hernquist 2003). The total fraction of the mass lost by a single stellar population with Salpeter (1955) IMF amounts to $\sim 70\%$ (BC03) and is even higher for the top-heavy IMFs of Kroupa (2001) or Chabrier (2003). Furthermore, the simulations do not allow for infall of primordial gas at later times. Consequently, they cannot prove that descendants of galaxies that once showed up in the quasar luminosity function and after the shutdown of star formation reached red colors, will remain quiescent forever. Small amounts of newly accreted gas triggering star formation may be enough to shift a post-quasar galaxy outside the quiescent region of color-color space defined by Eq. 7.4, thus dropping their contribution to the observed galaxy population of massive quiescent red galaxies. Cosmological simulations at sufficient resolution might resolve this problem. At the very least, it would be interesting to test the behavior of simulated merger remnants hosting a supermassive black hole when a small but continuous gas supply is applied.

7.10.3.6 Dust distribution

Finally, the distribution of dust in the simulated galaxies might not reflect reality. A more efficient reddening would be obtained if a foreground screen of obscuring material were present. One possible mechanism that could produce such a configuration is a large-scale wind. The GADGET-2 code (Springel 2005b) used to run the simulations in principle allows for such a phenomenon, but an investigation of the velocity field of the gas in the simulations is required to check whether such a wind is effectively taking place.

7.10.4 Cosmic variance

From the observational side, cosmic variance is the dominant source of uncertainty for the determination of the number and mass density of massive quiescent galaxies. IRAC photometry over a MUSYC area and to a similar depth as FIRES and GOODS-South would be required to further constrain the fraction of massive quiescent galaxies that post-quasar galaxies can account for.

7.11 Summary

We confronted the model by Hopkins et al. (2006b) with observations of massive galaxies at $1.5 < z < 3$. The model translates the observed quasar luminosity function

into the abundance of massive merging galaxies and merger remnants. We derived the synthetic photometry for these systems from a set of binary merger SPH simulations with a range of masses, and including stellar and AGN feedback. We extracted mass-limited samples of $1.5 < z < 3$ galaxies with $M > 4 \times 10^{10}\ M_{\odot}$ and $M > 10^{11}\ M_{\odot}$ from the FIRES+GOODS-South and FIRES+GOODS-South+MUSYC surveys respectively. We tested the model by comparing the predicted number and mass densities, and the $U - V$ and $V - J$ color distributions with our observations of massive galaxies at $1.5 < z < 3$.

We find that the overall number density of galaxies with $M > 4 \times 10^{10}\ M_{\odot}$ in the FIRES and GOODS-South fields ($n = 4.4^{+1.3}_{-1.0} \times 10^{-4}\ Mpc^{-3}$ at $z \sim 1.9$ and $n = 2.5^{+1.0}_{-0.6} \times 10^{-4}\ Mpc^{-3}$ at $z \sim 2.6$) is in good agreement with the model prediction ($n = 4.8 - 5.6 \times 10^{-4}\ Mpc^{-3}$ at $z \sim 1.9$ and $n = 1.8 - 2.2 \times 10^{-4}\ Mpc^{-3}$ at $z \sim 2.6$). Likewise, the results obtained for the mass density are consistent: $\rho_* = 5.1^{+1.6}_{-1.2} \times 10^{7}\ M_{\odot}\ Mpc^{-3}$ at $z \sim 1.9$ and $\rho_* = 3.2^{+1.5}_{-0.8} \times 10^{7}\ M_{\odot}\ Mpc^{-3}$ at $z \sim 2.6$ for the observations and $\rho_* = 5.6 - 6.3 \times 10^{7}\ M_{\odot}\ Mpc^{-3}$ at $z \sim 1.9$ and $\rho_* = 2.1 - 2.4 \times 10^{7}\ M_{\odot}\ Mpc^{-3}$ at $z \sim 2.6$.

Separating massive galaxies by type, we find that the model photometry of the post-quasar population coincides with the region of $U - V$ versus $V - J$ color-color space that was defined by Labbé et al. (in preparation) to select quiescent red galaxies. The observed and modeled number and mass densities of massive ($M > 4 \times 10^{10}\ M_{\odot}$) quiescent red galaxies at $1.5 < z < 3$ are consistent within the error bars (see Table 7.1).

We added the MUSYC survey to our sample, increasing the area by a factor of 3, but by lack of IRAC data loosing the ability to break at least partially the age-dust degeneracy. As pointed out earlier by van Dokkum et al. (2006), the GOODS-South field is underdense in the $1.5 < z < 3$ redshift interval. Based on the FIRES+GOODS-South+MUSYC sample, we find that more than 25% of the $z \sim 2.6$ galaxies with $M > 10^{11}\ M_{\odot}$ and $U - V > 1.3$ and essentially all of the $z \sim 1.9$ galaxies satisfying the same criteria can be accounted for by the predicted post-quasar population. The fraction of observed quiescent galaxies at $z \sim 2.6$ that the model can account for increases if we use Maraston (2005) models to derive stellar masses for our observed galaxy sample.

Although less constrained, the predicted abundances of galaxies with star formation triggered by merging and galaxies with $SFR/M > 1$ Gyr^{-1} during the merging phases are also consistent with the observations. However, the predicted color distribution of star-forming galaxies does not match the observations. In particular the colors of red ($V - J > 1.8$) dusty starburst galaxies are not reproduced. We suggest a number of explanations for the lack of dusty red starburst galaxies in the model predictions. Possible reasons are an incomplete simulation of the observing procedure, differences in stellar population properties or merger characteristics between the observed and simulated galaxies, a different history for dusty starbursts than a merger-triggered scenario, additional gas (and dust) from the intergalactic environment or mass loss, and a different distribution of the dust, e.g., caused by the presence of large-scale outflows.

Finally, we find a pair excess at small angular scales, further strengthening the hypothesis that mergers play a key role in galaxy evolution.

Acknowledgments

We would like to thank the Institute for Theory and Computation for its hospitality during several working visits, and the Leids Kerkhoven-Bosscha Fonds for the generous travel support.

References

Adelberger, K. L., Steidel, C. C., Shapley, A. E., Hunt, M. P., Erb, D. K., Reddy, N. A.,& Pettini, M. 2004, ApJ, 607, 226
Bolzonella, M., Miralles, J.-M.,& Pelló, R. 2000, A&A, 363, 476
Bower, R. G., Benson, A. J., Malbon, R., Helly, J. C., Frenk, C. S., Baugh, C. M., Cole, S.,& Lacey, C. G. 2006, MNRAS, 370, 654
Calzetti, D., et al. 2000, ApJ, 533, 682
Chabrier, G. 2003, ApJ, 586, L133
Cowie, L. L., Songaila, A., Hu, E. M.,& Cohen, J. G. 1996, AJ, 112, 839
Cox, T. J., Dutta, S. N., Di Matteo, T., Hernquist, L., Hopkins, P. F., Robertson, B.,& Springel, V. 2006, ApJ, 650, 791
Croton, D. J. et al. 2006, MNRAS, 367, 864
Daddi, E., Cimatti, A., Renzini, A., Fontana, A., Mignoli, M., Pozzetti, L., Tozzi, P.,& Zamorani, G. 2004, ApJ, 617, 746
Daddi, E., et al. 2007a, astro-ph/07052831
Daddi, E., et al. 2007b, astro-ph/07052832
Dasyra, K. M., Tacconi, L. J., Davies, R. I., Genzel, R., Lutz, D., Naab, T., Burkert, A., Veilleux, S.,& Sanders, D. B. 2006, ApJ, 638, 745
De Lucia, G.,& Blaizot, J. 2007, MNRAS, 375, 2
Di Matteo, T., Springel, V.,& Hernquist, L. 2005, Nature, 433, 604
Erb, D. K., Steidel, C. C., Shapley, A. E., Pettini, M., Reddy, N. A.,& Adelberger, K. L. 2006, ApJ, 646, 107
Ferrarese, L.,& Merritt, D. 2000, ApJ, 539, L9
Förster Schreiber, N. M., et al. 2006, AJ, 131, 1891
Franx, M., et al. 2000, The Messenger 99, pp. 20-22
Franx, M., et al. 2003, ApJ, 587, L79
Gebhardt, K., et al. 2000, ApJ, 539, L13
Giavalisco, M.,& the GOODS Team 2004, ApJ, 600, L93
Gingold, R. A.,& Monaghan, J. J. 1977, MNRAS, 181, 375
Granato G. L., De Zotti, G., Silva, L., Bressan, A.,& Danese, L. 2004, ApJ, 600, 580
Hasinger, G., Miyaji, T.,& Schmidt, M. 2005, A&A, 441, 417
Hopkins, P. F., Hernquist, L., Cox, T. J., Di Matteo, T., Robertson, B.,& Springel, V. 2006a, ApJS, 163, 1
Hopkins, P. F., Hernquist, L., Cox, T. J., Robertson, B.,& Springel, V. 2006b, ApJS, 163, 50
Hopkins, P. F., Hernquist, L., Cox, T. J., Robertson, B.,& Krause, E. 2007, astro-ph/0701351
Kriek, M., et al. 2006, ApJ, 649, 71
Kroupa, P. 2001, MNRAS, 322, 231
Labbé, I., et al. 2003, AJ, 125, 1107
Labbé, I., et al. 2005, ApJ, 624, L81
Li, Y., et al. 2006, astro-ph/0608190
Lucy, L. B. 1977, AJ, 82, 1013
Magorrian, J., et al. 1998, AJ, 115, 2285
Maraston, C. 2005, MNRAS, 362, 799
Maraston, C., Daddi, E., Renzini, A., Cimatti, A., Dickinson, M., Papovich, C., Pasquali, A.,& Pirzkal, N. 2006, ApJ, 652, 85
Papovich, C., et al. 2006, ApJ, 640, 92
Pei, Y. C. 1992, ApJ, 395, 130
Pettini, M., Kellogg, M., Steidel, C. C., Dickinson, M., Adelberger, K. L.,& Giavalisco, M. 1998, ApJ, 508, 539

Pettini, M., et al. 2001, ApJ, 554, 981
Quadri, R., et al. 2007, ApJ, 654, 138
Reddy, N. A., Erb, D. K., Steidel, C. C., Shapley, A. E., Adelberger, K. L.,& Pettini, M. 2005, ApJ, 633, 748
Reddy, N. A., et al. 2006, ApJ, 644, 792
Richards, G. T., et al. 2005, MNRAS, 360, 839
Robertson, B., Cox, T. J., Hernquist, L., Franx, M., Hopkins, P. F., Martini, P.,& Springel, V. 2006, ApJ, 641, 21
Rudnick, G., et al. 2001, AJ, 122, 2205
Rudnick, G., et al. 2003, ApJ, 599, 847
Sanders, D. B., Soifer, B. T., Elias, J. H., Madore, B. F., Matthews, K., Neugebauer, G.,& Scoville, N. Z. 1988, ApJ, 325, 74
Shapley, A. E., Steidel, C. C., Pettini, M.,& Adelberger, K. L. 2003, ApJ, 588, 65
Somerville, R. S. 2004, in Multiwavelength mapping of galaxy formation and evolution, ed. R. Bender,& A. Renzini (Berlin: Springer) (astro-ph/0401570)
Somerville, R. S., Lee, K., Ferguson, H. C., Gardner, J. P., Moustakas, L. A.,& Giavalisco, M. 2004, ApJ, L171
Springel, V.,& Hernquist, L. 2003, MNRAS, 339, 289
Springel, V., Di Matteo, T.,& Hernquist, L. 2005a, ApJ, 620, L79
Springel, V., Di Matteo, T.,& Hernquist, L. 2005b, MNRAS, 361, 776
Steidel, C. C., Adelberger, K. L., Shapley, A. E., Pettini, M., Dickinson, M.,& Giavalisco, M. 2003, ApJ, 592, 728
Talbot, R. J,& Arnett, W. D., 1971, ApJ, 170, 409
Ueda, Y., Akiyama, M., Ohta, K.,& Miyaji, T. 2003, ApJ, 598, 886
van der Wel, A., Franx, M., Wuyts, S., van Dokkum, P. G., Huang, J., Rix, H.-W.,& Illingworth, G. D. 2006, ApJ, 652, 97
van Dokkum, P. G., et al. 2004, ApJ, 611, 703
van Dokkum, P. G., Kriek, M., Rodgers, B., Franx, M.,& Puxley, P. 2005, ApJ, 622, L13
van Dokkum, P. G., et al. 2006, ApJ, 638, 59
Wuyts, S., et al. 2007, ApJ, 655, 51
Yan, H. et al. 2004, ApJ, 616, 63

Nederlandse samenvatting

Van toen tot nu

DERTIEN en een half miljard jaar geleden bestond het heelal uit een saaie, bijna volledig homogene oersoep van deeltjes. Bijna, want op die gladde verdeling van energie en materie kwamen minuscule rimpelingen (kleiner dan 0.01%) voor. Hoe onbeduidend ze aanvankelijk ook waren, in deze fluctuaties lag de kiem van alle structuur die vandaag in het heelal aanwezig is: sterrenstelsels, sterren, planeten, inclusief wijzelf. Gebieden in het vroege heelal waar de dichtheid iets groter was dan gemiddeld oefenden een sterkere zwaartekrachtswerking uit op hun omgeving en waren daardoor in staat meer materiaal naar zich toe te trekken. Op die wijze groeiden kleine overdichtheden uit tot grote aantrekkingspolen in een kosmisch web. De hoofdrolspeler in de geschiedenis van structuurvorming is de zogenaamde donkere materie. Hoewel tot op heden niet rechtstreeks gedetecteerd, blijkt uit indirecte waarnemingen dat deze mysterieuze vorm van materie de totale massa aan zichtbare materie, waaruit sterren, planeten en wijzelf zijn opgebouwd, met een factor 6 overtreft. Aangetrokken tot de concentraties van donkere materie, verzamelde de zichtbare materie, die in het vroege heelal voornamelijk uit waterstof en helium bestond, zich in de knooppunten van het kosmisch web. Daar kon het gas afkoelen en sterren vormen. Door middel van kernfusie in het binnenste van deze sterren werden zwaardere chemische elementen dan waterstof en helium geproduceerd. Aan het einde van hun levensloop geven sterren een gedeelte van dit materiaal terug aan het interstellaire medium in de vorm van sterwinden of spectaculaire explosies. Uit het interstellaire gas dat op die manier verrijkt werd met zwaardere elementen ontstond vervolgens een nieuwe generatie van sterren, die de cyclus voortzetten.

Vier en een half miljard jaar geleden, toen deze cyclus aan de derde generatie toe was, ontstond een ster die wij Zon noemen. Eerdere generaties van sterren hadden voldoende zware elementen geproduceerd om in een schijf om de Zon de Aarde en enkele andere planeten te laten vormen. In de tijd die volgde, zou de aardkorst het toneel vormen van een merkwaardig schouwspel waarin het ooit door sterren gevormde materiaal zich in vele structuren ontwikkelde. Een van die structuren, die ons nauw aan het hart ligt, noemen we Mens.

Van nu tot toen

De gemeenschap die zich professioneel bezighoudt met het optekenen van de kosmische geschiedenis, of een aspect ervan, heeft wereldwijd de omvang van een dorp. Hoewel dit astronomendorp al vele eeuwen zoniet millennia bestaat, berust de zonet geschetste geschiedenis grotendeels op ontdekkingen van de afgelopen 100 jaar en resten er ook nu nog vele open vragen. Eén wijk van dit dorp bestudeert de vorming en

evolutie van sterrenstelsels. Sterrenstelsels zijn verzamelingen van miljarden sterren, ingebed in een enorme wolk of 'halo' van donkere materie. Ze kunnen beschouwd worden als de bouwstenen van het heelal. Sommige sterrenstelsels behoren op hun beurt weer tot grote groepen of 'clusters' van sterrenstelsels. Onze Zon maakt deel uit van de Melkweg, een spiraalsterrenstelsel waar nog steeds gas in nieuwe sterren wordt omgezet. In de jaren '20 ontdekte de Amerikaanse astronoom Edwin Hubble dat er naast de Melkweg nog talloze andere sterrenstelsels bestonden. Deze stonden op zulke gigantische afstanden dat het licht er miljoenen jaren over had gedaan om de Aarde te bereiken. Bovendien constateerde hij dat sterrenstelsels die verder van ons af gelegen zijn zich sneller van ons verwijderen. De ontdekking van de uitdijing van het heelal was daarmee een feit.

Inmiddels hebben de bouw van grotere telescopen en de ontwikkeling van gevoeligere detectoren het mogelijk gemaakt sterrenstelsels tot meer dan 10 miljard lichtjaar (een terugkijktijd van meer dan 10 miljard jaar) op te sporen. Aangezien ieder sterrenstelsel afzonderlijk op tijdschalen van honderdduizenden tot zelfs miljarden jaren evolueert, kunnen we hun levensloop niet 'live' volgen. In plaats daarvan beschikken we over een momentopname. Door de momentopnamen van sterrenstelsels op verschillende afstanden (en dus terugkijktijden) met elkaar te vergelijken, trachten sterrenkundigen een typische levensloop van een sterrenstelsel te traceren. De sleutelvragen zijn daarbij: **Wanneer zijn de sterren in sterrenstelsels gevormd?** en **Hoe en wanneer werd de massa waaruit een sterrenstelsel is opgebouwd bij elkaar gebracht?** De huidige theorieën over vorming en evolutie van sterrenstelsels beschrijven een hiërarchisch scenario waarbij aanvankelijk kleine groeperingen van gas en sterren in de loop der tijd samensmolten tot de grote sterrenstelsels die in het huidige heelal voorkomen. Hoeveel van dergelijke botsingen nodig waren, wanneer ze plaatsvonden, en of de meeste sterren toen al waren gevormd of niet, zijn vooralsnog onbeantwoorde vragen.

De kleuren van sterrenstelsels

Al spoedig na de ontdekking dat sommige lichtbronnen aan de hemel geen sterren of gasnevels binnen onze Melkweg waren, maar afzonderlijke sterrenstelsels op veel grotere afstanden, begon men de waargenomen sterrenstelsels te ordenen naar kleur, vorm en omgeving. In het lokale heelal treffen we een tweedeling aan tussen blauwe spiraalstelsels (ook wel laat-type stelsels genoemd) die een schijfvorm hebben, en rode elliptische stelsels (vroeg-type) met de vorm van een bol of rugbybal. Ook valt op dat de fractie elliptische stelsels aanzienlijk hoger is in clusters dan in een omgeving met lagere dichtheid aan sterrenstelsels. De verschillende eigenschappen van deze twee soorten sterrenstelsels duiden erop dat ofwel hun vormingsgeschiedenis verschilt, ofwel ze zich in een verschillende fase van hun evolutie bevinden. Bekend is dat de meest massieve sterren het helderst zijn en een kortere levensduur hebben dan minder massieve sterren. Ook zijn de zwaarste sterren het heetst en hebben ze daardoor een blauwe kleur. Het is daarom een logische conclusie dat de sterpopulatie van spiraalstelsels door de band genomen jonger is dan die van elliptische sterrenstelsels. De blauwe kleur van spiraalstelsels duidt er immers op dat de meest massieve sterren nog

Figuur 1 — Fragment van het Chandra Deep Field South, een stukje hemel waarvan we de waarnemingen in dit proefschrift analyseren. De afmeting van dit gebiedje aan de hemel bedraagt slechts een twintigste van de breedte van een vinger op gestrekte armlengte. De diepe waarnemingen tonen sterrenstelsels met een grote verscheidenheid aan vormen en helderheden. Ook alle kleine vlekjes op de foto zijn sterrenstelsels (Bron: NASA, ESA, M. Giavalisco (STScI) en het GOODS Team).

in leven zijn. Omgekeerd danken elliptische stelsels hun rode kleur aan het feit dat de meest massieve sterren reeds zijn opgebrand en het licht wordt gedomineerd door de zwakkere, rode sterren. De kleur van sterrenstelsels bevat dus belangrijke informatie over hun leeftijd.

Het vinden, bestuderen en interpreteren van sterrenstelsels in het jonge heelal is om tal van redenen een stuk gecompliceerder. In de eerste plaats ontvangen we minder licht van sterrenstelsels die zich op grote afstand bevinden. Vaak wordt daarom gekozen om met grote telescopen slechts een klein stukje van de hemel waar te nemen, maar dan met bijzonder lange belichtingstijden (tot tientallen uren). Zo beslaan de waarnemingen waarop dit proefschrift zich concentreert slechts een miljoenste van de gehele hemelbol. Zoals te zien is in Figuur 7.11, telt zelfs een klein deel ervan duizenden sterrenstelsels. De lessen die getrokken worden over de vormingsgeschiedenis van sterrenstelsels berusten op de aanname dat het betreffende stukje hemel representatief is voor het gehele heelal.

Een belangrijk aspect om rekening mee te houden is het feit dat de grote verwijderingssnelheid van ver weg gelegen sterrenstelsels tot een verschuiving van het licht naar langere golflengten (rodere kleuren) leidt. Dit fenomeen wordt 'roodverschuiving' genoemd en sterrenkundigen maken er dankbaar gebruik van om afstanden

tot sterrenstelsels mee te bepalen (zo ook in dit proefschrift). Het licht van een sterrenstelsel op 10 miljard lichtjaar afstand dat optische telescopen ontvangen, is zelfs dermate roodverschoven dat het oorspronkelijk als UV-licht door het betreffende stelsel werd uitgezonden. Een robuuste vergelijking van momentopnamen uit het nabije en verre heelal vereist daarom dat we de ver weg gelegen stelsels ook met nabije-infraroodcamera's waarnemen om zo het intrinsiek optische licht in kaart te brengen.

Tenslotte wordt de kleur van een sterrenstelsel, zelfs na correctie voor roodverschuiving, niet louter door de leeftijd van haar sterren bepaald. Stof, mits in voldoende mate aanwezig tussen de sterren, kan sterlicht absorberen en doet dit met een hogere efficiëntie bij blauwere golflengten dan bij rodere golflengten. Ook de aanwezigheid van een supermassief zwart gat in het centrum van een sterrenstelsel kan, mits het gevoed wordt met voldoende materiaal, een kleurverandering veroorzaken. Sterrenstelsels die tot de laatste categorie behoren, worden actieve stelsels genoemd. Actieve sterrenstelsels komen voor in allerlei soorten. Met name de zogenaamde 'quasars' komen in dit proefschrift aan bod.

In het afgelopen decennium is duidelijk geworden dat ook in het vroege heelal reeds een grote diversiteit aan sterrenstelsels voorkwam, in verschillende vormen en gewichten, van blauwe tot rode kleuren. Met name aan de ontdekking van rode sterrenstelsels in het vroege heelal hebben Leidse sterrenkundigen een grote bijdrage geleverd. Het is in navolging van dit werk dat dit proefschrift is geschreven. **De doelstelling van dit proefschrift is om de helderheid en de kleuren van ver weg gelegen sterrenstelsels, in het bijzonder die met rode kleuren, te interpreteren in termen van fysische grootheden: massa, leeftijd, hoeveelheid stof. Net zo belangrijk is het te weten met welke nauwkeurigheid we deze schattingen kunnen maken. Tenslotte gebruiken we de waargenomen kleuren en afgeleide grootheden om een model te toetsen dat de vorming van rode sterrenstelsels tracht te verklaren aan de hand van botsingen tussen sterrenstelsels die een quasar-fase teweegbrengen.**

Dit proefschrift

Bij mijn onderzoek naar de aard van rode sterrenstelsels op hoge roodverschuiving maakte ik gebruik van waarnemingen, modellen van stellaire populaties en hydrodynamische simulaties. De waarnemingen bestonden uit optische opnamen door de Hubble ruimtetelescoop, nabije-infraroodopnamen met behulp van de ISAAC camera op de Europese Very Large Telescope (VLT), en mid-infraroodopnamen door de Spitzer ruimtetelescoop. Verder werden spectroscopische waarnemingen uitgevoerd op enkele 8-10m klasse telescopen: VLT, Gemini South en Keck. Een spectroscopische waarneming houdt in dat de verdeling van de lichtintensiteit over verschillende golflengten wordt gemeten. Dit laat toe om erg nauwkeurig de roodverschuiving, en dus afstand van een sterrenstelsel, te bepalen.

In **hoofdstuk 2** meten we de grootte van sterrenstelsels die zich in clusters tot op 7 miljard lichtjaar afstand bevinden. Onze aandacht gaat daarbij in het bijzonder naar stelsels met een vroeg-type (elliptische of lensvormige) morfologie. In combinatie met spectroscopische waarnemingen, die informatie bevatten over de variatie in snelheden waarmee sterren in een sterrenstelsels bewegen, leiden we de massa af van deze

stelsels. Door de eigenschappen van clusterstelsels met eenzelfde massa op verschillende terugkijktijden met elkaar te vergelijken, schatten we dat de sterren in massieve vroeg-type clusterstelsels reeds 11 miljard jaar geleden werden gevormd. Dat is slechts 2 miljard jaar na de oerknal. Stelsels waarvoor deze methode een iets jongere leeftijd dan gemiddeld oplevert, hebben een relatief blauwere kleur, in overeenstemming met de eerder beschreven relatie tussen kleur en leeftijd.

Kennelijk speelt veel van de stervormingsactiviteit zich vroeger in de geschiedenis van het heelal af. Om die interessante periode 10 miljard jaar geleden te bestuderen, maken we in **hoofdstuk 3** een catalogus met nauwkeurige helderheden en kleuren van sterrenstelsels in het Chandra Deep Field South, een stukje hemel dat met nagenoeg het gehele arsenaal aan telescopen op aarde en in de ruimte is waargenomen. De catalogus bestaat uit metingen met 12 kleurfilters in het optische en infrarode deel van het spectrum. Met behulp van al deze kleurinformatie schatten we de roodverschuiving tot alle objecten. Een afstandsschatting op basis van kleuren wordt ook wel fotometrische roodverschuiving genoemd. Vergelijking met een uitgebreide database van (uiterst precieze) spectroscopische roodverschuivingen leert dat de afstandsschattingen betrouwbaar zijn. Voor de sterrenstelsels op 10 miljard lichtjaar die we uit de catalogus selecteerden, schatten we vervolgens de energie output die ze bij alle infrarode golflengten tesamen (golflengte 0.008 tot 1 millimeter) uitzenden. Indien het licht een puur stellaire oorsprong heeft, is dit een maat van de hoeveelheid stervorming die schuilgaat achter stofwolken. Wanneer stof licht absorbeert, warmt het immers op en zendt vervolgens de opgenomen energie weer uit bij infrarode golflengten. Activiteit rond een supermassief zwart gat in het centrum van een sterrenstelsel kan ook voor opwarming van stof zorgen, maar deze actieve sterrenstelsels verraden hun aard vaak door röntgenstraling. We vinden dat de som van alle totale infrarood emissie uitgezonden door sterrenstelsels op 10 miljard lichtjaar gedomineerd wordt door bronnen met een rode kleur in het UV, optisch en nabije infrarood deel van het spectrum. Onder de stelsels met een rode optische kleur bevinden er zich echter ook objecten die slechts een geringe hoeveelheid infrarood licht uitzenden. Gezien hun rode optische kleur en gebrek aan re-emissie door stof, lijkt het erop dat deze stelsels op het moment van waarneming nauwelijks enige stervorming vertonen, noch open en bloot, noch afgeschermd door stof.

Hoofdstuk 4 beschrijft hoe we voor 15 rode sterrenstelsels de spectroscopische roodverschuiving bepalen. Aangezien deze stelsels nauwelijks UV-licht uitzenden, vraagt het waarnemen van hun optische spectra het uiterste van zelfs de grootste telescopen op aarde. We vinden dat het kleurcriterium waarmee ze geselecteerd werden (gebaseerd op waarneming in slechts 2 filterbanden), efficient is om ver weg gelegen rode sterrenstelsels te selecteren. Slechts 2 van de 15 sterrenstelsels bevinden zich op meer nabij gelegen afstanden. Hun kleuren worden het best geïnterpreteerd als afkomstig van erg stoffige stervormende stelsels. Twee andere spectra vertonen kenmerken van activiteit rond een centraal zwart gat in het sterrenstelsel. We vinden dat de spectroscopische roodverschuivingen voor rode ver weg gelegen sterrenstelsels in goede overeenstemming is met de geschatte fotometrische roodverschuivingen. Deze vaststelling is van essentieel belang omdat we voor het merendeel van het onderzoek aangewezen zijn op de fotometrische methode. Fouten in de afstandsbepaling zouden

leiden tot het verkeerd inschatten van zowel intrinsieke helderheden als kleuren. Op hun beurt zou dit een nauwkeurige bepaling van massa's en leeftijden van sterrenstelsels verhinderen.

In **Hoofdstuk 5** richten we onze aandacht op fysieke eigenschappen als massa, leeftijd en stofgehalte van sterrenstelsels op 10 miljard lichtjaar. We maken in deze analyse gebruik van modellen voor de kleurevolutie van stellaire populaties. In het bijzonder staan we stil bij de vraag welke extra informatie mid-infrarood waarnemingen met de IRAC camera aan boord van de Spitzer ruimtetelescoop levert. We vinden dat voor sterrenstelsels met blauwe optische kleuren de IRAC waarnemingen weinig meerwaarde opleveren. Voor rode sterrenstelsels treedt er geen globale verschuiving van de massaverdeling op, maar de onzekerheden op de geschatte grootheden voor individuele sterrenstelsels nemen wel af met een factor 3. Bovendien stellen de IRAC waarnemingen ons in staat een onderscheid te maken tussen sterrenstelsels waarvan de rode kleur veroorzaakt wordt door stervorming die schuilgaat achter grote hoeveelheden stof, en stelsels die hun rode kleur danken aan een volwassen sterpopulatie. We concluderen ook dat, net als in het lokale heelal, de meest massieve sterrenstelsels in het vroege heelal een rodere kleur hebben dan hun minder massieve tegenhangers. Het bestaan van dergelijke massieve sterrenstelsels die zo vroeg in de geschiedenis van het heelal al over een relatief oude sterpopulatie beschikken, betekent een uitdaging voor de theoretische modellen.

Hoofstuk 6 bouwt voort op de vraag hoe nauwkeurig we fysieke eigenschappen van ver weg gelegen sterrenstelsels kunnen bepalen. Echte waarnemingen stellen ons maar in beperkte mate in staat om deze vraag te beantwoorden, omdat het antwoord simpelweg niet vaak voorhanden is. We benaderen de vraag daarom vanuit een andere invalshoek en betrekken computersimulaties van sterrenstelsels in de vergelijking. Deze simulaties worden gedraaid met een computerprogramma waarin allerlei fysische wetten, van zwaartekracht en vloeistofdynamica tot stervorming en het voeden van een centraal zwart gat, zijn ingeprogrammeerd. We kiezen ervoor simulaties van botsende sterrenstelsels te bestuderen omdat de stelsels voor, tijdens en na de botsing verschillende gedaanten en kleuren aannemen. Bovendien groeit het vermoeden dat zulke gebeurtenissen een belangrijke rol spelen in de evolutie van sterrenstelsels. Gegeven een beginconditie, in ons geval twee schijfstelsels die op het punt staan te botsen, rekent het programma de tijdsevolutie van het systeem uit. Op die wijze kan voor iedere willekeurige fase in de simulatie de totale massa aan sterren, hun gemiddelde leeftijd en de hoeveelheid licht dat geabsorbeerd wordt door stof berekend worden. Tevens berekenden we de kleuren zoals we ze zouden zien als we de gesimuleerde sterrenstelsels vanaf 10 miljard lichtjaar zouden waarnemen. Op basis van deze synthetische fotometrie schatten we vervolgens de massa, leeftijd en absorptie door stof alsof het echte waarnemingen waren. Vergelijking met de echte waarden leert dat de eigenschappen van rode elliptische, 'volwassen' sterrenstelsels (de eindfase van de simulatie) goed gereproduceerd kunnen worden. Dit in tegenstelling tot eerdere fases in de evolutie wanneer er nog actief sterren worden gevormd. In dergelijke omstandigheden vormen systematische onderschattingen van de massa en leeftijd met een factor 1.5 geen uitzondering. Het onderscheid tussen veel en erg veel absorptie door stof is nauwelijks te maken.

In **hoofdstuk 7** tenslotte gebruiken we onze kennis van afstanden tot en fysieke eigenschappen van ver weg gelegen sterrenstelsels om een theoretisch model te toetsen dat een essentiële rol toeschrijft aan quasars in de evolutie van sterrenstelsels en met name de vorming van rode sterrenstelsels. Zoals eerder vermeld, zijn quasars een soort actieve sterrenstelsels. Hoog-energetische processen zorgen ervoor dat deze objecten tot de grenzen van het waarneembaar heelal betrekkelijk helder oplichten. De huidige consensus is dat een dergelijke gigantische hoeveelheid energie bij de aanvoer van materiaal naar het centrale supermassieve zwarte gat van een sterrenstelsel vrijkomt. Simulaties van botsende sterrenstelsels tonen aan dat tijdens de botsing voldoende materiaal naar het centrum wordt gevoerd om zowel een grote hoeveelheid sterren te vormen als een zwart gat te voeden. Wanneer de quasar actief wordt, verhindert die volgens het model nieuwe stervorming. Aannemend dat iedere quasar die in het heelal wordt waargenomen correspondeert met een botsing tussen twee gasrijke sterrenstelsels, vertaalt het model vervolgens de waargenomen hoeveelheid quasars naar het aantal botsende stelsels in de loop van de tijd. Wij toetsen twee voorspellingen van dit model door vergelijking met onze waarnemingen. Ten eerste het aantal massieve sterrenstelsels (in aantal per volume en massa per volume, en voor 'volwassen' en stervormende stelsels afzonderlijk). We vinden hierbij een opmerkelijk goede overeenkomst. De resultaten zijn consistent met de stelling dat ieder rood 'volwassen' stelsel ooit een quasar fase heeft ondergaan. Ten tweede vergelijken we de kleurverdeling van waargenomen en gesimuleerde stelsels. De voorspelde kleuren voor 'volwassen' stelsels zijn in overeenstemming. Dit geldt echter niet voor de kleurverdeling van stervormende stelsels. De rode kleuren van stervormende stelsels met veel stof worden niet gereproduceerd door het model.

Curriculum vitae

Op 14 december 1980 ben ik geboren te Mortsel (België). Toen ik als 14-jarige besefte dat veel van de pioniersgeest van de ruimtevaart in 1972 op de maan was achtergelaten, besloot ik niet astronaut maar astronoom te worden. Wij leefden toen nog in het enige zonnestelsel, het heelal dijde nog niet versneld uit en voorbij 10 miljard lichtjaar leefden slechts een handvol quasars en radiostelsels. Zelf volgde ik de richting Latijn-Wiskunde aan het Sint-Jan Berchmanscollege te West-Malle.

In september 1998 stak ik de rivieren over en begon de opleiding sterrenkunde aan de Universiteit Leiden. Tijdens mijn studie volgde ik te Castel Gandolfo (Vaticaanstad) een zomerschool over sterrestanten en onderzocht ik tijdens een zomerproject aan Caltech onder begeleiding van Prof. dr. Pieter van Dokkum de vormingsgeschiedenis van vroeg-type sterrenstelsels in clusters. In december 2002 slaagde ik cum laude voor het doctoraalexamen sterrenkunde.

In januari 2003 luidde een waarneemsessie met de 10 meter Keck telescoop mijn promotietijd in. Dit proefschrift beschrijft de resultaten van het onder begeleiding van Prof. dr. Marijn Franx en Prof. dr. Pieter van Dokkum verrichte onderzoek. Ik nam deel aan conferenties in Leiden, Cambridge, Vlieland, Marseille, Agios Nikolaos (Kreta) en Durham. Verder presenteerde ik mijn onderzoeksresultaten in Pasadena (SSC en Carnegie Observatories), Tucson (NOAO), New Haven (Yale), Cambridge (CfA), Baltimore (STScI) en Heidelberg (MPIA). Een belangrijk deel van mijn onderzoek werd uitgevoerd tijdens werkbezoeken aan Prof. dr. Pieter van Dokkum (Yale), Dr. Ivo Labbé (Carnegie Observatories) en Prof. dr. Lars Hernquist (CfA). Tijdens de NOVA herfstschool (Dwingeloo) en Novicosmo zomerschool (Novigrad, Kroatië) kreeg ik de gelegenheid mijn sterrenkundige kennis te verbreden. Met plezier heb ik geassisteerd bij het Sterrenkundig Practicum en het college Sterren. Tevens gaf ik een tiental lezingen voor niet-sterrenkundig publiek in heel Nederland.

Na mijn promotie zal ik mijn onderzoek naar de evolutie van sterrenstelsels voortzetten als Keck fellow aan het Harvard-Smithsonian Center for Astrophysics (Cambridge, USA).

Nawoord

De sterrenstelsels die ik bestudeerde, gaan zonder naam, slechts voorzien van een identificatienummer, door het leven. Op deze plek wil ik graag de regels omtrent nomenclatuur doorbreken en de verre lichtbronnen opdragen aan al wie van dichtbij heeft geholpen bij de totstandkoming van dit proefschrift.

De Sterrewacht bood me iedere dag een fijne en stimulerende werkomgeving, waar dankzij de inzet van het secretariaat en de computergroep alles probleemloos verliep. In het bijzonder wil ik mijn groepsgenoten in binnen- en buitenland bedanken voor alle hulp, boeiende discussies en motiverende gesprekken: Ivo, Natascha, Ned, Arjen, Maaike, Mariska, Rik, Ryan, Phil en TJ, ik heb veel van jullie geleerd. Verscheidene werkbezoeken aan Yale, Carnegie en CfA werden financieel mogelijk gemaakt door het Leids Kerkhoven-Bosscha Fonds. De mooie herinneringen aan die periodes in het buitenland heb ik te danken aan de gastvrijheid en het vrolijke gezelschap van Milan, Michelle, Kamson en de Juan gang: Tamara, Ben en Anton, binnenkort zien we elkaar vaker.

Eenmaal uitgereisd en terug op de Sterrewacht kon ik altijd een beroep doen op lotgenoten Dominic, Isa, Simon, Liesbeth, Martijn en Roderik om het kantinevoedsel te trotseren en te mijmeren over het sterrenkundige leven.

Minder wetenschappelijk, maar net zo essentieel, was de steun van familie en vrienden buiten de wetenschap bij het realiseren van dit proefschrift. In de eerste plaats mijn ouders, die me van jongsaf hebben gesteund in het nastreven van mijn dromen zonder ooit verwachtingen op te leggen. Tante Imelda wil ik bedanken voor haar prachtige schilderij op de omslag.

Tenslotte het Leidse leven; SKC H1 leerde me driemaal per week dat niets te serieus genomen moet worden. De Volleyrd Lopers leverden een unieke combinatie van puur sportgevoel en hechte vriendschap, een gezonde geest én een gezond lichaam. Ilona, Ruud, Diana, het is goed te weten dat je altijd bij iemand terecht kan. Femke, dankzij jou weet ik dat de wereld groter is dan het heelal alleen. Bedankt!